

# Infrared Camera-based Imaging Techniques for Solar-grade Silicon

Von der Fakultät für Mathematik und Physik  
der Gottfried Wilhelm Leibniz Universität Hannover  
zur Erlangung des Grades  
Doktor der Naturwissenschaften  
Dr. rer. nat.  
genehmigte Dissertation

von

Dipl.-Phys. Peter Pohl  
geboren am 7.10.1976 in Forchheim

2007

Referent: Prof. Dr. Rolf Brendel  
Korreferent: Prof. Dr. Herbert Pfnür  
Tag der Promotion: 23.05.2007

Socialism failed because it couldn't tell the economic truth;  
capitalism may fail because it couldn't tell the ecological  
truth.

[Lester Brown, 2006]

## **Keywords**

Lock-in thermography

Trapping

Lifetime

## **Schlagwörter**

Lock-in Thermographie

Trapping

Ladungsträgerlebensdauer

# Abstract

This work is focused on both developing and investigating the capabilities of infrared camera-based characterisation techniques feasible of measuring the efficiency limiting parameters of crystalline silicon solar cell material. Three techniques are investigated, which measure the infrared (IR) emission of either photogenerated or bias-induced free excess carriers using lock-in thermography, namely the infrared lifetime mapping (ILM), the infrared trap mapping (ITM) and the infrared capacitance mapping (ICM) techniques. The ILM technique has been introduced already in the year 2000 as contactless carrier lifetime imaging technique. The measures suggested therein to enhance the sensitivity are implemented in the presented work in an improved experimental setup. The additionally used gold mirror behind the sample – instead of the conventionally used blackbody – increases strongly the sensitivity of the technique. The mirror behind the sample redirects the emitted IR radiation of the free carriers to the IR camera. Based on our theoretical calculations and experimental findings we prove that under typical measurement conditions using a mirror increases the sensitivity by a factor of 1.85 at a detection wavelength of  $8\ \mu\text{m}$ . The underlying photon flux model is capable of predicting the sensitivity of any modified ILM setup. We quantify the sensitivity of ILM measurements by the noise equivalent lifetime  $NEL$ . The theoretically derived  $NEL$  agrees within 35 % with the experimental findings obtained using either a midwave or a longwave IR camera. Both IR cameras applied in this work yield comparable  $NEL$ s. Using our setup, lifetimes as short as  $1\ \mu\text{s}$  are measurable with an accuracy of 10 % at a spatial pixel resolution of  $200\ \mu\text{m}$  in a measurement period of 14 min. Theoretically, it is expected that reducing the spatial resolution to  $5.5\ \text{mm}$  by using larger and fewer detectors in the focal plane array allows the measurement of lifetimes of  $1\ \mu\text{s}$  with 10 % error in just 1 s. The application of the ILM method to multicrystalline silicon (mc-Si) allowed the spatially resolved determination of the interstitial iron concentration  $[\text{Fe}_i]$  down to  $5 \times 10^{10}\ \text{cm}^{-3}$ . In particular, in the vicinity of the grain boundaries,  $[\text{Fe}_i]$  was clearly increased. The ITM technique allows the investigation of spatially distributed minority-carrier trapping centres in silicon wafers, which cause a pronounced increase in lifetime with decreasing injection density at very low injection levels. By applying a single-level trap model to the lifetime data, mappings of the trap density  $N_t$ , the energy level  $E_t$  and the recombination lifetime  $\tau_r$  are generated. Measurements on monocrystalline Czochralski-grown silicon wafers show striation-related inhomogeneities of the trap density and a very homogeneous distribution of energy levels, suggesting that only one sort of trap is measured. We observe that regions of increased  $N_t$  are associated with a decreased  $\tau_r$ . Our measurements indicate that the ITM technique detects either oxygen-related precipitates (OPs) or secondary defects generated in the stress field of the OPs, whereas the  $\tau_r$  mappings reveal regions of increased recombination due to the OPs themselves. On typical block-cast mc-Si wafers, we observe a strong correlation between regions of increased  $N_t$  and regions of increased dislocation density  $N_{\text{dis}}$ . Furthermore, areas of increased  $N_{\text{dis}}$  show a strong deterioration in  $\tau_r$  after phosphorus gettering. We demonstrate that one single spatially resolved measurement of the IR emission signal of as-delivered mc-Si without any surface treatment already reveals poorly getterable regions, which decrease the efficiency in mc-Si solar cells. We expect that reducing the spatial resolution to  $5\ \text{mm}$  facilitates an in-line applicability of a qualitative measurement in just 1 s. The ICM technique measures the spatially resolved capacitance, which can be used to generate mappings of the base-doping concentration of solar cells. ICM detects the charge carrier density  $Q$  in the space charge region. In combination with the applied voltage  $U$  the junction capacitance  $C = Q/U$  is deduced. The doping concentration is then extracted from the  $C$ - $U$  data. After a measurement period of 28 min we find a sensitivity – expressed by the noise equivalent capacitance  $NEC$  – of  $1\ \text{nF cm}^{-2}$ , corresponding to a noise equivalent carrier density  $NECD$  of  $3 \times 10^{10}\ \text{cm}^{-2}$  at a lateral resolution of  $170\ \mu\text{m}$ .

# Zusammenfassung

Im Mittelpunkt dieser Arbeit stehen die Entwicklung und Charakterisierung Infrarot-Kamera-basierter Messmethoden, mit deren Hilfe die Effizienz-limitierenden Parameter von kristallinem Silizium-Solarzellenmaterial gemessen werden können. Folgende drei Methoden werden untersucht, welche die emittierte Infrarotstrahlung von entweder photogenerierten oder spannungsinduzierten freien Ladungsträgern durch Lock-in Thermographie messen: (i) *infrared lifetime mapping* (ILM), (ii) *infrared trap mapping* (ITM) und *infrared capacitance mapping* (ICM). Die ILM-Technik wurde bereits im Jahr 2000 als kontaktlose, bildgebende Lebensdauerermessmethode vorgestellt. Die darin vorgeschlagenen Maßnahmen zur Steigerung der Sensitivität der Methode werden in dieser Arbeit in einem selbstgebauten verbesserten Messaufbau umgesetzt. Zusätzlich wird in dieser Arbeit durch die Verwendung eines Spiegels hinter der Probe – anstelle des üblicherweise verwendeten Schwarzkörperstrahlers – deutlich die Sensitivität der ILM-Technik verbessert. Theoretische Rechnungen und experimentelle Daten zeigen, dass unter typischen Messbedingungen die Verwendung eines Spiegels die Sensitivität der ILM-Technik um einen Faktor 1.85 bei einer Detektionswellenlänge von  $8\ \mu\text{m}$  verbessert. Das zugrunde liegende Photonenflussmodell ermöglicht eine Vorhersage der Sensitivität jedes modifizierten Messaufbaus. Die Sensitivität der ILM-Messungen wird durch die *noise equivalent lifetime NEL* beschrieben. Die theoretisch abgeleitete *NEL* stimmt mit der experimentell ermittelten *NEL* einer Midwave und Longwave IR-Kamera innerhalb von 35% überein. Beide Kamerasysteme liefern eine vergleichbare *NEL*. Mit dem verwendeten Messaufbau sind Lebensdauern von  $1\ \mu\text{s}$  mit einer Genauigkeit von 10% und bei einer räumlichen Pixelauflösung von  $200\ \mu\text{m}$  innerhalb einer Messdauer von 14 min messbar. Theoretisch wird erwartet, dass eine Reduktion der Ortsauflösung auf  $5.5\ \text{mm}$  durch den Einsatz von flächenmäßig größeren, jedoch weniger Detektorpixeln die Messung von Lebensdauern von  $1\ \mu\text{s}$  bei 10% Fehler innerhalb 1 s erlaubt. Die Anwendung der ILM-Technik auf multikristallines Silizium (mc-Si) ermöglichte die ortsaufgelöste Bestimmung der interstitiellen Eisenkonzentration  $[\text{Fe}_i]$  bis zu  $5 \times 10^{10}\ \text{cm}^{-3}$ . Insbesondere in der Umgebung von Korngrenzen war  $[\text{Fe}_i]$  erhöht. Die ITM-Technik ermöglicht die Untersuchung räumlich verteilter Minoritätsladungsträger-Haftstellen (Traps) in Silizium, welche zu einem ausgeprägten Anstieg der Lebensdauer bei sinkender Injektionsdichte führen. Die Anwendung eines Ein-Niveau-Trapmodells auf die Lebensdauerermessdaten ermöglicht die Bestimmung der lokalen Trapdichte  $N_t$ , des Energieniveaus  $E_t$  und der Rekombinationslebensdauer  $\tau_T$ . Messungen an einkristallinem Czochralski-Silizium zeigen ringförmige Inhomogenitäten der Trapdichte, wobei sich eine homogene Verteilung der Energieniveaus der Traps zeigt, was darauf hindeutet, dass nur eine Art Haftstellen vorhanden ist. Bereiche erhöhter  $N_t$ -Werte zeigen oft ein reduziertes  $\tau_T$ . Unsere Messungen deuten darauf hin, dass die ITM-Technik entweder sauerstoff-korrelierte Präzipitate (OPs) oder solche Defekte detektiert, die im Verzerrungsfeld der OPs generiert werden. Die  $\tau_T$ -Mappings hingegen zeigen Gebiete erhöhter Rekombination durch die OPs selbst. Bei typischem blockgeggessenem mc-Si wird eine starke Korrelation von  $N_t$  mit der Versetzungsdichte  $N_{\text{dis}}$  beobachtet. Außerdem zeigen Gebiete mit erhöhter  $N_{\text{dis}}$  eine nennenswerte Verschlechterung von  $\tau_T$  nach Phosphorgetterung. Weiter wird gezeigt, dass eine einzige Messung der IR-Emission von gesägtem mc-Si ohne jede Oberflächenbehandlung bereits solche Gebiete detektiert, die die Effizienz von Silizium-Solarzellen verschlechtert. Theoretisch wird erwartet, dass wiederum eine Reduktion der Ortsauflösung auf  $5\ \text{mm}$  eine In-line-Anwendung durch qualitatives Messen innerhalb 1 s ermöglicht. Die ICM-Methode erlaubt die ortsaufgelöste Bestimmung der Kapazität und damit der Basisdotierung von Solarzellen. ICM bestimmt die Ladungsträgerdichte  $Q$  in der Raumladungszone. In Kombination mit der angelegten Spannung  $U$  kann die Kapazität  $C = Q/U$  berechnet werden. Die Dotierkonzentration wird aus den  $C$ - $U$  Daten extrahiert. Nach einer Messzeit von 28 min wird eine Sensitivität – ausgedrückt in Form der *noise equivalent capacitance NEC* – von  $1\ \text{nF cm}^{-2}$  erreicht,

was einer *noise equivalent carrier density*  $NECD$  von  $3 \times 10^{10} \text{ cm}^{-2}$  bei einer lateralen Auflösung von  $170 \mu\text{m}$  entspricht.





# Contents

<b>List of Abbreviations</b>	<b>v</b>
<b>List of Symbols</b>	<b>vi</b>
<b>1 Introduction</b>	<b>1</b>
<b>2 Generation and Recombination Processes in Crystalline Silicon</b>	<b>5</b>
2.1 Absorption of light in silicon . . . . .	5
2.1.1 Photogeneration of free carriers . . . . .	5
2.1.2 Free-carrier absorption . . . . .	7
2.1.3 Absorbance of a thick coplanar layer . . . . .	8
2.2 Carrier recombination mechanisms . . . . .	10
2.2.1 Definition of carrier lifetime . . . . .	10
2.2.2 Radiative band-to-band recombination . . . . .	11
2.2.3 Auger recombination . . . . .	12
2.2.4 Recombination via intermediate states . . . . .	13
2.2.5 Surface recombination . . . . .	15
2.2.6 Effective lifetime . . . . .	16
<b>3 Electrical Characterisation Techniques</b>	<b>19</b>
3.1 Carrier lifetime measurements . . . . .	19
3.1.1 Transport equations . . . . .	20
3.1.1.1 Pulsed optical excitation . . . . .	20
3.1.1.2 Transient and steady-state lifetime measurements . . . . .	22
3.1.2 Microwave-detected photoconductance decay (MW-PCD) . . . . .	23
3.1.2.1 Differential effective lifetime . . . . .	23
3.1.2.2 The Semilab WT-2000 MW-PCD system . . . . .	24
3.1.3 Quasi-steady-state photoconductance (QSSPC) . . . . .	25
3.2 Resistivity measurements . . . . .	26

---

<b>4</b>	<b>Impact of Trapping and Depletion-Region Modulation on Carrier Lifetime Measurements</b>	<b>29</b>
4.1	Minority-carrier trapping . . . . .	31
4.1.1	Hornbeck-Haynes trapping model . . . . .	31
4.1.2	Impact on photoconductance-based measurements . . . . .	32
4.1.3	Impact on free-carrier absorption-based measurements . . . . .	33
4.1.3.1	Single-level trapping . . . . .	33
4.1.3.2	Multiple-level trapping . . . . .	37
4.2	Depletion-region modulation . . . . .	38
4.2.1	Depletion-region modulation at surfaces . . . . .	38
4.2.2	Depletion region modulation at charged bulk defects . . . . .	40
4.2.2.1	Charged line defects . . . . .	41
4.2.2.2	Charged spherical defects . . . . .	43
4.2.2.3	Effect of temperature . . . . .	45
<b>5</b>	<b>Infrared Camera-based Charge Carrier Imaging</b>	<b>47</b>
5.1	Infrared thermography basics . . . . .	47
5.1.1	Fundamentals . . . . .	47
5.1.2	Infrared cameras . . . . .	49
5.1.2.1	Correction for spatial inhomogeneity . . . . .	50
5.1.2.2	Noise Equivalent Temperature Difference <i>NETD</i> . . . . .	50
5.1.2.3	Quantum Well Infrared Photodetector (QWIP) camera . . . . .	51
5.1.2.4	Mercury-Cadmium-Telluride (MCT) IR-camera . . . . .	52
5.2	Measurement principle . . . . .	53
5.2.1	Basic principles . . . . .	53
5.2.2	Calibration procedure . . . . .	56
5.2.3	Measurement setup . . . . .	57
5.2.4	Lock-in technique . . . . .	59
5.3	Sensitivity analysis . . . . .	62
5.3.1	Optical model . . . . .	64
5.3.2	Experimental verification . . . . .	69
5.3.3	Noise Equivalent Carrier Density . . . . .	73
5.4	Summary and conclusion . . . . .	74

<b>6</b>	<b>Infrared Lifetime Mapping (ILM)</b>	<b>77</b>
6.1	Previous work . . . . .	77
6.2	Determination of the effective lifetime . . . . .	79
6.3	Sensitivity analysis – Noise Equivalent Lifetime . . . . .	80
6.3.1	Theoretical derivation . . . . .	80
6.3.2	Temperature-dependent <i>NEL</i> measurements . . . . .	81
6.3.3	Discussion . . . . .	82
6.4	Application of ILM to mono- and multicrystalline silicon wafers . . .	84
6.4.1	Comparison with MW-PCD measurements . . . . .	84
6.4.2	Temperature-dependent comparison with QSSPC lifetime measurements . . . . .	87
6.4.3	Imaging of interstitial iron in multicrystalline silicon . . . . .	89
6.5	Summary . . . . .	93
<b>7</b>	<b>Infrared Trap Mapping (ITM)</b>	<b>95</b>
7.1	Previous work . . . . .	95
7.2	Experimental method . . . . .	96
7.3	Application of ITM to silicon wafers . . . . .	96
7.3.1	Impact of the trap density on the recombination lifetime in Cz-Si . . . . .	96
7.3.2	Minority-carrier trapping versus depletion region modulation in multicrystalline silicon . . . . .	101
7.3.3	ITM analysis of multicrystalline silicon wafers . . . . .	104
7.3.3.1	As-grown mc-Si . . . . .	105
7.3.3.2	Impact of phosphorus gettering . . . . .	106
7.3.4	Trap mapping without surface passivation . . . . .	108
7.4	Summary and conclusion . . . . .	111
<b>8</b>	<b>Infrared Capacitance Mapping (ICM)</b>	<b>113</b>
8.1	Capacitance of an abrupt <i>pn</i> -junction . . . . .	113
8.2	Measurement principle . . . . .	115
8.3	Application of ICM . . . . .	116
8.3.1	Calibration with FZ silicon solar cells . . . . .	116
8.3.1.1	Sample preparation . . . . .	116
8.3.1.2	Determination of the calibration constant . . . . .	117
8.3.2	Doping concentration distribution in EFG silicon . . . . .	118
8.4	Sensitivity analysis . . . . .	119
8.5	Summary and conclusion . . . . .	122

<b>References</b>	<b>123</b>
List of publications - Journal papers	137
List of publications - Conference papers	138

## List of Abbreviations

Abbreviation	Description
Al, AlGaAs	aluminium, aluminium gallium arsenide
Au	gold
B	boron
CB	conduction band
CDI	carrier density imaging
Cz	Czochralski (silicon)
DLIT	dark lock-in thermography
EFG	edge-defined film-fed grown (silicon)
FeGa	iron gallium
Fe <sub>i</sub>	interstitial iron
FZ	float zone (silicon)
Ga, GaAs	gallium, gallium arsenide
ICM	infrared capacity mapping
ILM	infrared lifetime mapping
ILIT	illuminated lock-in thermography
ITM	infrared trap mapping
LED	light emitting diode
mc	multicrystalline (silicon)
MCT	mercury cadmium telluride
MFCA	modulated free-carrier absorption
MW-PCD	microwave-detected photoconductance decay
O <sub>i</sub>	interstitial oxygen
PECVD	plasma-enhanced chemical vapour deposition
POCl <sub>3</sub>	phosphorus oxychloride
QSSPC	quasi-steady-state photoconductance
QWIP	quantum well infrared photodetector
Si	silicon
SiN <sub>x</sub>	amorphous silicon nitride
SRV	surface recombination velocity
SRH	Shockley-Read-Hall
TIDLS	temperature and injection-dependent lifetime spectroscopy
TiPdAg	titanium palladium silver
VB	valence band

## List of Symbols

Symbol	Description
$A$	absorbance
$a_0$	lattice constant
$B$	coefficient of radiative band-band recombination
$c$	vacuum velocity of light
$C$	capacitance per unit area
$C_n, C_p$	Auger coefficients
$D_{it}$	interface state density
$D_n, D_p$	diffusion coefficient for electrons and holes
$E, E_{Si}$	emissivity, emissivity of silicon wafer
$E$	energy
$E_B$	band bending
$E_C$	conduction band edge
$E_F$	Fermi level
$E_{Fn}, E_{Fp}$	electron and hole Fermi level
$E_g$	bandgap energy
$E_p$	phonon energy
$E_t$	defect energy state
$E_V$	valence band edge
$f_{li}, f_s$	lock-in frequency, sampling frequency
$G, G_{th}$	generation rate, thermal generation rate
$h$	Planck constant
$I$	current
$I$	illumination intensity
$k$	Boltzmann constant
$M$	calibration factor of the ICM technique
$m$	calibration factor of the ILM technique taking electrons and holes into account
$m_p$	calibration factor of the ILM technique for holes
$M_{BB}$	specific blackbody irradiation
$n$	electron density in non-equilibrium
$N$	number of frames
$n_0$	equilibrium electron concentration
$n_1$	SRH electron concentration
$N_A, N_D$	acceptor and donor concentration

Symbol	Description
$N_{\text{dis}}$	dislocation density
$N_{\text{dop}}$	doping density
$N_{\text{s}}$	density of spherical defects
$NEC$	noise equivalent capacity
$NECD$	noise equivalent carrier density
$NEL$	noise equivalent lifetime
$NETD$	noise equivalent temperature difference
$n_i$	intrinsic carrier concentration
$n_{\text{s}}$	electron concentration at the surface
$n_{\text{t}}$	density of trapped carriers
$N_{\text{t}}$	density of defect or trapping centres
$N_{\text{C}}, N_{\text{V}}$	density of states in the conduction and valence band
$p_0$	equilibrium hole concentration
$p_1$	SRH hole concentration
$p_{\text{s}}$	hole concentration at the surface
$q$	elementary charge
$Q_{\text{B}}$	line charge density
$QE$	quantum efficiency
$r, r_{\text{d}}, r_{\text{i}}$	radius, radius of space-charge region, inner radius
$R, R_{\text{Si}}$	reflectance, reflectance of silicon wafer
$R$	recombination rate
$R_{\text{b}}$	rear surface reflection
$R_{\text{f}}$	front surface reflection
$S$	surface recombination velocity
$S$	infrared camera signal
$S_{0^\circ}$	infrared camera in-phase signal
$S_{90^\circ}$	infrared camera $90^\circ$ -phase shifted signal
$SNR$	signal-to-noise ratio
$t$	time
$T$	temperature in units of K
$T_{\text{W}}, T_{\text{BG}}, T_{\text{BB}}$	temperature of wafer, background, blackbody in K
$T, T_{\text{Si}}$	transmittance, transmittance of silicon wafer
$U$	bias voltage
$U_{\text{bi}}$	built-in potential
$U$	net recombination rate

Symbol	Description
$U_b, U_S$	net bulk recombination rate, net surface recombination rate
$U_{SRH}, U_A, U_{rad}$	net Shockley-Read-Hall, Auger, radiative recombination rate
$U_{tot}$	total net recombination rate
$v_{th}$	thermal velocity of charge carriers
$W$	width of the sample
$W$	width of the depletion region
$X_L$	absorption length
$x, y, z$	distance
$Z$	spatial resolution
$\alpha$	absorption coefficient
$\alpha_n, \alpha_p$	free-carrier absorption coefficient for electrons and holes
$\Delta n, \Delta p$	excess electron and hole concentrations
$\Delta n'$	excess electron and hole concentration due to depletion region modulation at charged extended defects
$\Delta n_a$	apparent excess carrier concentration
$\Delta n_{cop}$	crossover point of excess carrier concentration
$\Delta n_s$	excess carrier concentration at the surface
$\Delta E_{Si}, \Delta R_{Si},$	change of emissivity, reflectance and
$\Delta T_{Si}$	transmittance of a silicon wafer
$\Delta S$	change of camera signal
$\Delta \sigma$	excess conductivity
$\epsilon_0$	free space permittivity
$\epsilon_s$	static permittivity of silicon
$\phi$	electrostatic potential with respect to the electrostatic potential in the bulk
$\Phi$	photon flux density
$\Phi_{BB}, \Phi_{Si}$	photon flux density emitted by blackbody and silicon wafer
$\Gamma$	proportionality factor to convert into camera signal
$\lambda, \lambda_{det}, \lambda_{ex}$	wavelength, detection wavelength, excitation wavelength
$\mu_n, \mu_p$	mobility of electrons and holes
$\nu$	photon frequency
$\vartheta$	temperature in units of °C
$\vartheta_W, \vartheta_{BG}, \vartheta_{BB}$	temperature of wafer, background, blackbody in °C



---

---

Symbol	Description
$\rho, \rho_{\text{sheet}}$	resistivity, sheet resistance
$\sigma_n, \sigma_p$	capture cross section for electrons and holes
$\tau$	carrier lifetime
$\tau_a$	apparent carrier lifetime
$\tau_A$	Auger recombination lifetime
$\tau_b$	bulk carrier lifetime
$\tau_d$	detrapping capture time constant
$\tau_{\text{eff}}$	effective carrier lifetime
$\tau_{n0}, \tau_{p0}$	capture time constants for electrons and holes
$\tau_r$	recombination lifetime
$\tau_{\text{rad}}$	radiative recombination carrier lifetime
$\tau_{\text{SRH}}$	SRH recombination lifetime
$\tau_t$	trapping capture time constant



# Chapter 1

## Introduction

Over the past decade, the photovoltaic market has been continuously growing due to governmental subsidies especially in Japan and Germany. However, solar electricity is still too expensive and the major challenge for the solar industry is to further reduce the cost for solar electricity.

In principle, there are two ways to reduce the cost [1]: (i) the experience curve of mass production. In general, the experience curve effect states that the more often a task is performed the lower will be the cost of doing it. Each time the cumulative production volume doubles, value-added cost (including administration, marketing, distribution, and manufacturing) fall by a constant and predictable percentage. The experience curve of the photovoltaic market over more than one decade shows that the temporarily averaged cost reduces annually by  $\sim 20\%$ .

Another way to reduce cost is (ii) research and development to create more efficient solar cells with less expensive processes. Thereby, one path is to increase the production throughput and automation of process control using fast and preferably contactless in- and offline characterisation tools. The global market share of silicon solar cells made on crystalline silicon exceeded 90% over the past years. In 2005, 38% market share is going to monocrystalline silicon, 52% to multicrystalline and 3% to ribbon-grown silicon solar cells [2]. In particular, the latter two multicrystalline and ribbon-grown silicon wafers reveal strongly inhomogeneous lateral distributions of defects. Hence, characterisation techniques giving spatially resolved information on the electronic properties of multicrystalline silicon wafers are indispensable. Over the last few years spatially resolved characterisation methods using cameras sensitive in the infrared have become increasingly important tools for the assessment of material quality and the detection and analysis of technological problems and failures in crystalline solar cell production.

Already in 1989 thermography systems combined with noise reduction by a lock-in system have been used by Kuo *et al.* [3] for detecting microcracks in copper foils deposited on polyimide substrates. Balageas *et al.* [4] applied lock-in thermography to the characterisation of the spatial distribution of electromagnetic fields by using thin resistive photothermal films. Busse *et al.* [5] developed thermal wave imaging for depth profiling of different materials. In photovoltaics the classical steady-state thermography using an infrared camera (IR-camera) has proven to be very useful to test solar cells and modules [6, 7]. The advantage of using an IR-camera over point-by-point scanning techniques is the parallel use of  $10^6$  detectors in the focal plane array of the IR-camera, reducing the measurement period for a high-resolution

lifetime mapping from hours to minutes or even seconds. Thanks to further development by Breitenstein and Langenkamp *et al.* [8–12], who adapted the method of lock-in thermography to the requirements of solar cell research, this method has found widespread use in the photovoltaics community. Their method, dark lock-in thermography (DLIT), is a versatile tool for the detection and spatially resolved characterisation of failures in solar cells. An advancement of this characterisation technique is illuminated lock-in thermography (ILIT), which has been introduced in 2004 [13, 14]. This technique allows the measurement and investigation of current paths under illumination. Hence, it reveals the distribution of all power losses within the solar cell under realistic operational conditions.

Another path has been opened by Bail *et al.* [15] in 2000 with the introduction of the infrared lifetime mapping (ILM) technique, which determines the carrier lifetime from the infrared absorption or emission of light-generated free carriers as imaged with an IR-camera. The physical principle of the ILM technique originates from the ability of free carriers to absorb and emit infrared radiation. Since an IR-camera detects both transmitted as well as emitted infrared radiation, it has to be ensured that one of the two processes dominates. It follows that two modes of the ILM technique exist, which are termed *absorption-* and *emission-*ILM.

A schematic illustrating the absorption and emission-mode of the ILM technique is shown in Fig. 1.1. Historically, the ILM technique has first been applied in absorption-mode [15], shown in Fig. 1.1(a). In order to extract the excess carrier density  $\Delta n$  from the infrared absorption, an infrared radiation source (preferably a blackbody) is placed behind the sample under investigation. The temperature of the infrared radiation source is higher than the wafer temperature  $T_{\text{BG}} > T_{\text{W}}$  to ensure that the absorption of infrared radiation in the sample dominates. In principle, the IR-camera records two images: one image is recorded with above-bandgap illumination of the sample in order to generate excess carriers and a second one without illuminating the wafer. In general, in absorption-mode an increased carrier concentration results in an increased absorption and, hence, the IR-camera, which detects the transmitted infrared radiation, measures a decreased IR-camera signal. The difference image

$$\Delta S = m\Delta nW \quad (1.1)$$

is proportional to the photogenerated excess carrier concentration  $\Delta n$  times the wafer thickness  $W$ . The proportionality factor  $m$  between the camera signal and the free-carrier concentration times the wafer thickness is obtained by a calibration performed by recording the infrared transmission signal of several silicon wafers of known doping concentrations. In this way, the ILM technique is a free-carrier imaging technique. Using the measured photogeneration rate  $G$  of the excess-carrier-generating light, the effective lifetime can be directly calculated.

The emission-mode is illustrated in Fig. 1.1(b). The crucial difference to the absorption-mode is that the wafer temperature is now higher than the background

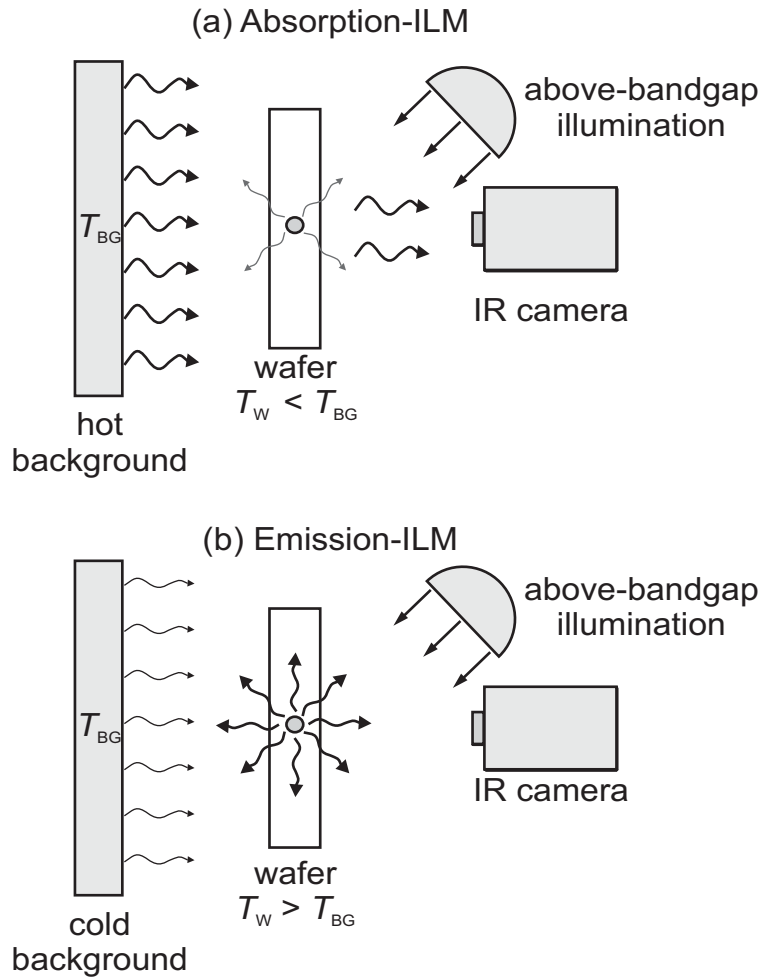


Figure 1.1: Schematic of the infrared lifetime mapping (ILM) principle in (a) absorption-mode and (b) emission-mode.

temperature  $T_W > T_{BG}$ . In emission-mode, more infrared photons are emitted with increasing carrier concentration, resulting in an increased infrared signal.

Bail *et al.* [15] demonstrated the absorption-ILM technique (qualitatively also emission-ILM) as described above on high-lifetime float-zone silicon wafers. The sensitivity of their ILM setup was not sufficiently good to analyse solar-grade silicon material used by the photovoltaic industry. In order to measure also low lifetimes typical for multicrystalline silicon material, they suggested three measures to enhance the sensitivity of the technique: (i) the application of lock-in technology to average images and to reduce the noise, (ii) imaging of the infrared emission of a heated sample to enhance the signal without saturating the camera, and (iii) the use of a long-wave IR-camera instead of a mid-wave IR-camera to observe radiation that interacts more strongly with free carriers. In the scope of this work the measures (i)-(iii) are realized, together with a fourth measure (iv) the use of a mirror instead of a blackbody behind the sample.

We show that the sensitivity of our in-house-built ILM setup is strongly increased by the measures (i)-(iv), so that lifetimes in the range of  $\mu\text{s}$  become measurable in a few seconds. Using a self-developed optical model including all optical properties of relevant components of our experimental setup, we show that the sensitivity of emission-ILM using a mirror behind the sample is most sensitive. The application of our improved ILM technique to multicrystalline silicon wafers allows for the first time imaging of the interstitial iron concentration.

In block-cast multicrystalline silicon wafers abnormally high carrier lifetimes are frequently measured when minority-carrier trapping centres are present in a significant concentration [16, 17]. However, the high apparent lifetimes obtained from photoconductance-based or – as in the present work – from free-carrier absorption-based measurement techniques at low injection levels should not be confused with the recombination lifetime of the material under test [17, 18]. At excess carrier concentrations comparable to or below the trap density, charge neutrality implies that the presence of minority-carrier traps causes a relative increase in the concentration of majority carriers, leading to an increase in the steady-state photoconductance [17] or free-carrier absorption.

Based on injection-dependent ILM measurements, we develop the infrared trap mapping (ITM) technique, which allows for the spatially resolved investigation of distributed minority-carrier trapping centres. In multicrystalline silicon wafers, the experimental findings reveal that an increased density of minority-carrier traps correlates with an increased dislocation density, whereby those areas show a strong deterioration in the recombination lifetime during phosphorus gettering. Therefore, the ITM technique is feasible of giving a comprehensive assessment of the solar cell efficiency potential of multicrystalline silicon wafers.

Moreover, based on the excellent sensitivity of our carrier imaging technique, we introduce the infrared capacitance mapping (ICM) technique, which allows the spatially resolved determination of the capacitance of  $pn$ -junctions. Due to the growth process of ribbon-grown silicon material, it is unknown whether the base doping concentration is homogeneous or not. The application of our ICM technique to ribbon-grown silicon wafers allows the determination of the spatially-resolved distribution of the base doping concentration, which is according to our experimental findings homogeneous.

# Chapter 2

## Generation and Recombination Processes in Crystalline Silicon

In this Chapter, the theoretical background of the generation and recombination processes in crystalline silicon is given. Besides the fundamental physics of free-carrier absorption and emission in the infrared wavelength region, particular attention is paid to the interpretation of carrier lifetime measurements.

### 2.1 Absorption of light in silicon

Absorption in silicon is classified into four different types: (i) absorption associated with electron excitation across the energy gap  $E_g$ , (ii) absorption due to the presence of free carriers, (iii) absorption associated with impurities or lattice defects and (iv) absorption associated with lattice vibration. In general, the absorption strongly depends on the wavelength  $\lambda$  and all of the processes (i) - (iv) contribute in parallel to the total absorption coefficient  $\alpha(\lambda)$  of a semiconductor.

For photon energies  $h\nu > E_g$  the absorption is dominated by process (i), the absorption associated with electron excitation from the valence into the conduction band, whereas the processes (ii) - (iv) are negligible. The intrinsic absorption results in the generation of electron-hole pairs, being thus the basic process for semiconductor-based photovoltaics.

For photon energies  $h\nu < E_g$  electron excitation across the energy gap becomes less likely and the other three processes dominate. The absorption associated with impurities, lattice defects and lattice vibration are typically related to specific energy levels. Hence, the corresponding absorption processes (iii) and (iv) take place at specific wavelengths. These processes are used to detect for instance the concentration of interstitial oxygen [19] and substitutional carbon [20] in silicon at a detection wavelength of 9.0  $\mu\text{m}$  and at 16.5  $\mu\text{m}$ , respectively. However, the processes (iii) and (iv) are not relevant for the present work. This work focuses on the absorption due to the presence of free carriers, the so-called *free-carrier absorption*.

#### 2.1.1 Photogeneration of free carriers

Silicon is an indirect-bandgap semiconductor, which means that the maximum energy in the valence band (VB)  $E_V$  and the minimum energy in the conduction band

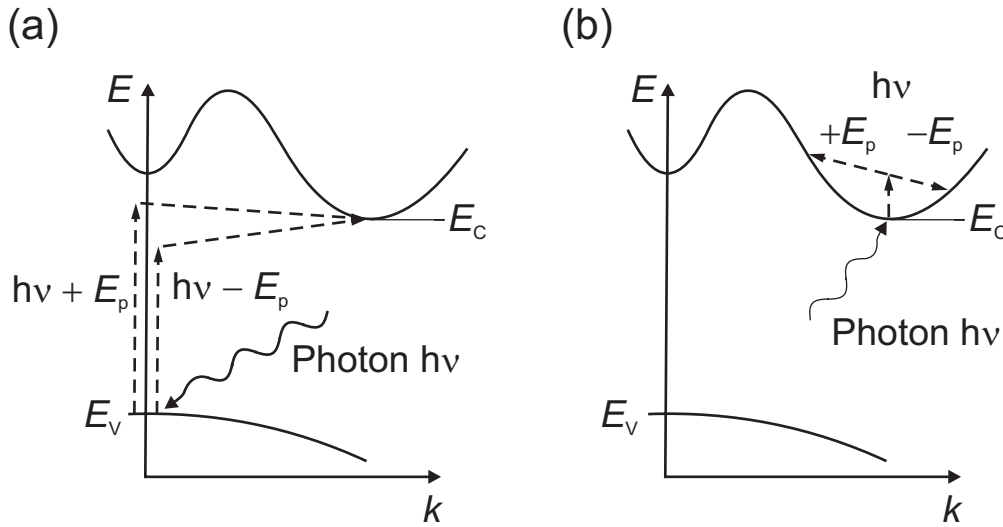


Figure 2.1: Schematic energy-crystal momentum diagram  $E(k)$  of an indirect-bandgap semiconductor, showing (a) the fundamental absorption of a photon by the excitation of an electron from the valence to the conduction band and (b) the absorption of a photon by free carriers in the conduction band, which does not result in the generation of electron-hole pairs. Both processes involve the emission or absorption of a phonon with energy  $E_p$ .

(CB)  $E_C$  occur at different values of the crystal momentum  $k$  as shown in Fig. 2.1(a). Direct transitions of electrons from the VB to the CB require photon energies much larger than energy gap  $E_g$ . Indirect transitions as indicated in Fig. 2.1(a) involve, besides the photon and generated free electron, a third particle, a phonon. Lattice vibrations or phonons possess due to the large mass of the atoms a large momentum along with a small energy, which allows for the conservation of energy and momentum. Depending on the energy of the absorbed photon, a phonon can either be absorbed or an additional one emitted, which leads to a heating of the crystal. The probability of light being absorbed by an absorption process involving a third particle is much lower than an absorption process involving only two particles. Hence, the absorption coefficient of silicon is low compared to direct semiconductors such as gallium arsenide and light can pass a few 10 to 100  $\mu\text{m}$  distance into the crystal prior to absorption.

The absorption coefficient  $\alpha$  due to band-to-band absorption together with the corresponding absorption length  $X_L = 1/\alpha$  of silicon is shown in Fig. 2.2 as solid line. The absorption length  $X_L$  is the mean free path length of a photon before it is absorbed in the silicon crystal. For photon energies larger than the bandgap  $E_g = 1.12 \text{ eV}$  at 300 K, corresponding to photon wavelength of  $\lambda < 1.11 \mu\text{m}$ ,  $\alpha$  varies over more than seven orders of magnitude. At  $\lambda = 1 \mu\text{m}$  the absorption length is  $X_L = 160 \mu\text{m}$ .



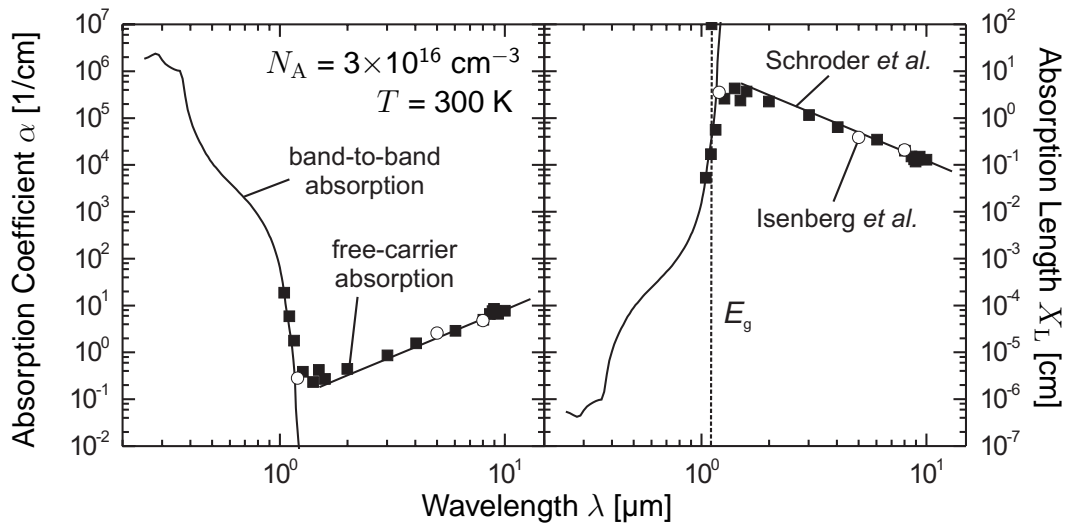


Figure 2.2: Absorption coefficient  $\alpha$  (left side) and corresponding absorption length  $X_L = 1/\alpha$  (right side) of silicon. Intrinsic band-to-band absorption (solid line  $\lambda < 1.11 \mu\text{m}$  [21]) causes electron-hole pair generation. In contrast, free-carrier absorption (symbols [22]) does not result in the generation of electron-hole pairs. Additionally, the free-carrier absorption coefficient is theoretically calculated using the parametrisation of Schroder *et al.* [23] (solid line  $\lambda > 1.11 \mu\text{m}$ , Eq. (2.2)) and Isenberg *et al.* [24] at wavelengths 1.2, 5.0 and 8.0  $\mu\text{m}$ .

### 2.1.2 Free-carrier absorption

Free-carrier absorption (FCA) involves transitions of either free electrons or holes between states in the same energy band (intraband absorption) or states in different energy bands (interband absorption). As in the case of photogeneration in indirect semiconductors discussed in the previous Section, direct transitions between two states in the same energy band are not possible via absorption or emission of a photon only. Various scattering mechanisms for the excited electron or hole are possible. Exemplary, in Fig. 2.1(b), the absorption of a photon by a free electron within the CB is shown, which requires either the emission or the absorption of a phonon due to the requirement of momentum conservation. This holds for indirect as well as direct semiconductors. The absorption of a photon by free holes in the VB can be treated correspondingly.

The free-carrier absorption may be treated using the quantum theory of transition probabilities between states of different energy. However, in addition to the electronic transitions, also transitions between different phonon states have to be taken into account [25, 26]. A similar result is obtained using the semi-classical theory of Drude [27], which uses the approach of the motion of a charge carrier in the presence of an external electric field. Both theories reveal that all characteristic features of the carrier absorption are in reasonable agreement with the experiment. However, the application of these models is rather difficult, as not all required parameters are

known, in particular at low free-carrier concentrations.

Schroder *et al.* [23] proposed a parametrisation for FCA, which is most widely used in the characterisation of silicon samples and has become a common standard. Schroder's parametrisation is based on empirical data for *p*-type [28, 29] and *n*-type [29, 30] silicon and accounts for the wavelength as well as the carrier concentration dependence of the absorption coefficient:

$$\alpha_n \cong 1.0 \times 10^{-18} \frac{\lambda^2}{[\mu\text{m}^2]} \frac{n}{[\text{cm}^{-3}]}, \quad (2.1)$$

$$\alpha_p \cong 2.7 \times 10^{-18} \frac{\lambda^2}{[\mu\text{m}^2]} \frac{p}{[\text{cm}^{-3}]}. \quad (2.2)$$

According to this parametrisation, the absorption of the free carriers is proportional to the concentration of free electrons  $n$  and free holes  $p$ , respectively. Moreover, it is proportional to the square of the wavelength  $\lambda$ . Equation (2.1) and (2.2) enable the quantitative determination of free carrier densities using infrared detectors and are thus important equations for this thesis.

It is noteworthy that during the work for this thesis a new parametrisation for FCA has been proposed by Isenberg *et al.* [24, 31], which is based on the semi-classical approach as outlined by Smith [27]. This parametrisation is given for *p*- and *n*-type silicon for wavelengths 1.2, 5.0 and 8.0  $\mu\text{m}$ . It is applicable for free carrier concentrations ranging from  $10^{15}$  to  $10^{21} \text{ cm}^{-3}$ . However, as stated in Ref. 24, the standard parametrisation of Schroder *et al.* [23] is equivalent to the new parametrisation up to free carrier concentrations of  $3 \times 10^{16} \text{ cm}^{-3}$ , as shown in Fig. 2.2. Hence, the empirical model of Schroder used in this work is appropriate, as all samples used in this work have free carrier concentrations below  $3 \times 10^{16} \text{ cm}^{-3}$ . The benefit of the parametrisation by Isenberg *et al.* [24, 31] arises from the fact that also highly doped layers, such as diffused solar cell emitters with doping concentrations above  $10^{19} \text{ cm}^{-3}$  can be quantitatively analysed using infrared absorption techniques.

### 2.1.3 Absorbance of a thick coplanar layer

In general, light passing through a silicon layer will be absorbed and the incident light intensity  $I_0$  at the surface of the layer exponentially decreases with the distance  $x$  passed into the layer. The resulting light intensity within the layer is given by the expression

$$I = I_0 e^{-\alpha x}, \quad (2.3)$$

where  $\alpha$  is the absorption coefficient, which strongly depends on the wavelength.

Figure 2.3 illustrates a light beam (normalised to a light intensity of 1) impinging normally onto the surface of a coplanar silicon layer of thickness  $W$  with front and rear side reflections  $R_f$  and  $R_b$ , respectively.

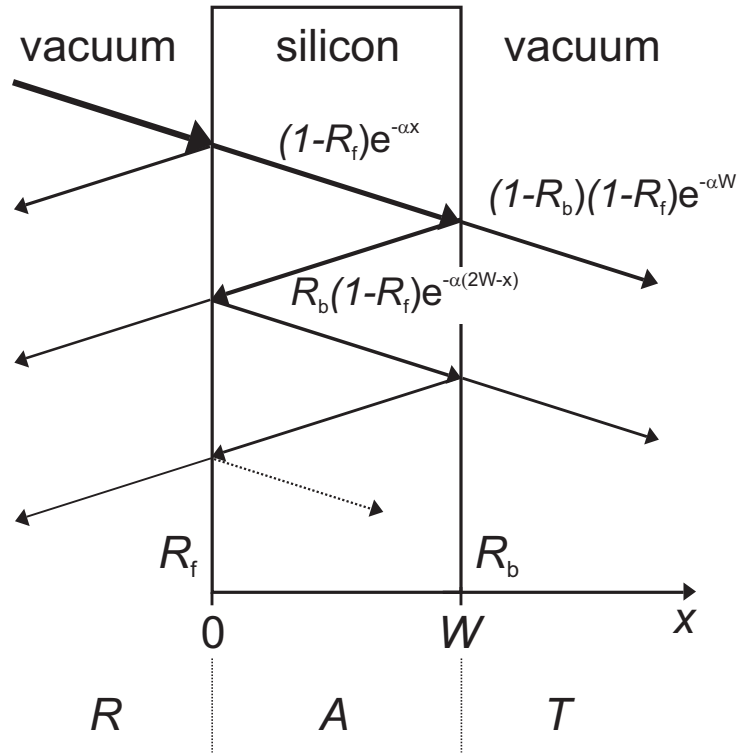


Figure 2.3: A light beam normalised to a light intensity of 1 impinges normally onto the surface of a coplanar silicon layer of thickness  $W$  with front and rear side reflections  $R_f$  and  $R_b$ . Summation over all intensity contributions yields the total reflectance  $R$ , transmittance  $T$  and absorbance  $A$ .

In order to determine the total reflectance  $R$  of the layer, we have to add all intensity contributions reflected by the sample and obtain

$$R = R_f + \frac{(1 - R_f)^2 R_b e^{-2\alpha W}}{1 - R_f R_b e^{-2\alpha W}}. \quad (2.4)$$

Summation over all transmitted intensity contributions yields the total transmittance  $T$  of the layer

$$T = \frac{(1 - R_f)(1 - R_b) e^{-\alpha W}}{1 - R_f R_b e^{-2\alpha W}}. \quad (2.5)$$

The total intensity of the incident light has to be conserved, which means that

$$1 = R + T + A. \quad (2.6)$$

Combining Eqs. (2.4) to (2.6), we obtain the absorbance

$$A = \frac{(1 - R_f)(1 - e^{-\alpha W}) + (1 - R_f) R_b e^{-2\alpha W} (e^{\alpha W} - 1)}{1 - R_f R_b e^{-2\alpha W}}. \quad (2.7)$$

Finally, it should be noted that due to the wavelength-dependence of  $\alpha(\lambda)$ ,  $R_f(\lambda)$  and  $R_b(\lambda)$ , the total reflectance  $R(\lambda)$ , transmittance  $T(\lambda)$  and absorbance  $A(\lambda)$  depend also on the wavelength.

## 2.2 Carrier recombination mechanisms

Generation in semiconductors is a process whereby electron-hole pairs are created. A typical generation process in solar cells as discussed in the previous Section is the absorption of light of appropriate wavelength shining on a semiconductor. The energy needed by the electron for the transition from the VB into the CB originates from the absorbed photon. Another generation mechanism is impact ionization, whereby highly excited charge carriers lose energy by the creation of electron-hole pairs. A third fundamental process is thermal generation via defect states, where the energy comes from multi-phonon excitation.

The principle of detailed balance, which is a very general principle, states that under equilibrium conditions each generation process must equal and balance in detail its inverse process [32]. The inverse to generation is the recombination process by which an electron annihilates with a hole. The energy released during a recombination event is transferred to a photon, an electron or hole and/or phonons, depending on the recombination mechanism. The three fundamental recombination mechanisms and their corresponding generation processes are:

- (i) radiative recombination ( $\leftrightarrow$  photogeneration),
- (ii) Auger recombination ( $\leftrightarrow$  impact ionization), and
- (iii) recombination via defect levels in the forbidden bandgap ( $\leftrightarrow$  multi-phonon excitation).

Recombination processes can occur within the bulk and at the surfaces of the semiconductor. The recombination in the bulk of a semiconductor is composed of intrinsic and extrinsic recombination processes. The intrinsic recombination processes (i) and (ii) are even present in ideal semiconductors, whereas the extrinsic recombination process (iii) is related to impurities or crystallographic defects.

A special case of process (iii) is surface recombination. The surface of a semiconductor represents an abrupt discontinuity of the crystal structure. The interruption of the lattice continuity causes a large number of non-saturated silicon, so-called dangling bonds, producing defect levels within the forbidden bandgap.

### 2.2.1 Definition of carrier lifetime

The absorption of photons may generate excess electron-hole pairs. The concentration of free carriers in illuminated semiconductors is hence in excess of their

equilibrium values. In the dark at thermal equilibrium, the product of the concentration of free electrons in the CB  $n_0$  and holes in the VB  $p_0$  is constant and equals the square of the intrinsic carrier concentration:  $n_0 p_0 = n_i^2$ . This relation is valid for doped and undoped semiconductors at equilibrium. Illumination increases the free carrier concentration for electrons to  $n = n_0 + \Delta n$  and that of holes to  $p = p_0 + \Delta p$ , where  $\Delta n$  and  $\Delta p$  are the generated excess electron and hole concentrations. This disturbs the state of thermal equilibrium and  $np > n_i^2$ .

If the light is switched off, the carrier concentrations decay back to their equilibrium values, where the semiconductor reaches again the state of minimum free energy. Assuming that the charge carriers are spatially homogeneous distributed throughout the sample and that no minority-carrier trapping centres are present,  $\Delta n = \Delta p$  holds. In this case, the decay of the excess carrier concentration  $\Delta n$  can be described by the rate equation

$$\frac{\partial \Delta n(t)}{\partial t} = -U(\Delta n(t), n_0, p_0), \quad (2.8)$$

where the net recombination rate  $U$  is defined as the difference between the total recombination rate  $R$  and the thermal generation rate  $G_{\text{th}}$ , that is  $U \equiv R - G_{\text{th}}$ . At equilibrium,  $U$  vanishes and  $R = G_{\text{th}}$ . In general,  $U$  is a polynomial in  $\Delta n$ , whereby the coefficient of zeroth degree vanishes, because  $U(\Delta n = 0) \equiv 0$  [33].  $U$  is commonly assumed to be proportional to  $\Delta n$ , thus, the carrier lifetime is defined as

$$\tau(n_0, p_0, \Delta n) \equiv \frac{\Delta n(t)}{U(\Delta n, n_0, p_0)}, \quad (2.9)$$

where it has to be kept in mind that the recombination rate typically depends in general in a nonlinear manner on the excess carrier concentration.

### 2.2.2 Radiative band-to-band recombination

In general, as in chemical kinetics, the rate of recombination events per unit volume is regarded as being proportional to a characteristic coefficient and the frequency of collision, which is itself proportional to the concentrations of the participating species. In the case of radiative band-to-band recombination, the recombination rate is proportional to the product of electron and hole concentrations  $n \times p$ . The recombination process involves the emission of a photon with energy approximately equal to that of the bandgap. Thermalisation of excited charge carriers by carrier-phonon interaction ensures that any initial excess carrier energy well above the band edges is lost before the radiative recombination occurs.

The net radiative recombination rate  $U_{\text{rad}}$  is given by

$$U_{\text{rad}} = B (np - n_i^2), \quad (2.10)$$

where  $B$  is the coefficient of radiative recombination corresponding to the transition probability for the electron falling from an occupied state in the CB to an unoccupied state in the VB. Applying Eq. (2.9) results in a radiative recombination lifetime of

$$\tau_{\text{rad}} = \frac{1}{B(n_0 + p_0 + \Delta n)} \quad . \quad (2.11)$$

In a direct semiconductor such as GaAs, radiative recombination occurs more rapidly than in an indirect semiconductor such as silicon, because a two-step process involving a phonon is required in the latter case. In silicon, the rate of radiative recombination is considered to be small or even negligible compared to other recombination processes [34]. At room temperature ( $T = 300$  K), the radiative recombination coefficient for GaAs is  $B = 3 \times 10^{-10} \text{ cm}^{-3}\text{s}^{-1}$  [35] and that of Si is  $B = 1 \times 10^{-14} \text{ cm}^{-3}\text{s}^{-1}$  [36]. Hence, radiative recombination in Si is four orders of magnitude less likely than in GaAs.

### 2.2.3 Auger recombination

Similar to its inverse process impact ionization, Auger recombination requires the interaction of three charge carriers. In addition to the recombining electron-hole pair, it involves a third free charge carrier to which the recombination energy is transferred by exciting it to a higher energy level in its respective band. From that excited level it relaxes subsequently back to the band edge by emitting a series of phonons. With the third particle being an electron or a hole, two possible recombination paths arise which are termed electron-electron-hole (eeh) process and electron-hole-hole (ehh) process. The third particle is most likely a majority carrier because of the higher availability. Hence, in  $p$ -type Si under low-injection conditions, the ehh process is more likely to occur since the rate of this process is proportional to the square of the hole concentrations. The net Auger recombination rate is proportional to the product of the densities of the charge carriers involved and, thus, can be expressed as

$$U_A = C_n (n^2 p - n_i^2 n_0) + C_p (np^2 - n_i^2 p_0) \quad , \quad (2.12)$$

where  $C_n$  and  $C_p$  are the proportionality factors of the two Auger processes (eeh and ehh) also referred to as Auger coefficients. Most commonly quoted values for Auger coefficients are those determined in Ref. 37 with  $C_n = 2.8 \times 10^{-31} \text{ cm}^6\text{s}^{-1}$  and  $C_p = 0.99 \times 10^{-31} \text{ cm}^6\text{s}^{-1}$ . Typically, Auger recombination dominates over radiative recombination in silicon [38]. From Eq. (2.12) one can determine the Auger lifetimes in  $p$ - and  $n$ -type materials under low-injection (li) conditions:

$$\tau_{A,\text{li}} = \frac{1}{C_p p_0^2} \quad \text{for } p\text{-type semiconductors and} \quad (2.13)$$

$$\tau_{A,\text{li}} = \frac{1}{C_n n_0^2} \quad \text{for } n\text{-type semiconductors.} \quad (2.14)$$

Obviously,  $\tau_{A,li}$  is independent of the injection level, whereas under high-injection (hi) conditions, the Auger lifetime is independent of the doping density:

$$\tau_{A,hi} = \frac{1}{(C_n + C_p)\Delta n^2} \quad \text{for } p \text{ and } n\text{-type semiconductors.} \quad (2.15)$$

The situation is actually more complicated than in the idealised view presented above. The Auger lifetime  $\tau_{A,hi}$  has a lower than quadratic dependence ( $\tau_{A,hi} \propto \Delta n^{1.65}$  [37, 39]), whereas  $\tau_{A,li}$  is severely underestimated at lower doping concentrations. In both cases the Coulomb interaction between electrons and holes has to be taken into account to explain these deviations from the ideal Auger process [40]. A number of empirical parametrisations of the Auger lifetime in Si for arbitrary doping and injection densities have been published within recent years [41–44]. We apply the parametrisation of Kerr *et al.* [44] for the Auger recombination rate

$$R_A = np \left( 1.8 \times 10^{-24} n_0^{0.65} + 6 \times 10^{-25} p_0^{0.65} + 3 \times 10^{-27} \Delta n^{0.8} \right) \quad (2.16)$$

in order to calculate the Auger lifetime  $\tau_A = \Delta n / U_A$  as shown in Fig. 2.5, assuming in good approximation that  $U_A \approx R_A$ , which holds for  $\Delta n > 100 \times n_i^2 / N_{\text{dop}}$  with  $N_{\text{dop}}$  being the doping concentration of the material [45].

### 2.2.4 Recombination via intermediate states

Impurities or crystallographic imperfections in a semiconductor are flaws which often produce discrete energy levels within the forbidden bandgap. An elegant and powerful description of the recombination via such intermediate states has been developed by Shockley and Read [46] and Hall [47] in 1952. Depending on the nature of the transition process, an electron making a transition from the CB into an intermediate-state level in the bandgap transfers its energy to the crystal atoms by multiple emissions of phonons or is converted into light or both. When the electronic potential energy is transformed into vibration energy of the lattice, the process is called thermal recombination. The electron within the intermediate-state level may transit into the VB, completing the recombination event. In the literature, such intermediate states are often termed as "traps", which has lead to ambiguities since traps are also considered as non-recombination active defect levels, which a capable of capturing a carrier and subsequently releasing it back into the band from which it came. In the present work we distinguish between recombination centres, capable of capturing electrons as well as holes, and trapping centres, which only capture charge carriers of one type.

According to Shockley, Read and Hall (SRH) [46, 47], the recombination rate can for sufficiently small defect concentrations be described by the equation:

$$U_{\text{SRH}} = \frac{np - n_i^2}{\tau_{p0}(n + n_1) + \tau_{n0}(p + p_1)}, \quad (2.17)$$

where the capture time constants for electrons  $\tau_{n0} \equiv (\sigma_n v_{\text{th}} N_t)^{-1}$  and holes  $\tau_{p0} \equiv (\sigma_p v_{\text{th}} N_t)^{-1}$  are proportional to the inverse product of the capture cross sections for electrons  $\sigma_n$  and holes  $\sigma_p$ , the defect concentration  $N_t$  and the thermal velocity  $v_{\text{th}}$ . The so-called SRH densities  $n_1$  and  $p_1$  are given by

$$n_1 \equiv N_C \exp\left(-\frac{E_C - E_t}{kT}\right) \quad \text{and} \quad p_1 \equiv N_V \exp\left(-\frac{E_t - E_V}{kT}\right). \quad (2.18)$$

$E_t$  is the energy level of the recombination centre and  $N_C$  and  $N_V$  are the effective densities of states in the conduction and the valence band, respectively.  $n_1$  and  $p_1$  equal the electron and hole density if the Fermi-level would coincide with the defect energy level  $E_t$ . Using  $\Delta n = \Delta p$  and Eq. (2.9), the SRH lifetime can be expressed as

$$\tau_{\text{SRH}} = \frac{\tau_{p0}(n_0 + n_1 + \Delta n) + \tau_{n0}(p_0 + p_1 + \Delta n)}{n_0 + p_0 + \Delta n}. \quad (2.19)$$

This equation can be further simplified in the cases of low and high-injection condition. Under high-injection conditions (i.e.,  $\Delta n \gg n_0 + p_0, n_1, p_1$ ), Eq. (2.19) is independent of the defect energy level, the doping concentration and the injection level:

$$\tau_{\text{SRH,hi}} = \tau_{p0} + \tau_{n0}. \quad (2.20)$$

According to Eq. (2.20), the high-injection SRH lifetime is limited by the slower of the two capture processes.

Under low-injection conditions (i.e.,  $\Delta n \ll n_0 + p_0$ ), the SRH lifetime is independent of the injection level:

$$\begin{aligned} \tau_{\text{SRH,li}} &= \tau_{p0} \left(\frac{n_1}{p_0}\right) + \tau_{n0} \left(1 + \frac{p_1}{p_0}\right) \quad \text{for } p\text{-type semiconductors, and} \\ \tau_{\text{SRH,li}} &= \tau_{n0} \left(\frac{p_1}{n_0}\right) + \tau_{p0} \left(1 + \frac{n_1}{n_0}\right) \quad \text{for } n\text{-type semiconductors.} \end{aligned} \quad (2.21)$$

Equations (2.21) further simplify if only centres with energy levels close to the middle of the bandgap are considered. For doping densities  $N_{\text{dop}}$  above  $10^{12} \text{ cm}^{-3}$ , the SRH densities  $p_1$  and  $n_1$  are small compared to  $p_0$  and  $n_0$  and the SRH lifetime is given by

$$\begin{aligned} \tau_{\text{SRH,li}} &= \tau_{n0} \quad \text{for } p\text{-type semiconductors with deep-level centres and} \\ \tau_{\text{SRH,li}} &= \tau_{p0} \quad \text{for } n\text{-type semiconductors with deep-level centres.} \end{aligned} \quad (2.22)$$



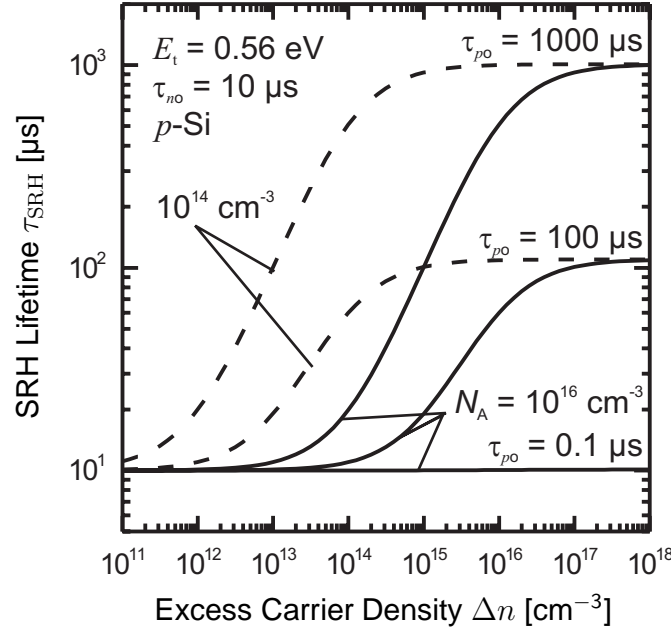


Figure 2.4: Calculated Shockley-Read-Hall lifetime  $\tau_{\text{SRH}}$  of a deep-level centre in  $p$ -type silicon as a function of the injection level  $\Delta n$  and hole capture time constants  $\tau_{p0}$  for two different doping concentrations  $N_A$ .

This shows that under low-injection conditions and in the case of a deep recombination centre the SRH lifetime is only given by the capture of the *minority* carriers, which has led to the synonym *minority-carrier lifetime* for the SRH lifetime of a deep-level centre.

As an example, Fig. 2.4 shows injection-dependent lifetime curves  $\tau_{\text{SRH}}$  assuming a deep-level centre and  $p$ -type silicon of two different doping concentrations  $N_A$ . As  $\tau_{p0}$  and  $\tau_{n0}$  essentially reflect the values of the capture-cross sections, the strongest injection level dependence is obtained for strongly asymmetric capture cross sections  $\sigma_p \ll \sigma_n$ . Moreover, the injection level corresponding to the maximum slope shifts linearly with the doping concentration.

### 2.2.5 Surface recombination

Recombination at the surface of a semiconductor can be treated as a special case of the SRH recombination. In general, at surfaces or interfaces the lattice periodicity is disturbed in an otherwise uniform crystal structure. This results in a large number of unsaturated dangling bonds, which create, due to statistical variations in the bond angles and distances of neighbouring atoms, a large density of intermediate states within the bandgap [48, 49]. However, in contrast to the single-level recombination centres in the bulk the surface states are continuously distributed within the bandgap, resulting in an energy-dependent interface state density  $D_{\text{it}}(E)$

[ $\text{cm}^{-2} \text{eV}^{-1}$ ] rather than a fixed defect concentration  $N_t$  [ $\text{cm}^{-3}$ ] for the bulk defects. Neglecting carrier transitions between the intermediate energy states, the standard SRH expression (2.17) has to be integrated over the entire bandgap to obtain the overall surface recombination rate

$$U_S = (n_s p_s - n_i^2) \int_{E_V}^{E_C} \frac{v_{\text{th}} D_{\text{it}}(E)}{\frac{n_s + n_1(E)}{\sigma_p(E)} + \frac{p_s + p_1(E)}{\sigma_n(E)}} dE. \quad (2.23)$$

Note that apart of  $D_{\text{it}}$ ,  $n_1$  and  $p_1$  also the capture-cross sections  $\sigma_n$  and  $\sigma_p$  are functions of the energy.  $n_s$  and  $p_s$  refer to the carrier concentrations at the surface. Since the surface recombination rate  $U_S$  is a rate per unit area, the definition of a surface carrier lifetime using Eq. (2.9) is not possible. Instead, the *surface recombination velocity* (SRV) is defined via

$$S \equiv \frac{U_S(\Delta n_s, n_0, p_0)}{\Delta n_s}. \quad (2.24)$$

For an unpassivated surface, the SRV is limited to the thermal velocity  $v_{\text{th}}$  due to the large number of dangling bonds.

In many practical cases, a charge-induced surface potential is present so that the carrier concentrations at the surface  $n_s$  and  $p_s$  differ from the carrier concentrations in the bulk. Commonly used passivation layers for silicon such as silicon oxide, silicon carbide or silicon nitride films are known to possess positive fixed charges, which cause in addition to a reduced  $D_{\text{it}}$  the so-called "*field effect passivation*", where one type of charge carrier is reduced at the surface by the charge-induced band bending. For SRH recombination, the recombination rate is maximal if  $\sigma_n n_s = \sigma_p p_s$  (for equal capture-cross sections,  $n_s = p_s$ ), since both electrons and holes are required in a recombination event. Consequently, the field effect passivation is based on a decreased recombination rate due to strongly differing  $n_s$  and  $p_s$ . This effect is also taken advantage of when highly doped surface layers are used to reduce the concentration of one carrier type, referred to as *floating junctions* [50] or *back surface fields* [51], depending on whether the conduction type of the bulk material is changed or not.

In this work, 70 nm thick  $\text{SiN}_x$  films are deposited in a remote plasma-enhanced chemical vapor deposition system at  $400^\circ\text{C}$  [52], which results in a high-quality surface passivation. Best passivation quality is obtained for  $\text{SiN}_x$  with a refractive index of  $n_{\text{SiN}} = 2.4$  at a wavelength of 632 nm [33].

## 2.2.6 Effective lifetime

The various recombination mechanisms described above occur in parallel and independent of each other. The total recombination rate is the sum of the rates corresponding to the individual processes described in the previous Sections:

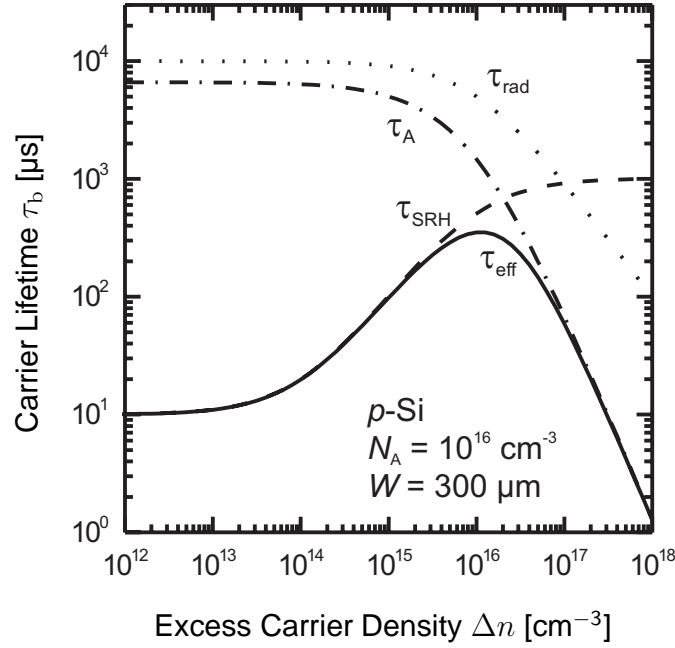


Figure 2.5: Calculated bulk carrier lifetime  $\tau_b$  as a function of the injection level  $\Delta n$  for  $p$ -type silicon with a doping concentration of  $N_A = 10^{16} \text{ cm}^{-3}$ . The bulk carrier lifetime is calculated according to Eq. (2.26). The radiative lifetime  $\tau_{\text{rad}}$  is determined according to Eq. (2.11) and the Auger lifetime  $\tau_A$  is calculated using the parametrisation of Kerr [38] according to Eq. (2.16). For the SRH lifetime  $\tau_{\text{SRH}}$  we use the calculated curve given in Fig. 2.4 for the case of  $\tau_{p0} = 1000 \text{ } \mu\text{s}$ ,  $\tau_{n0} = 10 \text{ } \mu\text{s}$  and  $E_t = 0.56 \text{ eV}$ .

$$U_{\text{tot}} = U_{\text{rad}} + U_A + U_{\text{SRH}} + U_S. \quad (2.25)$$

The first three recombination rates, namely radiative recombination  $U_{\text{rad}}$ , Auger recombination  $U_A$  and SRH recombination  $U_{\text{SRH}}$ , are usually lumped into a bulk recombination rate  $U_b = U_{\text{rad}} + U_A + U_{\text{SRH}}$  with corresponding bulk recombination lifetime  $\tau_b$ . In carrier lifetime measurements all recombination channels are present and hence an effective lifetime defined as  $\tau_{\text{eff}} \equiv \Delta n / U_{\text{tot}}$  is determined. Using Eqs. (2.9) and (2.25) one obtains

$$\frac{1}{\tau_{\text{eff}}} = \frac{1}{\tau_{\text{rad}}} + \frac{1}{\tau_A} + \frac{1}{\tau_{\text{SRH}}} + \frac{2S}{W} = \frac{1}{\tau_b} + \frac{2S}{W}. \quad (2.26)$$

In order to illustrate the interaction of the various recombination paths, in Fig. 2.5, the calculated bulk carrier lifetime  $\tau_b$  for a 300  $\mu\text{m}$  thick  $p$ -type silicon wafer with a doping concentration of  $N_A = 10^{16} \text{ cm}^{-3}$  is shown. Surface recombination via defect states is neglected. In the injection range from  $\Delta n = 1 \times 10^{12} \text{ cm}^{-3}$  to  $1 \times 10^{15} \text{ cm}^{-3}$ , mainly the SRH recombination limits the effective lifetime, which is typical for the measurements shown in this thesis.



# Chapter 3

## Electrical Characterisation Techniques

In this Chapter, the electrical measurement techniques are briefly discussed, which we apply to characterise the samples investigated in this work. Special attention is paid to recombination lifetime measurements, which allow a direct comparison of the carrier lifetimes determined using the infrared-camera-based techniques. The methods described include the microwave-detected photoconductance decay technique, the quasi-steady-state photoconductance method and the four-point-probe technique.

### 3.1 Carrier lifetime measurements

The effective recombination lifetime  $\tau_{\text{eff}}$  as defined by expression (2.26) quantifies the rate of recombination occurring within a silicon sample. A variety of techniques exist for measuring the carrier lifetime, as defined by Eq. (2.26). The carrier lifetime is of particular importance, since it allows the prediction of the performance of finished solar cells from partially processed substrates and can be used to optimise and monitor the process sequence in the solar cell production. The effective lifetime can be obtained by monitoring the excess carrier density from the voltage across a barrier layer [53–55], from the photoconductance [56], from the luminescence [57–60] or from the free-carrier absorption [15, 61–63]. All these methods, except measuring the voltage across a barrier, are contactless techniques, which enable one to investigate the sample in an early stage of the production process.

Photoconductance-based techniques are presently applied not only in research laboratories but also in industrial solar cell production lines [64, 65]. The measurement of the photoconductance is non-destructive and possible with microwave reflection [66], capacitive [67] or inductive coupling to a resonator circuit [68]. However, in recent years camera-based imaging techniques, which either detect the free-carrier absorption [15, 62] or the luminescence [69–73], became increasingly important, since these techniques provide short measurement periods in combination with a high spatial resolution. In this work, the applicability of a free-carrier-absorption-based technique using an infrared camera is investigated in detail. Thereby the measured effective lifetime is compared with photoconductance-based techniques.

### 3.1.1 Transport equations

For the sake of simplicity, we assume in the following that (i) the semiconductor is homogeneously doped and non-degenerate, (ii) the bulk lifetime  $\tau_b$  and the mobility of the electrons  $\mu_n$  and holes  $\mu_p$  is location-independent and (iii) the dimensions of the sample and of the laterally homogeneous excitation light intensity is sufficiently large, so that we can reduce our considerations to the 1-dimensional case. The theory of recombination dynamics of excess electron-hole pairs  $\Delta n(z, t)$  as a function of the depth from the sample surface  $z$  and time  $t$  is described by the ambipolar diffusion equation [74]

$$\frac{\partial \Delta n(z, t)}{\partial t} = G(z, t) - \frac{\Delta n(z, t)}{\tau_b} + D_a \frac{\partial^2 \Delta n(z, t)}{\partial z^2} - \mu_a E \frac{\partial \Delta n(z, t)}{\partial z}, \quad (3.1)$$

where  $G(z, t)$  is the photogeneration rate,  $\Delta n(z, t)/\tau_b$  is the bulk recombination rate,  $D_a = (n + p) / (n/D_p + p/D_n)$  is the ambipolar diffusion coefficient and  $\mu_a = (n - p) / (n/\mu_p + p/\mu_n)$  the ambipolar mobility. Please note that Eq. (3.1) is valid for all injection levels, but generally not analytically solvable. Under low-injection conditions (i) the electric field  $E$  is negligible for the minority-carrier transport [75], (ii) the bulk recombination lifetime  $\tau_b$  is independent of injection level, (iii) the ambipolar diffusion coefficient can be replaced by the minority-carrier diffusion coefficient and is also independent of injection-level. Hence, assuming  $p$ -type silicon the ambipolar diffusion equation simplifies to

$$\frac{\partial \Delta n(z, t)}{\partial t} = G(z, t) - \frac{\Delta n(z, t)}{\tau_b} + D_n \frac{\partial^2 \Delta n(z, t)}{\partial z^2}. \quad (3.2)$$

Expression (3.2) is – in contrast to the ambipolar diffusion equation (3.1) – analytically solvable. Assuming a sample of thickness  $W$  with equally passivated surfaces, the loss of excess carriers at the two surfaces at  $z = \pm W/2$  is given by the boundary conditions

$$-D_n \left. \frac{\partial \Delta n(z, t)}{\partial z} \right|_{z=-\frac{W}{2}} = -S \Delta n\left(-\frac{W}{2}, t\right) \quad \text{and} \quad -D_n \left. \frac{\partial \Delta n(z, t)}{\partial z} \right|_{z=+\frac{W}{2}} = +S \Delta n\left(+\frac{W}{2}, t\right), \quad (3.3)$$

where  $S$  is the surface recombination velocity (SRV).

In the following, we discuss the solutions of Eq. (3.2) for the two special cases of a pulsed and a slowly decaying optical excitation assuming the realistic case of a non-uniform excitation and non-zero surface recombination.

#### 3.1.1.1 Pulsed optical excitation

Assuming the excitation pulse width is short compared to the response time of the excited system, the pulsed optical excitation can be described by a Dirac delta

function at  $t = 0$ , i.e.  $G(z, t) = G_0(z)\delta(t)$ . The solution of Eq. (3.2) averaged (integrated) over the wafer thickness can then be written as [76, 77]

$$\Delta n_{\text{av}}(t) = \sum_{i=0}^{\infty} B_i \frac{\sin(a_i W/2)}{a_i} \exp\left(-\frac{t}{\tau_i}\right), \quad (3.4)$$

where the coefficients  $B_i$  depend on the sample thickness  $W$ , the surface recombination velocity  $S$ , the absorption coefficient  $\alpha(\lambda)$ , the optical reflectance  $R$  of the semiconductor at the wavelength of optical excitation and the illumination intensity  $\Phi$ . The decay time constants  $\tau_i$  are given by the expression

$$\frac{1}{\tau_i} = \frac{1}{\tau_b} + a_i^2 D_n, \quad (3.5)$$

where the  $a_i$  are given by the non-algebraic equation

$$\cot a_i W = \frac{D_n^2 a_i^2 - S^2}{2 D_n a_i S}, \quad (3.6)$$

which is numerically solvable for  $a_i$ . With increasing  $i$  the values of  $a_i$  increase monotonically ( $a_{i+1} > a_i$ ) and, thus, the decay time constants  $\tau_i$  decrease with increasing  $i$ . This results in a vanishing impact of the higher (faster) decay modes after a certain period.

The multiexponential decay is due to the non-uniform excitation and the distribution of the excess carriers within the sample shortly after the excitation pulse is terminated. At  $t = 0$  the maximum of the excess carrier concentration is located near the surface. For increasing  $t$  the maximum of the excess carrier concentration moves, driven by a concentration gradient, towards half wafer thickness. The transport is limited by the surface recombination and the diffusion coefficient. The impact of the higher modes vanishes gradually and only the ground mode  $\tau_0$  remains. For a 300  $\mu\text{m}$  thick planar  $p$ -type silicon wafer ( $\tau_b = 1$  ms and  $S = 10^5$  cm/s), which is excited with a light pulse at a wavelength of  $\lambda = 904$  nm, the impact of the higher modes vanishes after a few 100 ns [33]. For large  $t$ ,  $\Delta n$  decays monoexponentially with time constant  $\tau_0$ , which equals the measured effective carrier lifetime  $\tau_{\text{eff}}$  being 3.1  $\mu\text{s}$  for the considered case. In general, with decreasing  $S$  the impact of the higher decay modes becomes less important [77].

Considering only the fundamental mode of the transcendental Eq. (3.6) [78] and provided that the surface recombination velocity  $S$  is small and equal for both surfaces of the sample, allows a linear approximation of the tangent function in Eq. (3.6). Inserting  $a_0$  into Eq. (3.5), the effective carrier lifetime  $\tau_{\text{eff}} \equiv \tau_0$  can be written as [79]

$$\frac{1}{\tau_{\text{eff}}} = \frac{1}{\tau_b} + \frac{2S}{W}, \quad (3.7)$$

which is accurate to within 4% for  $S < D/4W$  [80].

### 3.1.1.2 Transient and steady-state lifetime measurements

Assuming that a non-zero optical excitation that varies exponentially with decay time constant  $\tau_{\text{decay}}$ , the generation rate  $G(z, t) = g(z)e^{-\frac{t}{\tau_{\text{decay}}}}$  in Eq. (3.2) cannot be neglected. Integration of Eq. (3.2) over the wafer thickness  $W$  with the boundary conditions of Eq. (3.3) yields [81]

$$\frac{\partial \Delta n_{\text{av}}(t)}{\partial t} = G_{\text{av}}(t) - \frac{\Delta n_{\text{av}}(t)}{\tau_{\text{eff}}(\Delta n_{\text{av}})}, \quad (3.8)$$

where

$$\Delta n_{\text{av}}(t) = \frac{1}{W} \int_{-W/2}^{+W/2} \Delta n(z, t) dz \quad \text{and} \quad G_{\text{av}}(t) = \frac{1}{W} \int_{-W/2}^{+W/2} G(z, t) dz, \quad (3.9)$$

and

$$\frac{\Delta n_{\text{av}}(z, t)}{\tau_{\text{eff}}(\Delta n_{\text{av}})} = \frac{1}{W} \left[ \int_{-W/2}^{+W/2} \frac{\Delta n(z, t)}{\tau_{\text{b}}(\Delta n)} dz + S \Delta n \left( \frac{-W}{2}, t \right) + S \Delta n \left( \frac{+W}{2}, t \right) \right]. \quad (3.10)$$

From Eq. (3.8) we can derive two fundamentally different modes for measuring the effective lifetime. (i) Using a short light pulse of decay time constant  $\tau_{\text{decay}}$  and assuming that the effective carrier lifetime  $\tau_{\text{eff}} \gg \tau_{\text{decay}}$ , the transient lifetime  $\tau_{\text{eff.trans}}$  is determined. (ii) In the steady-state mode, the excess carrier density is measured under constant illumination conditions and the steady-state lifetime  $\tau_{\text{eff.ss}}$  is determined. For this two extreme cases Eq. (3.18) simplifies to

$$\tau_{\text{eff.trans}} = - \frac{\Delta n_{\text{av}}}{\frac{\partial \Delta n_{\text{av}}}{\partial t}} \quad \text{for transient mode and} \quad (3.11)$$

$$\tau_{\text{eff.ss}} = \frac{\Delta n_{\text{av}}}{G_{\text{av}}} \quad \text{for steady-state mode.} \quad (3.12)$$

The infrared camera-based lifetime measurement technique discussed in Chapter 6 determines the steady-state lifetime according to Eq. (3.12). Evaluation of the transient lifetime data after the photogeneration has decreased to small levels corresponds to a pulsed optical excitation, as discussed in Sec. 3.1.1.1, whereby the solution of Eq. (3.4) only includes the monoexponential decay of the photogenerated carriers.

It should be noted that for large surface recombination velocities the solution of the differential equation Eq. (3.8) under the boundary conditions Eq. (3.3) shows that the spatial excess carrier density distribution in the wafer and, hence,  $\tau_{\text{eff}}$  is different under steady-state and transient illumination [76, 81, 82]. The carrier recombination at the surfaces, especially at the illuminated front surface, turns out to be predominant in the steady-state mode.



### 3.1.2 Microwave-detected photoconductance decay (MW-PCD)

The microwave-detected photoconductance decay (MW-PCD) [83–86] technique measures the transient decay of the photoconductance after a pulsed optical excitation, as discussed in Sec. 3.1.1.1. The excess photoconductance and, thus, the excess photoconductivity  $\Delta\sigma$  is proportional to the average excess carrier density  $\Delta n_{\text{av}}$

$$\Delta\sigma(t) = q(\mu_n + \mu_p) \Delta n_{\text{av}}(t), \quad (3.13)$$

where  $\Delta\sigma(t)$  is measured using microwaves reflected by the light-generated free carriers in the wafer.

Experimentally, the multiexponential decay during the initial period of a few hundred nanoseconds is usually not analysed and only the monoexponential asymptotic decay is used to determine  $\tau_{\text{eff}}$ :

$$\Delta n_{\text{av}}(t) = \Delta n_{\text{av},0} \exp\left(-\frac{t}{\tau_{\text{eff}}}\right). \quad (3.14)$$

In general, the reflected microwave power is a non-linear function of the conductivity of the sample  $\sigma_0$  and is only linearly proportional to the conductivity if the light-induced change of the conductivity  $\Delta\sigma$  is much smaller than  $\sigma_0$ , i.e.  $\Delta\sigma \ll \sigma_0$ . Hence, a light-bias is typically applied, where a steady-state background carrier density  $\Delta n_b$  is generated by a constant white bias-light illumination and an additional carrier density  $\delta n$  is generated by a short laser pulse with  $\Delta n_b \gg \delta n$ . In this way, the so-called differential lifetime is measured.

#### 3.1.2.1 Differential effective lifetime

The differential lifetime is defined as the change of the excess carrier density  $\partial\Delta n$  with changing recombination rate  $\partial U_{\text{eff}}(\Delta n)$  at a specific bias-light-generated excess carrier concentration  $\Delta n_b$ :

$$\tau_{\text{eff,diff}}(\Delta n_b) \equiv \left[ \frac{\partial U_{\text{eff}}(\Delta n)}{\partial \Delta n} \right]_{\Delta n_b}^{-1}. \quad (3.15)$$

Only if  $U_{\text{eff}}$  is linear in  $\Delta n$  and, thus, the effective carrier lifetime is injection-level independent, i.e.  $U_{\text{eff}} = \Delta n/\tau_{\text{eff}}$ , the differential effective lifetime equals the actual effective lifetime  $\tau_{\text{eff,diff}} = \tau_{\text{eff}}$ . However, in general, the carrier lifetime is injection-dependent and, hence, we find  $\tau_{\text{eff,diff}} \neq \tau_{\text{eff}}$  [87], where the difference between the differential and actual lifetime can be significant. Since the solar cell is an electronic device which works under constant illumination conditions, the actual effective lifetime  $\tau_{\text{eff}}$  is the relevant for solar cells.

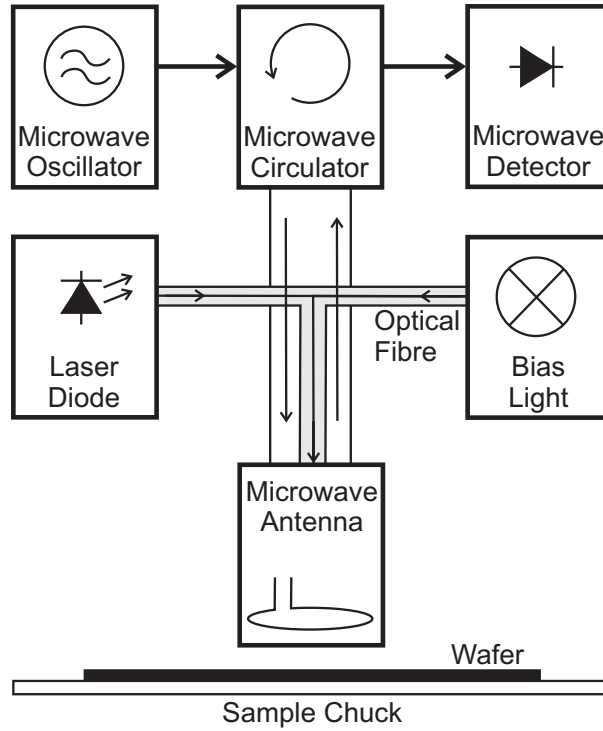


Figure 3.1: Schematic of the Semilab WT-2000 MW-PCD system used in this study.

In order to obtain the effective lifetime  $\tau_{\text{eff}}$  at a specific bias-light-induced carrier density  $\Delta n = \Delta n_b$  from light-biased PCD measurements, Eq. (3.15) has to be integrated [88]

$$\frac{1}{\tau_{\text{eff}}(\Delta n_b)} = \frac{U_{\text{eff}}(\Delta n_b)}{\Delta n_b} = \frac{1}{\Delta n_b} \int_0^{\Delta n_b} \frac{1}{\tau_{\text{eff,diff}}(\Delta \hat{n})} d\Delta \hat{n}. \quad (3.16)$$

The difference of the differential and actual effective lifetime has been investigated in detail in a series of publications [87–91].

### 3.1.2.2 The Semilab WT-2000 MW-PCD system

In this study, we use a Semilab WT-2000 MW-PCD system which consists of an excitation/detection unit including a detector, an oscillator, a circulator and an antenna. The excess carriers are generated by 100 ns light pulses from a 904 nm diode laser with a pulse rate of 1.6 kHz. The microwaves are generated by a tunable Gunn diode able to generate microwaves in the frequency range from 10.043 GHz to 10.558 GHz. In order to obtain maximum signal amplitudes, the microwave frequency is adjusted for each sample. Additionally, halogen bias light adjustable between 0 and 2 suns is applicable. Both the laser light and the halogen bias light are coupled into a bundle of optical fibres which end close to the centre of the microwave antenna, as shown schematically in Fig. 3.1. The excitation/detection unit is integrated into a

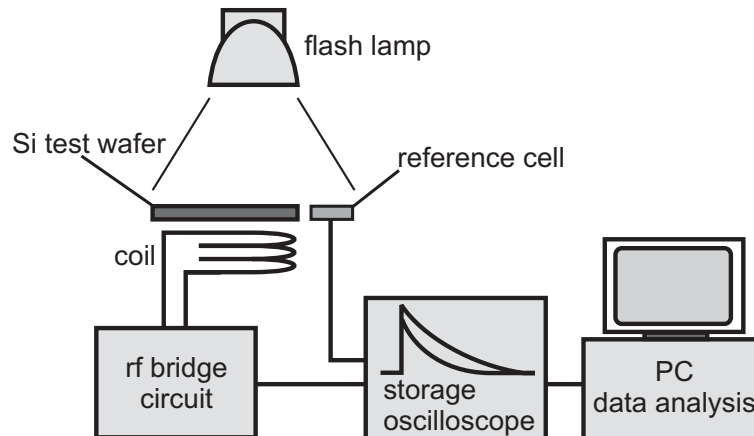


Figure 3.2: Schematic of the QSSPC setup. The quasi-steady-state illumination conditions allow to determine the carrier lifetime over a wide injection range using a single flash only.

mapping system that is moveable within the sample plane across the wafer surface to perform spatially resolved lifetime measurements of wafers.

A scanning resolution down to  $\sim 125 \mu\text{m}$  can be realised. Indeed, the spatial resolution is rather limited by carrier diffusion than by the minimum scanning resolution of the detector head. Due to the diffusion of excess carriers (excited by light coming from the optical fibre with radius  $0.5 \text{ mm}$ ) into neighbouring areas with differing carrier lifetime, the measured lifetime is averaged over the microwave-detected area ( $\sim 1 \text{ cm}^2$ ).

The detector measures the reflected microwave signal, which depends on the excess photoconductivity  $\Delta\sigma(t)$ , hence, on the carrier density  $\Delta n_{\text{av}}(t)$  of the sample. An automated fitting routine evaluates only the mono-exponential asymptotic decay curve of the excess carriers according to Eq. (3.14).

### 3.1.3 Quasi-steady-state photoconductance (QSSPC)

Measuring the quasi-steady-state photoconductance\* (QSSPC) is a widespread technique to determine the absolute lifetime of a silicon sample [68]. The experimental apparatus used in this work was fabricated by Sinton Consulting and a schematic is given in Fig. 3.2. The sample is illuminated with a slowly decaying flash with a decay time constant of  $\sim 2 \text{ ms}$ . Due to the slow decay time, the sample is measured under quasi-steady-state conditions. The quasi-steady-state condition is maintained as long as the flash time constant is much longer than the effective carrier lifetime of the sample. The sample under test is inductively coupled to a radio-frequency (rf) bridge circuit. The coil generates a magnetic field inducing eddy currents in

\*The term *quasi-steady-state* refers to the fact that the electron-hole generation rate proceeds with a decay time constant much longer than the time necessary for the charge carriers to reach steady-state conditions.

the sample. Increasing the conductivity of the sample increases the eddy current strength, which leads to an increased absorption of energy from the resonant circuit. The calibration of the resonant circuit is done by measuring the output voltage of the rf circuit as a function of the dark conductance of wafers with known base doping concentrations.

The excess carrier concentration  $\Delta n(t)$  is calculated from the measured change of the photoconductance and, therefore, from the excess conductivity  $\Delta\sigma(t)$  according to Eq. (3.13), where  $\mu_n$  and  $\mu_p$  are the electron and hole mobilities, which are functions of the dopant density  $N_{\text{dop}}$  and injection level  $\Delta n$  [43, 92–96]. In the original QSSPC analysis software used in the present work, an empirical mobility model published in Ref. 43 is applied:

$$\mu_n + \mu_p = 1800 \frac{1 + \exp \left[ 0.8431 \times \ln \left( \frac{\Delta n + N_{\text{dop}}}{N_{\text{ref}}} \right) \right]}{1 + 8.36 \times \exp \left[ 0.8431 \times \ln \left( \frac{\Delta n + N_{\text{dop}}}{N_{\text{ref}}} \right) \right]}, \quad (3.17)$$

where  $N_{\text{ref}} = 1.2 \times 10^{18} \text{ cm}^{-3}$ .

A generalised QSSPC analysis procedure has been introduced by Nagel *et al.* [81], which accounts for the fact that the QSSPC technique is a quasi-steady-state rather than a steady-state technique and, hence, Eq. (3.8) has to be applied to obtain the effective lifetime of a sample, which results in

$$\tau_{\text{eff}} = \frac{\Delta n(t)}{G(t) - \frac{\partial \Delta n(t)}{\partial t}}. \quad (3.18)$$

The illumination intensity  $I(t)$  incident on the sample is measured by a reference solar cell in units of suns. Knowing the short-circuit current density of the reference solar cell at one sun illumination intensity  $J_{\text{sc.1sun}}$  enables the calculation of the generation rate  $G(t)$  within the sample according to

$$G(t) = \frac{I(t) \cdot J_{\text{sc.1sun}}}{q} f_{\text{abs}}, \quad (3.19)$$

where  $f_{\text{abs}}$  is the optical absorption fraction of the sample taking reflection and transmission losses into account. For the typically silicon nitride-passivated silicon wafers investigated in the present work an optical absorption fraction  $f_{\text{abs}} = 0.85$  is used.

In the system used in this work, the spatial resolution is limited by the radius of the coil. The analysed photoconductance is averaged over a sample area of  $\sim 6 \text{ cm}^2$ .

## 3.2 Resistivity measurements

The resistivity  $\rho$  of a silicon wafer is directly related to its doping concentration  $N_{\text{dop}}$ . Moreover,  $\rho$  is related to the sheet resistance  $\rho_{\text{sheet}}$ , which is frequently used to characterize thin semiconductor layers, such as diffused emitters. In the present work,

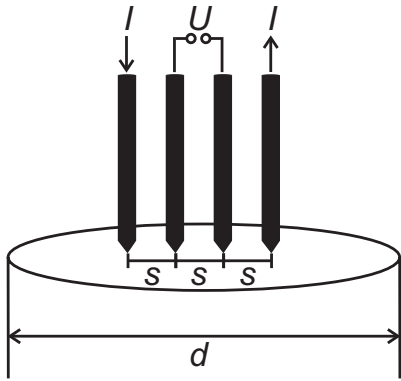


Figure 3.3: Resistivity measurement using a collinear four-point-probe arrangement. Since the inner probes used to measure the voltage carry no current, contact resistance effects can be completely avoided.

the resistivity is obtained via a 4-point probe measurement system from Napson corporation (RT-70/RG 7B).

The technique has first been applied to semiconductors by Valdes [97]. As illustrated in Fig. 3.3, the four probes are arranged in a collinear configuration with equal spacing  $s$ . A small current  $I$  from a constant-current source is passed through the outer two probes and the voltage  $U$  is measured via the inner two probes. The resistivity  $\rho$  given in  $\Omega\text{cm}$  is

$$\rho = F2\pi s \frac{U}{I}, \quad (3.20)$$

where  $F$  is a correction factor depending on the sample geometry. The correction factor is known and can be found in Ref. 98. Under typical measurement conditions ( $d/s < 20$ ,  $d$  is the sample width for a rectangular sample and is the diameter for a circular wafer),  $F$  depends mainly on the sample thickness  $W$ . The function  $F(W)$  is implemented into the software of the 4-point probe system.

The dopant concentration  $N_{\text{dop}}$  for  $n$  and  $p$ -type silicon can be determined directly from the measured resistivity  $\rho$  using Irvin's curve [99,100]. For boron-doped silicon the doping density  $N_{\text{dop}}$  can be calculated from the measured resistivity according to

$$N_{\text{dop}} = \frac{1.33 \times 10^{16}}{\rho} + \frac{1.082 \times 10^{17}}{\rho [1 + (54.56 \rho)^{1.105}]}, \quad (3.21)$$

with  $\rho$  in units of  $\Omega\text{cm}$  and  $N_{\text{dop}}$  in units of  $\text{cm}^{-3}$ .

The emitter sheet resistance  $\rho_{\text{sheet}}$  expressed in units of ohms per square ( $\Omega/\square$ ) is given by

$$\rho_{\text{sheet}} = \frac{\rho}{W} = 4.53 \frac{U}{I}, \quad (3.22)$$

where a very thin layer is assumed with  $W \leq s/2$ .



# Chapter 4

## Impact of Trapping and Depletion-Region Modulation on Carrier Lifetime Measurements

If Shockley-Read-Hall recombination via a single-level centre [46,47] is assumed to be the lifetime-limiting process, the low-injection lifetime should be independent of the injection level, as shown in Fig. 4.1. A frequently used technique for measuring injection-dependent lifetime curves is the QSSPC [68] technique. In the present work, also the ILM [15,62] technique is used to measure injection-dependent lifetime curves. Both techniques determine the lifetime under the assumption that the photo-generated average excess electron concentration equals the average excess hole concentration,  $\Delta n_{av} = \Delta p_{av}$ . However, there exist different mechanisms leading to a strongly increased “apparent” lifetime at low injection levels indicated in Fig. 4.1 (discussion in the next Section). These mechanisms are not based on recombination processes and disturb the above-mentioned mobile charge carrier equity, i.e.  $\Delta n_{av} \neq \Delta p_{av}$ .

In the following, we consider two different effects to be of potential relevance for QSSPC and ILM measurements: (i) minority-carrier trapping and (ii) depletion region modulation at charged surfaces or bulk defects.

In the first Section, we discuss (i) the simple single-level minority-carrier trapping model, which was introduced by Hornbeck and Haynes [101,102]. The model is based on the assumption that trapping centres capture only minority charge carriers and do not interact with the majority carriers. We assume that recombination of the trapped minority-carriers is, due to a very strong asymmetry in the capture cross sections for electrons and holes not possible. Under steady-state conditions, the trapped minority-carriers lead due to the charge neutrality to an increase in the concentration of majority carriers, thus increasing the conductivity (measured by QSSPC) and the infrared emission (measured by ILM) of the sample. Macdonald and Cuevas [17] redefined the same model to steady-state conditions and adapted it to QSSPC measurements. As the IR-camera-based lifetime mapping technique discussed in the present work measures the lifetime under steady-state conditions as well, we follow the line of arguments given in Ref. 17 and adapt this model to our IR-camera-based lifetime mapping technique. The Hornbeck and Haynes model was originally introduced for a single-level trap. After revisiting the single-level model, we extend the theory to the generalized case of multiple trap levels.

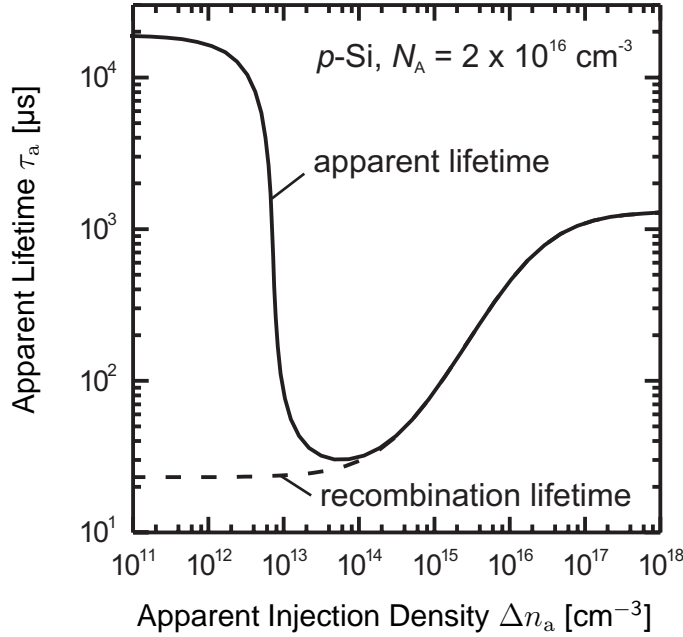


Figure 4.1: Calculated injection-dependent apparent lifetime curve  $\tau_a(\Delta n_a)$  using the Hornbeck and Haynes theory [101,102] for a *p*-type silicon wafer ( $N_A = 2 \times 10^{16}$  cm<sup>-3</sup>,  $T = 300$  K) assuming a trap density  $N_t = 5 \times 10^{13}$  cm<sup>-3</sup> and an energetic depth of the trap centres of  $E_t - E_V = 0.76$  eV. Additionally, a midgap Shockley-Read-Hall recombination centre is assumed with asymmetric capture cross sections  $\sigma_n/\sigma_p = 60$ . The increased apparent lifetime under low-injection conditions should not be confused with the recombination lifetime of the sample.

An alternative explanation of the increasing lifetime with decreasing injection level is given by the (ii) depletion region modulation effect at surfaces [103–106] discussed in Section 4.2.1. Charges on top of the silicon surface or a diffused *pn*-junction produce a space-charge region close to the silicon surface or in the *pn*-junction, respectively. Photogenerated electrons and holes reduce the space-charge region width. This leads to an accumulation of excess electrons and holes at the edges of the space-charge region in addition to the excess electrons and holes in the quasi-neutral regions [74,105]. The accumulated electrons and holes at the space-charge region edge increase the conductivity and the infrared emission of the sample.

Depletion region modulation at charged surfaces is well known and often discussed in the literature. As our injection-dependent ILM lifetime measurements on multicrystalline silicon wafers reveal a strong increase of the apparent lifetime with decreasing injection level especially in dislocated areas, we introduce in Sec. 4.2.2 a simple model taking a possible depletion region modulation effect at charged extended defects in the bulk of the silicon wafer into account.



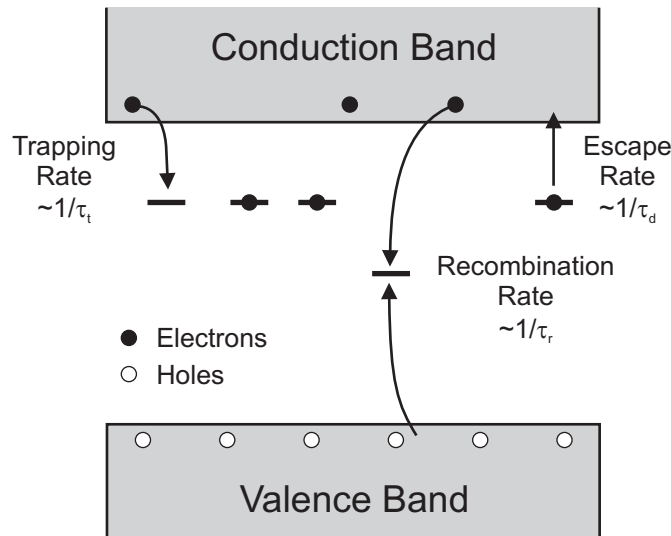


Figure 4.2: Energy-band diagram of a  $p$ -type silicon wafer with one trapping and one recombination centre.

## 4.1 Minority-carrier trapping

The terminology for a *trap* is used in the literature for both (i) a SRH recombination centre, which captures electrons as well as holes and thus contributes to recombination, and (ii) a defect centre, which only captures one type of carrier and does not act as a recombination centre. For the sake of clarity, we distinguish throughout this work between (i) a trapping centre, which only captures and releases one type of carrier, and (ii) a recombination centre, which is capable of capturing electrons and holes. In reality it exists a floating transition between (i) and (ii) depending on the capture-cross sections of electrons and holes and the trap energy level.

### 4.1.1 Hornbeck-Haynes trapping model

The band diagram depicted in Fig. 4.2 shows the main features of the Hornbeck and Haynes trapping model. We assume a  $p$ -type silicon wafer (electrons are the minority carriers), but the formalism described here also holds for  $n$ -type silicon. There are two distinct types of localised states in the bandgap: one type is a SRH recombination centre, where the recombination rate of electron-hole pairs occurs via deep defect states and is proportional to the inverse of the recombination lifetime  $\tau_r$ . Of course, the total recombination lifetime may be injection-dependent in accordance with standard SRH, Auger and radiative recombination models. The other type is a trap level with trap density  $N_t$ , which only captures electrons, but does not contribute to recombination. The hole capture cross section is vanishingly small and can be neglected. The minority-carriers are captured with a trapping rate proportional to the inverse of the capture time constant  $\tau_t$ , which is the mean time before trapping when all traps are empty. The trapped carriers escape back to

the conduction band at a rate proportional to the inverse of the detrapping time constant  $\tau_d$ , which is simply the time spent in a trap. The detrapping time constant is assumed to be independent of the proportion of traps occupied.

According to the Hornbeck-Haynes trapping model, the differential equations describing the kinetics of carrier populations in  $p$ -type material can be written as

$$\frac{d \Delta n}{dt} = G - \frac{\Delta n}{\tau_r} + \frac{n_t}{\tau_d} - \frac{\Delta n (1 - n_t/N_t)}{\tau_t}, \quad (4.1)$$

$$\frac{d n_t}{dt} = -\frac{n_t}{\tau_d} + \frac{\Delta n (1 - n_t/N_t)}{\tau_t}, \quad (4.2)$$

where  $G$  is the photogeneration rate of electron-hole pairs and  $n_t$  is the density of occupied traps. In Eqs. (4.1) and (4.2)  $(1 - n_t/N_t)$  is the fraction of empty traps.

Under steady-state conditions, the left-hand sides of the differential Eqs. (4.1) and (4.2) vanish and we obtain

$$\Delta n = G\tau_r, \text{ and} \quad (4.3)$$

$$n_t = \frac{N_t \Delta n}{\Delta n + N_t \tau_t / \tau_d}. \quad (4.4)$$

From Eq. (4.3) it follows that for a given photogeneration rate  $G$  the density of excess electrons  $\Delta n$  remains equal to what is expected when no traps are present. As a consequence of charge neutrality, however, the trapping of electrons leads to an increased number of excess holes  $\Delta p$  in the valence band. The presence of minority-carrier traps causes a relative increase in the concentration of majority carriers by  $n_t$ :

$$\Delta p = \Delta n + n_t. \quad (4.5)$$

### 4.1.2 Impact on photoconductance-based measurements

The relative increase in the concentration of majority carriers by  $n_t$  results in an increased photoconductance of the sample. Using Eqs. (3.13) and (4.5), the excess conductivity

$$\Delta\sigma = q(\Delta n\mu_n + \Delta p\mu_p) = q\Delta n(\mu_n + \mu_p) + qn_t\mu_p \quad (4.6)$$

depends on  $\mu_n$  and  $\mu_p$  being the mobilities of electrons and holes, respectively.

The effective lifetime determined by the QSSPC technique is commonly derived from the excess photoconductivity and the photogeneration rate by assuming that

$\Delta n = \Delta p$ . As in case of minority-carrier trapping  $\Delta n \neq \Delta p$ , an apparent lifetime  $\tau_a$  is determined according to the expression

$$\tau_a = \frac{\Delta\sigma}{qG(\mu_n + \mu_p)}. \quad (4.7)$$

The apparent carrier lifetime  $\tau_a$  may be considerably larger than the recombination lifetime  $\tau_r$ , which can be demonstrated by combining Eqs. (4.6) and (4.7) to

$$\tau_a = \frac{q\Delta n(\mu_n + \mu_p) + qn_t\mu_p}{qG(\mu_n + \mu_p)} = \frac{\Delta n}{G} + \frac{n_t}{G} \left( \frac{\mu_p}{\mu_n + \mu_p} \right) \equiv \frac{\Delta n_a}{G}, \quad (4.8)$$

where the apparent excess carrier density is defined via  $\Delta n_a \equiv \Delta n + n_t \frac{\mu_p}{\mu_n + \mu_p}$ .

Using Eqs. (4.3) and (4.4), the apparent carrier lifetime  $\tau_a$  is expressed as a function of the trap concentration  $N_t$ , the ratio of capture-to-escape time constants  $\tau_t/\tau_d$  and the recombination lifetime  $\tau_r$ :

$$\tau_a = \tau_r \left[ 1 + \frac{N_t}{(\Delta n + N_t \tau_t/\tau_d)} \frac{\mu_p}{(\mu_n + \mu_p)} \right]. \quad (4.9)$$

Under steady-state conditions, we combine using Eqs. (4.3) and (4.8) to obtain  $R = \frac{\Delta n}{\tau_r} = \frac{\Delta n_a}{\tau_a}$ , which is essentially a result of the assumption that the recombination rate  $R$  is independent of the minority-carrier trapping effects.

In Fig. 4.1 a calculated injection-dependent apparent lifetime curve  $\tau_a(\Delta n_a)$  according to Eq. (4.9) for a  $p$ -type silicon wafer is shown. The strong increase of  $\tau_a(\Delta n_a)$  with decreasing injection-level reveals that the measured apparent lifetime  $\tau_a$  should not be confused with the recombination lifetime  $\tau_r$ .

### 4.1.3 Impact on free-carrier absorption-based measurements

The above-mentioned equations hold for steady-state photoconductance-based lifetime measurements. Here, we derive very similar expressions valid for free-carrier absorption-based measurements.

#### 4.1.3.1 Single-level trapping

If minority-carrier trapping centres are present in a sample, charge neutrality requires an increased density of majorities, leading to an additional steady-state infrared emission signal. The infrared emission signal according to Eq. (1.1) becomes

$$\Delta S = m_p \left( 1 + \frac{\alpha_n}{\alpha_p} \right) \Delta n W + m_p n_t W, \quad (4.10)$$

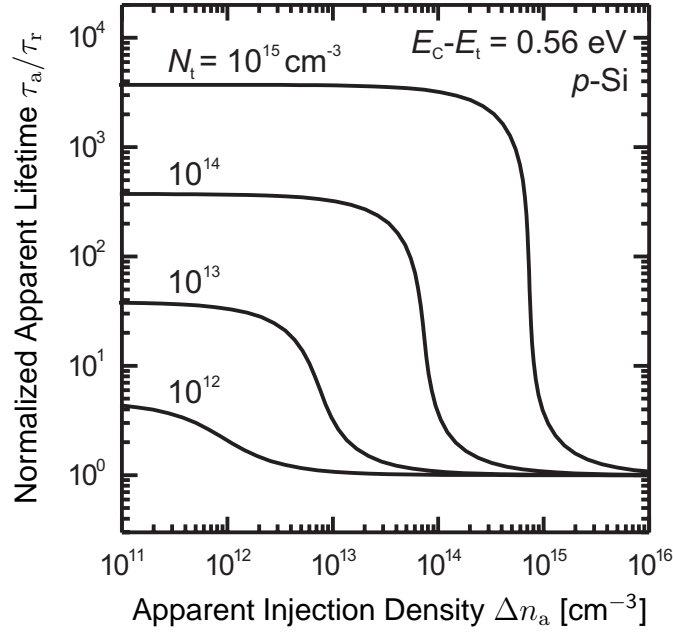


Figure 4.3: Injection-dependent apparent lifetime curves  $\tau_a(\Delta n_a)$  calculated using the Hornbeck and Haynes model for a midgap trap [101] ( $p$ -type silicon,  $T = 340$  K). The impact of the trapping centres increases with the trap density  $N_t$ .

where  $m_p$  is a calibration factor taking only holes into account, since in the present work the calibration of the ILM technique is performed with  $p$ -type silicon wafers, as explained in Sec. 5.2.2. Hence, the term in brackets accounts for the fact that by above-bandgap illumination electron-hole pairs are generated. The second term in Eq. (4.10) accounts for the infrared signal of not-trapped majority carriers. For  $n$ -type material, the calibration factor  $m_p$  in the second term of Eq.(4.10) has to be replaced by  $m_p\alpha_n/\alpha_p$ .

Following the line of arguments given in the previous Section, we find for the apparent ILM lifetime

$$\tau_a = \tau_r \left[ 1 + \frac{N_t}{\Delta n + N_t(\tau_t/\tau_d)} \frac{\alpha_p}{\alpha_p + \alpha_n} \right]. \quad (4.11)$$

The optical absorption coefficients for electrons  $\alpha_n$  and holes  $\alpha_p$  are known at the detection wavelength  $\lambda_{\text{det}}$  of the infrared camera [23]. For  $n$ -type material,  $\alpha_p$  in the numerator has to be replaced by  $\alpha_n$ . The apparent carrier concentration  $\Delta n_a$  is again related to the actual excess carrier concentration  $\Delta n$  via [18]

$$\frac{\Delta n}{\tau_r} = \frac{\Delta n_a}{\tau_a}, \quad (4.12)$$

Moreover, the trap centre energy level is determined by [101]

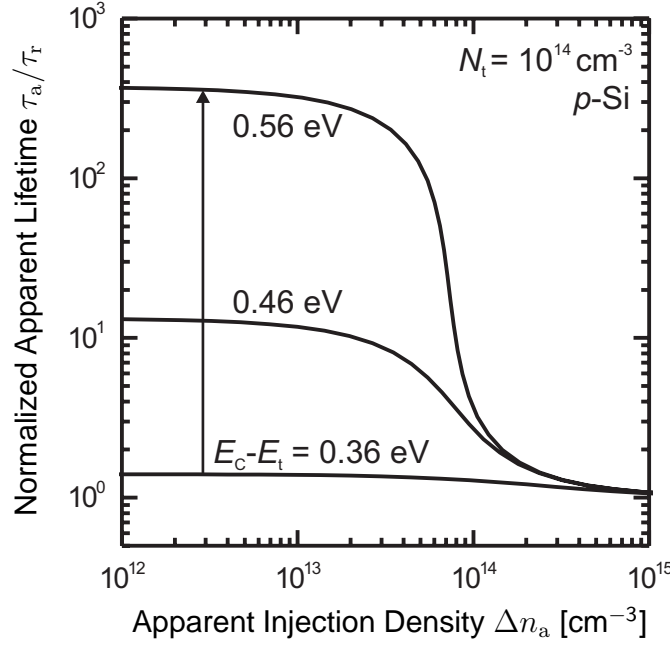


Figure 4.4: Injection-dependent apparent lifetime curves  $\tau_a(\Delta n_a)$  calculated using the Hornbeck and Haynes model for a single-level trap [101] (*p*-type silicon,  $T = 340$  K). The impact of the trapping centres increases with the energetic depth of the traps  $E_C - E_t$ .

$$E_C - E_t = kT \ln \left[ \frac{N_C}{N_t} \left( \frac{\tau_d}{\tau_t} \right) \right], \quad (4.13)$$

where  $N_C$  is the effective density of states in the conduction band.

In Chapter 7, we apply the Eqs. (4.11)-(4.13) by an automated fitting routine to fit our injection-dependent ILM measurements to determine the trap density  $N_t$ , the trap ionization energy ( $E_C - E_t$ ) and the recombination lifetime  $\tau_r$ .

## Discussion

In the double-logarithmic plot of  $\tau_a(\Delta n_a)$ , the  $\Delta n_a^{\text{mns}}$  value that has the maximum negative slope shifts linearly with  $N_t$ , which is shown in Fig. 4.3, assuming  $N_t$  values ranging from  $1 \times 10^{12}$  to  $1 \times 10^{15}$   $\text{cm}^{-3}$ . The maximum negative slope  $\Delta n_a^{\text{mns}}$  is defined via the expression  $\partial^2 (\ln \tau_a) / \partial (\ln \Delta n_a)^2 \big|_{\Delta n_a^{\text{mns}}} = 0$ . Based on Eqs. (4.11) and (4.12) we find the following simple expression for the trap density

$$N_t = \Delta n_a^{\text{mns}} \left( \frac{\alpha_p}{\alpha_p + \alpha_n} + \frac{\tau_t}{\tau_d} \right). \quad (4.14)$$

The ratio  $\tau_t/\tau_d$  is usually rather small compared to the ratio  $\frac{\alpha_p}{\alpha_p+\alpha_n}$ . Thus, this equation simplifies further to  $N_t \approx \Delta n_a^{\text{mns}} \alpha_p / (\alpha_p + \alpha_n)$ . According to Eq. (4.11), the increase of  $\tau_a/\tau_r$  under lowest injection conditions in Fig. 4.3 is attributed to an increasing  $\tau_d/\tau_t$  ratio, where  $E_t$  is kept constant. However, according to Eq. (4.13) for constant energy level  $E_t$  an increased trapping rate – proportional to  $1/\tau_t$  – is associated to an increased trap density  $N_t$  revealing that the increase of  $\tau_a/\tau_r$  under lowest injection conditions depends in fact only on the trap density  $N_t$ .

In Fig. 4.4 the dependence of  $\tau_a/\tau_r$  on the energy trap level  $E_C - E_t$  is shown. The limit of  $\tau_a/\tau_r$  under lowest injection conditions increases with increasing  $E_C - E_t$  corresponding to an increased energetic depth of the minority-carrier trapping centres. With increasing energetic depth the detrapping rate proportional to  $1/\tau_d$  decreases, as thermionic emission of trapped carriers is less probable.

### 3-step evaluation procedure

As an alternative to the application of an automated fitting routine, the following three-step evaluation procedure is applied in Sec. 7.3.1 to a Czochralski silicon sample. An additional advantage of the three-step evaluation procedure besides the simple applicability is that only three lifetime images are needed to determine all trap-related parameters. However, it has to be noted that it is often difficult to know from only three ILM images if the assumptions for the following steps (i)-(iii) are fulfilled. The procedure is expressed for a  $p$ -type semiconductor,  $n$ -type material can be treated analogously:

(i) For  $\Delta n \gg N_t$ , Eq.(4.11) simplifies to  $\tau_a = \tau_r$ . In this case, our camera signal directly gives the spatially resolved recombination lifetime  $\tau_r(x, y)$ .

(ii) For  $\Delta n \ll N_t$ , Eq.(4.11) simplifies to

$$\frac{\tau_t}{\tau_d} = \frac{\tau_r}{(\tau_a - \tau_r)} \frac{\alpha_p}{(\alpha_p + \alpha_n)}. \quad (4.15)$$

Hence, using the result for  $\tau_r(x, y)$  from step (i) we obtain the spatially resolved ratio  $\frac{\tau_t}{\tau_d}(x, y)$ .

(iii) Knowing  $\tau_r$  and  $\tau_t/\tau_d$ , we determine the trap density  $N_t(x, y)$  using the expression

$$N_t = \Delta n_a \frac{1 - \tau_r/\tau_a}{\frac{\alpha_p}{\alpha_p+\alpha_n} + (\tau_t/\tau_d)(\tau_a/\tau_r - 1)}. \quad (4.16)$$

This equation is directly derived from Eqs.(4.11) and (4.12) and it is valid within the entire injection range, where trapping effects impact the lifetime. To calculate  $N_t$  from the measurements, we use a  $\Delta n_a$  value close to the maximum negative slope of the measured  $\tau_a(\Delta n_a)$  dependence in a double-logarithmic plot (see Fig. 7.2) as this gives the smallest uncertainty in  $N_t$ .

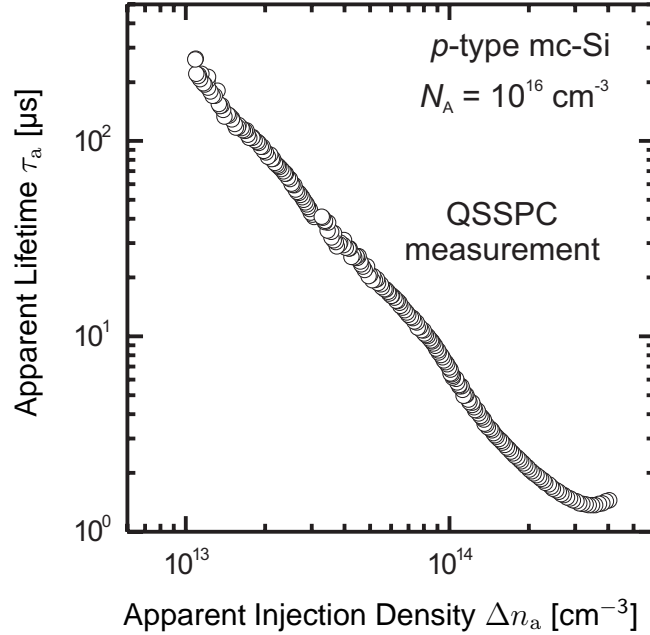


Figure 4.5: Injection-dependent lifetime curve of a 320  $\mu\text{m}$  thick  $p$ -type multicrystalline silicon wafer measured using the QSSPC technique. The increase of  $\tau_a$  with decreasing  $\Delta n_a$  is extended over more than one order of magnitude in  $\Delta n_a$ , which cannot be modeled by the single-level trapping model nor by the defect-related depletion region modulation model.

#### 4.1.3.2 Multiple-level trapping

The single-level trap model described in the previous Section is in most cases sufficient to fit injection-dependent lifetime curves, which are influenced by trapping, as it was shown by many authors [17, 18, 107, 108]. However, in some experiments on mc-Si wafers we have observed an unusual increase of  $\tau_a$  with decreasing  $\Delta n_a$  over more than one order of magnitude in  $\Delta n_a$ , as shown in Fig. 4.5, which cannot be modelled by the single-level trapping model. We attribute this to a distribution of multiple trap levels. Fortunately, extending Eq. (4.11) to more than one trap level is rather simple and results in the expression

$$\tau_a = \tau_r \left[ 1 + \frac{\alpha_p}{\alpha_p + \alpha_n} \sum_{i=1}^j \frac{N_{t,i}}{\Delta n + N_{t,i}(\tau_{t,i}/\tau_{d,i})} \right], \quad (4.17)$$

where the index  $j$  represents the number of trap levels taken into account.

Figure 4.6 shows calculated  $\tau_a(\Delta n_a)$  curves at different temperatures  $T$  for a single-level midgap trap (solid lines) and an exemplary distribution of 5 trap levels (dashed lines) around the middle of the silicon bandgap. The temperature-dependence is solely given by Eq. (4.13). The inset of Fig. 4.6 shows the parameters used for the multiple-trap distribution. As expected, the  $\Delta n_a$  range over which the increase of

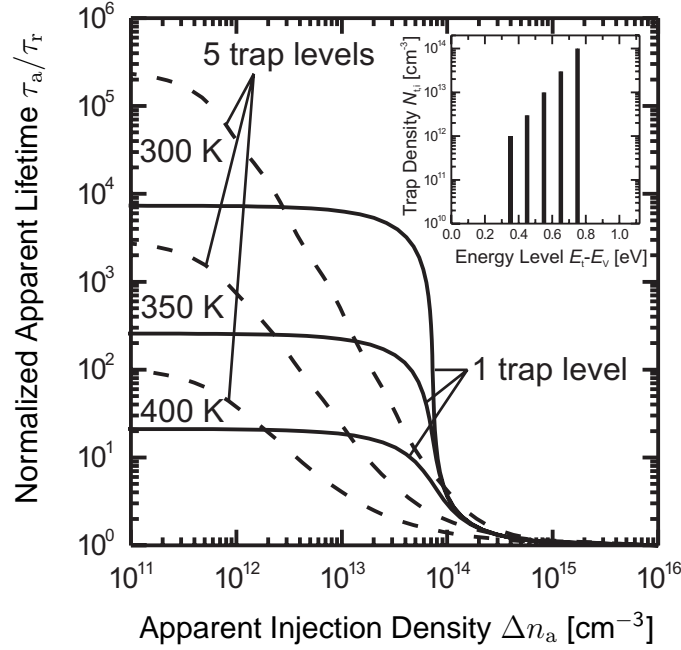


Figure 4.6: Temperature and injection-dependent apparent lifetime curves  $\tau_a(\Delta n_a, T)$ , calculated using the Hornbeck and Haynes minority-carrier trapping model for a single-level trap (solid lines) and a distribution of 5 trap levels with different trap densities (dashed lines) as shown in the inset.

$\tau_a$  with decreasing  $\Delta n_a$  takes place is considerably broadened for the multiple-level trapping compared to the single-level case.

## 4.2 Depletion-region modulation

### 4.2.1 Depletion-region modulation at surfaces

The simple minority-carrier trapping model is well capable of explaining the increase of the apparent lifetime with decreasing injection level quantitatively. A second effect producing an increased apparent lifetime at low injection levels is depletion-region modulation at charged or diffused surfaces [103–106]. As already mentioned in Sec. 2.2.5, passivation layers such as silicon nitride or silicon oxide films on a silicon surface contain positive fixed charges  $Q_f$ , which produce a space-charge region close to the surface of  $p$ -type silicon wafers. The surface charge leads to a band bending  $q\phi_S$  at the surface, as it is sketched in Fig. 4.7. Charge neutrality requires that the sum of all charge densities, the fixed positive charge density  $Q_f$  in the passivation layer, the additional charge density in the surface traps  $Q_{it}$  and the space charge density in the silicon  $Q_{Si}$ , equals zero:

$$Q_f + Q_{it} + Q_{Si} = 0. \quad (4.18)$$



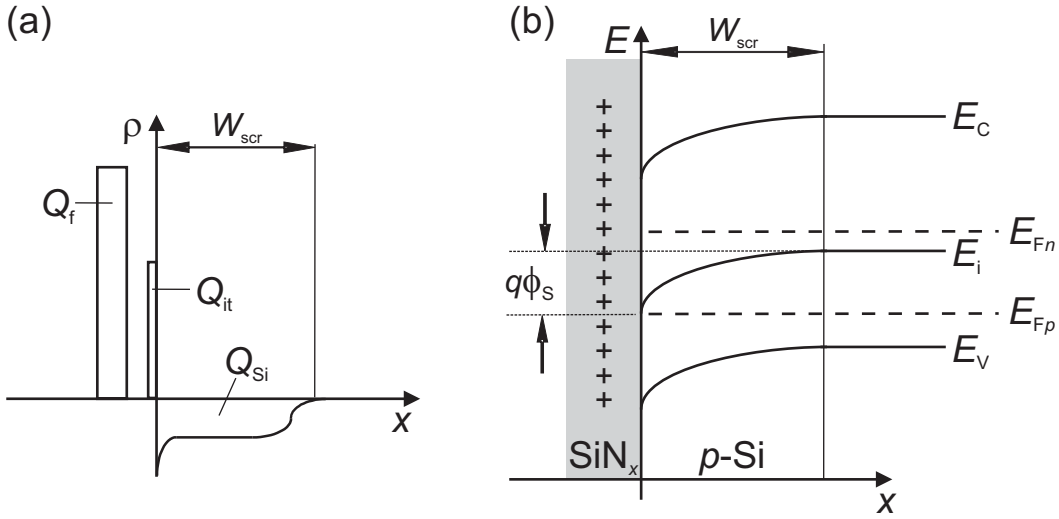


Figure 4.7: (a) Charge density distribution  $\rho(x)$  and (b) band diagram of a  $p$ -type silicon wafer passivated with silicon nitride ( $\text{SiN}_x$ ). The fixed positive charges  $Q_f$  of the  $\text{SiN}_x$  layer on top of the silicon surface induce a band bending in the silicon. Charge neutrality requires that the sum of the positive fixed charges  $Q_f$  in the  $\text{SiN}_x$  layer, the additional charge in the surface traps  $Q_{\text{it}}$  and the space charge in the silicon  $Q_{\text{Si}}$  equal zero. Photogeneration of electrons and holes reduces the space-charge region width  $W_{\text{SCR}}$ . The additional holes at the space-charge region edge increase the conductivity as well as the infrared emission of the sample.

Photogeneration of electrons and holes reduces the space-charge region width  $W_{\text{SCR}}$ , leading to an accumulation of additional holes at the edge of the space-charge region [74, 105]. Analogously, an accumulation of additional electrons is taking place in the inversion layer at the surface. The additional holes and electrons increase the conductivity and the infrared emission of the sample. This effect has been demonstrated for silicon-oxide and silicon-nitride passivated silicon wafers [103, 104] using photoconductance-based measurement techniques. Note that in  $pn$ -junctions the modulation of space charges leads to the same effect, which has been demonstrated for phosphorus- and boron-diffused silicon wafers [105, 106].

In the present work, high-quality surface passivation is achieved by deposition of silicon nitride ( $\text{SiN}_x$ ) layers onto the silicon wafer surface. The  $\text{SiN}_x$  passivation layers are known to possess a large positive fixed charge density of around  $Q_f = 10^{12} \text{ cm}^{-2}$  [109], which causes a charge-induced band bending at the silicon surface, as shown in Fig. 4.7. In order to estimate the impact of the positively charged  $\text{SiN}_x$  passivation layers on our lifetime measurements, we show in Fig. 4.8 calculated injection-dependent apparent lifetime curves  $\tau_a(\Delta n_a)$  calculated using the device simulation program PC1D for typical cases studied in the present work. We assume a 250  $\mu\text{m}$  thick  $p$ -type silicon wafer of doping concentration  $N_A = 10^{16} \text{ cm}^{-3}$  and a fixed positive charge density of the  $\text{SiN}_x$  of  $Q_f = 10^{12} \text{ cm}^{-2}$  [110] on both wafer surfaces. Moreover, we assume negligible surface recombination using a surface recombination velocity of  $S = 0.4 \text{ cm/s}$ . Assuming a broad range of bulk

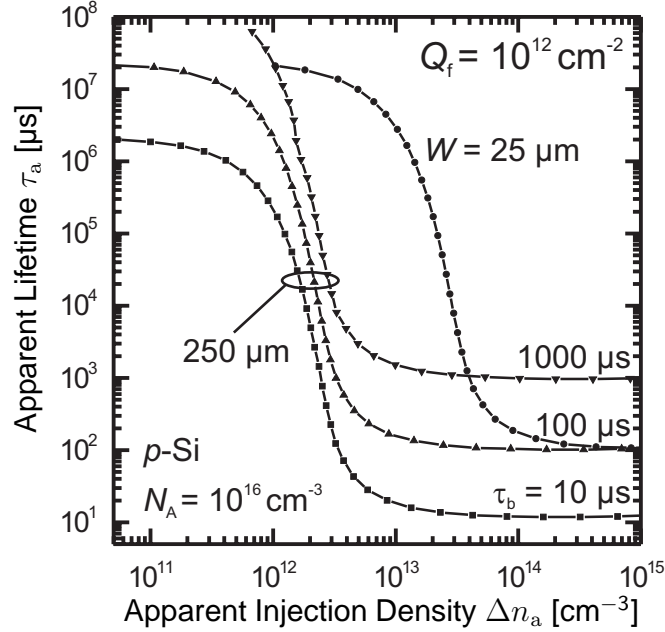


Figure 4.8: Calculated injection-dependent apparent lifetime curves  $\tau_a(\Delta n_a)$  determined using the device simulation program PC1D assuming a fixed positive charge density  $Q_f = 10^{12} \text{ cm}^{-2}$  on top of both surfaces of a  $p$ -type silicon wafer with doping concentration  $N_A = 10^{16} \text{ cm}^{-3}$ . The curves are calculated for the three bulk recombination lifetimes  $\tau_b = 10, 100, 1000 \text{ } \mu\text{s}$ . The strong increase of  $\tau_a$  with decreasing  $\Delta n_a$  shifts linearly with decreasing wafer thickness  $W$  from 250 to 25  $\mu\text{m}$ .

recombination lifetimes  $\tau_b = 10, 100, 1000 \text{ } \mu\text{s}$ , we find the point of the strongest increase of the apparent lifetime  $\tau_a$  with decreasing apparent carrier density  $\Delta n_a$  to be approximately constant at  $\Delta n_a \approx 2 \times 10^{12} \text{ cm}^{-3}$ . As in the present work carrier lifetimes are typically measured for  $\Delta n_a > 1 \times 10^{13} \text{ cm}^{-3}$ , an impact of a depletion region modulation at charged surfaces is not expected. The strong increase of  $\tau_a$  with decreasing  $\Delta n_a$  shifts linearly with decreasing wafer thickness  $W$  from 250 to 25  $\mu\text{m}$ , revealing that depletion region modulation at charged surfaces impacts mainly lifetime measurements of thin silicon wafers.

#### 4.2.2 Depletion region modulation at charged bulk defects

Here, we consider a possible depletion region modulation effect at charged extended defects within the bulk of the silicon material. Structural defects in silicon can appear in different forms such as charged lines (dislocations) and charged spheres (e.g., precipitates or extended defect clusters). We will treat these two important special cases in the following.

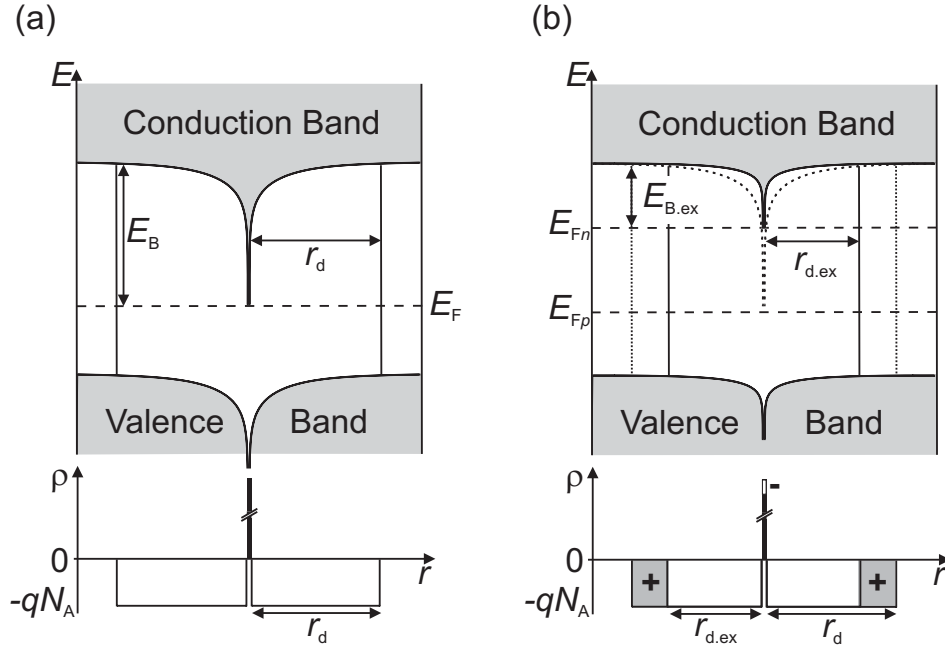


Figure 4.9: Energy-band diagram of a  $p$ -type silicon wafer with a line defect (a dislocation) in the centre of the scheme. The defect is assumed to be positively charged. (a) The charge neutrality condition requires that the sum of all charges inside the space-charge cylinder with radius  $r_d$  is equal to the line charge density  $Q_B$  at the dislocation. The band bending  $E_B$  is determined by the line charge  $Q_B$  and the doping density  $N_A$ . (b) Illumination of the sample causes a splitting of the quasi-Fermi levels  $E_{F_n}$  for electrons and  $E_{F_p}$  for holes, reducing the band bending  $E_{B,ex}$  and the radius  $r_{d,ex}$  of the space-charge region.

#### 4.2.2.1 Charged line defects

Figure 4.9(a) shows the energy-band diagram of a  $p$ -type semiconductor with a line defect (a dislocation) in the centre. In the following, we assume a  $p$ -type semiconductor (the  $n$ -type case can be treated analogously), where the line defect is assumed to be positively charged. The charge neutrality condition requires that the sum of all charges inside a space-charge cylinder in  $p$ -type material of doping concentration  $N_A$  is equal to the line charge  $Q_B$  (in units of C/cm) at the dislocation, thus determining the radius  $r_d$  of the space-charge region [111]

$$Q_B = qN_A\pi r_d^2. \quad (4.19)$$

The negative charge density in the space-charge region is assumed to be constant and equal to the doping concentration  $N_A$  (abrupt depletion region approximation). The Poisson equation in cylindrical coordinates for the electrostatic potential  $\phi$  in the space-charge region

$$\frac{1}{r} \frac{\partial}{\partial r} \left( r \frac{\partial \phi}{\partial r} \right) = \frac{qN_A}{\epsilon_0 \epsilon_s} \quad \text{for } r_i < r < r_d \quad (4.20)$$

is solved by integration over the radius  $r$  from the outer edge  $r_d$  [112]. In the case of cylindrical symmetry, the radius  $r = 0$  is difficult to handle, so we define a minimum inner radius  $r_i$ , which is equal to half the distance between two silicon atoms ( $r_i = 0.055$  nm).  $\varepsilon_s = 11.7$  is the static permittivity of silicon.

Using this approach, we derive the following relationship between  $r_d$  and the band bending  $E_B$  at the line defect:

$$E_B = -\frac{q^2 N_A r_d^2}{4\varepsilon_0 \varepsilon_s} \left[ 2 \ln \left( \frac{r_i}{r_d} \right) + \left( 1 - \frac{r_i^2}{r_d^2} \right) \right], \quad (4.21)$$

which can be solved for  $r_d(E_B)$  using a numerical procedure.

Illumination of the sample leads to the generation of excess charge carriers  $\Delta n$ , which correspond to a quasi-Fermi level splitting of

$$E_{F_n} - E_{F_p} = kT \ln \left( \frac{\Delta n (\Delta n + N_A)}{n_i^2} \right), \quad (4.22)$$

with  $E_{F_n}$  and  $E_{F_p}$  being the quasi-Fermi levels for electrons and holes, respectively. For the intrinsic carrier concentration  $n_i$  we use the parameterisation given in Ref. 113. In general, the Poisson equation in cylindrical coordinates is not analytically solvable for  $\phi(r)$  under illumination. Hence, we assume the following simplifying approximation for the band bending  $E_{B,\text{ex}}$  under illumination:

$$E_{B,\text{ex}} = E_B - (E_{F_n} - E_{F_p}), \quad (4.23)$$

that is, under illumination the band bending is reduced by the quasi-Fermi level splitting. It was shown that Eq. (4.23) holds for the case of strong inversion [114]. However, it has to be kept in mind that with decreasing  $E_{B,\text{ex}}$  an increasing deviation from Eq. (4.23) may be expected.

The reduction of the band bending  $E_{B,\text{ex}}$  leads to a reduction of the radius  $r_{d,\text{ex}}$  of the space-charge region, as shown in Fig. 4.9(b). The additional number of free carriers due to the reduction in the width of the space-charge region per volume is then given by

$$\Delta n' = N_A 2\pi (r_d^2 - r_{d,\text{ex}}^2) N_{\text{dis}}, \quad (4.24)$$

where  $N_{\text{dis}}$  is the number of dislocations per area (unit  $\text{cm}^{-2}$ ).

Assuming steady-state conditions, the recombination rate  $R = \Delta n / \tau_r$  equals the generation rate  $G$  and the apparent lifetime  $\tau_a(\Delta n_a)$  can be calculated using the expression

$$\tau_a = \frac{\Delta n_a}{G} = \frac{\Delta n + \Delta n'}{\Delta n / \tau_r} = \tau_r \left( 1 + \frac{\Delta n'}{\Delta n} \right), \quad (4.25)$$

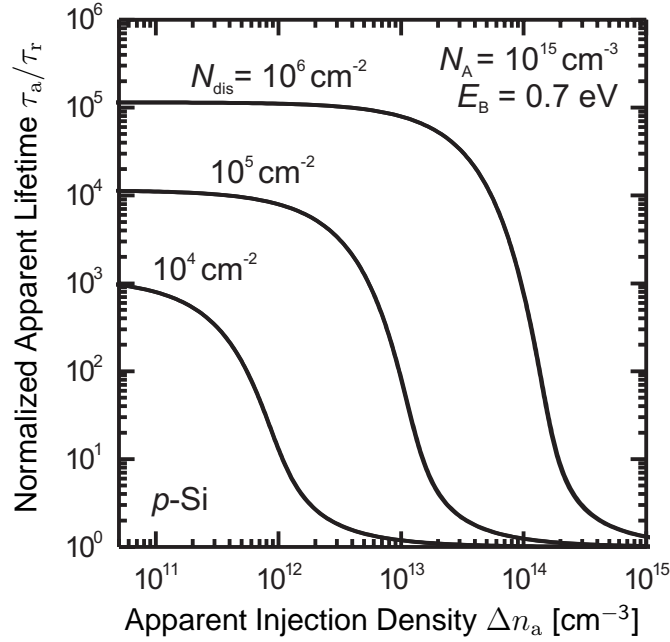


Figure 4.10: Injection-dependent apparent lifetime curves  $\tau_a(\Delta n_a)$  calculated using the depletion region modulation model for dislocations ( $p$ -type silicon,  $N_A = 10^{15} \text{ cm}^{-3}$ ,  $T = 350 \text{ K}$ ,  $E_B = 0.7 \text{ eV}$ ). The impact of the space-charge region formed around the charged dislocations increases with the dislocation density  $N_{\text{dis}}$ . Exactly the same curves are obtained for charged spheres, assuming a concentration of charged spheres ranging from  $N_S = 1.04 \times 10^{13}$  to  $1.04 \times 10^{15} \text{ cm}^{-3}$ .

where  $\Delta n_a = \Delta n + \Delta n'$ .

Combining Eqs. (4.22) and (4.24) with Eq. (4.25) gives the calculated  $\tau_a(\Delta n_a)$  curves shown in Figs. 4.10 and 4.11, where we assume  $E_B = 0.7 \text{ eV}$ . Using Eq. (4.19) yields for  $N_A = 1 \times 10^{16} \text{ cm}^{-3}$  a line charge equivalent to 0.41 elementary charges per nm, changing to a line charge equivalent to 0.31 elementary charges per nm for  $N_A = 1 \times 10^{14} \text{ cm}^{-3}$ . The impact of the depletion region modulation effect increases linearly with increasing  $N_{\text{dis}}$ , as shown in Fig. 4.10. This behaviour is qualitatively very similar to that obtained from the single-level trapping model shown in Fig. 4.3. In addition, in Fig. 4.11 we plot  $\tau_a(\Delta n_a)$  curves for various doping concentrations  $N_A$ , illustrating that an increasing doping concentration  $N_A$  results in a stronger depletion region modulation effect.

#### 4.2.2.2 Charged spherical defects

Using the same approach as discussed in the previous Section enables us to estimate the impact of a depletion region modulation effect attributed to charged spherical defects. In silicon such nearly spherical defects might e.g. be oxygen precipitates [115]. The physical principle is equivalent for charged spheres and lines so that we

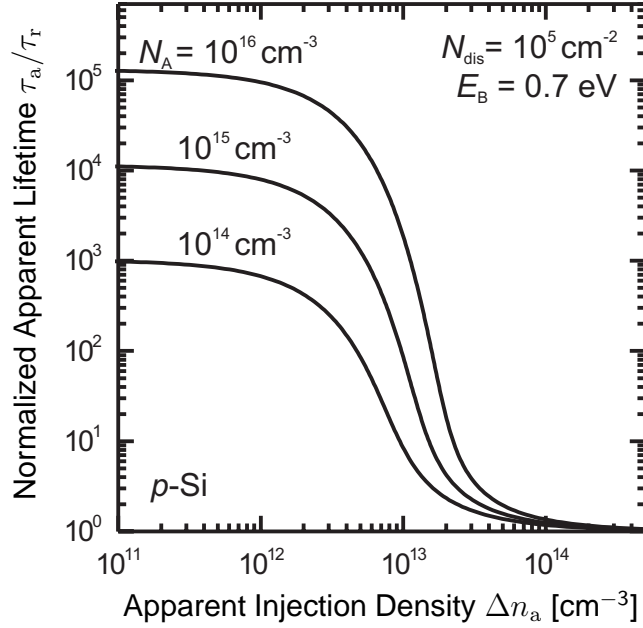


Figure 4.11: Injection-dependent apparent lifetime curves  $\tau_a(\Delta n_a)$  calculated using the depletion region modulation model for dislocations ( $p$ -type silicon,  $N_{\text{dis}} = 10^5 \text{ cm}^{-2}$ ,  $T = 350 \text{ K}$ ,  $E_B = 0.7 \text{ eV}$ ). The impact of the space-charge region formed around the charged dislocations increases with the doping concentration  $N_A$ .

can use again Fig. 4.9 to illustrate the underlying physical mechanisms.

The neutrality condition requires the sum of all charges inside a space-charge sphere in  $p$ -type silicon of doping concentration  $N_A$  to be equal to the charge  $Q_B$  of the sphere, thus, determining the radius  $r_d$  of the space-charge region

$$Q_B = qN_A \frac{4}{3} \pi r_d^3. \quad (4.26)$$

We now solve the Poisson equation in spherical coordinates for the electrostatic potential  $\phi$  in the space-charge region

$$\frac{1}{r^2} \frac{\partial}{\partial r^2} \left( r \frac{\partial \phi}{\partial r} \right) = \frac{qN_A}{\varepsilon_0 \varepsilon_s} \quad \text{for } r_i < r < r_d. \quad (4.27)$$

Double integration of Eq. (4.27) with the boundary condition that the electric field vanishes at the depletion region edge results in the following equation [115]:

$$E_B = \frac{q^2 N_A r_i^2}{3 \varepsilon_0 \varepsilon_s} \left[ \left( \frac{r_d}{r_i} \right)^3 - \frac{3}{2} \left( \frac{r_d}{r_i} \right)^2 + \frac{1}{2} \right]. \quad (4.28)$$

The reduction of the band bending  $E_{B,\text{ex}}$  (see Eq. (4.23)) leads to a reduction of the radius  $r_{d,\text{ex}}$  of the space-charge region. The additional number of free carriers caused by the change of the space-charge region width is then given by

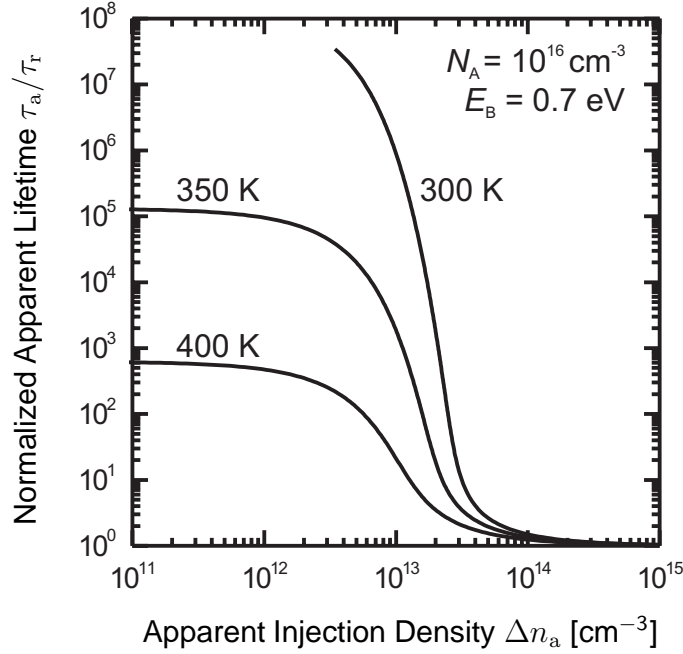


Figure 4.12: Temperature- and injection-dependent apparent lifetime curves  $\tau_a(\Delta n_a, T)$  calculated using the depletion region model for charged dislocations. The impact of the depletion region modulation effect decreases with increasing temperature.

$$\Delta n' = N_A \frac{4}{3} \pi (r_d^3 - r_{d.ex}^3) N_S, \quad (4.29)$$

where  $N_S$  is the density of spherical defects per volume (unit  $\text{cm}^{-3}$ ).

Combining Eq. (4.25) with Eqs. (4.28) and (4.29) results in practically the same set of  $\tau_a(\Delta n_a)$  curves as shown in Fig. 4.10. In fact, these curves hold for both cases charged lines as well as charged spheres. However, instead of the stated  $N_{\text{dis}}$  values for each curve, the concentration of spherical defects values ranges from  $N_S = 1.04 \times 10^{13}$  to  $1.04 \times 10^{15} \text{ cm}^{-3}$ .

#### 4.2.2.3 Effect of temperature

As shown in Fig. 4.12, the temperature dependence of the  $\tau_a(\Delta n_a, T)$  curves is very pronounced. This dependence is based on Eq. (4.22), where the main contribution comes from the intrinsic carrier concentration  $n_i$ , which rises from  $0.97 \times 10^{10} \text{ cm}^{-3}$  to  $5.47 \times 10^{12} \text{ cm}^{-3}$  when increasing the temperature from 300 to 400 K [113]. Due to this increase the splitting of the quasi-Fermi levels  $E_{F_n} - E_{F_p}$  decreases. As a consequence of this, the same illumination intensity has less impact on the modulation of the depletion region when increasing the temperature.

A comparison of  $\tau_a(\Delta n_a)$  curves calculated using our depletion region modulation model for structural defects and the minority-carrier trapping model reveals that the impact of both effects decreases with increasing temperature. Hence, in general, these two effects cannot be easily discriminated by temperature-dependent measurements of the injection-dependent lifetime curves.



# Chapter 5

## Infrared Camera-based Charge Carrier Imaging

In this Chapter we introduce our improved in-house built experimental setup, which allows to perform spatially resolved measurements of photogenerated or voltage-induced free-carriers using highly sensitive infrared cameras. In addition to the implementation of the measures suggested earlier [15] to improve the sensitivity of the ILM setup, we introduce another measure, which nearly doubles the sensitivity of the experimental setup by using a gold mirror behind the sample instead of the conventionally used blackbody.

The ILM technique is an optical measurement system and, thus, the sensitivity strongly depends on the optical parameters of the used components. In order to compare the sensitivity of arbitrary experimental setups, we introduce an optical model, which takes all relevant parameters into account. The experimental findings of the sensitivity relations between different experimental setups agree well with theoretical results obtained from our optical model.

### 5.1 Infrared thermography basics

#### 5.1.1 Fundamentals

At a finite temperature, each body spontaneously emits electromagnetic radiation, which is called thermal radiation. The magnitude of the thermal radiation of a blackbody is expressed as specific irradiation  $M_{\text{BB}}(\lambda, T)$  (unit  $\text{W}/\text{m}^2\mu\text{m}$ ), which is the electromagnetic power irradiated per wavelength and per area into the half-space.  $M_{\text{BB}}(\lambda, T)$  as a function of the wavelength  $\lambda$  and temperature  $T$  is given by Planck's law

$$M_{\text{BB}}(\lambda, T) = \frac{2\pi hc^2}{\lambda^5} \frac{1}{e^{\left(\frac{hc}{\lambda kT}\right)} - 1}, \quad (5.1)$$

where  $h$  is the Planck constant,  $c$  the velocity of light in vacuum and  $k$  the Boltzmann constant. The infrared detectors used in the present work might be considered as photon counters, which generate for each absorbed infrared photon one electron-hole pair. Hence, not the irradiated electromagnetic power, but the corresponding

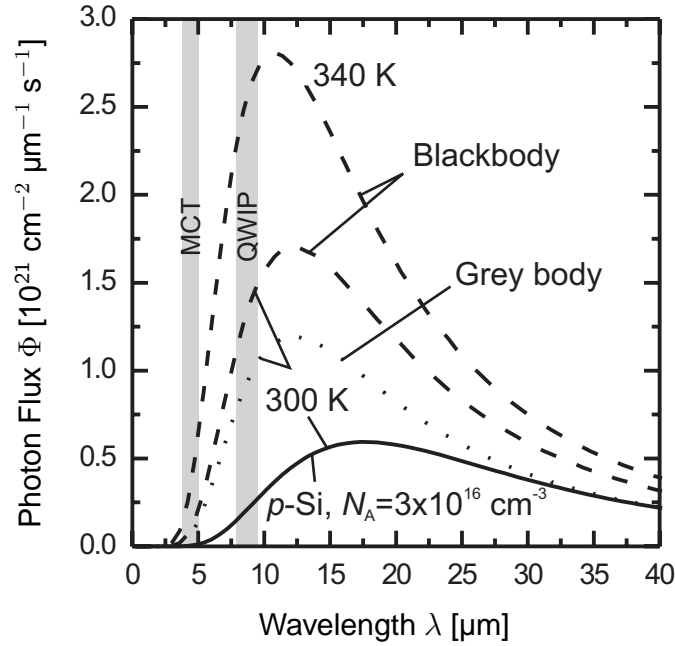


Figure 5.1: Calculated spectral distribution of the photon flux  $\Phi(\lambda, T)$  of a blackbody at 2 different temperatures (300 K and 340 K, dashed lines). In addition, at room temperature  $\Phi(\lambda, T)$  is shown of a grey body with emissivity  $E = 70\%$  (dotted line) and a  $p$ -type silicon sample with thickness  $300 \mu\text{m}$ , assuming a doping concentration of  $N_A = 3 \times 10^{16} \text{ cm}^{-3}$  and a front side reflection  $R_f = 30\%$  (solid line). Due to free-carrier emission the emissivity of silicon increases with increasing  $\lambda$ , reaching  $E_{\text{Si}} = 70\%$  for  $\lambda > 35 \mu\text{m}$ . The grey areas illustrate the wavelength range in which photons are detected by the IR-cameras used in this thesis.

number of irradiated photons of the sample is important. The photon flux of a blackbody irradiated within a differential wavelength range by a plane unit area into the half-space is simply the specific irradiation divided by the energy of the photon  $\Phi_{\text{BB}}(\lambda, T) \equiv M_{\text{BB}}(\lambda, T)/E_\gamma = M_{\text{BB}}(\lambda, T) \cdot \frac{\lambda}{hc}$  (unit  $\text{m}^{-2}\mu\text{m}^{-1} \text{ s}^{-1}$ ).

Figure 5.1 shows the calculated spectral distribution of the photon flux of a blackbody at 2 different temperatures (300 K and 340 K). At room temperature the maximum photon flux is at  $\lambda = 12 \mu\text{m}$ . The increase of the temperature of 40 K increases the cumulated photon flux by nearly 50%.

A blackbody is by definition an object that absorbs all electromagnetic radiation that falls onto it. No radiation passes through it and none is reflected, which means according to Eq. (2.6) that at each wavelength the total absorption  $A(\lambda) \equiv 1$ . In contrast, a grey body is defined having an absorption of  $A < 1$ , which is constant over the entire wavelength range. A real specimen such as silicon is a selective absorber, which means that the absorption depends on optical properties and varies with  $\lambda$ .

According to Kirchhoff's law, which is based on detailed balance considerations,

the total absorption always equals the total emission  $A \equiv E$ , which means that the probability of a surface to absorb radiation  $A$  has to be equal to the emission probability  $E$ . In the present work, most measurements are based on the detection of emitted infrared radiation. Hence, we use in the following the term total emissivity  $E$  instead of the equivalent quantity  $A$ . In the wavelength range being of interest for the present work, the emissivity  $E(\alpha)$  of silicon depends on the free-carrier absorption coefficient  $\alpha$  given by Eqs. (2.1) and (2.2). It follows from Eqs. (2.1) and (2.2) that the emissivity  $E(n, \lambda)$  depends on the concentration of free carriers  $n$  and the wavelength  $\lambda$ . Taking the above considerations into account, one obtains for the photon flux irradiated by a silicon sample at temperature  $T$

$$\Phi_{\text{Si}}(\lambda, T, n) = E_{\text{Si}}(n, \lambda) \cdot \Phi_{\text{BB}}(\lambda, T) = E_{\text{Si}}(n, \lambda) \frac{2\pi c}{\lambda^4} \frac{1}{e^{\frac{hc}{\lambda kT}} - 1}. \quad (5.2)$$

The solid line in Fig. 5.1 shows the calculated spectral distribution of the photon flux  $\Phi_{\text{Si}}$  assuming a 300  $\mu\text{m}$  thick  $p$ -type silicon sample with doping concentration  $N_{\text{A}} = 3 \times 10^{16} \text{ cm}^{-3}$  at room temperature. The front and rear side reflection are assumed to be  $R_{\text{f}} = 30\%$ . The emissivity  $E_{\text{Si}}(N_{\text{A}}, \lambda)$  is calculated using Eq. (2.7). Compared to the blackbody (dashed line) the photon flux maximum shifts from 12 to 17  $\mu\text{m}$  towards a larger wavelength. With increasing  $\lambda$  the emissivity increases, reaching a saturation value of  $E_{\text{Si}} = 70\%$  for  $\lambda > 35 \mu\text{m}$ . Thus, in this wavelength range one observes an asymptotic approximation of the photon flux curve to that of a grey body of same temperature with  $E = 70\%$  in the entire wavelength range.

### 5.1.2 Infrared cameras

In the present work, we use two different IR-cameras. One absorbs radiation in the mid-range infrared region from 4-5  $\mu\text{m}$  and the other one in the long-range infrared region from 7.7 - 9.0  $\mu\text{m}$ .

First, we discuss the spatial and temporal noise of IR-cameras. The detector of an IR-camera is a focal plane array which consists of typically  $\sim 10^5$  infrared detectors. The sensitivity of thermography systems is expressed in terms of temperature resolution, as the figure of merit is the local temperature of any scene. Since in the present work the temperature of the samples under test is spatially homogeneous and constant during the measurement, an expression of the sensitivity in terms of temperatures is not appropriate. However, the temperature resolution is by default given for any IR-camera system. Hence, it is convenient to convert the temperature resolution into the sensitivity of the quantity to be measured, which is done in Secs. 6.3 and 8.4.

In general, the temperature resolution of an IR-camera is limited by spatial and temporal noise. Since the inhomogeneity due to the spatial noise can be corrected for, most IR-cameras are only limited by their temporal noise.

### 5.1.2.1 Correction for spatial inhomogeneity

The spatial noise is based on different responsivities of the individual detector pixels. In practice, the correction of the spatial inhomogeneity is done in real-time in the readout integrated circuit subsequently after recording the images. The IR-cameras used in the present work are corrected by a 2-point-correction. This is done by recording two images of a spatially homogeneous blackbody at different temperatures and calculating the average camera signal of the detector matrix at the 2 temperatures. From the deviation of the camera signal of each pixel to the average value of the image, correction coefficients are calculated, which enable to correct the offset and responsivity of each pixel. After a successful correction procedure the spatial inhomogeneity plays only a minor role compared to the temporal noise discussed in the following.

### 5.1.2.2 Noise Equivalent Temperature Difference $NETD$

The noise level of an IR-camera-based temperature mapping system is usually expressed by a noise equivalent temperature difference  $NETD$ . The  $NETD$  is deduced from the temporal noise  $\sigma_{\text{tn}}$  of the detector, which is defined as the average temporal noise of all detector pixels. The temporal noise  $\sigma_{\text{tn},ij}$  at position  $(i, j)$  in the pixel array is defined as the standard deviation of  $N$  subsequently recorded values at blackbody temperature  $T_{\text{BB}}$ :

$$\sigma_{\text{tn},ij} = \frac{\sum_{l=1}^N (S_{ij,l} - \langle S_{ij} \rangle)^2}{N - 1}, \quad (5.3)$$

where  $S_{ij,l}$  is the  $l$ -th camera signal at position  $(i, j)$  and  $\langle S_{ij} \rangle$  is the average of the camera signal at position  $(i, j)$ .

The responsivity curve of the IR-camera is achieved when the camera signal  $S(T_{\text{BB}})$  is measured at various blackbody temperatures  $T_{\text{BB}}$  and averaged over the entire detector matrix

$$S(T_{\text{BB}}) = \frac{\sum_{i=1}^{n_x} \sum_{j=1}^{n_y} S_{ij}(T_{\text{BB}})}{n_x n_y}, \quad (5.4)$$

where  $n_x$  and  $n_y$  are the numbers of columns and rows of the detector array, respectively.

The  $NETD$  is derived from Eqs. (5.3) and (5.4) as the product of the temporal noise and the derivative of the responsivity curve:

$$NETD(T_{\text{BB}}) = \left[ \frac{dS(T)}{dT} \Big|_{T_{\text{BB}}} \right]^{-1} \sigma_{\text{tn}}(T_{\text{BB}}) = c \sigma_{\text{tn}}(T_{\text{BB}}), \quad (5.5)$$

with  $c$  being a calibration constant to convert from camera digits into temperatures. If all pixels of the detector array have the same noise properties (typically achieved after a 2-point correction), it does not matter whether the temporal noise  $\sigma_{\text{tn}}$  is calculated from successive measurements of one pixel according to Eq. (5.3) or from evaluating  $n$  pixels of one image nominally showing a homogeneous blackbody with constant temperature  $T_{\text{BB}}$ .

In general, the *NETD* depends strongly on the blackbody temperature  $T_{\text{BB}}$ , the detector integration time and the optics. The *NETD* is typically specified at room temperature ( $\vartheta_{\text{BB}} = 25^\circ\text{C}$ ). A comparison between the *NETD* of the IR-cameras used in the present work as specified by the producer and measured by the author according to the described procedure is given in Table 5.1.

### 5.1.2.3 Quantum Well Infrared Photodetector (QWIP) camera

If not otherwise stated we use the QWIP camera (AIM 640Q, manufacturer AIM) for all measurements presented in this thesis. The detector of the QWIP camera consists of  $640 \times 486$  infrared detectors, which are based on a multi-quantum well structure of epitaxially-grown GaAs/AlGaAs. Intersub-band transitions between two-dimensional sub-bands in the CB of QWIP detectors allow the detection of infrared light between  $3 \mu\text{m}$  and  $25 \mu\text{m}$  [118, 121]. In Fig. 5.2(a), the potential distribution of the CB along the growth direction of the QWIP detector is shown. In region 1, optical excitation of electrons by infrared light of appropriate wavelength occurs into the quasi-continuum of the drift-zone (region 2). The charge carriers are stopped by a potential wall and are captured in region 3. Subsequently, the carriers reach via a tunnelling process (region 4) again region 1, where the process from region 1-4 repeats [122]. Due to the uniformly grown heterostructure, a photo-current is generated effectively suppressing the noise.

In Fig. 5.2(b), the spectral quantum efficiency measurement provided by the manufacturer of the QWIP detector used in this thesis is shown. The quantum efficiency

Table 5.1: *NETD* at a blackbody temperature of  $\vartheta_{\text{BB}} = 25^\circ\text{C}$  of the IR-cameras used in the present work, as specified by the manufacturer and measured by the author under the used measurement conditions.

IR-camera	specified <i>NETD</i>	measured <i>NETD</i>
QWIP AIM 640Q	20 mK [116]	$(27 \pm 2)$ mK
MCT Jade MWIR 320×256	17 mK [117]	$(17 \pm 1)$ mK

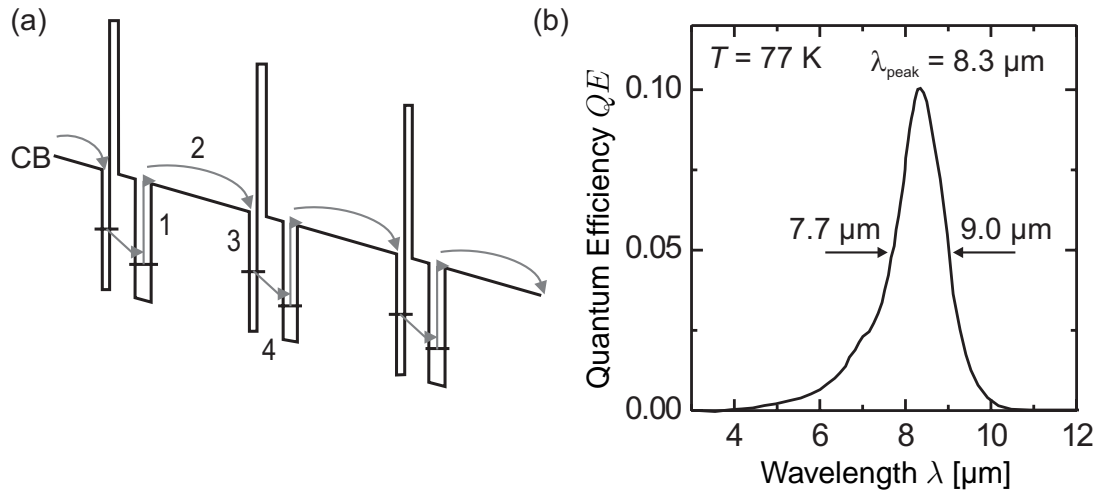


Figure 5.2: (a) Schematic band diagram along the growth direction of a quantum-well infrared photo (QWIP) detector. Description of the processes 1-4 see text. (b) Spectral quantum efficiency of the QWIP detector used in this thesis. The detector is cooled down to a temperature of  $T = 77 \text{ K}$ . Absorption of infrared light occurs at  $\lambda_{\text{peak}} = (8.3 \pm 0.7) \mu\text{m}$ . [104, 118]

at  $\lambda_{\text{peak}} = 8.3 \mu\text{m}$  is 0.1 and is low compared to other infrared detectors. Despite the low quantum efficiency, the temperature resolution  $NETD$  is 20 mK at room temperature as stated in Table 5.1.

#### 5.1.2.4 Mercury-Cadmium-Telluride (MCT) IR-camera

The second IR-camera used in this thesis for a sensitivity analysis in comparison with the QWIP camera is based on an MCT detector (Jade MWIR 320, manufacturer Cedip Infrared Systems). MCT is a ternary semiconductor compound which exhibits a cut-off wavelength that depends on the alloy composition. Photons with energy greater than the semiconductor bandgap energy excite electrons into the CB, thereby increasing the conductivity of the material. Such an electron is collected by a suitable external readout circuit and transformed into an electrical signal. The peak wavelength depends on the material's bandgap energy and can easily be varied by changing the alloy composition. In Fig. 5.3, the external spectral quantum efficiency of the MCT detector used in this thesis is shown. The cut-off wavelengths are due to the bandgap of the MCT detector at  $4.8 \mu\text{m}$  and an edge filter at  $3.7 \mu\text{m}$ . The quantum efficiency of approximately 90% in the wavelength range between  $3.7 \mu\text{m}$  and  $4.8 \mu\text{m}$  is quite high compared to the QWIP detector. However, the temperature resolution  $NETD$  of 17 mK at room temperature is comparable to the  $NETD$  of 20 mK of the QWIP detector. This is due to the fact that at room temperature for a blackbody maximum emission of infrared photons occurs at  $\lambda = 12 \mu\text{m}$  (see Fig. 5.1). Thus, the QWIP camera has about 10 times more photons to detect with a 10 times smaller quantum efficiency.

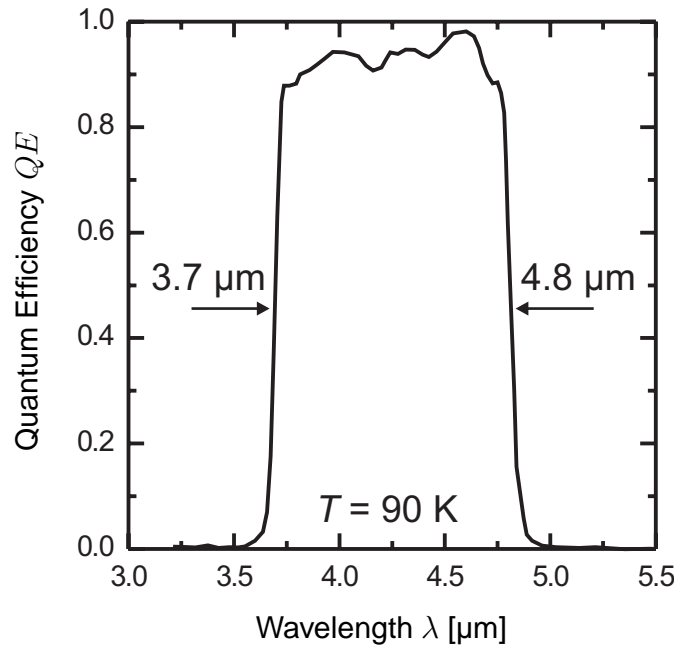


Figure 5.3: Spectral quantum efficiency of the Mercury-Cadmium-Telluride (MCT) detector used in this thesis. The detector is cooled down to a temperature of  $T = 90$  K. Absorption of infrared light occurs between  $\lambda = 3.7 \mu\text{m}$  to  $4.8 \mu\text{m}$  with a quantum efficiency of 90%. The cutoff wavelengths are due to the bandgap of the MCT detector at  $4.8 \mu\text{m}$  and an edge filter at  $3.7 \mu\text{m}$ . [119, 120]

## 5.2 Measurement principle

### 5.2.1 Basic principles

As already addressed in the Introduction of this thesis, the IR-camera-based techniques discussed in the present work take advantage of the ability of free carriers to absorb and emit infrared radiation. The mathematical description for the two cases of the IR-camera-based technique illustrated in Fig. 1.1 is quite simple. We assume that other radiation sources than a blackbody behind the wafer at temperature  $T_{\text{BB}}$  and the wafer itself at temperature  $T_{\text{W}}$  are negligible. Please note that for the sake of simplicity we do not advertise the wavelength-dependence of all variables.

The IR-camera detector is a photon counter. Hence, the camera signal  $S$  is proportional to the photon flux emitted by the wafer  $\Phi_{\text{Si}}(T_{\text{W}})$ , which, according to Eq. (5.2), depends on the wafer temperature  $T_{\text{W}}$  and the free carrier concentration of the wafer  $N_{\text{dop}}$  as long as no carrier-generating light is present. Additionally, the camera also detects infrared photons emitted by the blackbody  $\Phi_{\text{BB}}(T_{\text{BB}})$  with temperature  $T_{\text{BB}}$  multiplied with the transmittance  $T_{\text{Si}}(N_{\text{dop}})$  of the silicon sample. The camera signal is then given by the equation

$$\begin{aligned}
S &= \Gamma \cdot [\Phi_{\text{Si}}(T_{\text{W}}) + T_{\text{Si}}(N_{\text{dop}}) \cdot \Phi_{\text{BB}}(T_{\text{BB}})] \\
&= \Gamma \cdot [E_{\text{Si}}(N_{\text{dop}}) \cdot \Phi_{\text{BB}}(T_{\text{W}}) + T_{\text{Si}}(N_{\text{dop}}) \cdot \Phi_{\text{BB}}(T_{\text{BB}})] , \quad (5.6)
\end{aligned}$$

where  $\Gamma$  is a proportionality factor accounting for the fact that not all emitted photons are absorbed by the detector. Due to illumination with light of appropriate wavelength excess carriers  $\Delta n$  are generated, resulting in a modified camera signal

$$S_{\text{ex}} = \Gamma \cdot [E_{\text{Si}}(N_{\text{dop}} + \Delta n) \cdot \Phi_{\text{BB}}(T_{\text{W}}) + T_{\text{Si}}(N_{\text{dop}} + \Delta n) \cdot \Phi_{\text{BB}}(T_{\text{BB}})] . \quad (5.7)$$

Please note that  $\Delta n$  accounts here for photogenerated electrons and holes. The difference between Eqs. (5.7) and (5.6) is only caused by the light-generated excess carriers  $\Delta n$  and is given by:

$$\begin{aligned}
\Delta S &= \Gamma \cdot [\Delta E_{\text{Si}} \cdot \Phi_{\text{BB}}(T_{\text{W}}) + \Delta T_{\text{Si}} \cdot \Phi_{\text{BB}}(T_{\text{BB}})] \\
&= \Gamma \cdot \Delta E_{\text{Si}} \cdot [\Phi_{\text{BB}}(T_{\text{W}}) - \Phi_{\text{BB}}(T_{\text{BB}})] , \quad (5.8)
\end{aligned}$$

where  $\Delta E_{\text{Si}} \equiv E_{\text{Si}}(N_{\text{dop}} + \Delta n) - E_{\text{Si}}(N_{\text{dop}})$  and  $\Delta T_{\text{Si}} \equiv T_{\text{Si}}(N_{\text{dop}} + \Delta n) - T_{\text{Si}}(N_{\text{dop}})$ . Applying  $\Delta E + \Delta T + \Delta R = 0$  we assume in the second step of Eq. (5.8), that the change of the emissivity and the transmission of the silicon sample are equal, which is a good approximation due to the typically low free-carrier absorption coefficient causing a negligible change of the reflectance  $\Delta R_{\text{Si}}$ .

**Expression (5.8) is the basic formulation of all IR-camera-based methods introduced in the present work.** The only parameter depending on the excess carrier density  $\Delta n$  in Eq. (5.8) is the emissivity change  $\Delta E_{\text{Si}}(N_{\text{dop}}, \Delta n)$ . Hence, a measurement of the excess carrier density  $\Delta n$  is only possible if  $T_{\text{W}} \neq T_{\text{BB}}$ , otherwise the change of the camera signal would always be 0. For  $T_{\text{W}} > T_{\text{BB}}$  the change of the camera signal  $\Delta S$  is positive – as shown in Fig. 1.1(b) for emission-ILM – and for  $T_{\text{W}} < T_{\text{BB}}$ ,  $\Delta S$  is negative – as shown in Fig. 1.1(a) for absorption-ILM.

The change of the photon flux  $E_{\text{Si}}\Phi_{\text{BB}}(T_{\text{W}})$  due to a change of the carrier density in the sample is illustrated in Fig. 5.4. We consider the infrared emission of a 300  $\mu\text{m}$  thick  $p$ -type Si sample at temperature  $T_{\text{W}} = 340 \text{ K}$ . The increase of the carrier density by  $\Delta n = 5 \times 10^{15} \text{ cm}^{-3}$  increases the emissivity of the sample, resulting in a shift of the calculated spectral distribution of the photon flux towards the blackbody curve at the same temperature. The detectable photons are given by the difference of the curves with and without excess carriers in the spectral responsivity range of the QWIP camera.

Under typical measurement conditions, Eq. (5.8) can be further simplified. Experimentally, one observes that the camera signal depends linearly on the carrier density per area, hence, we use the first derivative of the Taylor series of  $\Delta E_{\text{Si}}(N_{\text{dop}}, \Delta n)$



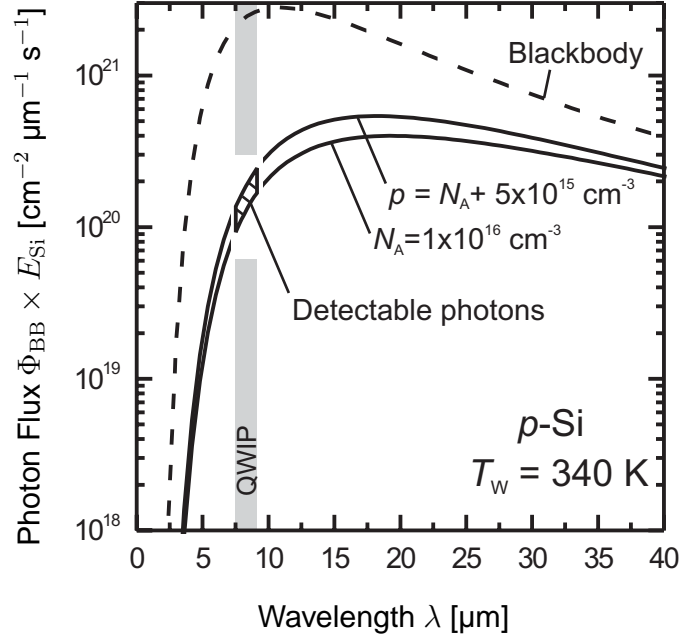


Figure 5.4: Calculated spectral distribution of the photon flux  $\Phi$  emitted from a blackbody (dashed line) and a 300  $\mu\text{m}$  thick  $p$ -type Si sample with and without excess carriers of density  $\Delta n = 5 \times 10^{15} \text{ cm}^{-3}$  (solid lines) at a sample temperature of  $T_W = 340 \text{ K}$ . The increase of the carrier density increases the emissivity of the sample, resulting in a shift of the calculated spectral distribution of the photon flux towards the blackbody curve at the same temperature. The photons detectable by the QWIP camera are given by the difference of the curves with and without excess carriers in the spectral responsivity range.

$$\begin{aligned}
 \Delta S &= \Gamma \cdot \left. \frac{\partial E_{\text{Si}}}{\partial(\alpha W)} \right|_{\alpha_{\text{dop}}} \Delta \alpha W \cdot [\Phi_{\text{BB}}(T_W) - \Phi_{\text{BB}}(T_{\text{BB}})] \\
 &= \Gamma \cdot \left. \frac{\partial E_{\text{Si}}}{\partial(\alpha W)} \right|_{\alpha_{\text{dop}}} \chi \cdot \Delta n \cdot \lambda^2 \cdot W \cdot [\Phi_{\text{BB}}(T_W) - \Phi_{\text{BB}}(T_{\text{BB}})] \\
 &= m \Delta n W,
 \end{aligned} \tag{5.9}$$

where we substitute  $\Delta \alpha$  by Eqs. (2.1) and (2.2) with  $\chi = 3.7 \times 10^{18} \text{ } \mu\text{m}^{-2} \text{ cm}^2$  if  $\lambda$  is expressed in units of  $\mu\text{m}$  and  $\Delta n$  in units of  $\text{cm}^{-3}$ . For small  $\alpha$  the first derivative of  $E_{\text{Si}}$  is constant. Since all other parameters except the quantity  $\Delta n W$  to be measured are constant, we introduce the calibration factor of the measurement system

$$m \equiv \Gamma \cdot \left. \frac{\partial E_{\text{Si}}}{\partial(\alpha W)} \right|_{\alpha_{\text{dop}}} \chi \lambda^2 [\Phi_{\text{BB}}(T_W) - \Phi_{\text{BB}}(T_{\text{BB}})]. \tag{5.10}$$

A detailed analysis, which accounts for arbitrary configurations of the setup, is given in Sec. 5.3.1.

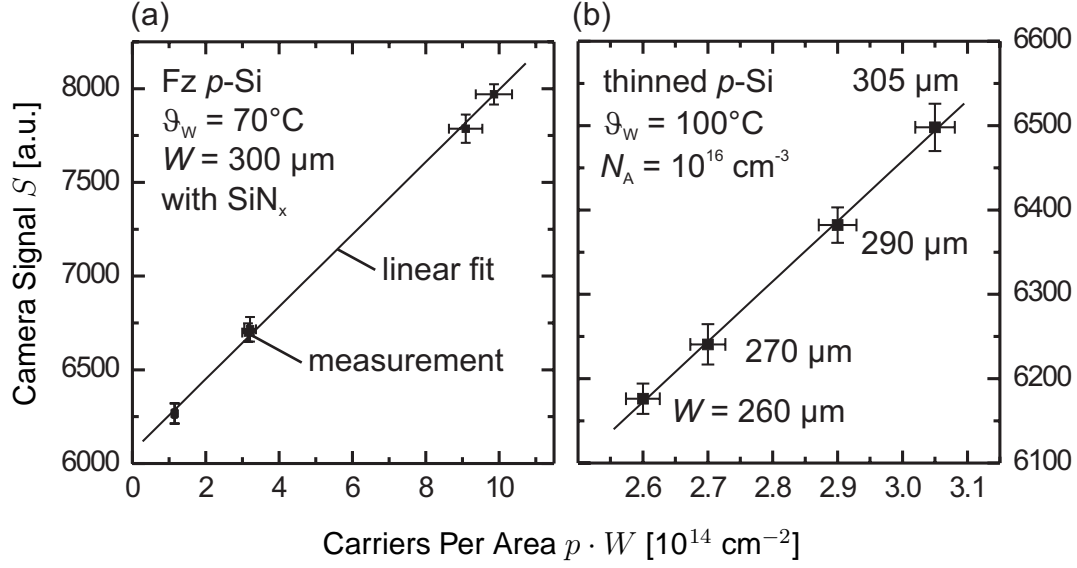


Figure 5.5: Calibration of the camera via a set of  $p$ -type FZ-Si wafers with (a) different doping concentration  $N_A$  and constant wafer thickness  $W$  and (b) different  $W$  and constant  $N_A$ . The calibration factor for holes  $m_p$  is given in Table 5.2. The calibration factor  $m$  taking electrons and holes into account is calculated via  $m = 1.37 \times m_p$ .

### 5.2.2 Calibration procedure

The conversion of the camera signal  $\Delta S$  to an excess carrier density  $\Delta n$  follows the procedure proposed by Bail *et al.* [15]. The calibration is performed by recording the infrared emission signal of several silicon wafers of known doping concentrations. The proportionality factor  $m$  between the camera signal  $S$  and the free-carrier concentration times the wafer thickness  $n \cdot W$  is obtained from a linear fit to the measured data. In Fig. 5.5(a), an exemplary calibration curve is shown using a set of  $p$ -type FZ-Si wafers with  $\text{SiN}_x$  passivation layers. The linear fit with slope  $m_p$  of the curve reflects only a calibration factor for holes. In order to account for the fact that electron-hole pairs are generated by above-bandgap illumination,  $m_p$  has to be adapted for electrons as well to obtain  $m$ :

$$m = \frac{\alpha_p + \alpha_n}{\alpha_p} m_p = 1.37 \times m_p. \quad (5.11)$$

Generally, the calibration wafers have to possess equivalent optical properties as the sample under test. Hence, in the present work it is taken care of comparable surface properties between the calibration wafers and measured samples.

It is noteworthy that the camera signal  $S$  and, thus, the change of the camera signal  $\Delta S$  according to Eq. (5.9) only depends on the carrier density per area  $\Delta n W$  (unit  $\text{cm}^{-2}$ ). Hence, also a set of wafers with equivalent doping concentrations but different thickness's might be used for calibration, as it is demonstrated in Fig. 5.5(b).

Table 5.2: Exemplary calibration factors for holes  $m_p$  as calculated from the linear fits shown in Fig. 5.5. The wafer temperature  $\vartheta_W$  is given in the Table and the temperature of the background is  $\vartheta_{BB} = 16$  °C.

	Temperature $\vartheta_W$ [°C]	$m_p$ [ $10^{12}$ cm <sup>2</sup> ]
Fz-Si with SiN <sub>x</sub>	70	$1.93 \pm 0.07$
thinned wafers	100	$7.15 \pm 0.16$

### 5.2.3 Measurement setup

The in-house-built experimental lock-in thermography setup that was built in this work for emission-ILM is shown in Fig. 5.6(a). The wafer under test is placed on a heated gold mirror. The IR-camera observes the wafer that is heated to a constant temperature higher than the background temperature  $T_W > T_{BG}$ . In contrast to the schematic shown in Fig. 1.1, where the background is behind the sample, the background is now placed between the LED array and the sample under test. The background is realized by a water-cooled glass plate in front of the diode array. The gold mirror is tilted by a small angle of  $\sim 7^\circ$ , so that the camera observes the homogeneous background radiation emitted by the glass plate in front of the LED array and reflected by the wafer and the gold mirror. If the gold mirror would not be tilted, the camera would observe a strongly inhomogeneous background radiation emitted by the camera itself, which would originate either from the detector chip cooled to a temperature of  $-210^\circ\text{C}$  or from the objective and the surrounding background being at room temperature. The typical distance between the gold mirror and the IR-camera is 30 cm and between the gold mirror and the glass plate is 22 cm. The LED array illuminates the wafer with above-bandgap light at  $\sim 880$  nm. The excitation light is periodically turned on and off and generates excess charge carriers modulating the infrared emission. The emission change is detected by using a digital lock-in technique, which will be described in detail in the next Section. The lock-in evaluation of the images recorded by the IR-camera is performed in real-time by a personal computer, which is indicated in Fig. 5.6(b).

#### Gold-plated heating stage

The advantage of the gold mirror behind the sample is twofold: it doubles the sensitivity by re-directing the infrared light emitted through the back of the sample towards the camera and it gives an easy means of controlling the wafer temperature using a simple setup. The gold mirror has a reflectivity of 98 % in the wavelength region from 3 to 10  $\mu\text{m}$ . Hence, the mirror mainly reflects the infrared background signal emitted by the glass plate in front of the LED array. The experimental setup

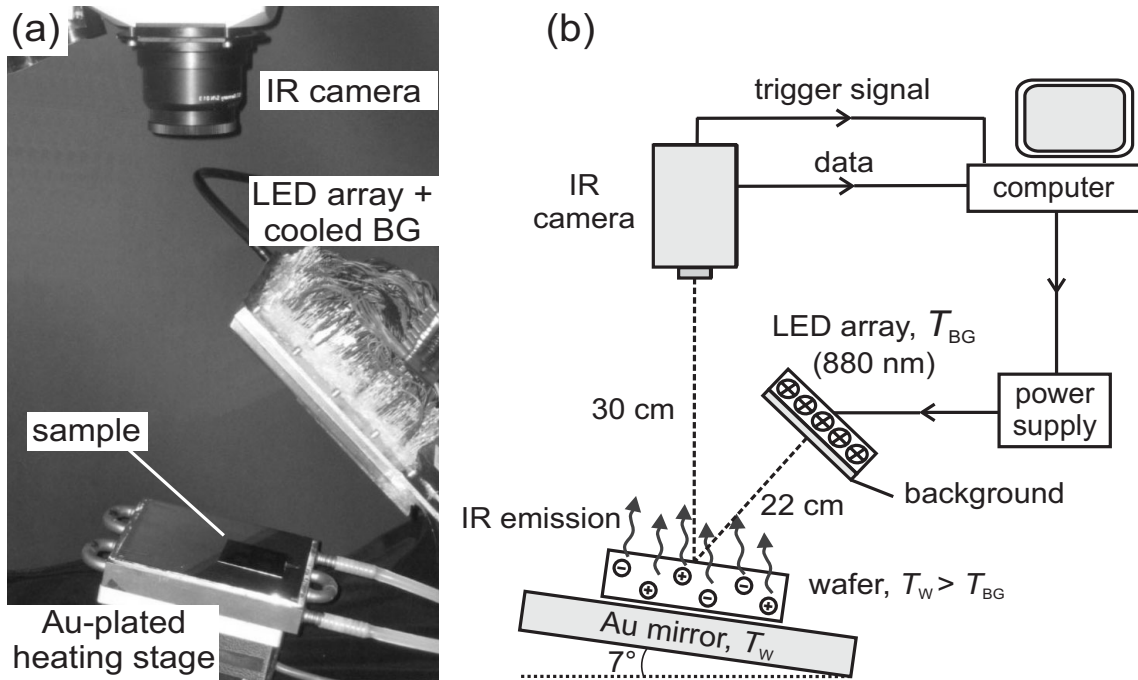


Figure 5.6: Experimental setup of the infrared lifetime mapping (ILM) technique in the emission-mode. The wafer is heated to a temperature  $T_W$  higher than the background temperature  $T_W > T_{BG}$  by a heater of low infrared emissivity. The intensity-modulated excitation light (realised by means of an 880 nm LED array) causes a modulated infrared emission by photogenerated free carriers which is observed by the camera.

is thus simpler than the earlier approach used by other authors [15, 62, 123, 124] who cooled or heated the wafer by air streams. However, the gold mirror will only improve the signal-to-noise ratio if the wafer under test has a weak infrared absorption. A highly doped wafer with zero infrared transmission cannot be measured.

The gold mirror is embedded into a copper block, which is kept at a well-defined temperature by a thermostat (HAAKE F3 S). The copper block is additionally mounted on an electronically-controlled heating plate (Präzitherm 2860SR PZ14ET). The combination of both the heater and the thermostat allows for a temperature accuracy of the wafer of  $\pm 1^\circ\text{C}$  in a wafer temperature range between 40 and  $100^\circ\text{C}$ . The sample can be heated to a temperature from 20 -  $200^\circ\text{C}$ .

### Infrared cameras

The detectors of the IR-cameras used in the present work were discussed in detail in Sec. 5.1.2. If not otherwise stated the QWIP camera has been used for all measurements. The QWIP camera records images with a frame rate of 38.9 Hz. In case of the MCT camera we use a frame rate of 80 Hz. Both cameras allow for a

spatial resolution up to 170  $\mu\text{m}$ , which is only limited by the used optics.

### LED array with cooled background

In order to apply a lock-in technique with a lock-in frequency down to 20 Hz, LEDs are chosen as illumination source due to their very low rise and fall time of only 10 ns. The effective rise and fall time is 50  $\mu\text{s}$  and is limited by the power source of the LED array. Our in-house-built LED array consists of 700 diodes, which emit radiation at a wavelength of  $\lambda_{\text{ex}} = 880 \text{ nm}$  with a beam angle of  $\pm 22^\circ$ . At 880 nm the absorption length in silicon is 26  $\mu\text{m}$ , which ensures that the typically 300  $\mu\text{m}$  thick wafers absorb all photons which are not reflected at the front side of the wafer. The illumination intensity is tunable by a power source, allowing a photon flux up to  $4 \times 10^{17} \text{ cm}^{-2}\text{s}^{-1}$  corresponding to 1.5 suns (AM1.5G). The homogeneity of the illumination intensity depends on the illuminated area. For a  $5 \times 5 \text{ cm}^2$  sample an accuracy of  $\pm 3\%$  and for a  $10 \times 10 \text{ cm}^2$  sample an accuracy of  $\pm 8\%$  is achieved.

A glass plate is hermetically sealed to the metal plate, in which the LEDs are mounted. The space between the metal and glass plate is flushed by water, which is tempered by a thermostat (HAAKE DC50 K40). The glass plate is transparent at 880 nm (transmittance is 90%) and opaque in the infrared region from 4 to 10  $\mu\text{m}$ . Hence, it represents an infrared background radiator at constant background temperature  $T_{\text{BG}}$  (typically 16°C), which is reflected by the gold mirror and observed by the IR-camera. The background temperature can be varied between 15 and 60°C.

### Personal computer and power control devices

The IR-camera sends the digitised images to a frame grabber (NI IMAQ PCI1424) in the computer, where during the measurement an infrared in-phase and 90°-phase-shifted signal is calculated applying the digital lock-in technique described in the next Section. The software for the data recording and evaluation is implemented by the author. The personal computer controls the modulation of the power supply of the LED arrays, using a lock-in frequency of typically  $f_{\text{li}} = 2.43 \text{ Hz}$ .

#### 5.2.4 Lock-in technique

The digital lock-in technique used to evaluate the images of the IR-camera is discussed in detail by Breitenstein and Langenkamp in Ref. 12. In general, the application of a lock-in technique features three advantages:

- (i) it suppresses offset signals and measures only signal changes,
- (ii) it measures phase-sensitive and
- (iii) it reduces noise.

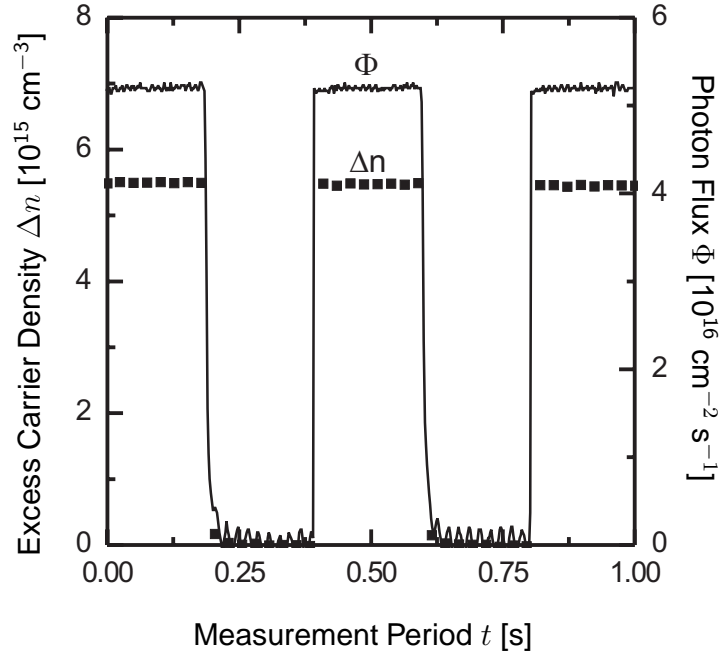


Figure 5.7: Time-resolved lock-in measurement of a 300  $\mu\text{m}$  thick  $p$ -type Si wafer with doping concentration  $N_A = 3 \times 10^{15} \text{ cm}^{-3}$  and effective carrier lifetime 600  $\mu\text{s}$ . The excess carrier density  $\Delta n(t)$  has been calculated from the camera signal  $\Delta S(t)$ . The electrical signal corresponding to  $\Delta n(t)$  is in-phase to the square-shaped-modulated photon flux  $\Phi(t)$ .

In the present work, camera signal changes are caused by a change in the free-carrier density and as a consequence of this a change of the infrared emission signal  $S$  of the sample. Excess free carriers are optically or electrically excited with a lock-in frequency  $f_{\text{li}}$ . The camera periodically records  $n$  infrared images per lock-in time period  $1/f_{\text{li}}$  with sampling frequency  $f_s$  synchronous to the lock-in frequency  $f_{\text{li}}$ , which means that  $f_{\text{li}} = f_s/n$ . The number of samples per period has to be larger than 4 and an even number [12], being typically  $n = 16$  for the measurements presented here. The QWIP camera has a sampling frequency of 38.9 Hz resulting in a lock-in frequency of  $f_{\text{li}} = 2.43$  Hz. The camera signal  $S$  is correlated with a harmonic correlation functions  $K$  having the same lock-in frequency  $f_{\text{li}}$ . We use the following narrow-band correlation functions

$$K_{0^\circ}^j = 2 \sin\left(\frac{2\pi(j-1)}{n}\right) \quad K_{90^\circ}^j = -2 \cos\left(\frac{2\pi(j-1)}{n}\right) \quad (5.12)$$

in order to calculate the infrared in-phase  $S_{0^\circ}$  and  $90^\circ$  phase-shifted signal  $S_{90^\circ}$ :

$$\begin{aligned}
S_{0^\circ} &= \frac{2}{nN} \sum_{i=1}^N \sum_{j=1}^n \sin\left(\frac{2\pi(j-1)}{n}\right) S_{i,j} \quad \text{and} \quad (5.13) \\
S_{90^\circ} &= \frac{-2}{nN} \sum_{i=1}^N \sum_{j=1}^n \cos\left(\frac{2\pi(j-1)}{n}\right) S_{i,j},
\end{aligned}$$

where  $N$  is the number of averaged lock-in periods and  $S_{i,j}$  the  $j$ -th image of the  $i$ -th lock-in period. The amplitude  $A$  and the phase  $\Theta$  are:

$$\begin{aligned}
A &= \sqrt{(S_{0^\circ})^2 + (S_{90^\circ})^2} \quad \text{and} \quad (5.14) \\
\Theta &= \arctan\left(\frac{S_{90^\circ}}{S_{0^\circ}}\right) \quad (-180^\circ \text{ if } S_{0^\circ} \text{ is negative})
\end{aligned}$$

The *electrical signal* based on the infrared emission of the excess charge carriers reacts in a time range corresponding to the carrier lifetime of the silicon samples, which is typically lower than 1 ms. Since this is small compared to the lock-in time period of  $1/2.43 \approx 0.4$  s, we can assume in good approximation that the excess carrier density  $\Delta n(t)$  reacts instantaneously to changes of the square-shaped illumination intensity and is, thus, in-phase to the excitation signal. Hence, we use the infrared in-phase signal  $S_{0^\circ}$  to calculate the excess carrier density. The *thermal signal* of the thermally thin wafer (such as a 300  $\mu\text{m}$  thick silicon wafer), which is caused by the modulated heating of the sample, is known to be  $90^\circ$  phase-shifted to the excitation, if the heating is spatially homogeneous [12]. Hence, it contributes only to  $S_{90^\circ}$  and is negligible for the in-phase signal  $S_{0^\circ}$ . In Fig. 5.7, a time-resolved lock-in measurement of a 300  $\mu\text{m}$  thick  $p$ -type silicon wafer with doping concentration  $N_A = 3 \times 10^{15} \text{ cm}^{-3}$  is shown. The excess carrier density  $\Delta n(t)$  has been calculated from the camera signal  $\Delta S(t)$ . It is obvious that  $\Delta n(t)$  is in-phase with the optical excitation  $\Phi(t)$ .

In order to measure the carrier lifetime at a defined injection level, we apply a wide-band excitation (square-shaped modulation of the illumination intensity). The excess carrier density can be described by a d.c. part and the sum of its Fourier components

$$\Delta n'(t) = \frac{\Delta n}{2} + \Delta n \left( \frac{2}{\pi} \sin \omega t + \frac{2}{3\pi} \sin 3\omega t + \frac{2}{5\pi} \sin 5\omega t + \dots \right). \quad (5.15)$$

The application of the sin/-cos correlation of Eq. (5.12) is frequency-selective and results in the calculation of only the signal contribution of the first harmonic of Eq. (5.15). In order to calculate the signal change of the camera  $\Delta S$  corresponding to  $\Delta n$  we have to multiply the in-phase signal with  $\pi/2$ :

$$\Delta S = \frac{\pi}{2} S_{0^\circ}. \quad (5.16)$$

### Signal-to-noise ratio

The application of a lock-in evaluation using a synchronous sin/-cos correlation results in the noise of the lock-in components, namely the in-phase and 90°-phase-shifted signal, as described in Ref. 12:

$$S_{0^\circ;90^\circ}^{\text{noise}} = \frac{\sqrt{2} NETD}{c\sqrt{N}}, \quad (5.17)$$

which is given here in units of camera digits. The temperature noise of the amplitude signal is

$$A^{\text{noise}} = \frac{2 NETD}{\sqrt{N}} \quad (5.18)$$

given in units of mK. The number of frames  $N$  can be expressed as the product of the frame rate  $f_{\text{frame}}$  and the acquisition time of the lock-in measurement  $t_{\text{acq}}$ ,  $N = f_{\text{frame}} t_{\text{acq}}$ , which shows that the noise generally is proportional to the inverse of the square root of the measurement period and, thus, the signal-to-noise ratio improves with  $\sqrt{N}$ .

The noise level of a lock-in thermography system can be measured by recording a steady-state scene such as a blackbody at room temperature in the lock-in mode [12]. In this case the in-phase and 90°-phase-shifted images are dominated by the system noise.

## 5.3 Sensitivity analysis

In the Introduction, we already defined the two principle forms of the ILM technique according to Fig. 1.1(a) and (b), namely the absorption ( $T_W < T_{BG}$ ) and emission-ILM ( $T_W > T_{BG}$ ), which differ only in the temperature relation between the sample temperature  $T_W$  and background temperature  $T_{BG}$ . Bail *et al.* [15] showed that the emission-mode is in principle more sensitive due to the possibility of applying higher integration times of the IR-camera, because a silicon wafer emits less infrared radiation due to its lower emissivity than a blackbody heated to the same temperature. However, besides this technical problem, under ideal conditions, equal signal strengths in emission and absorption-mode are expected. Further, Bail *et al.* [15] explained that the signal-to-noise ratio improves for (i) ILM in emission-mode with increasing temperature of the sample under test under otherwise constant measurement conditions and improves for (ii) ILM in absorption-mode with increasing



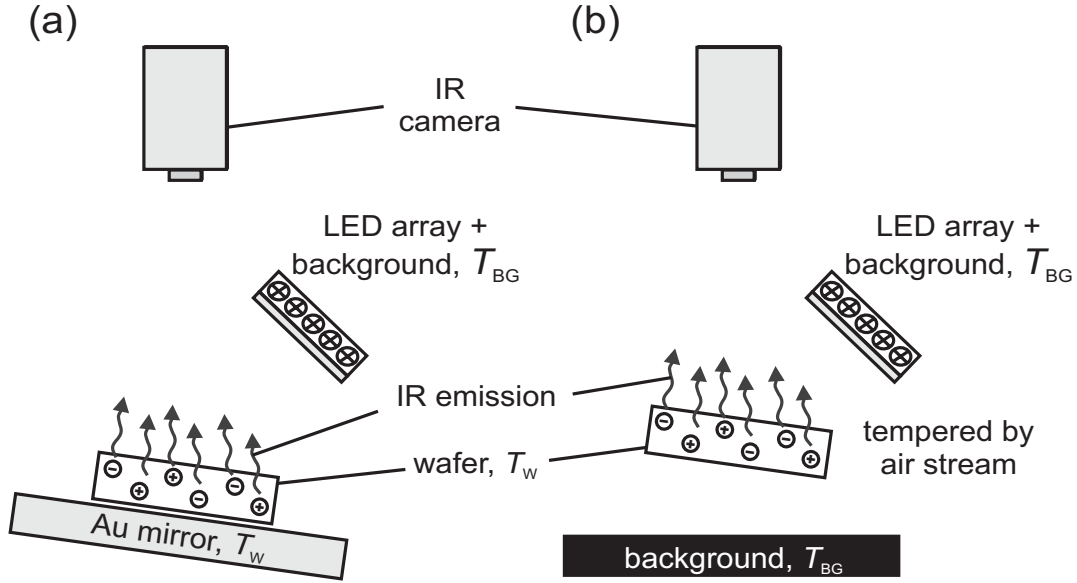


Figure 5.8: Experimental setup of the infrared lifetime mapping (ILM) technique using (a) a gold mirror and (b) a blackbody behind the sample. Depending on the temperature of the wafer  $T_W$  and the background  $T_{BG}$ , the ILM technique is performed in emission ( $T_W > T_{BG}$ ) or absorption-mode ( $T_W < T_{BG}$ ). The gold mirror enhances the sensitivity by re-directing the infrared emission of the wafer or the infrared background to the IR-camera. An optical model including the photon fluxes emitted by the wafer, the gold mirror and the background is given in Fig. 5.9.

temperature of the blackbody radiator under otherwise constant measurement conditions. This was experimentally verified shortly after the beginning of this work by Schubert *et al.* [124] by measuring the infrared signal  $\Delta S$  of a high-lifetime sample with varying wafer and background temperature.

In the following, we differentiate between two further modes of the ILM method, which only differ in the emissivity of the used background behind the sample as illustrated in Fig. 5.8. One mode is defined by using a mirror behind the sample with low emissivity as shown in Fig. 5.8(a), which represents the setup typically used in the present work. The other mode is defined by using a blackbody behind the sample with high emissivity as illustrated in Fig. 5.8(b). Please note that each of the two modes can additionally be performed in emission and absorption-mode, resulting in conclusion in four modes, which we will discuss and compare in the following.

In this Section we derive and experimentally verify a model for the sensitivity of IR-camera-based charge carrier imaging techniques. This model holds for arbitrary  $T_W$  and  $T_{BG}$  and accounts for the presence of the Au-mirror.

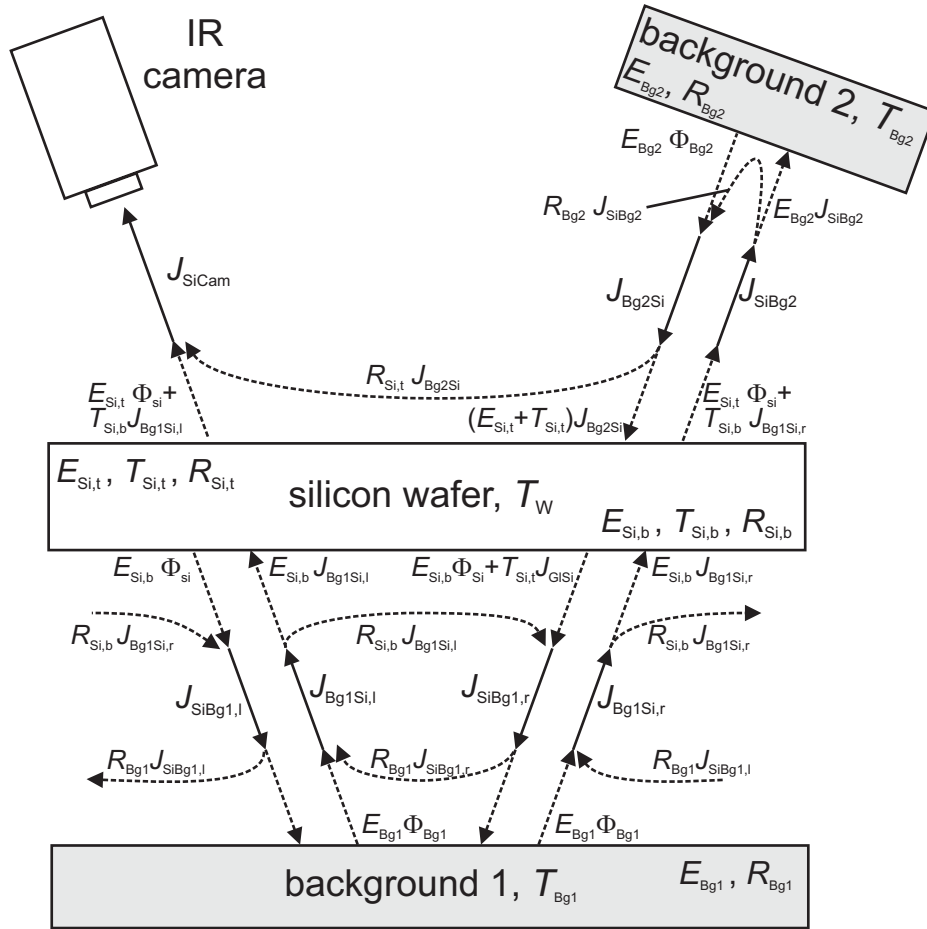


Figure 5.9: Flow diagram of the photon fluxes emitted and absorbed by all relevant parts of the ILM setup, including the photon fluxes emitted by the silicon wafer, the background behind (Background 1) and in front (Background 2) of the silicon wafer. This model is used to compare the sensitivity of the ILM setups shown in Fig. 5.8. Please note, that the schematic holds for both setups, namely ILM using a gold mirror (Fig. 5.8(a)) and using a blackbody (Fig. 5.8(b)) behind the sample. Hence, depending on the given emissivity  $E_{Au}$  and reflectivity  $R_{Au}$ , the background behind the silicon wafer represents a gold mirror ( $E_{Au} \sim 0$ ) or a blackbody ( $E_{Au} \sim 1$ ).

### 5.3.1 Optical model

Figure 5.9 gives a schematic representation of the ILM setup including all photon fluxes emitted or absorbed by the wafer and the two backgrounds, which can be considered as both sources as well as drains of photons. For the sake of simplicity we assume (i) that the surfaces of the silicon wafer and the two backgrounds possess homogeneous optical properties and (ii) that the length and width of the silicon wafer and background 1 is large compared to the distance between them. Under these assumptions the photon flux model shown in Fig. 5.9 holds for both cases shown in Fig. 5.8(a) and (b). Both setups consist of two backgrounds, namely

background 1 at temperature  $T_{Bg1}$  and background 2 at temperature  $T_{Bg2}$ , where the optical properties are described by the emissivity  $E_{Bg1}$  and reflectance  $R_{Bg1}$  for background 1 and the emissivity  $E_{Bg2}$  and reflectance  $R_{Bg2}$  for background 2. Transmittance of the two backgrounds is negligible, so that with known emissivity also the reflectance is known since the sum of both equals 1, i.e.  $E + R = 1$ . The silicon wafer being at temperature  $T_W$  is optically characterised by its emissivity  $E_{Si,i}$ , transmittance  $T_{Si,i}$  and reflectance  $R_{Si,i}$ , where the index  $i = t, b$  denotes the surface at the top and bottom side of the wafer, respectively. Note that in principle the transition from Fig. 5.8(a) using a mirror to Fig. 5.8(b) using a blackbody behind the sample is simply realised by a change of the temperature relation from  $T_W = T_{Bg1} \neq T_{Bg2}$  to  $T_W \neq T_{Bg1} = T_{Bg2}$  and a change of the emissivity of the background 1 from  $E_{Bg1} = 0$  to 1.

Depending on its temperature, the silicon wafer emits a photon flux of  $E_{Si}(n, \lambda) \cdot \Phi_{BB}(T_W, \lambda)$  on each side of the wafer according to Eq. (5.2) with  $n$  being the carrier density of the wafer. For the sake of simplicity, we omit the variables in parenthesis in the following discussion and simplify the notation of the blackbody radiation exemplary for the silicon wafer to  $\Phi_{BB}(T_W, \lambda) \equiv \Phi_{Si}$ . Analogously, for the two backgrounds we define the photon fluxes  $\Phi_{Bg1}$  and  $\Phi_{Bg2}$ . The optical properties of both backgrounds, of course, do not depend on the carrier density  $n$ . Since the infrared detector is cooled to a temperature of  $-210^\circ\text{C}$  the emitted photon flux is negligible. In general, the wavelength-dependence is accounted for by multiplying it with the responsivity curve of the detector shown in Fig. 5.2 and integrating all equations over the wavelength  $\lambda$ .

Our model aims at calculating the photon flux density  $J_{SiCam}$  as function of the carrier density  $n$ , which radiates from the silicon wafer to the IR-camera. In general, we consider all photon flux densities  $J_{xy,i}$  radiating from  $x$  to  $y$ , where  $x$  and  $y$  are either the silicon wafer (Si) or background 1 (Bg1) or 2 (Bg2) or the IR-camera (Cam). Optionally, we distinguish due to the V-form of the ILM setup between two branches  $i = l, r$ , which denote the left (l) and the right branch (r) for photons transferred between the silicon wafer and background 1. The camera itself emits and reflects (the reflectance of the objective of the IR-camera is negligible due to its anti-reflection coating) no radiation, so that the photon flux density  $J_{CamSi}$  is negligible. Hence, the flow diagram shown in Fig. 5.9 with the seven photon flux densities defines the following seven coupled linear equations.

$$J_{SiCam} = E_{Si,t} \Phi_{Si} + T_{Si,b} J_{Bg1Si,l} + R_{Si,t} J_{Bg2Si} \quad (5.19)$$

$$J_{Bg2Si} = E_{Bg2} \Phi_{Bg2} + R_{Bg2} J_{SiBg2} \quad (5.20)$$

$$J_{SiBg2} = E_{Si,t} \Phi_{Si} + T_{Si,b} J_{Bg1Si,r} \quad (5.21)$$

$$J_{Bg1Si,r} = E_{Bg1} \Phi_{Bg1} + R_{Bg1} J_{SiBg1,l} \quad (5.22)$$

$$J_{Bg1Si,l} = E_{Bg1} \Phi_{Bg1} + R_{Bg1} J_{SiBg1,r} \quad (5.23)$$

$$J_{SiBg1,r} = E_{Si,b} \Phi_{Si} + T_{Si,t} J_{Bg2Si} + R_{Si,b} J_{Bg1Si,l} \quad (5.24)$$

$$J_{SiBg1,l} = E_{Si,b} \Phi_{Si} + R_{Si,b} J_{Bg1Si,r} \quad (5.25)$$

Exemplary, we explain Eq. (5.19), the others can be deduced in a similar way. In case of Eq. (5.19), the photon flux density radiating from the silicon wafer to the IR-camera is composed of three components: the photon flux emitted by the silicon wafer at the top side  $E_{\text{Si,t}}\Phi_{\text{Si}}$ , the photon flux  $J_{\text{Bg1Si,l}}$  radiating from Background 1 to the silicon wafer and being transmitted through the wafer  $T_{\text{Si,b}}J_{\text{Bg1Si,l}}$  and the photon flux coming from background 2 and being reflected at the front side of the wafer  $R_{\text{Si,t}}J_{\text{Bg2Si}}$ .

Applying the other six coupled linear equations and solving for  $J_{\text{SiCam}}$  yields

$$\begin{aligned}
J_{\text{SiCam}} &= E_{\text{Si,t}}\Phi_{\text{Si}} + T_{\text{Si,b}} \frac{E_{\text{Bg1}}\Phi_{\text{Bg1}} + R_{\text{Bg1}}E_{\text{Si,b}}\Phi_{\text{Si}}}{1 - R_{\text{Bg1}}R_{\text{Si,b}}} \\
&+ T_{\text{Si,b}} \frac{R_{\text{Bg1}}T_{\text{Si,t}} \left( E_{\text{Bg2}}\Phi_{\text{Bg2}} + R_{\text{Bg2}}E_{\text{Si,t}}\Phi_{\text{Si}} + R_{\text{Bg2}}T_{\text{Si,b}} \frac{E_{\text{Bg1}}\Phi_{\text{Bg1}} + R_{\text{Bg1}}E_{\text{Si,b}}\Phi_{\text{Si}}}{1 - R_{\text{Bg1}}R_{\text{Si,b}}} \right)}{1 - R_{\text{Bg1}}R_{\text{Si,b}}} \\
&+ R_{\text{Si,t}} \left( E_{\text{Bg2}}\Phi_{\text{Bg2}} + R_{\text{Bg2}}E_{\text{Si,t}}\Phi_{\text{Si}} + R_{\text{Bg2}}T_{\text{Si,b}} \frac{E_{\text{Bg1}}\Phi_{\text{Bg1}} + R_{\text{Bg1}}E_{\text{Si,b}}\Phi_{\text{Si}}}{1 - R_{\text{Bg1}}R_{\text{Si,b}}} \right)
\end{aligned} \tag{5.26}$$

as a function of the carrier density  $n$ , the temperatures and the optical properties of all relevant parts of the setup.

### Comparison of the camera signal for different ILM setups

The generation of excess charge carriers  $\Delta n$  results in an increase of the absorption coefficient  $\alpha$  according to Eqs. (2.1) and (2.2). Hence, the optical parameters of the silicon wafer vary, given by the emissivity  $E_{\text{Si}}$ , reflectance  $R_{\text{Si}}$  and transmittance  $T_{\text{Si}}$ . Calculating the photon flux density in the excited  $J_{\text{SiCam,exc}}$  and non-excited  $J_{\text{SiCam}}$  state and subtracting both yields the change of the camera signal  $\Delta S$

$$\Delta S = \Gamma \cdot \Delta J = \Gamma \cdot (J_{\text{SiCam,exc}} - J_{\text{SiCam}}), \tag{5.27}$$

where  $\Gamma$  is the proportionality constant given in Eq. (5.9).

Under ideal conditions we are able to derive two simple expressions for the two extreme cases shown in Fig. 5.8(a) and (b), namely ILM using a perfect mirror and ILM using a blackbody behind the sample. For both cases we assume that the silicon wafer has no surface reflection and that the optical properties of the top and bottom surface are identical. Using a perfect blackbody behind the sample with  $E_{\text{Bg1}} = 1$  results in  $J_{\text{SiCam}} = E_{\text{Si}}\Phi_{\text{Si}} + T_{\text{Si}}\Phi_{\text{Bg1}}$  in the non-excited state and a corresponding term for the excited state. Applying Eq. (5.27) we obtain for the change of the camera signal  $\Delta S_{\text{Blackbody}}$  using a blackbody behind the sample

$$\Delta S_{\text{Blackbody}} = \Gamma \cdot (\Delta E_{\text{Si}}\Phi_{\text{Si}} + \Delta T_{\text{Si}}\Phi_{\text{Bg1}}), \tag{5.28}$$

where  $\Delta E_{\text{Si}} = E_{\text{Si,exc}} - E_{\text{Si}}$  and  $\Delta T_{\text{Si}} = T_{\text{Si,exc}} - T_{\text{Si}}$ . With  $\Delta E_{\text{Si}} + \Delta T_{\text{Si}} = 0$  we further simplify the expression to

$$\begin{aligned}\Delta S_{\text{Blackbody}} &= \Gamma \cdot \Delta E_{\text{Si}} (\Phi_{\text{Si}} - \Phi_{\text{Bg1}}) \\ &= \Gamma \cdot \Delta E_{\text{Si}} [\Phi_{\text{BB}}(T_{\text{W}}) - \Phi_{\text{BB}}(T_{\text{Bg1}})].\end{aligned}\quad (5.29)$$

This expression is equivalent to Eq. (5.8), which we derived assuming similar conditions. For the sake of completeness we notify that for sufficiently small absorption coefficients  $\alpha$  the change of the emissivity is in first approximation  $\Delta E_{\text{Si}} \approx \Delta \alpha W$ .

Analogously, we derive in case of ILM using a mirror a similar expression. Assuming a perfect mirror behind the sample with  $R_{\text{Bg1}} = 1$  and a perfect blackbody in front of the sample with  $E_{\text{Bg2}} = 1$  results in the change of the camera signal  $\Delta S_{\text{Mirror}}$

$$\Delta S_{\text{Mirror}} = \Gamma \cdot [2\Delta E_{\text{Si}} - (E_{\text{Si,exc}}^2 - E_{\text{Si}}^2)] [\Phi_{\text{BB}}(T_{\text{W}}) - \Phi_{\text{BB}}(T_{\text{Bg2}})].\quad (5.30)$$

Note that for a sufficiently small absorption coefficient  $\alpha$ , the term in brackets gives in first approximation  $2\Delta E_{\text{Si}} - (E_{\text{Si,exc}}^2 - E_{\text{Si}}^2) \approx 2\Delta \alpha W$ .

The expressions (5.29) and (5.30) define the four modes of the ILM setup. The emission and absorption-mode is for both equations defined by the factor  $[\Phi_{\text{BB}}(T_{\text{W}}) - \Phi_{\text{BB}}(T_{\text{BB}})]$ , where we replace the temperature of the background 1 and 2 by the blackbody temperature  $T_{\text{BB}}$ . If the factor is positive, ILM is performed in emission-mode and if the factor is negative, ILM is performed in absorption-mode. The exchange of the wafer temperature and the blackbody temperature results only in a change of the sign of the infrared signal, the absolute value stays the same. Interesting is the direct comparison of the ILM technique using a mirror and using a blackbody by dividing Eqs. (5.29) and (5.30), which results in

$$\frac{\Delta S_{\text{Mirror}}}{\Delta S_{\text{Blackbody}}} = \frac{2\Delta E_{\text{Si}} - (E_{\text{Si,exc}}^2 - E_{\text{Si}}^2)}{\Delta E_{\text{Si}}}.\quad (5.31)$$

The above equation holding for a surface reflection of  $R_{\text{f}} = R_{\text{b}} = 0$  is plotted in Fig. 5.10 (solid line) versus the wavelength assuming a *p*-type FZ silicon wafer with  $N_{\text{A}} = 1 \times 10^{16} \text{ cm}^{-3}$  under low-injection conditions. As expected for a sufficiently small absorption coefficient  $\alpha$ , at wavelength  $\lambda < 2 \text{ }\mu\text{m}$  the ratio approaches 2. With increasing  $\lambda$  the ratio decreases, being 1.89 in the detection range of the QWIP camera at  $\lambda = 8.3 \text{ }\mu\text{m}$ . In addition, we plot the ratio obtained using Eqs. (5.27) and (5.26) for the case of a polished FZ wafer with  $R_{\text{f}} = R_{\text{b}} = 30\%$  (dashed line). At  $\lambda = 8.3 \text{ }\mu\text{m}$  the ratio is 1.81, which further decreases with increasing wavelength.

In Fig. 5.11, the calculated camera signal  $\Delta S$  is plotted versus the wafer temperature  $T_{\text{W}}$  assuming again a *p*-type FZ silicon wafer with  $N_{\text{A}} = 1 \times 10^{16} \text{ cm}^{-3}$  under low-injection conditions ( $R_{\text{f}} = R_{\text{b}} = 30\%$ ). The camera signal  $\Delta S$  increases with increasing wafer temperature  $T_{\text{W}}$ . The ratio of  $\Delta S$  using a mirror and a blackbody

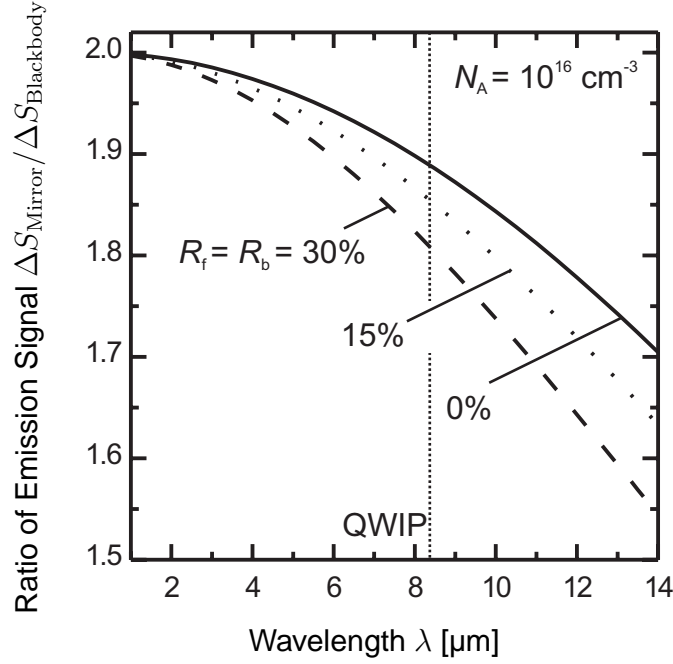


Figure 5.10: Theoretically calculated ratio of the infrared emission signal obtained with the ILM setup using a perfect mirror with  $R_{Bg1} = 1$  (Fig. 5.8(a)) and using a perfect blackbody  $E_{Bg1} = 1$  (Fig. 5.8(b)) behind the silicon wafer. The emissivity of blackbody 2 is assumed to be  $E_{Bg2} = 1$ . The ratio of the infrared signal obtained with the two setups is calculated using Eqs. (5.27) and (5.26). We assume a FZ silicon wafer with surface reflection  $R_f = R_b = 0\%$ ,  $15\%$ ,  $30\%$ . In the wavelength-detection range of the QWIP camera at  $\lambda = 8.3 \mu\text{m}$  the ratio is 1.81 for  $R_f = R_b = 30\%$ .

is kept constant at 1.81. For  $\vartheta_W < -50^\circ\text{C}$  the curves begin to saturate since the infrared emission of the wafer is negligible compared to the infrared absorption. According to Eqs. (5.29) and (5.30) the camera signal is then only proportional to  $-\Phi_{BB}(T_{BB})$  with  $T_{BB} = 300 \text{ K}$ .

For the same sample the calculated ratio of the camera signal obtained using a mirror and a blackbody behind the sample  $\Delta S_{\text{Mirror}}/\Delta S_{\text{Blackbody}}$  is shown in Fig. 5.12 for various temperatures of the background and the wafer ( $R_f = R_b = 30\%$ ). It is obvious that independently of the relation between the temperatures of the wafer and the background under the assumed conditions using an ideal mirror and ideal blackbodies, the ratio  $\Delta S_{\text{Mirror}}/\Delta S_{\text{Blackbody}}$  remains constantly at 1.81. If the sample temperature equals the background temperature the ratio cannot be calculated leading in the presented calculation to large numerical mistakes, which we intentionally plot for the sake of clarity to differentiate between ILM in emission and absorption-mode.

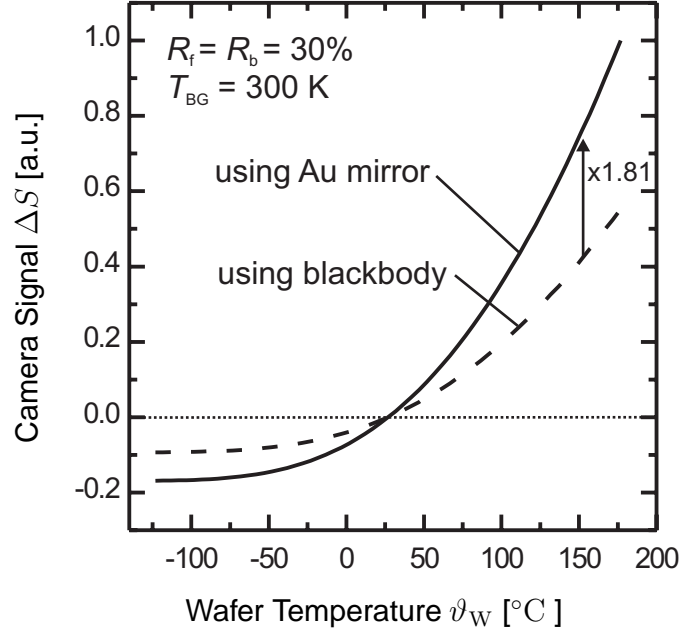


Figure 5.11: Calculated camera signal  $\Delta S$  plotted versus the wafer temperature  $T_W$  assuming a  $p$ -type FZ silicon wafer with  $N_A = 1 \times 10^{16} \text{ cm}^{-3}$  under low-injection conditions ( $R_f = R_b = 30\%$ ). In case of ILM using a mirror (Fig. 5.8(a)) the temperature of background 1 is  $T_{Bg1} = T_W$  and of background 2 is constantly being  $T_{Bg2} = 300 \text{ K}$ . In case of ILM using a blackbody (Fig. 5.8(b)) behind the sample  $T_{Bg1} = T_{Bg2} = 300 \text{ K}$ . The curves are calculated at  $\lambda = 8.3 \text{ }\mu\text{m}$ . In general, the camera signal  $\Delta S$  increases with increasing wafer temperature  $T_W$ . The ratio of  $\Delta S$  using a mirror and a blackbody keeps always 1.81. For  $\vartheta_W < -50^\circ\text{C}$  the curves begin to saturate since the infrared emission of the wafer is negligible compared to the infrared absorption, which is constant at  $T_{Bg} = 300 \text{ K}$ .

### 5.3.2 Experimental verification

The experimental comparison between the sensitivity of the different ILM setups is based on measuring the calibration factor  $m_p$  defined in Eq. (5.11). The calibration procedure is performed using a set of polished FZ silicon wafers with surface reflectivity of 30%. We investigate the ILM setup (i) using a mirror as shown in Fig. 5.8(a) and (ii) using a blackbody behind the sample as shown in Fig. 5.8(b). The optical properties are measured in the wavelength-detection range of the QWIP IR-camera by an FTIR spectrometer (Bruker Equinox 55). In case of (i) we determine the reflectance of the gold mirror to  $R_{Bg1} = 98 \pm 1.5\%$  and the emissivity of the glass plate to  $E_{Bg2} = 95 \pm 1.5\%$ . The wafer temperature equals the temperature of background 1  $T_W = T_{Bg1}$  and background 2 is at temperature  $T_{Bg2} = T_{BB}$ , which is also termed blackbody temperature. In case of (ii) the wafer is not lying on a gold mirror, but is fixed in a height of 10 cm above background 1. The temperatures of the wafer and background 1 are not coupled anymore. The wafer is homogeneously

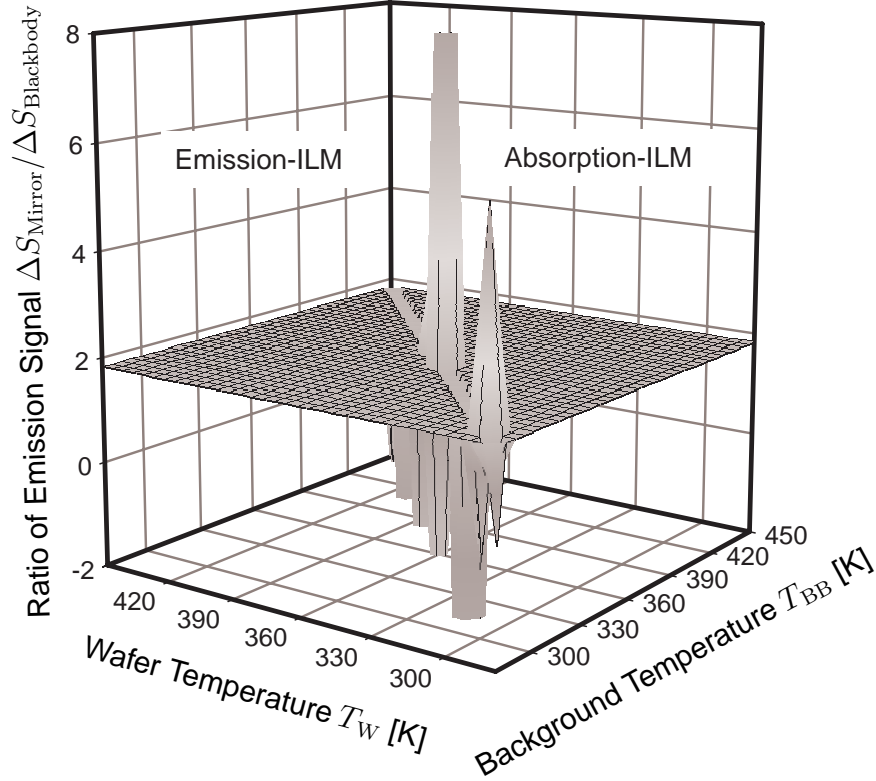


Figure 5.12: Ratio of the camera signal  $\Delta S_{\text{Mirror}}/\Delta S_{\text{Blackbody}}$  with varying temperature of the sample  $T_W$  and the background  $T_{\text{BB}}$  for the same sample as used in Fig. 5.11. The intentionally plotted numerical mistakes at  $T_W = T_{\text{BB}}$  separate the emission-ILM from absorption-ILM. The ratio is calculated assuming the ideal conditions mentioned in Fig. 5.10. The calculated ratio assuming realistic conditions is shown in Fig. 5.13.

tempered by an air stream homogenously flowing along the top and bottom surface of the wafer. The temperatures of background 1 and 2 are equal  $T_{\text{Bg1}} = T_{\text{Bg2}} = T_{\text{BB}}$ . The emissivity of the glass plate is again  $E_{\text{Bg2}} = 95 \pm 1.5\%$ . Background 1 is realised by a coated metal plate with an emissivity of  $E_{\text{Bg1}} = 98 \pm 1.5\%$ .

The calibration factor  $m_p$  can also be used for the comparison between theory and experiment since according to Eqs. (5.9) and (5.27) the camera signal is

$$\Delta S = 1.37 m_p \Delta nW = \Gamma \Delta J. \quad (5.32)$$

In the following, we use Eq. (5.32) to compare two different setups. Exemplarily, we calculate the ratio of the camera signals obtained using a mirror and a blackbody behind the sample

$$\frac{\Delta S_{\text{Mirror}}}{\Delta S_{\text{Blackbody}}} = \frac{m_{p,\text{Mirror}}}{m_{p,\text{Blackbody}}} = \frac{\Delta J_{\text{Mirror}}}{\Delta J_{\text{Blackbody}}} \quad (5.33)$$



Table 5.3: Experimentally determined ratio of the calibration factor  $m_{p,\text{Mirror}}/m_{p,\text{Blackbody}}$  obtained with the ILM setup using a Au-mirror (Fig. 5.8(a)) and using a blackbody behind the sample (Fig. 5.8(b)). The measurements are performed applying the ILM technique in cases (a) and (b) in emission-mode ( $T_W > T_{\text{BB}}$ ) and (c) in absorption-mode ( $T_W < T_{\text{BB}}$ ). The theoretical ratios are calculated applying Eqs. (5.27) and (5.26) using the experimentally determined optical parameters as mentioned in text. The optical properties are determined each with an absolute error of 1.5% leading to the theoretical errors stated in the table. Ideal conditions as discussed in Sec. 5.3.1 would result in a ratio of 1.81, independent of  $T_W$  and  $T_{\text{BB}}$ .

	$\vartheta_W$ [°C]	$\vartheta_{\text{BB}}$ [°C]	$m_{p,\text{Mirror}}/m_{p,\text{Blackbody}}$	
			experiment	theory
(a)	60	16	$1.94 \pm 0.19$	$1.83 \pm 0.07$
(b)	80	16	$1.91 \pm 0.15$	$1.81 \pm 0.07$
(c)	25	60	$1.56 \pm 0.22$	$1.47 \pm 0.09$

with  $m_{p,\text{Mirror}}$  and  $m_{p,\text{Blackbody}}$  being the experimentally determined calibration factors of the mirror and the blackbody setup. The theoretically calculated photon fluxes  $\Delta J_{\text{Mirror}}$  and  $\Delta J_{\text{Blackbody}}$  are also related to the mirror and blackbody setup.

In Tab. 5.3, experimentally determined values of the ratio  $m_{p,\text{Mirror}}/m_{p,\text{Blackbody}}$  are shown, which are measured for three different temperature relations of the wafer  $T_W$  and blackbody temperature  $T_{\text{BB}}$ , namely (a), (b) and (c). In the cases (a) and (b), ILM is performed in emission-mode applying temperatures of (a)  $\vartheta_W = 60^\circ\text{C}$  and  $\vartheta_{\text{BB}} = 16^\circ\text{C}$  and (b)  $\vartheta_W = 80^\circ\text{C}$  and  $\vartheta_{\text{BB}} = 16^\circ\text{C}$ . Increasing the wafer temperature  $\vartheta_W$  from  $60^\circ\text{C}$  to  $80^\circ\text{C}$  decreases the ratio only slightly from  $1.94 \pm 0.19$  to  $1.91 \pm 0.15$ . In the case of absorption-ILM (c), we obtain for  $\vartheta_W = 25^\circ\text{C}$  and  $\vartheta_{\text{BB}} = 60^\circ\text{C}$  a ratio of  $1.56 \pm 0.22$ , which is  $\sim 20\%$  lower compared to the cases (a) and (b).

In the previous Section, we have shown that under ideal conditions the ratio of  $\Delta S_{\text{Mirror}}/\Delta S_{\text{Blackbody}}$  is expected to be equal in emission and absorption-mode. The measured strong decrease is surprising at first glance, but can be explained by the non-ideal conditions. Using Eqs. (5.27) and (5.26) and applying the optical properties of all relevant objects specified above, we calculate the theoretical ratios shown also in Tab. 5.3. The agreement between experiment and theory is very good within the given error limits. The strong decrease of the ratio in absorption-mode (case (c) in Tab. 5.3) is theoretically underlined, which is also demonstrated in Fig. 5.13.

Finally, in Tab. 5.4 we compare the experimentally determined ratio of the calibration factor  $m_{p,\text{Emission}}/m_{p,\text{Absorption}}$  obtained by ILM in emission and absorption-

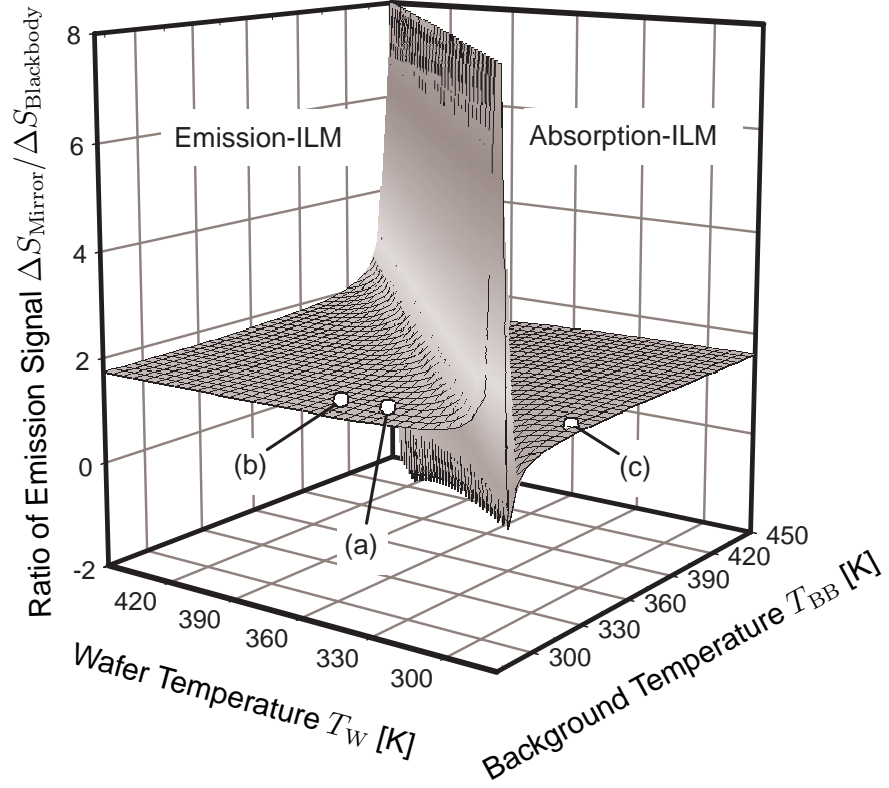


Figure 5.13: Ratio of the camera signal  $\Delta S_{\text{Mirror}}/\Delta S_{\text{Blackbody}}$  with varying temperature of the sample  $T_W$  and the background  $T_{\text{BB}}$  for the same sample as used in Fig. 5.11. The ratio is calculated assuming the realistic conditions mentioned in Sec. 5.3.2. The calculated ratio assuming ideal conditions is shown in Fig. 5.12. In addition, the experimentally determined values (white circles) are plotted, which are given in Tab. 5.3.

mode. For this only the temperature of the wafer and the blackbody radiator is exchanged under otherwise constant conditions. Under ideal conditions a ratio of 1 is expected. Experimentally, we find for the temperature relation  $\vartheta_{W,\text{BB}} = 60^\circ\text{C}$  and  $\vartheta_{\text{BB},W} = 25^\circ\text{C}$  in case of ILM using a mirror  $m_{p,\text{Emission}}/m_{p,\text{Absorption}} = 1.26 \pm 0.10$ . In case of ILM using a blackbody we find  $m_{p,\text{Emission}}/m_{p,\text{Absorption}} = 1.14 \pm 0.22$ . Both ratios are larger than unity. For ILM using a mirror the ratio is  $\sim 10\%$  increased compared to ILM using a blackbody behind the sample.

Again we calculate the ratio under the realistic conditions specified at the beginning of this Section. Theoretically we obtain for ILM using a mirror  $m_{p,\text{Emission}}/m_{p,\text{Absorption}} = 1.35 \pm 0.10$  and for ILM using a blackbody we calculate  $m_{p,\text{Emission}}/m_{p,\text{Absorption}} = 1.06 \pm 0.02$ . The agreement is well within the experimental uncertainty. The theoretical model again explains the deviations obtained under ideal and realistic conditions.

Table 5.4: Experimentally determined ratio of the calibration factor  $m_{p,\text{Emission}}/m_{p,\text{Absorption}}$  obtained by ILM in emission and absorption-mode by exchanging the temperature of the wafer  $T_W$  and the blackbody radiator  $T_{\text{BB}}$ . The theoretical ratios are calculated applying Eqs. (5.27) and (5.26) under the same conditions as used in Tab. 5.3. Ideal conditions as discussed in Sec. 5.3.1 would result in a ratio of 1, independent of  $T_W$  and  $T_{\text{BB}}$ .

	$\vartheta_{W/\text{BB}} [^{\circ}\text{C}]$	$\vartheta_{\text{BB}/W} [^{\circ}\text{C}]$	$m_{p,\text{Emission}}/m_{p,\text{Absorption}}$	
			experiment	theory
Mirror	60	25	$1.26 \pm 0.10$	$1.35 \pm 0.10$
Blackbody	60	25	$1.14 \pm 0.22$	$1.06 \pm 0.02$

In conclusion, we find that our theoretical model is capable of explaining sensitivity changes related to changes of the optical and thermal properties of the setup. The detailed analysis reveals that the ILM setup using a mirror behind the sample is - depending on the chosen temperature relation of the wafer and the blackbody radiator - by a factor of  $\sim 1.9$  more sensitive than the ILM setup using a blackbody behind the sample.

### 5.3.3 Noise Equivalent Carrier Density

The *NETD* is a most widespread characteristic given for any commercial IR-camera in order to describe the sensitivity in terms of temperatures. Since our carrier imaging technique measures carrier densities, we quantify the sensitivity of the method by the noise equivalent carrier density *NECD*. The *NECD* is the carrier density per area a sample has to have in order to yield a signal-to-noise ratio of unity.

In order to determine the *NECD* experimentally, we use a non-passivated and thus low-lifetime boron-doped FZ silicon wafer. The wafer is polished on both sides (front reflectance  $R_f = 30\%$ ), (100)-oriented, 321  $\mu\text{m}$  thick, *p*-type and has a resistivity of 1.4  $\Omega\text{cm}$ . We select an area of 12  $\text{cm}^2$  on the wafer with a spatially homogeneous lifetime. In this area, we measure an average lifetime of  $(3.7 \pm 0.4)$   $\mu\text{s}$  by MW-PCD using a white bias intensity of 1 sun. We measure the IR-camera signal  $\Delta S$  at various temperatures applying a photon flux density of  $\Phi_{\text{Gen}} = 2.75 \times 10^{17} \text{ cm}^{-2}\text{s}^{-1}$  in the same area. The static pattern noise of the camera was corrected for by a two-point correction.

The *NECD* is then deduced from the spatial fluctuation in the camera signal. The noise equivalent carrier density *NECD* is given in units of carriers per area and is deduced by the expression

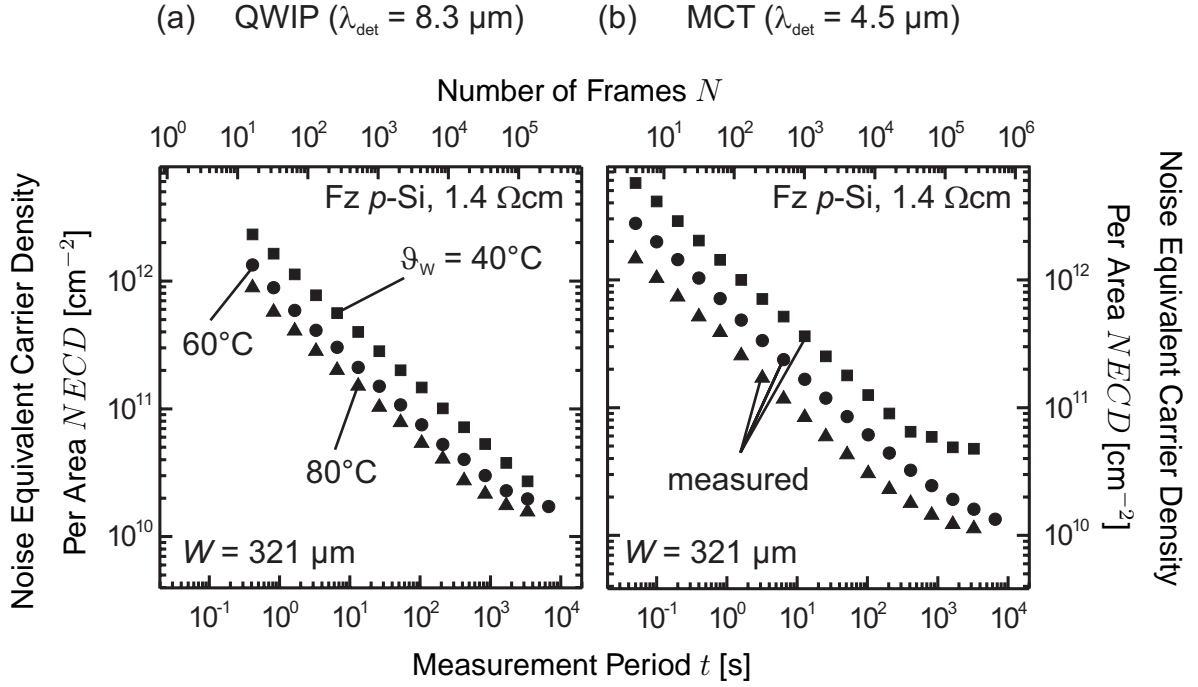


Figure 5.14: Comparison of experimental noise equivalent carrier density  $NECD$  at different wafer temperatures ( $40^\circ\text{C}$ ,  $60^\circ\text{C}$  and  $80^\circ\text{C}$ ) measured using (a) the QWIP and (b) the MCT camera.

$$NECD = \frac{StdDev(\Delta S)}{m}, \quad (5.34)$$

where  $StdDev(\Delta S)$  is the standard deviation of the camera signal  $\Delta S$ .

Figure 5.14 shows the measured  $NECD$  as a function of the measurement period and the wafer temperature  $T_W$  for both the QWIP and MCT detector, determined at a spatial resolution of  $200\ \mu\text{m}$ . In case of the QWIP camera (Figure 5.14(a)) at a wafer temperature of  $80^\circ\text{C}$  we find a  $NECD$  of  $10^{11}\ \text{cm}^{-2}$  after a measurement period of 27 s. This corresponds to 10% accuracy for measuring a carrier density per area of  $10^{12}\ \text{cm}^{-2}$ . In case of the MCT camera (Figure 5.14(b)) the  $NECD$  decreases to carrier densities of only  $10^{10}$  elementary charges per  $\text{cm}^2$  at a spatial resolution of  $200\ \mu\text{m}$ . This indicates that the IR-camera method should be capable of measuring the capacitance of  $pn$ -junctions, which is indeed realised in Chapter 8. For a further discussion of the experimental data we relate to Sec. 6.3, where the noise is expressed in terms of a noise equivalent lifetime.

## 5.4 Summary and conclusion

In this Chapter we introduced our improved in-house-built emission-ILM setup, which implements the measures suggested earlier to increase the sensitivity of the

charge carrier imaging technique. Moreover, we demonstrated that the sensitivity of IR-camera-based charge carrier imaging measurements is significantly improved by a gold mirror behind the sample which redirects the emitted infrared radiation of the free carriers to the infrared camera.

A detailed analysis of our in-house-built ILM setup using an optical model taking all photon fluxes into account, which are emitted and absorbed by all relevant components of the experimental setup, was presented. In general, the ILM technique can be performed in emission and absorption-mode. Moreover, we defined two further modes being (i) ILM using a mirror and (ii) ILM using a blackbody behind the sample under test. Modes (i) and (ii) can be performed each in absorption or emission-mode, resulting in four different modes, which all have been investigated in this Chapter. Based on our theoretical calculations it turned out that under typical measurement conditions using a mirror behind the sample at a detection wavelength of  $8\ \mu\text{m}$  increases the sensitivity by a factor of  $\sim 1.85$  compared to the use of a blackbody behind the sample. Moreover, under realistic experimental conditions emission-ILM yields an infrared emission signal up to 25% increased compared to absorption-ILM. Our experimental findings agree well within 8% with the theoretical results obtained by the photon flux model, which is, hence, well capable of predicting the sensitivity of any modified ILM setup.

We expressed the noise of our carrier imaging technique in terms of the noise equivalent carrier density per area *NECD*. For a measurement period of 32 min, the *NECD* is as small as  $10^{10}$  elementary charges per  $\text{cm}^2$  at a spatial resolution of  $200\ \mu\text{m}$ .

Due to our experimental findings we recommend to apply IR-camera-based charge carrier imaging measurements in emission mode using a mirror behind the sample. A mirror behind the sample (i) gives an easy means to control the wafer temperature and (ii) nearly doubles the sensitivity.



# Chapter 6

## Infrared Lifetime Mapping (ILM)

In the past, several contacting as well as contactless lifetime mapping techniques have been applied to characterize inhomogeneities in silicon wafers. The most widespread contactless technique is microwave-detected photoconductance decay (MW-PCD, see Sec. 3.1.2), which generates a lifetime mapping from point-by-point measurements. Due to the scanning principle, a typical measurement requires periods of hours for recording a high-resolution (pixel resolution 200  $\mu\text{m}$ ) lifetime mapping. In order to accomplish faster high-resolution lifetime mappings in the range of minutes or even seconds, Bail *et al.* [15] introduced the infrared lifetime mapping (ILM) technique.

In the following, we apply our improved experimental setup introduced in the previous Chapter to determine spatially resolved carrier lifetime images. The sensitivity of our setup allows an accurate imaging of lifetimes in the range of  $\mu\text{s}$  in measurement periods of a few seconds.

We describe the sensitivity in terms of the noise equivalent lifetime *NEL*. By definition [15] *the NEL is the carrier lifetime a sample has to have in order to yield a signal-to-noise ratio of unity*. The *NEL* was derived in Ref. 15 for the very extreme cases of the absorption- or the emission-ILM technique, however, it has never been tested experimentally. In this work, the theory of the *NEL* is extended to a generally valid expression. Good agreement is obtained between the experimentally determined and the theoretically calculated *NEL*.

We apply our improved ILM technique to mono- and multicrystalline silicon wafers. The measured lifetimes agree well with the results obtained by the microwave-detected photoconductance decay and quasi-steady-state photoconductance techniques.

Finally, we use the ILM technique to determine for the first time a spatially resolved image of the interstitial iron concentration of a multicrystalline silicon wafer, revealing that the recombination-active interstitial iron is predominantly found in the vicinity of grain boundaries.

### 6.1 Previous work

The idea of using free-carrier absorption or emission of infrared radiation in semiconductors to measure the carrier concentration and - as a consequence - to determine

the carrier lifetime is not new and has been frequently applied over the past decades. Several contactless, non-destructive optical techniques utilizing infrared absorption have been reported to measure the carrier lifetime.

As early as 1963, Nillson [125] published a paper entitled *Determination of carrier lifetime, diffusion length, and surface recombination velocity in semiconductors from photo-excited infrared absorption*. Nillson introduced a technique being capable of measuring the lifetime of free carriers in germanium wafers by photoinduced modulation of the infrared absorption. A single thermocouple detector with a time constant of 10 ms was used to analyse the transmitted infrared radiation.

A similar technique was used in 1971 by Afromowitz [126] to detect the carrier lifetime in gallium phosphide. They performed pump-and-probe experiments to determine the steady-state absorption changes using a pulsed Argon laser at  $\lambda = 515$  nm for pumping and a tungsten halogen lamp in combination with a monochromator system for probing. A lead selenide detector was used to determine the infrared absorption in the wavelength-range from 1.8 to 8  $\mu\text{m}$ . The same technique was applied to mercury cadmium telluride samples to determine their carrier lifetime [127].

For silicon samples White and Smith [128] suggested in 1977 to use the infrared emission signal of integrated circuits heated to 380 K to determine the carrier density. Moreover, they introduced a measurement setup based on pulsed optical excitation of excess carriers detectable by a lock-in infrared detector. The authors suggested to apply this pump-and-probe setup to investigate the injected carrier density in the vicinity of defects, knowing that the carrier density depends on the local recombination time. In the following year, Schroder *et al.* [23] investigated the wavelength and carrier-density dependence of the free-carrier absorption coefficient by transmission measurements on diffused and ion-implanted silicon wafers, resulting in the parameterisation of the free-carrier absorption coefficient given in Eqs. (2.1) and (2.2), which is used throughout this work.

Please note that based on Schroder's contribution Bail *et al.* [15] suggested in the year 2000 to use IR-cameras to measure the spatially resolved sheet resistance of diffused silicon wafers, which has been successfully demonstrated by Isenberg and coworkers [129, 130] in 2004 for monocrystalline silicon wafers. In order to measure the correct values of the sheet resistance, Isenberg *et al.* [24] introduced a new parameterisation for the free-carrier absorption coefficient of highly doped silicon, which we discussed in Sec. 2.1.2.

Since the 1980ies other authors have applied pump-and-probe experiments by measuring the transient transmitted infrared radiation using a fast infrared detector. In this way, recombination lifetimes of cast polycrystalline silicon [131] and monocrystalline silicon [132–135] were determined. Based on the same idea the so-called modulated free-carrier absorption (MFCA) technique was developed by Sanii *et al.* [136], evaluating besides the amplitude of the signal additionally the phase shift of the transmitted infrared radiation. This technique was further developed to a state allowing point-by-point lifetime mappings by Glunz *et al.* [61]. The MFCA



technique is in principle capable of measuring the absolute value of the infrared absorption by free-carriers and to calculate the effective lifetime. However, due to sensitivity reasons, MFCA measurements are almost always performed in a dynamic mode, evaluating the phase shift between the modulated optical excitation and infrared transmittance signal. Due to the scanning principle, a high-resolution mapping (200  $\mu\text{m}$ ) requires measurement periods in the range of hours.

### History of the ILM technique

ILM overcomes the necessity of scanning the sample since a highly sensitive IR-camera is used instead of a single IR-detector. As already mentioned, in the original ILM publication of 2000 [15] three measures to further enhance the sensitivity have been suggested: (i) the application of lock-in technology to average images and to reduce the noise, (ii) imaging of the infrared emission of a heated sample to enhance the signal without saturating the camera, and (iii) the use of a long-wave IR-camera instead of a mid-wave IR-camera to observe radiation that interacts more strongly with free carriers.

In the year 2001, Riepe *et al.* implemented suggestion (i) [62]. Unfortunately, they renamed the ILM technique to carrier density imaging (CDI). Note that ILM and CDI, thus, stand for the same measurement technique and for the sake of simplicity we use the abbreviation ILM throughout this thesis. Measure (ii) was demonstrated experimentally in Ref. 123. Isenberg *et al.* [123, 137] applied the ILM technique additionally to diffused silicon samples and as-cut multicrystalline silicon wafers, showing that the method is in principle capable of determining the carrier lifetime if an appropriate calibration is performed.

In the present work, we implement in our in-house-built setup, in addition to the measures (i)-(iii), a fourth measure: (iv) the optical enhancement of the infrared emission by a mirror placed behind the sample.

For the sake of completeness, note that there exists an additional method being capable of determining the carrier lifetime, which was introduced by Brendel *et al.* [138] in 2002. Using an IR-camera, the method images the lateral photoexcited charge carrier density profile of a silicon wafer, which is illuminated by above-bandgap light in a spot. The camera detects the radial decay of excess carriers, which yields information on the minority-carrier diffusion length and, hence, on the effective carrier lifetime.

## 6.2 Determination of the effective lifetime

All lock-in measurements presented in this work are performed under steady-state conditions, which implies that the recombination rate  $R$  equals the generation rate  $R = G$ . The generation rate corresponds to the number of absorbed photons, which is the product of the photon flux  $\Phi_{\text{Gen}}$  times the absorbed contribution of the photon

flux, which is for a 300  $\mu\text{m}$  thick sample in good approximation  $(1-R_f)$  with  $R_f$  being the front surface reflection of the silicon sample. Applying Eq. (2.9) results in

$$\frac{\Delta n}{\tau_{\text{eff}}} \equiv R = G = \frac{\Phi_{\text{Gen}}(1 - R_f)}{W}, \quad (6.1)$$

where  $\Phi_{\text{Gen}}$  can easily be measured by a calibrated reference solar cell. Using Eqs. (5.9) and (5.16) gives a simple relationship between the infrared in-phase signal  $S_{0^\circ}$  and the effective lifetime

$$\tau_{\text{eff}} = \frac{S_{0^\circ} \frac{\pi}{2}}{m\Phi_{\text{Gen}}(1 - R_f)}. \quad (6.2)$$

## 6.3 Sensitivity analysis – Noise Equivalent Lifetime

### 6.3.1 Theoretical derivation

The *NEL* is theoretically deduced in Ref. 15 from the *NETD* of the camera. The given derivation therein considers only the emission or the absorption of free carriers, which is only valid if the wafer temperature is much higher than the background temperature  $T_W \gg T_{\text{BB}}$  or vice versa. The derivation of the theoretical value of the *NEL* presented in this work follows the line of arguments given in Ref. 15, however it (i) considers both the emission and absorption of free carriers and (ii) takes into account the applied lock-in technique.

A good approximation of the photon flux of a blackbody is

$$\Phi(\lambda, T) = \frac{2\pi c}{\lambda^4} \frac{1}{e^{\frac{hc}{\lambda k T}} - 1} \approx \frac{2\pi c}{\lambda^4} e^{-\frac{hc}{\lambda k T}}. \quad (6.3)$$

Applying the expression to the camera contrast following from the change of the infrared emission due to excess free carriers given by Eq. (5.9) results in

$$\begin{aligned} \Delta S &= \Gamma \left. \frac{\partial E_{\text{Si}}}{\partial(\alpha W)} \right|_{\alpha_{\text{dop}}} \chi \Delta n \lambda^2 W [\Phi(\lambda, T_W) - \Phi(\lambda, T_{\text{BB}})] \\ &\approx \Gamma \left. \frac{\partial E_{\text{Si}}}{\partial(\alpha W)} \right|_{\alpha_{\text{dop}}} \chi \Delta n \lambda^2 W \frac{2\pi c}{\lambda^4} \left[ e^{-\frac{hc}{\lambda k T_W}} - e^{-\frac{hc}{\lambda k T_{\text{BB}}}} \right] \\ &= \Gamma \left. \frac{\partial E_{\text{Si}}}{\partial(\alpha W)} \right|_{\alpha_{\text{dop}}} \chi \Delta n \lambda^2 W \frac{2\pi c}{\lambda^4} e^{-\frac{hc}{\lambda k T_W}} \left[ 1 - e^{\frac{hc}{\lambda k} \frac{T_{\text{BB}} - T_W}{T_{\text{BB}} T_W}} \right] \\ &= \Gamma \left. \frac{\partial E_{\text{Si}}}{\partial(\alpha W)} \right|_{\alpha_{\text{dop}}} \chi \Phi_{\text{Gen}}(1 - R_f) \lambda^2 \tau_{\text{eff}} \frac{2\pi c}{\lambda^4} e^{-\frac{hc}{\lambda k T_W}} \left[ 1 - e^{\frac{hc}{\lambda k} \frac{T_{\text{BB}} - T_W}{T_{\text{BB}} T_W}} \right], \quad (6.4) \end{aligned}$$

where we have replaced  $\Delta nW$  by expression (6.1).

The detection limit of the camera corresponding to the  $NETD$  is

$$\begin{aligned} \Delta S &= \frac{\pi}{2} \cdot S_{0^\circ} = \frac{\pi}{2} \cdot \Gamma \cdot \left[ \Phi(\lambda, T_W + \sqrt{2}NETD) - \Phi(\lambda, T_W) \right] \frac{1}{\sqrt{N}} \\ &\approx \frac{\pi}{2} \cdot \Gamma \cdot \frac{2\pi c}{\lambda^4} e^{-\frac{hc}{\lambda k T_W}} \left[ e^{\frac{hc}{\lambda k} \frac{\sqrt{2}NETD}{(T_W + \sqrt{2}NETD) \cdot T_W}} - 1 \right] \frac{1}{\sqrt{N}} \\ &\approx \frac{\pi}{2} \cdot \Gamma \cdot \frac{2\pi c}{\lambda^4} e^{-\frac{hc}{\lambda k T_W}} \left[ \frac{hc}{\lambda k} \frac{\sqrt{2}NETD}{T_W^2} \right] \frac{1}{\sqrt{N}}, \end{aligned} \quad (6.5)$$

where we use Eqs. (5.16) and (5.17) in order to take into account that a lock-in technique is applied.

Equating Eqs. (6.4) and (6.5) and solving for the effective lifetime  $\tau_{\text{eff}}$  results in the noise equivalent lifetime  $NEL$ :

$$NEL = \frac{hc}{k} \frac{\frac{\pi}{2} \sqrt{2}NETD}{T_W^2 \lambda^3 \chi \Phi_{\text{Gen}}(1 - R_f)} \frac{1}{\left. \frac{\partial E}{\partial(\alpha W)} \right|_{\alpha_{\text{dop}}}} \frac{1}{\sqrt{N}} \frac{1}{1 - e^{\frac{hc}{\lambda k} \frac{T_{\text{BB}} - T_W}{T_{\text{BB}} T_W}}}. \quad (6.6)$$

The last factor of the equation shows that the  $NEL$  is infinite if the wafer temperature equals the background temperature  $T_W = T_{\text{BB}}$ . In case of  $T_W \gg T_{\text{BB}}$ , the last factor approaches unity and can be neglected. Expression (6.6) can also be applied to calculate the  $NEL$  of the ILM technique in absorption-mode when replacing  $T_W$  by  $T_{\text{BB}}$  and  $\left. \frac{\partial E}{\partial(\alpha W)} \right|_{\alpha_{\text{dop}}}$  by the derivative of the transmittance  $\left. \frac{\partial T}{\partial(\alpha W)} \right|_{\alpha_{\text{dop}}}$ .

### 6.3.2 Temperature-dependent $NEL$ measurements

In order to determine the  $NEL$  experimentally, we use the measurements shown in Fig. 5.14. The measured FZ silicon wafer was already described in Sec. 5.3.3. The experimentally measured  $NEL$  is derived according to Eqs. (5.34) and (6.2), where  $NEL = NECD / [\Phi_{\text{Gen}}(1 - R_f)]$ . Hence, the  $NEL$  is deduced from the spatial fluctuation of the lifetime determined by ILM.

Figure 6.1(a) and (b) show the experimental  $NEL$  as a function of the measurement period and the wafer temperature  $T_W$  using the QWIP and MCT camera, respectively. The temperature of the background is 15°C and the pixel resolution is 200  $\mu\text{m}$ . As expected, the  $NEL$  decreases with the square root of the measurement period. The measurement made using the QWIP camera reaches an  $NEL$  of 2.8  $\mu\text{s}$  at a wafer temperature of 40°C and after a measurement period of 6 s. At a wafer temperature of 80°C after 6 s we measure an  $NEL$  of 1  $\mu\text{s}$ . After 14 min the  $NEL$  decreases at 40°C to 0.27  $\mu\text{s}$  and at 80°C to 0.1  $\mu\text{s}$ . The latter case corresponds to 10 % accuracy for measuring an effective lifetime of 1  $\mu\text{s}$ . At 80°C the MCT camera achieves a slightly better  $NEL$ , being 0.65  $\mu\text{s}$  after 6 s and 0.07  $\mu\text{s}$  after 14 min.

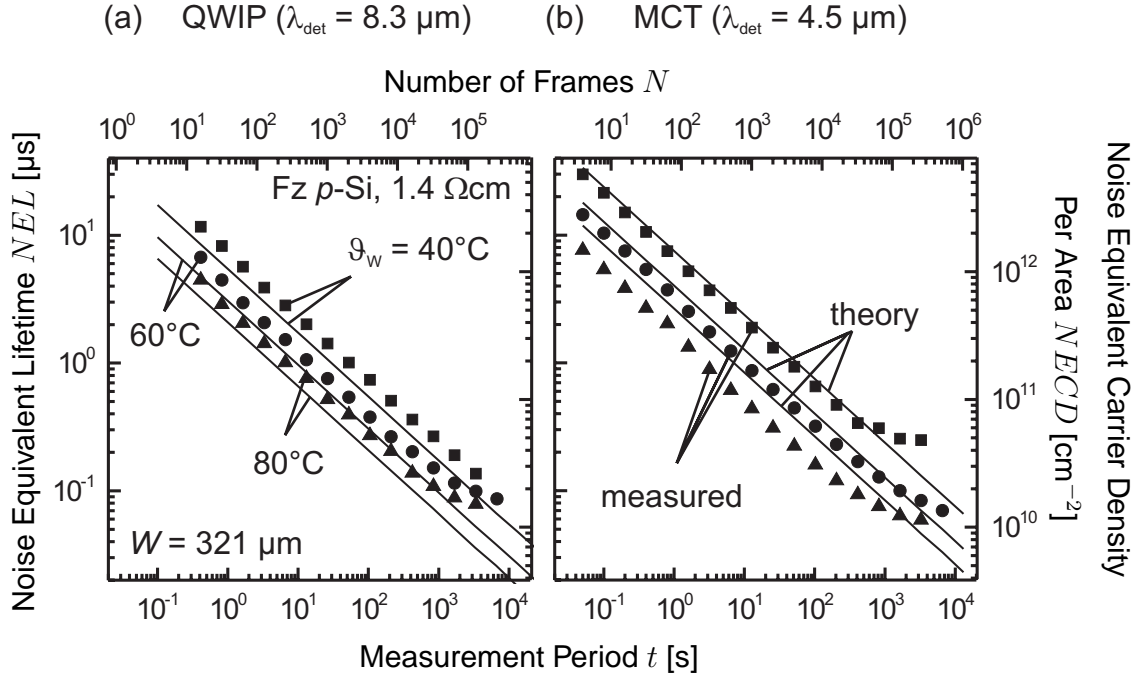


Figure 6.1: Comparison of experimental noise equivalent lifetime  $NEL$  at different wafer temperatures ( $40^\circ\text{C}$ ,  $60^\circ\text{C}$  and  $80^\circ\text{C}$ ) on a sample with  $\tau_{\text{eff}} = 3.4 \mu\text{s}$  measured with the ILM technique using (a) the QWIP and (b) the MCT camera. The theoretical  $NEL$  is derived from Eq. (6.6). The lateral resolution of the ILM measurement is  $200 \mu\text{m}$ . In addition, the right scale shows additionally the noise equivalent carrier density  $NECD$ .

### 6.3.3 Discussion

The comparison between the  $NEL$  measurements at  $\vartheta_{\text{W}} = 80^\circ\text{C}$  using the QWIP and MCT camera reveals that the MCT camera achieves experimentally a lower  $NEL$ . In general, the noise decreases further with increasing wafer temperature, which is explained by Eq. (6.6). Applying expression (6.6) results in the  $NEL$  curves calculated at each temperature shown in Fig. 6.1, where we take into account the temperature-dependent  $NETD$ , as derived in Sec. 5.1.2.2. The  $NETD$  is measured using a blackbody and is calculated according to Eq. (5.5). The  $NETD$  values are listed in Table 6.1. In case of the QWIP detector the  $NETD$  varies from 27 mK at  $\vartheta_{\text{W}} = 40^\circ\text{C}$  to 22 mK at  $80^\circ\text{C}$  ( $NETD = 25 \text{ mK}$  at  $60^\circ\text{C}$ ). For the MCT detector we measure at  $40^\circ\text{C}$  the  $NETD = 16 \text{ mK}$  and at  $80^\circ\text{C}$  the  $NETD = 8 \text{ mK}$  ( $NETD = 12 \text{ mK}$  at  $60^\circ\text{C}$ ). The values of the calculated  $NEL$  are up to 30% lower than the corresponding values of the measured  $NEL$  in case of the QWIP (Fig. 6.1(a)) detector. In case of the MCT detector (Fig. 6.1(b)) the calculated  $NEL$  is larger than measured. In particular at  $80^\circ\text{C}$  the  $NEL$  is up to 40% larger compared to the corresponding values of the measured  $NEL$ . The  $NEL$  theory thus yields the correct order of magnitude, although the deviation is larger than the estimated error of the  $NETD$ , which is at  $80^\circ\text{C}$  19% for the QWIP detector and 29% for the

Table 6.1: Experimentally determined  $NETD$  at different wafer temperatures  $\vartheta_W = 40, 60, 80^\circ\text{C}$ . The  $NETD$  is used to calculate the  $NEL$  according to Eq. (6.6) for the QWIP and MCT IR-camera as shown in Fig. 6.1(a) and Fig. 6.1(b), respectively.

$\vartheta_W$ [ $^\circ\text{C}$ ]	40 $^\circ\text{C}$	60 $^\circ\text{C}$	80 $^\circ\text{C}$
$NETD$ [mK]			
QWIP	27	25	22
MCT	16	12	8

MCT detector.

### Reduction of $NEL$ by reducing the spatial resolution

In order to reduce the measurement period  $t$ , it is possible to reduce the lateral resolution  $Z$ . Note that a reduced lateral resolution is associated with an increased  $Z$ . One way to reduce the lateral resolution is to manufacture focal plane arrays with fewer and larger detector pixels in order to increase the number of photons that is collected per detector. Such focal plane arrays should be much simpler to produce and are thus probably less expensive.

Another way is to average the signal of neighbouring pixels (pixel binning) resulting in a reduced spatial resolution, since the imaged sample area per pixel sub-array  $A = Z^2$  increases. The number of photons that is collected per pixel sub-array is proportional to the imaged area  $A$ . As the  $NEL$  decreases with the inverse of the square root of number of collected photons, it follows that the  $NEL \propto Z^{-1}$ . Figure 6.2 shows lines of constant  $NEL$  as a function of the lateral resolution  $Z$  and measurement period  $t$ . The lines are calculated from a linear fit of the experimentally obtained  $NEL_{\text{exp}}$  measured at  $\vartheta_W = 80^\circ\text{C}$  with the QWIP camera (see Fig. 6.1(a)), where a spatial resolution of  $Z = 200\ \mu\text{m}$  was used. The lines of constant  $NEL$  are given by the simple expression  $NEL = NEL_{\text{exp}}/Z$ . For in-line characterisation in a solar cell production line a measurement time of 1 s is required. For measuring a lifetime of 1  $\mu\text{s}$  with 10 % accuracy an  $NEL$  of 0.1  $\mu\text{s}$  is required. According to our noise analysis this is achievable with a lateral reduction of the resolution to  $Z = 5.5\ \text{mm}$ .

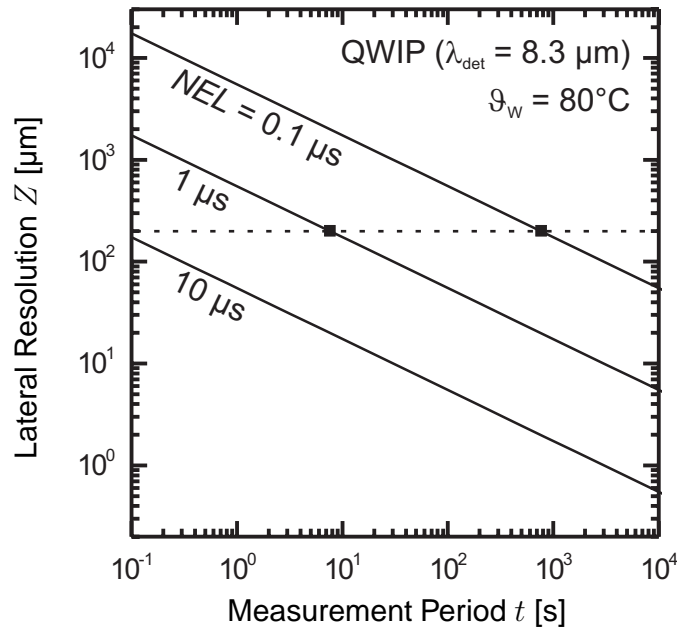


Figure 6.2: Lines of constant noise equivalent lifetime  $NEL$  as a function of the measurement period  $t$  and spatial resolution  $Z$ . These theoretical curves are calculated from a linear fit to the experimental data (squares) obtained at a wafer temperature  $\vartheta_w = 80^\circ\text{C}$  with the QWIP camera shown in Fig. 6.1(a), which is measured at a spatial resolution of  $Z = 200\ \mu\text{m}$ .

## 6.4 Application of ILM to mono- and multicrystalline silicon wafers

### 6.4.1 Comparison with MW-PCD measurements

#### ILM on float-zone silicon wafers

First, we compare the lifetimes measured by the ILM technique to those measured by the MW-PCD technique on a FZ-Si sample. The MW-PCD technique is also capable of determining carrier lifetimes with high spatial resolution. The FZ-Si wafer is  $p$ -type,  $300\ \mu\text{m}$  thick and has a resistivity of  $1.4\ \Omega\text{cm}$ . Both sides of the wafer are surface-passivated with a  $50\ \text{nm}$  thick amorphous silicon layer [139, 140]. Figure 6.3 shows a lifetime mapping of a quarter of a  $4''$  Si wafer as measured by ILM at  $70^\circ\text{C}$  (Fig. 6.3(a)) in comparison with a lifetime mapping by MW-PCD (Fig. 6.3(b)) at room temperature and at a bias light illumination of  $0.7$  suns. The ILM measurement is recorded at an absorbed photon flux that corresponds to  $1$  sun illumination intensity. Over the sample area, the measured lifetimes vary from a few tens of  $\mu\text{s}$  up to  $\sim 600\ \mu\text{s}$  due to a pronounced inhomogeneity of the surface passivation. The ILM measurement took  $0.8\ \text{s}$ , whereas the MW-PCD measurement

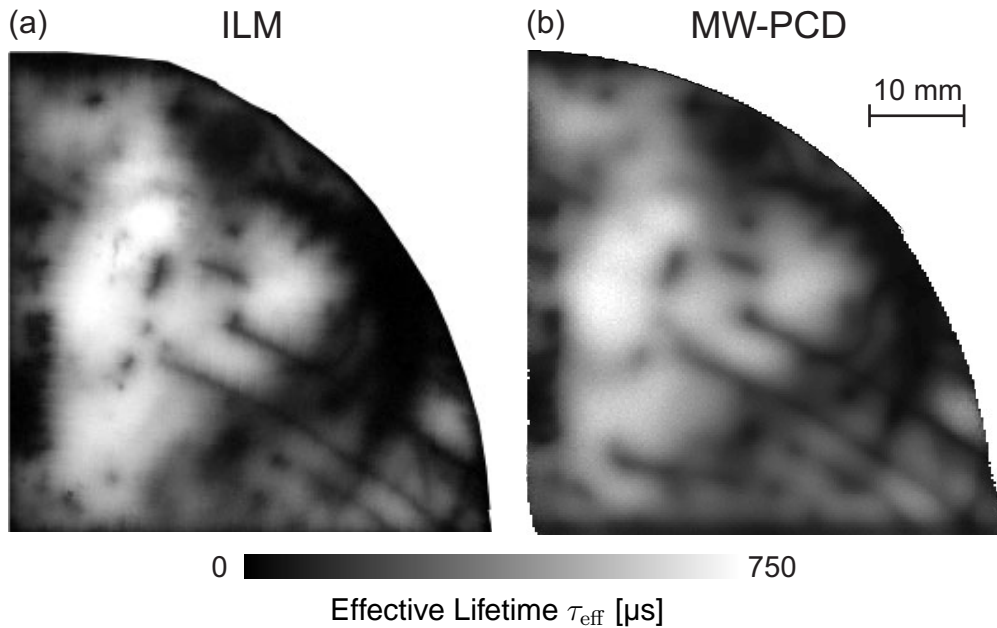


Figure 6.3: (a) Measurement by the ILM technique at 70°C of a surface-passivated silicon wafer with a lateral resolution of 200  $\mu\text{m}$  and a measurement period of 0.8 s. (b) Measurement by MW-PCD at room temperature and at a bias light illumination of 0.7 suns of the sample shown in (a). The chosen step width is 250  $\mu\text{m}$  and the measurement period is 1 h.

took 1 h, despite a slightly poorer resolution. The lateral pixel resolution is 200  $\mu\text{m}$  for the ILM measurement, while the MW-PCD measurement is performed with a step width of 250  $\mu\text{m}$ . The area-averaged lifetime measured by MW-PCD is 339  $\mu\text{s}$ . The area-average lifetime measured by ILM is 352  $\mu\text{s}$ . The lifetime patterns agree well.

### ILM on multicrystalline silicon wafers

In addition, we demonstrate the ILM technique on a phosphorus-gettered *n*-type multicrystalline silicon wafer. The wafer is surface-passivated by means of silicon nitride films, 270  $\mu\text{s}$  thick and has a resistivity of 3  $\Omega\text{cm}$ . Again, the lifetime patterns agree very well. Both mappings are recorded at an absorbed photon flux that corresponds to 0.6 suns illumination intensity. As evidenced by the ILM lifetime mapping shown in Fig. 6.4(a), low lifetime regions can still be found after gettering. These regions include grain boundaries and regions with high densities of crystallographic defects [141]. The area-averaged lifetime of the ILM image is  $\langle\tau_{\text{eff}}\rangle = (267 \pm 162) \mu\text{s}$ . The area-averaged lifetime obtained using the MW-PCD technique shown in 6.4(b) is  $\langle\tau_{\text{eff}}\rangle = (293 \pm 153) \mu\text{s}$ . An exact agreement is not expected since ILM determines the actual effective lifetime at 70°C while MW-PCD determines a differential effective lifetime at room temperature. However, good agreement is not only found in high-lifetime regions, e.g., in region 1 we measure

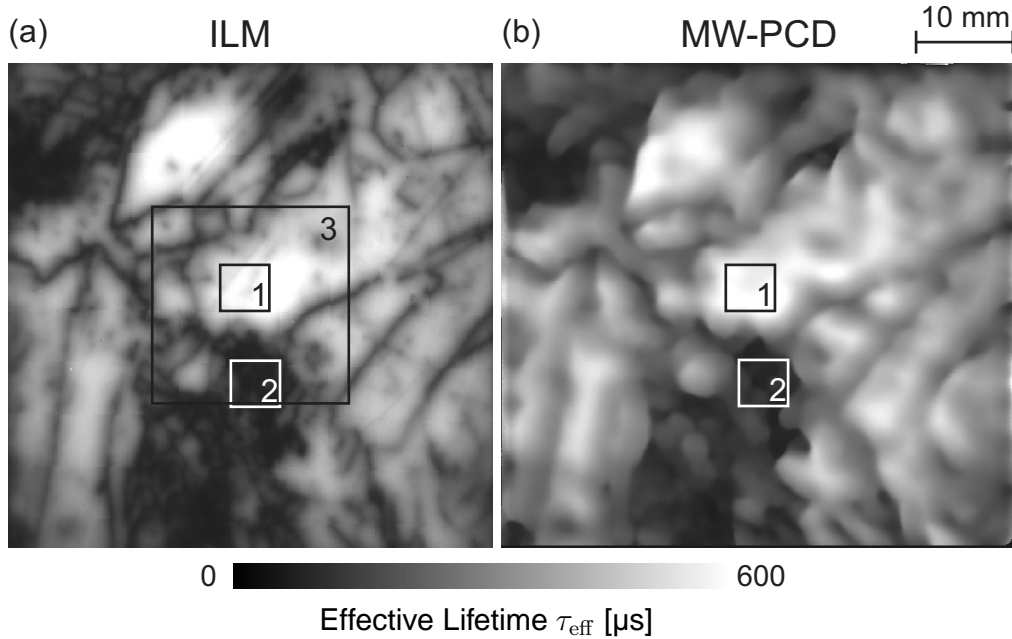


Figure 6.4: (a) Measurement of a gettered and surface-passivated *n*-type multicrystalline silicon wafer by the ILM technique at 70°C with a lateral resolution of 200  $\mu\text{m}$  and a measurement period of 1 s. (b) Measurement of the same sample by MW-PCD at room temperature and at a white bias light illumination of 0.6 suns. The scanning resolution is 125  $\mu\text{m}$  and the measurement period is 4 h.

an effective lifetime of  $\langle\tau_{\text{eff}}\rangle_1 = (597 \pm 26) \mu\text{s}$  by ILM and  $\langle\tau_{\text{eff}}\rangle_1 = (600 \pm 23) \mu\text{s}$  by MW-PCD. In the low-lifetime region 2,  $\langle\tau_{\text{eff}}\rangle_2 = (32.9 \pm 19.2) \mu\text{s}$  is measured by ILM and  $\langle\tau_{\text{eff}}\rangle_2 = (43.5 \pm 18.6) \mu\text{s}$  is measured by MW-PCD.

It is noteworthy that the measurement period of the ILM image is 1 s with an optical resolution of 200  $\mu\text{m}$ . In contrast, the measurement period of the MW-PCD mapping is 4 h due to the low scanning step width of 125  $\mu\text{m}$ . Here, we state only scanning step width, as it is obvious that the contrast and resolution of the ILM image is clearly superior to those obtained by the MW-PCD measurement. This is due to the fact that the MW-PCD measures, due to technical reasons, an averaged lifetime in an area of  $\sim \text{mm}^2$ .

Additionally, we measure the injection-dependent effective lifetime  $\tau_{\text{eff}}(\Delta n)$  of the same wafer using the QSSPC technique. The effective lifetime  $\tau_{\text{eff}}(\Delta n)$  is measured in area 3, as marked in Fig. 6.4(a), and is shown in Fig. 6.5. Averaging of the effective lifetime, as measured by ILM in the same area, yields  $\langle\tau_{\text{eff}}\rangle_3 = 276 \mu\text{s}$  determined at an average injection level of  $\langle\Delta n\rangle_3 = 8 \times 10^{14} \text{ cm}^{-3}$ . At the same injection level we measure an area-averaged lifetime of  $\langle\tau_{\text{eff}}\rangle_3 = 291 \mu\text{s}$  using the QSSPC technique. Good agreement is found within 6% deviation.

### ILM on EFG silicon wafers

Finally, we compare the ILM and MW-PCD technique on a boron-doped edge-



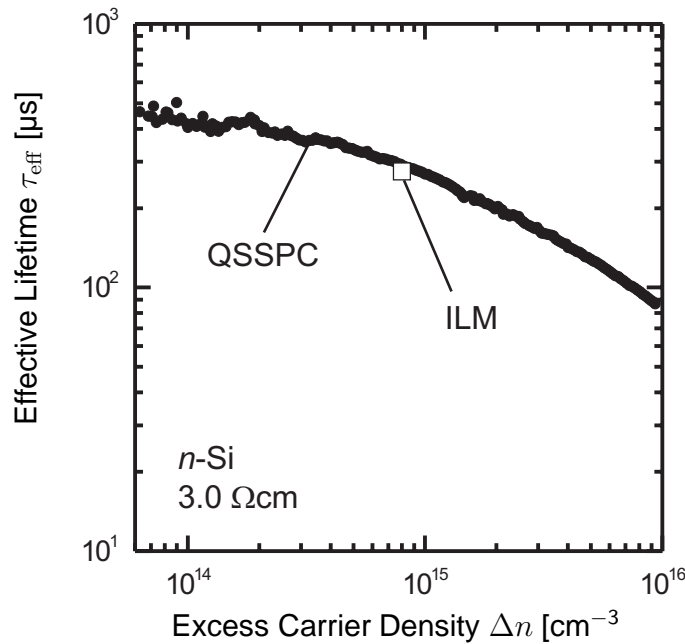


Figure 6.5: Injection-dependent lifetime measurement of the mc-Si wafer shown in Fig. 6.4 using the QSSPC technique (circles) at room temperature. The QSSPC measures the effective lifetime in the  $2 \times 2 \text{ cm}^2$  area marked in Fig. 6.4(a) as area 3. For comparison we average the ILM lifetime (square) in the same area.

defined film-fed grown (EFG [142]) silicon wafer. The wafer is  $p$ -type,  $280 \mu\text{s}$  thick and has a resistivity of  $3.5 \Omega\text{cm}$ . Both sides of the wafer are surface-passivated with  $70 \text{ nm}$  thick silicon nitride layers. Both mappings shown in Fig. 6.6 are recorded at an absorbed photon flux that corresponds to  $0.33$  suns illumination intensity. Again, the agreement of the lifetime pattern between the ILM image shown in Fig. 6.6(a) and the MW-PCD mapping shown in Fig. 6.6(b) is excellent. As in this case the lifetime is determined under low-injection conditions, no injection-dependence of the effective lifetime is expected and, thus, the differential effective lifetime determined by MW-PCD should equal the actual effective lifetime measured by the ILM technique. The area-averaged lifetime measured by ILM is  $\langle \tau_{\text{eff}} \rangle = (10.3 \pm 10.0) \mu\text{s}$  and the one measured by MW-PCD is  $\langle \tau_{\text{eff}} \rangle = (9.7 \pm 10.5) \mu\text{s}$ , revealing an absolute agreement within  $6\%$ .

#### 6.4.2 Temperature-dependent comparison with QSSPC lifetime measurements

In order to check the ILM technique in the range of short lifetimes, we investigate an Al-doped Czochralski (Cz) silicon wafer with a resistivity of  $2.0 \Omega\text{cm}$ . The lifetime in this material is known to be dominated by an Al-related defect species [143, 144]. Both wafer surfaces are once more passivated with  $80 \text{ nm}$  of silicon nitride

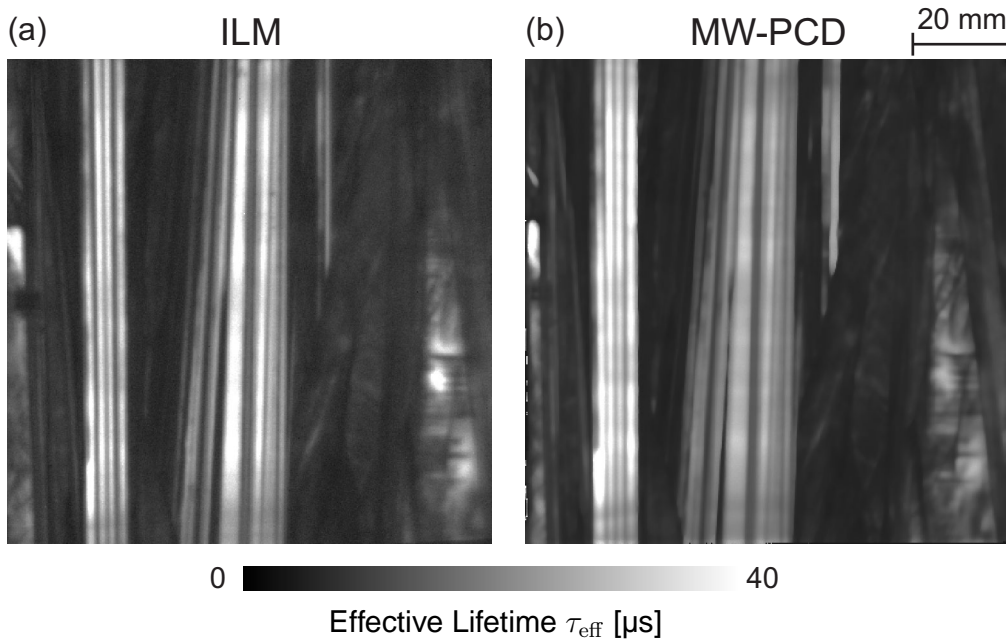


Figure 6.6: (a) Measurement by the ILM technique at  $70^\circ\text{C}$  of a surface-passivated  $p$ -type EFG silicon wafer with a lateral resolution of  $200\ \mu\text{m}$  and a measurement period of 1 s. (b) Measurement by MW-PCD at room temperature of the sample shown in (a). The scanning resolution is  $250\ \mu\text{m}$  and the measurement period is 2 h.

deposited by plasma-enhanced chemical vapour deposition. Bulk recombination is thus dominant [143]. The squares in Fig. 6.7 show the lifetimes measured by ILM at temperatures  $T_W$  ranging from  $70^\circ\text{C}$  to  $150^\circ\text{C}$ . The lifetimes vary from  $2\ \mu\text{s}$  to  $50\ \mu\text{s}$  for an photon flux of  $1.3 \times 10^{17}\ \text{cm}^{-2}\text{s}^{-1}$ . The sample was also measured with the quasi-steady-state photoconductance technique at various injection levels and temperatures. Both methods yield the same carrier lifetimes with a deviation of only 11% when averaged over all measured temperatures. The QSSPC and the ILM technique both measure effective lifetimes and not differential lifetimes.

Temperature- and injection-dependent carrier lifetime measurements have been used in the literature to characterise defect levels in silicon [143, 145]. Schmidt [143] has demonstrated the so-called temperature- and injection-dependent lifetime spectroscopy (TIDLS) method applying the QSSPC technique on the Al-doped Cz silicon wafer investigated above. Hence, we omit a detailed temperature- and injection-dependent lifetime analysis by the ILM method, as this would result in the same energy level for the aluminium-related defect, which has been determined by Schmidt [143] to  $E_C - E_t = 0.36\ \text{eV}$ .

During the course of this work, Schubert *et al.* [146] have shown by means of temperature-dependent ILM measurements on an intentionally contaminated FZ silicon wafer that determined energy levels of defects agreed well with the results of other techniques. However, as in general in multicrystalline silicon typically more than one defect species is present, the extraction of a single defect level is rather

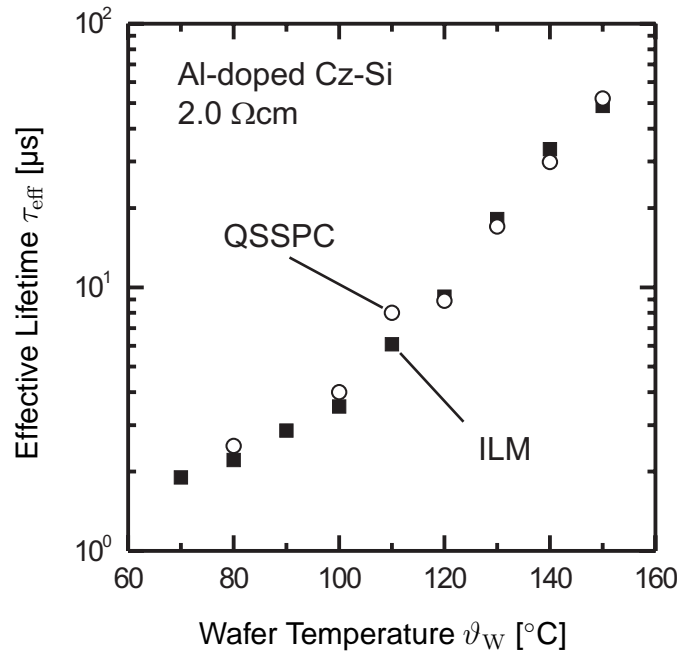


Figure 6.7: Temperature-dependent lifetime of an Al-doped silicon wafer with silicon nitride surface passivation. The wafer is measured by ILM (squares) and QSSPC (circles). The QSSPC data is taken from Ref. 143.

difficult.

### 6.4.3 Imaging of interstitial iron in multicrystalline silicon

Iron is known to be one of the most important contaminants in silicon [147, 148]. In *p*-type silicon, highly mobile interstitial iron ( $\text{Fe}_i$ ) atoms form electrically active iron-acceptor pairs with shallow substitutional acceptors such as boron, gallium and indium [149]. Iron-gallium ( $\text{FeGa}$ ) and iron-indium pairs are found to be much more effective recombination centres in *p*-type silicon [150] compared to iron-boron pairs. In general, strong illumination with white light dissociates the iron-acceptor pairs. Storage of the samples in the dark leads to a full repairing of the iron-acceptor pairs [150, 151]. We apply a simple method originally introduced in Ref. 152 and refined in Refs. 153 and 150 for the determination of the  $\text{Fe}_i$  concentration in silicon. In this method, the effective carrier lifetimes are measured before ( $\tau_0$ ) and after ( $\tau_1$ ) pair dissociation. Assuming that all other recombination processes remain unchanged, the interstitial iron concentration  $[\text{Fe}_i]$  is then calculated according to the expression

$$[\text{Fe}_i] = C(\Delta n, N_A) \left( \frac{1}{\tau_1} - \frac{1}{\tau_0} \right), \quad (6.7)$$

where  $C(\Delta n, N_A)$  is a calibration factor depending on the injection density  $\Delta n$

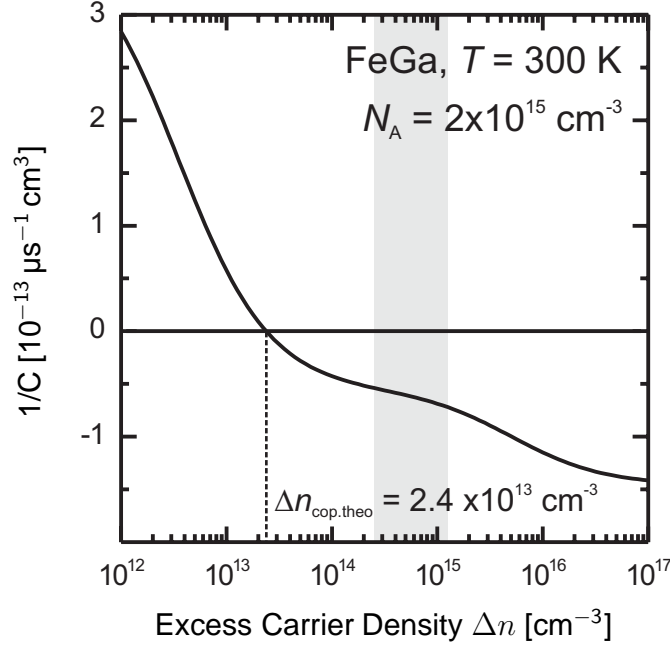


Figure 6.8: Inverse calibration factor  $1/C$  as a function of excess carrier density  $\Delta n$  at a doping concentration of  $N_A = 2 \times 10^{15} \text{ cm}^{-3}$  for gallium-doped  $p$ -type silicon at 300 K, as calculated in Ref. 150. The theoretically calculated crossover point  $\Delta n_{\text{cop,theo}}$  defines the characteristic excess carrier density at which the carrier lifetime remains unchanged after dissociation [153–155]. The shaded region corresponds to the measured injection range of the the ILM measurements shown in Figs. 6.10(a) and (b).

and the acceptor doping concentration  $N_A$ . Most accurate data on the calibration factor for the systems iron-boron, iron-gallium and iron-indium have recently been published by Schmidt and Macdonald [150]. Applying the defect parameters given in Ref. 150 for the iron-gallium pair, we calculate the calibration factor at a doping concentration of  $N_A = 2 \times 10^{15} \text{ cm}^{-3}$ . We assume that the energy level of interstitial iron lies at  $E_t = E_V + 0.38 \text{ eV}$  with capture cross sections of the electrons  $\sigma_n = 4 \times 10^{-14} \text{ cm}^2$  and the holes  $\sigma_p = 7 \times 10^{-17} \text{ cm}^2$ . The energy level of the donor FeGa has been determined to lie at  $E_t = E_V + 0.20 \text{ eV}$  with capture cross sections of the electrons  $\sigma_n = 4 \times 10^{-14} \text{ cm}^2$  and the holes  $\sigma_p = 2 \times 10^{-14} \text{ cm}^2$  [150]. Calculating the Shockley-Read-Hall lifetime using Eq. (2.19) for both defects and applying Eq. (6.7) yields the inverse of the calibration factor  $1/C(\Delta n, N_A = 2 \times 10^{15} \text{ cm}^{-3})$  shown in Fig. 6.8, which is independent of the iron concentration. The so-called crossover point  $\Delta n_{\text{cop}}$  defines the excess carrier density at which the carrier lifetime remains unchanged after dissociation [153–155]. In case of FeGa, the theoretically calculated crossover point is independent of the doping concentration at  $\Delta n_{\text{cop,theo}} = 2.4 \times 10^{13} \text{ cm}^{-3}$ . For  $\Delta n > \Delta n_{\text{cop,theo}}$  the carrier lifetime increases after dissociation, whereas for  $\Delta n < \Delta n_{\text{cop,theo}}$  the carrier lifetime decreases after dissociation of the FeGa pairs.

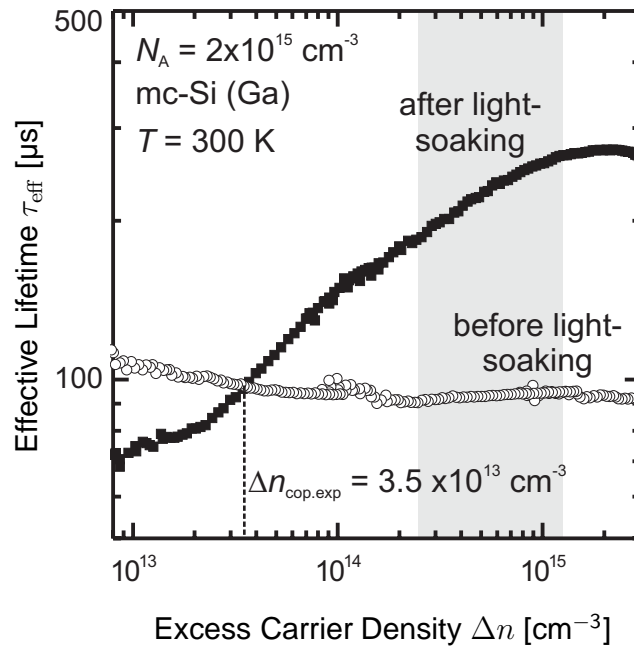


Figure 6.9: Injection-dependent lifetime curves  $\tau_{\text{eff}}(\Delta n)$  of a Ga-doped mc-Si wafer with doping concentration  $N_A = 2 \times 10^{15} \text{ cm}^{-3}$  before and after light-soaking (5 min at 4 suns) measured by the QSSPC technique. Experimentally, the crossover point is at an injection density of  $\Delta n_{\text{cop,exp}} = 3.5 \times 10^{13} \text{ cm}^{-3}$ . The shaded region corresponds to the measured injection range of the the ILM measurements shown in Figs. 6.10(a) and (b).

In the following, we apply the ILM technique to a gallium-doped multicrystalline silicon wafer with doping concentration  $N_A = 2 \times 10^{15} \text{ cm}^{-3}$  from the middle of a block-cast ingot [(100)-oriented, 280 thick  $\mu\text{m}$ ]. The samples have been supplied by the Japanese company Dai-ichi Kiden. In Fig. 6.9, injection-dependent lifetime curves  $\tau_{\text{eff}}(\Delta n)$  of the mc-Si wafer are shown before and after light-soaking at 4 suns for 5 min, as measured by the QSSPC technique. Experimentally, we find the crossover point at an injection density of  $\Delta n_{\text{cop,exp}} = 3.5 \times 10^{13} \text{ cm}^{-3}$  in good agreement with the theoretically calculated value given in Ref. 150 and shown in Fig. 6.8 of  $\Delta n_{\text{cop,theo}} = 2.4 \times 10^{13} \text{ cm}^{-3}$ . In the area measured by the QSSPC technique, at an injection density of  $\Delta n = 1 \times 10^{15} \text{ cm}^{-3}$  the effective lifetime  $\tau_{\text{eff}}$  increases due to the FeGa dissociation from 94 to 254  $\mu\text{s}$  by a factor of  $\sim 2.7$ .

Figure 6.10 shows the lifetime mapping of the wafer (a) before and (b) after light-soaking at 2 suns for 2 min. The ILM measurements are performed at a light intensity of  $\sim 0.4$  suns. For both mappings the excess carrier density ranges from  $\Delta n = 2 \times 10^{14} \text{ cm}^{-3}$  to  $2 \times 10^{15} \text{ cm}^{-3}$ , hence, the measurements are performed at injection levels well above the crossover point. As expected for the FeGa dissociation, a strong increase in lifetime is observed after light-soaking. Intriguingly, in some areas lifetimes up to 800  $\mu\text{s}$  are measured in the as-grown mc-Si after light-soaking, whereas before light-soaking in the same regions the lifetime is as low as 220  $\mu\text{s}$ . The area-averaged

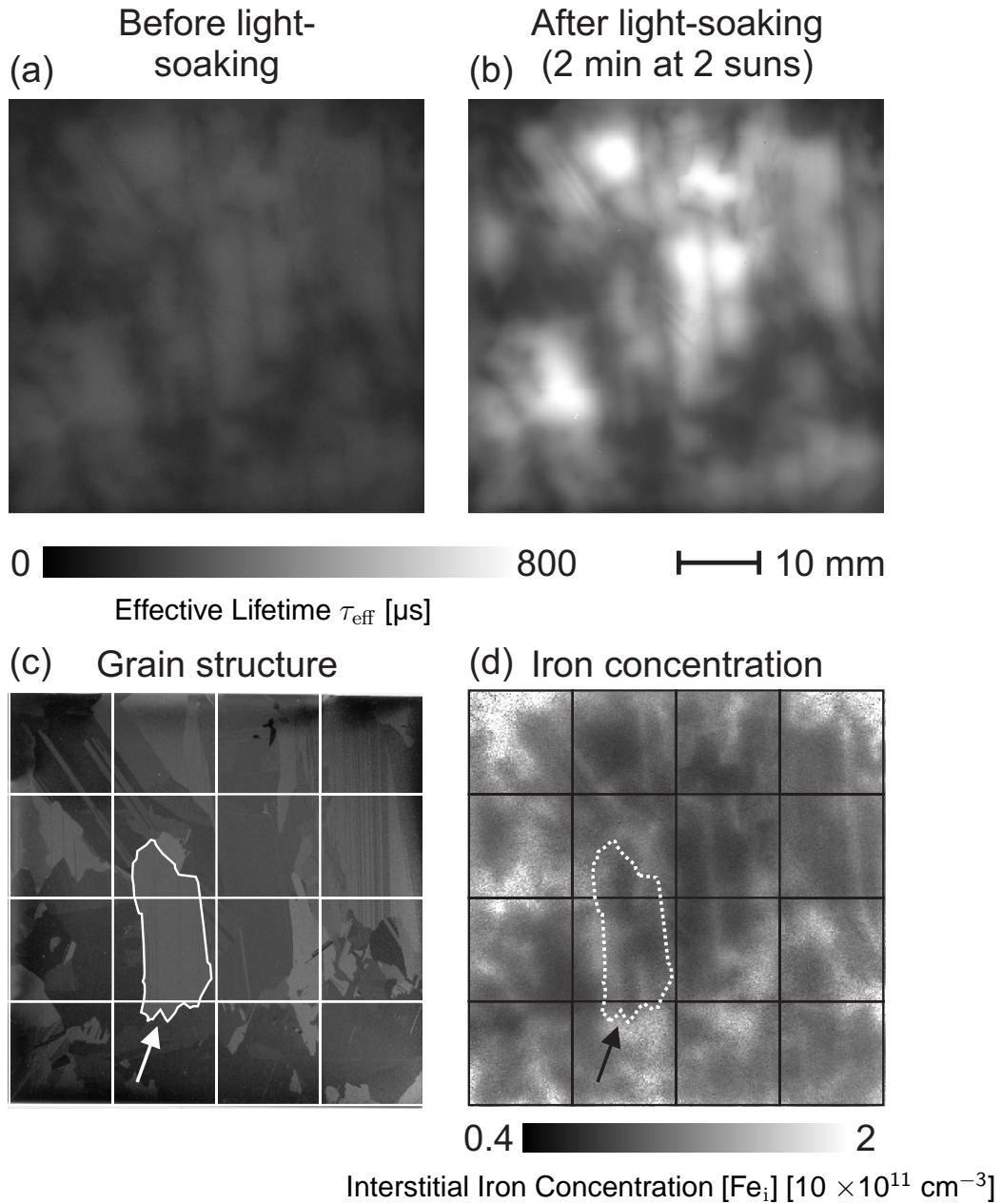


Figure 6.10: Infrared-camera lifetime mappings of a Ga-doped mc-Si wafer with doping concentration  $N_A = 2 \times 10^{15} \text{ cm}^{-3}$  (a) before light-soaking and (b) after light-soaking (2 min at 2 suns). The wafer temperature is  $50^\circ\text{C}$ . (c) Scanned picture of the wafer. (d) Iron concentration mapping calculated from (a) and (b) as described in the text.

lifetime of the sample is  $\langle\tau_{\text{eff}}\rangle = (127 \pm 44.3) \mu\text{s}$  before and  $(349 \pm 181) \mu\text{s}$  after light-soaking, suggesting in fact that iron is the main contaminant, dominating the lifetime in the form of highly recombination-active iron-gallium pairs before illumination.

From the lifetime mappings shown in Figs. 6.10(a) and (b), we calculate the inverse lifetime mappings and subtract both mappings. This procedure is allowed since the calibration factor  $C$  is in a good approximation constant within the measured injection range. For the sake of simplicity we average the inverse of the calibration factor  $1/C$  in the injection range marked as grey area corresponding to the measured injection range of the the ILM measurements shown in Figs. 6.10(a) and (b). Fortunately, the change of  $1/C$  over the measured injection range is small. Using the inverse of the calibration factor of  $1/C = (0.63 \pm 0.02) \times 10^{-13} \mu\text{s}^{-1} \text{cm}^3$ , we calculate the mapping of the interstitial iron concentration, as shown in Fig. 6.10(d). We find a very inhomogeneous distribution of recombination-active iron with  $[\text{Fe}_i]$  ranging from  $5 \times 10^{10} \text{cm}^{-3}$  to  $2 \times 10^{11} \text{cm}^{-3}$ . The area-averaged interstitial iron concentration is  $\langle[\text{Fe}_i]\rangle = (8.3 \pm 3.0) \times 10^{10} \text{cm}^{-3}$ . Regions of increased  $\text{Fe}_i$  concentrations correlate in some regions with grain boundaries. This can be seen by comparing the photograph in Fig. 6.10(c) of the silicon wafer directly with the iron concentration mapping in Fig. 6.10(d). One characteristic grain is marked in Figs. 6.10(c) and (d). In the vicinity of the grain boundary, the  $\text{Fe}_i$  concentration is increased. For example, on the bottom of the grain at the double-peak of the marked grain boundary – as shown by the arrow – we obtain an interstitial iron concentration of  $[\text{Fe}_i] = (1.2 \pm 0.2) \times 10^{11} \text{cm}^{-3}$ , which is twice as high compared to  $[\text{Fe}_i] = (6.0 \pm 0.3) \times 10^{10} \text{cm}^{-3}$  measured in the centre of the grain. Grain boundaries are known to be preferred sites for the formation of iron precipitates in mc-Si. Our measurements indicate that these precipitates might partly dissolve during the cooling of the mc-Si block, leading to an increased  $\text{Fe}_i$  concentration close to grain boundaries. However, it should be noted that not all grain boundaries are found to correlate with high  $\text{Fe}_i$  concentration.

## 6.5 Summary

We quantified the sensitivity of ILM measurements by the noise equivalent lifetime  $NEL$ . In the theory derived in this Chapter, the  $NEL$  agrees within 35% with the experimental findings obtained using either a midwave or a longwave infrared camera. Both infrared cameras applied in this work yield comparable  $NEL$ s. When combining all measures for increasing the sensitivity, lifetimes as short as  $1 \mu\text{s}$  became measurable with an accuracy of 10% at a spatial pixel resolution of  $200 \mu\text{m}$  in a measurement period of 14 min. After a measurement period of 1 s, an  $NEL$  of  $2 \mu\text{s}$  is measured at a wafer temperature of  $80^\circ\text{C}$ . Theoretically, it is expected that reducing the spatial resolution to  $5.5 \text{mm}$  by using larger and fewer detectors in the focal plane array could allow the measurement of a lifetime of  $1 \mu\text{s}$  with 10% error in just 1 s.

We found quantitative agreement within 11 % deviation between ILM lifetime measurements performed on mono- and multicrystalline silicon samples and conventional lifetime measurement techniques such as MW-PCD and QSSPC in the lifetime range from  $\mu\text{s}$  to  $\text{ms}$  and in the temperature range from  $50^\circ\text{C}$  to  $150^\circ\text{C}$ .

Application of the ILM method to a gallium-doped multicrystalline silicon wafer resulted for the first time in an image of the interstitial iron concentration down to  $5 \times 10^{10} \text{ cm}^{-3}$ . As an important result, in the vicinity of the grain boundaries the interstitial iron concentration was found to be increased.



# Chapter 7

## Infrared Trap Mapping (ITM)

In the following, we apply the ILM [15, 156] technique discussed in detail in the previous Chapter to measure spatially resolved carrier lifetimes over a broad injection range. In general, the effect of minority-carrier trapping has an impact also on ILM measurements. Hence, we apply, based on the Hornbeck and Haynes theory [101, 102] discussed in Sec. 4.1, the simple expressions taking the impact of minority-carrier trapping on ILM measurements into account. The application of this model to injection-dependent ILM measurements enables the spatially resolved determination of the concentration and the energy level of non-recombination-active minority-carrier traps in semiconductors. We term this method infrared trap mapping (ITM).

We apply the ITM method to Czochralski and multicrystalline silicon to demonstrate the usefulness of ITM for conventional solar-grade silicon materials [107, 157–159]. Keeping in mind that our carrier lifetime measurements might be affected by space-charge-region-dominated effects as well, we also apply the model introduced in Sec. 4.2.2.1, which takes possible impacts of space-charge regions surrounding extended structural defects such as dislocations into account.

### 7.1 Previous work

The existence of carrier trapping phenomena has been reported by various authors for germanium and *n*- and *p*-type silicon [101, 102, 160, 161]. Hornbeck and Haynes [101, 102] developed a model to explain the unusual photoconductance data measured in single-crystalline silicon. This model is very similar to a slightly earlier and independently developed model by Fan [161].

The physical origins of minority-carrier trapping in silicon wafers seem to be manifold and are not well understood up to now. In the year 1955 [101, 102], Hornbeck and Haynes found experimentally that temporary trapping of charge carriers in silicon strongly influences carrier lifetime measurements. They performed time-resolved carrier lifetime measurements by determining the resistance of silicon rods ( $0.2 \times 0.2 \times 2 \text{ cm}^3$ ), in which excess charge carriers were injected by a short pulse of light. Based on their theoretical description of the underlying trapping mechanism, which is also used in the present work (see Sec. 4.1), they were capable of determining the trap parameters, namely the trap density  $N_t$ , trap energy level  $E_t$ , the cross section for capture  $S$ , and the time which a minority-carrier spends in a trap  $\tau_d$ . In

*p*-type silicon, Hornbeck and Haynes [101] were able to identify two different traps, a shallow trap with an energy level at  $E_C - E_{t1} = 0.57$  eV, and with the time which an electron spends in a trap of  $\tau_d = 50$   $\mu$ s. In addition, they found a deep trap with  $E_C - E_{t2} = 0.72$  eV and  $\tau_d = 1$  s. In *n*-type silicon, they found two types of traps as well. They identified one sort of traps with energy level  $E_{t3} - E_V = 0.45$  eV and  $\tau_d = 45$  ms and the other sort of traps with  $E_{t4} - E_V = 0.72$  eV and  $\tau_d = 300$  s. For both in *n*- and *p*-type silicon the deep traps have been showing an additional loss mechanism via recombination of electron-hole-pairs.

In 1999, Macdonald and Cuevas [17] applied the simple theoretical model suggested by Hornbeck and Haynes [101,102] to injection-dependent QSSPC lifetime measurements on *p*-type multicrystalline silicon wafers. In *p*-type multicrystalline silicon wafers, typical trap energies of  $E_C - E_t = 0.39$  eV have been found.

More recently, Macdonald and Cuevas [162] showed that in boron-doped multicrystalline silicon at least two different types of traps may be present. One species can be removed by phosphorus gettering and is associated with of boron-related centres. The other type is impervious to gettering and is correlated with dislocations [162].

However, the mentioned measurement techniques typically average over a sample area of a few  $\text{cm}^2$ , whereas a good spatial resolution would be highly desirable to characterize distributions of trapping centres.

## 7.2 Experimental method

The infrared trap mapping (ITM) technique is derived from the ILM technique discussed in Sec. 5.2. The experimental setup is shown in Fig. 5.6. For the measurements presented in this Chapter the silicon wafers are heated to a constant temperature  $T_W = 343$  K. The background is generally cooled to a constant temperature  $T_{BG} = 290$  K.

After measuring spatially resolved injection-dependent lifetime curves of the sample using the ILM technique, we apply Eqs. (4.11)-(4.13) to all experimental data using an automated fitting routine based on a Downhill-simplex algorithm [163]. This fitting results in the local trap density  $N_t(x, y)$ , the trap ionization energy  $(E_C - E_t)(x, y)$  and the recombination lifetime  $\tau_r(x, y)$ . As our measurements are performed under low-injection conditions,  $\tau_r$  does not depend on the injection level.

## 7.3 Application of ITM to silicon wafers

### 7.3.1 Impact of the trap density on the recombination lifetime in Cz-Si

We apply the ILM technique to a (100)-oriented,  $0.33 \Omega\text{cm}$  *n*-type Czochralski silicon (Cz-Si) wafer with a thickness of  $280 \mu\text{m}$  and a interstitial oxygen concentration

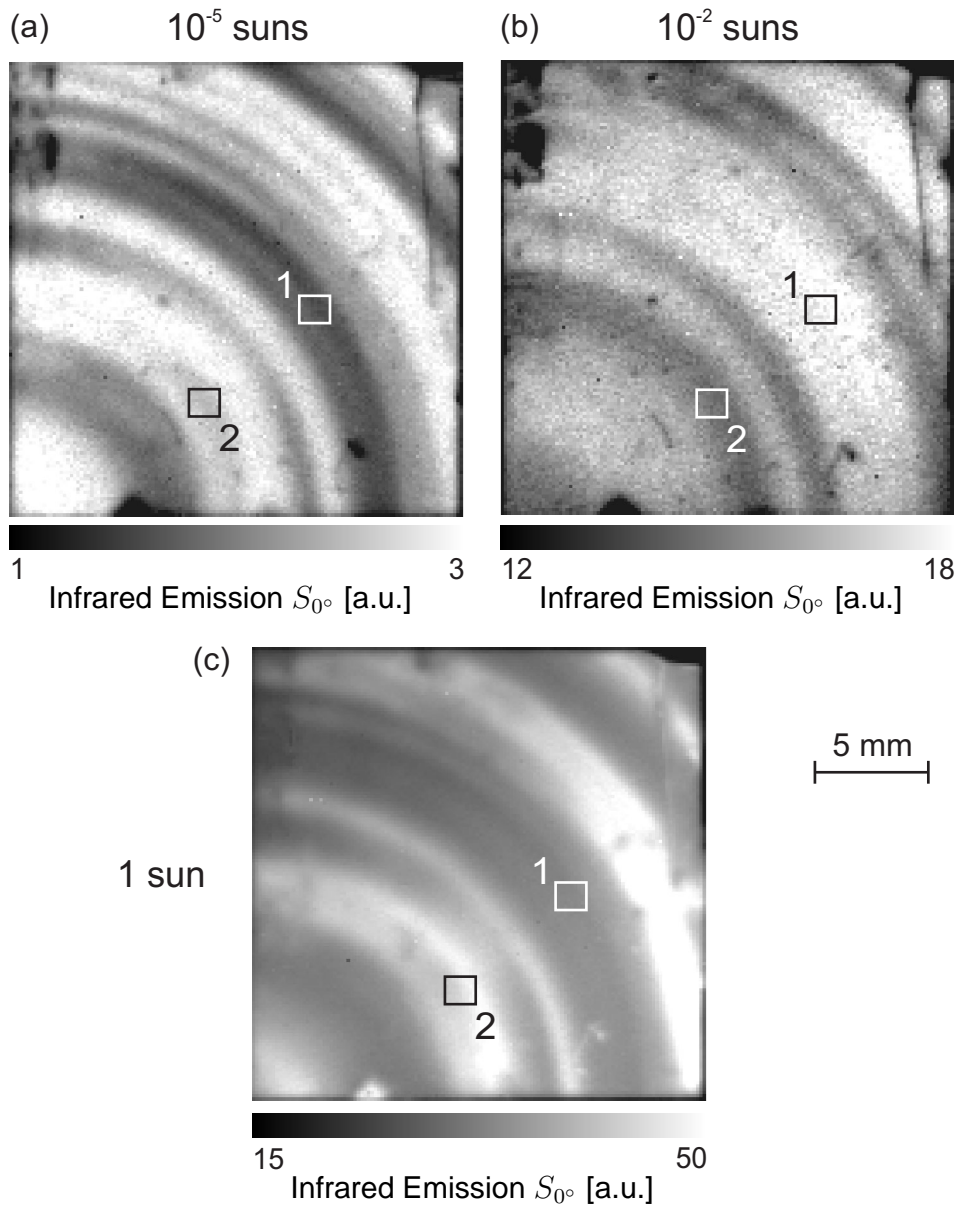


Figure 7.1: Infrared emission  $S_{0^\circ}$  of a Cz-Si wafer obtained using lock-in infrared emission measurements at  $70^\circ\text{C}$ . The mappings are measured at three different illumination intensities: (a)  $10^{-5}$  suns, (b)  $10^{-2}$  suns and (c) 1 sun. The absolute values of the three images are comparable.

$[\text{O}_i]=1.3\times 10^{18}\text{ cm}^{-3}$ ] [45]. The wafer is cut into pieces of  $2\times 2\text{ cm}^2$ . Both surfaces are passivated with 70 nm thick silicon nitride films deposited in a remote plasma-enhanced chemical vapour deposition system at  $400^\circ\text{C}$  [52].

Figure 7.1 shows three images of the infrared emission signal  $S_{0^\circ}$  of the same Cz-Si sample at three different illumination intensities ( $10^{-5}$  suns,  $10^{-2}$  suns and 1 sun). As expected, the overall excess-carrier emission signal decreases with decreasing illumination intensity. Surprisingly, the qualitative appearance of the images

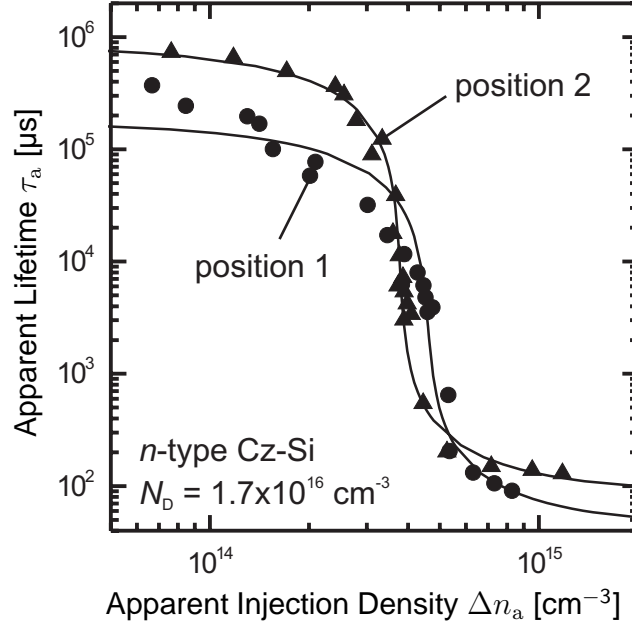


Figure 7.2: Exemplary injection-dependent lifetime curves  $\tau_a(\Delta n_a)$  at two different positions (marked in Fig. 7.1 and 7.3) of a Cz-Si wafer obtained using lock-in infrared emission measurements at 70°C.

completely changes with increasing illumination intensity. Brighter regions of the image shown in Fig. 7.1(b) correspond to darker regions in the other two images (Figs. 7.1(a) and (c)). This is demonstrated for the two regions marked in Fig. 7.1. Region 1 exhibits at  $10^{-2}$  suns (Fig. 7.1(b)) illumination intensity a higher infrared in-phase signal  $S_{0^\circ}$  than region 2. At  $10^{-5}$  suns (Fig. 7.1(a)) and 1 sun (Fig. 7.1(c)) illumination intensity we find an increased signal  $S_{0^\circ}$  in region 2 compared to region 1. Figure 7.2 shows two examples of injection-dependent apparent lifetime curves measured in the areas marked as 1 and 2 in Fig. 7.1. The two curves have been measured in  $1 \times 1 \text{ mm}^2$  areas with the lowest (circles, position 1) and highest (triangles, position 2) lifetimes at 1 sun illumination intensity. These curves clearly reveal a strong increase of the apparent lifetime  $\tau_a$  with decreasing injection level, which is typically observed when minority-carrier trapping occurs. Note that a similar dependence has also been measured on silicon nitride passivated *p*-type silicon wafers without the presence of trapping centres. This effect was attributed to the storage of electrons in the space charge region produced by the highly positively charged silicon nitride film [103]. We can exclude this effect here as we are only studying *n*-type silicon.

Applying Eqs. (4.11)-(4.13) to the experimental data of the Cz-Si wafer using an automated fitting routine results in the spatially resolved trap density image shown in Fig. 7.3(a). Fitting Eqs.(4.11) and (4.12) to the experimental data shown in Fig. 7.2 yields trap densities  $N_t$  of  $1.7 \times 10^{15} \text{ cm}^{-3}$  and  $1.4 \times 10^{15} \text{ cm}^{-3}$  for region 1 and 2, respectively. The trap density  $N_t(x, y)$  determined by the ITM method ranges from

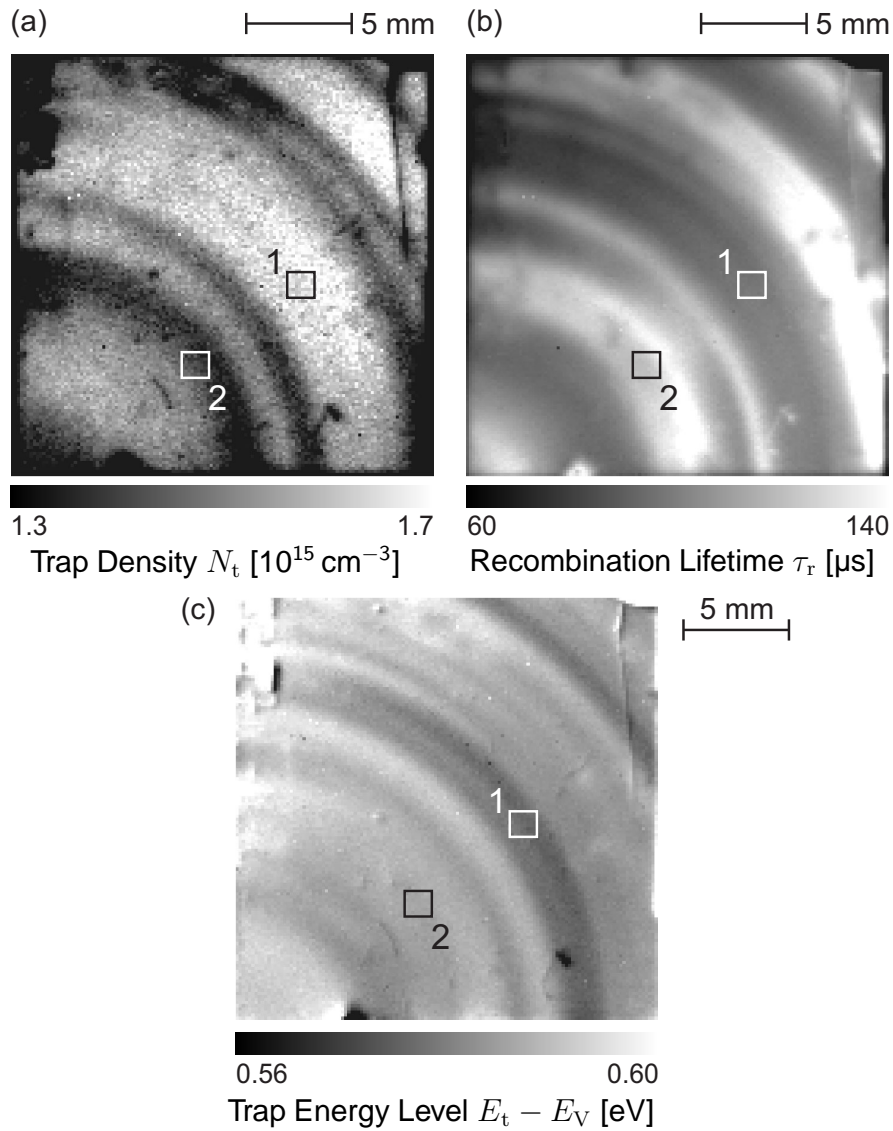


Figure 7.3: (a) Trap density  $N_t$  mapping of a Cz-Si wafer measured using ITM. (b) Mapping of the recombination lifetime  $\tau_r$  of the same sample measured using ILM. We find that regions of increased trap density correspond to regions of decreased recombination lifetime. (c) Mapping of the energy level of the trap centres  $E_t - E_V$  of the same sample. The image reveals a very homogeneous distribution around  $\langle E_t \rangle = E_V + (0.587 \pm 0.005) \text{ eV}$ .

$1.3$  to  $1.7 \times 10^{15} \text{ cm}^{-3}$ . Applying our three-step evaluation procedure as described in Sec. 4.1.3.1 to the three images of the Cz-Si wafer shown in Fig. 7.1 gives essentially the same results as the automated fitting routine. As can be seen from Fig. 7.2, the approximation  $\tau_r = \tau_a$  is well satisfied for the highest measured injection levels, thus, for the measurements shown both methods are applicable.

The area-averaged trap density shown in Fig. 7.3(a) is  $\langle N_t \rangle = (1.53 \pm 0.11) \times 10^{15} \text{ cm}^{-3}$ . It is interesting to note that, as can be seen from Fig. 7.3(a), there exists

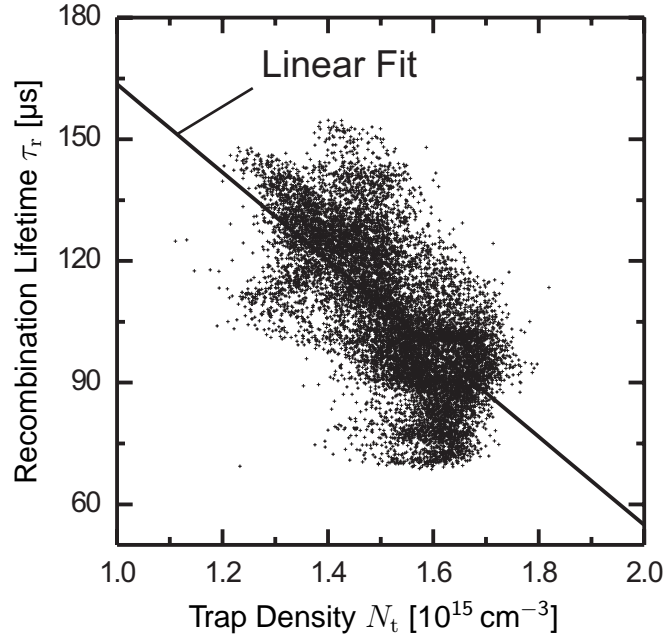


Figure 7.4: Plot of the recombination lifetime  $\tau_r$  vs the trap density  $N_t$  at each point of the mappings shown in Fig. 7.3. The linear fit results in a negative slope of  $-(1.09 \pm 0.01) \times 10^{-19} \text{ s cm}^{-3}$ .

an interrelation between areas of higher trap densities and striation patterns, which are caused by a variation of the oxygen content [164]. We find also that the regions of increased trap density in Fig. 7.3(a) correspond to regions of decreased recombination lifetime as shown in Fig. 7.3(b). In order to quantitatively underline this interrelation, we plot in Fig. 7.4 the recombination lifetime  $\tau_r$  versus the trap density  $N_t$  at each point of the mappings. A linear fit results in a negative slope of  $-(1.09 \pm 0.01) \times 10^{-19} \text{ s cm}^{-3}$ . Due to the fact that some oxygen-related defects (e.g., oxygen precipitates) are known as strong recombination centres, we assume that areas with increased  $\tau_r$  (region 2 in Fig. 7.3(b)) exhibit a lower concentration of oxygen-related defects and vice versa. Hence, regions with an increased  $N_t$  correlate with regions having an increased concentration of oxygen-related defects. However, it remains unclear whether the oxygen-related defects themselves or secondary defects generated in the stress field of the oxygen-related defects are the reason for the increased trap density  $N_t$ .

An image of the trap energy level  $E_t$  (calculated using Eq. (4.13)) corresponding to the  $N_t$  mapping shown in Fig. 7.3(c) reveals a very homogeneous distribution around  $\langle E_t \rangle = E_V + (0.587 \pm 0.005) \text{ eV}$ . The homogeneity in  $E_t$  over the measured area is better than 1%, whereas the homogeneity in  $N_t$  is  $\sim 7\%$ , suggesting that only one type of trap is measured. It has been shown recently that oxygen-related traps can be present in large concentrations in Cz-Si [18]. The fact that the energy level of the trapping centre is very deep is surprising at first glance. One reason might be that the deep traps are heavily charged, repelling majority carriers and

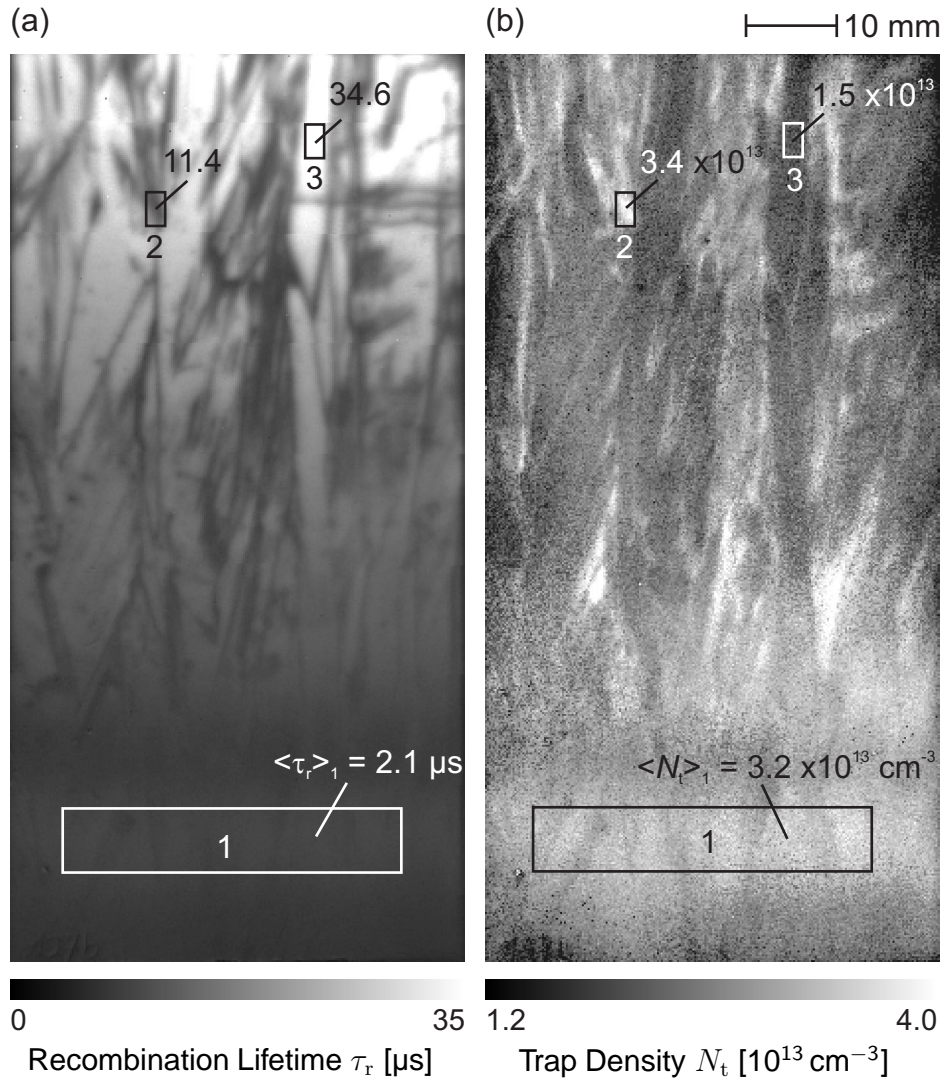


Figure 7.5: ILM and ITM measurements of a 250  $\mu\text{m}$  thick 1.5  $\Omega\text{cm}$   $p$ -type block-cast multicrystalline silicon wafer vertically cut from a brick. (a) Recombination lifetime image  $\tau_r(x, y)$  determined at an illumination intensity of 0.7 suns. (b) Trap density image  $N_t(x, y)$  of the same wafer. Both images are taken using the setup shown in Fig. 5.6 at a sample temperature of  $T_W = 349 \text{ K}$ .

therefore having only little recombination activity. However, the depth of the traps might also be a result of the oversimplification of the trap model [18].

### 7.3.2 Minority-carrier trapping versus depletion region modulation in multicrystalline silicon

We perform ITM measurements on 250  $\mu\text{m}$  thick 1.5  $\Omega\text{cm}$   $p$ -type mc-Si wafers, which are cut into pieces of  $10 \times 5 \text{ cm}^2$ . The wafers are vertically cut from an mc-Si brick. The wafer area covers the first 10 cm from the bottom of a cast brick. Both surfaces

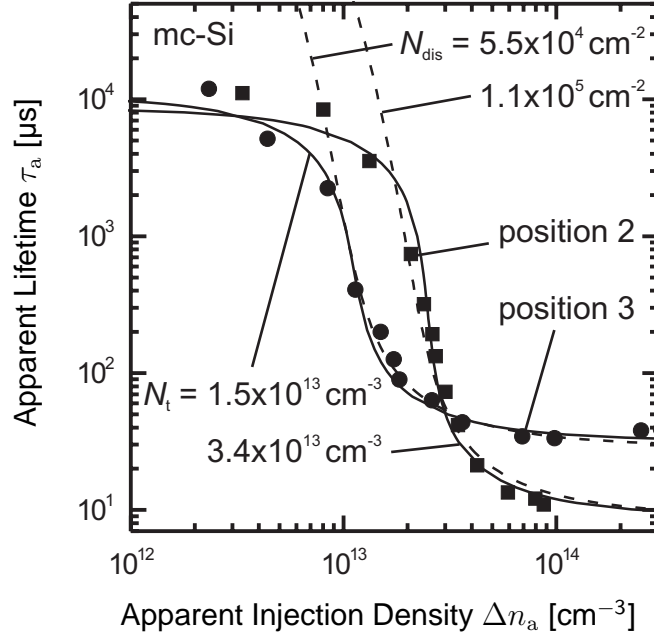


Figure 7.6: Exemplary injection-dependent lifetime curves  $\tau_a(\Delta n_a)$  at two different positions (marked in Fig. 7.5) of an mc-Si wafer obtained from lock-in infrared emission measurements. The minority-carrier trapping model of Hornbeck and Haynes (solid lines) and the depletion region model for dislocations (dashed lines) are used to fit the experimental data.

are passivated with 70 nm thick  $\text{SiN}_x$  films, deposited in a remote PECVD system at 400°C [52].

Figure 7.5(a) shows an image of the recombination lifetime  $\tau_r$  at an illumination intensity of 0.7 suns. Figure 7.5(b) shows the corresponding  $N_t$  image. At the bottom of the block within region 1, the area-averaged recombination lifetime  $\langle \tau_r \rangle_1 = (2.1 \pm 0.1) \mu\text{s}$  is much lower compared to the region including the first 3 cm from the top of the sample, where the area-averaged lifetime is  $\langle \tau_r \rangle = (22.7 \pm 7.7) \mu\text{s}$ . The trap density within region 1 is quite large with  $\langle N_t \rangle = (3.2 \pm 0.3) \times 10^{13} \text{ cm}^{-3}$ . In addition, it seems that the trap density  $N_t$  decreases with increasing recombination lifetime  $\tau_r$ . In region 2, we find  $\langle \tau_r \rangle_2 = (11.4 \pm 3.5) \mu\text{s}$  and  $\langle N_t \rangle_2 = (3.4 \pm 0.4) \times 10^{13} \text{ cm}^{-3}$ . In contrast, we find in the surrounding of region 2  $\langle \tau_r \rangle = (31.4 \pm 3.3) \mu\text{s}$  and  $\langle N_t \rangle = (1.8 \pm 0.2) \times 10^{13} \text{ cm}^{-3}$ , which suggests that a reduced  $N_t$  is associated with an increased  $\tau_r$ .

In addition, we plot in Fig. 7.6 the injection-dependent lifetime curves  $\tau_a(\Delta n_a)$  of the regions 2 and 3 as marked in Fig. 7.5. Using the single-level Hornbeck-Haynes model (black lines in Fig. 7.6), we obtain for region 3  $\langle N_t \rangle_3 = (1.5 \pm 0.2) \times 10^{13} \text{ cm}^{-3}$  and  $\langle \tau_r \rangle_3 = (34.6 \pm 3.4) \mu\text{s}$ .

As will be shown in the next Section, there is a clear correlation between areas of increased trap density and regions of increased dislocation density. Hence, we



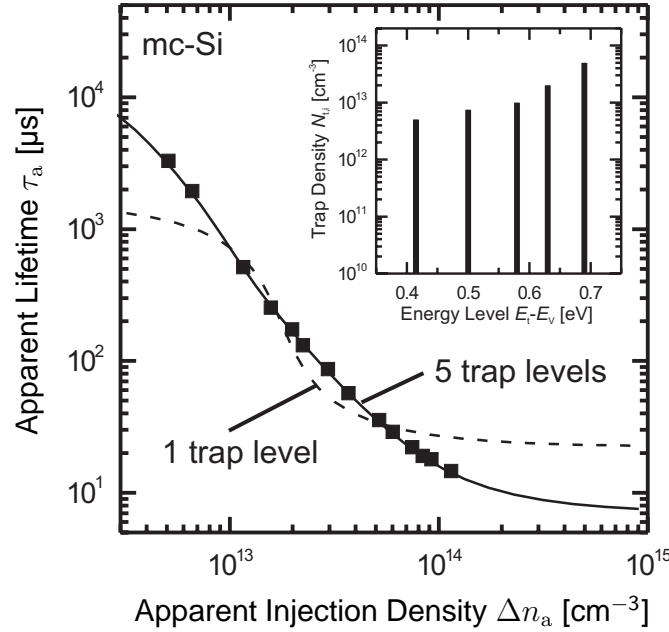


Figure 7.7: Injection-dependent lifetime curve  $\tau_a(\Delta n_a)$  of an mc-Si wafer obtained from lock-in infrared emission measurements. Applying the minority-carrier trapping model including multiple trap levels, a very good agreement between experiment and theory is achieved. Assumed densities and energy levels of the minority-carrier trapping centres are shown in the inset.

also apply the depletion region modulation model for charged line defects to the experimental data (dashed lines in Fig. 7.6). The dislocation density obtained by fitting the model presented in Sec. 4.2.2.1 to the measured data in region 2 is  $\langle N_{\text{dis}} \rangle_2 = 1.1 \times 10^5 \text{ cm}^{-2}$ . In region 3, we obtain a lower dislocation density of  $\langle N_{\text{dis}} \rangle_3 = 5.5 \times 10^4 \text{ cm}^{-2}$ . The comparison of the two applied models yields a better agreement between experiment and theory for the single-level trap model. Especially at low injection levels the depletion region modulation model shows a poor agreement with the experimental data. This might be due to the simplicity of our depletion region modulation model, in particular due to the approximation that the band-bending is simply reduced by the quasi-Fermi level splitting according to Eq. (4.23).

### Multiple trap levels

Figure 7.7 shows a measured injection-dependent lifetime curve of an mc-Si wafer neighbouring to the one shown in Fig. 7.5. The experimental data is measured at the bottom of the block after the application of a phosphorus-gettering treatment at  $850^\circ\text{C}$  using  $\text{POCl}_3$  (after removing the diffused  $n^+$ -regions and passivating both surfaces with  $\text{SiN}_x$ ). The increase of  $\tau_a$  with decreasing  $\Delta n_a$  extends over more than one order of magnitude in  $\Delta n_a$ , which cannot be explained by the single-level

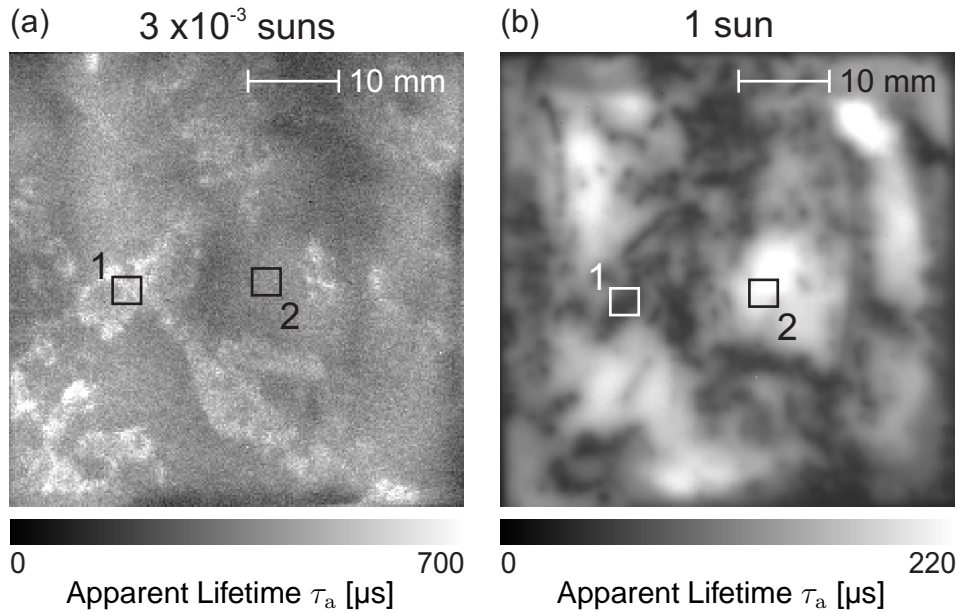


Figure 7.8: Apparent lifetime images  $\tau_a(x, y)$  of an mc-Si wafer obtained from lock-in infrared emission measurements at  $70^\circ\text{C}$ . The mappings are measured at two different illumination intensities: (a)  $3 \times 10^{-3}$  suns and (b) 1 sun.

Hornbeck-Haynes trapping model nor by the depletion region modulation model. A possible explanation of this behaviour is that more than one trap level is present. In Fig. 7.7, an exemplary  $\tau_a(\Delta n_a)$  curve (squares) is shown together with a multiple-level trap fit (solid lines) assuming 5 different trap levels. The trap densities and energy levels of the assumed traps are shown in the inset of the figure. At first glance, the energetic depth of the traps is surprising. However, the existence of such deep traps might be explained - as in the case of the Cz-Si wafer in Sec. 7.3.1 - by a strong positive charge of the traps and, thus, a very small capture cross-section of majority carriers (holes) in combination with a large capture cross-section of the minority-carriers (electrons).

### 7.3.3 ITM analysis of multicrystalline silicon wafers

We apply the ITM technique to typical *p*-type mc-Si wafers ( $1.5 \Omega\text{cm}$ ,  $230 \mu\text{m}$  thick), which are cut into pieces of  $5 \times 5 \text{cm}^2$ . Both surfaces are passivated with  $\text{SiN}_x$  films [52]. In order to investigate the influence of a phosphorus diffusion process on the recombination lifetime, we measure the wafers before and after a phosphorus gettering treatment, which is performed at a temperature of  $850^\circ\text{C}$  obtaining an emitter with an  $n^+$  sheet resistance of  $40 \Omega/\square$ . After the diffusion process the phosphorus layer is etched off to ensure equivalent conditions for the lifetime measurements.

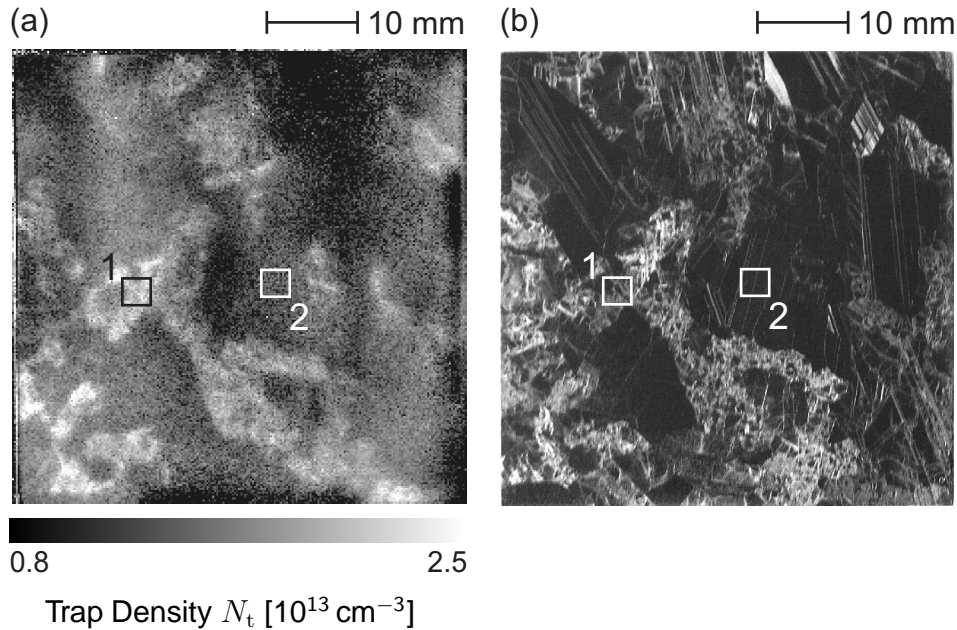


Figure 7.9: (a) Trap density image  $N_t(x, y)$  of the mc-Si wafer shown in Fig. 7.8, as obtained by ITM. (b) Scanned picture of the same wafer after removal of the silicon nitride passivation layers and application of a Dash [165] etch. Brighter regions correspond to areas of increased dislocation densities.

### 7.3.3.1 As-grown mc-Si

Figure 7.8 shows two lifetime images of the same mc-Si sample at two different illumination intensities ( $3 \times 10^{-3}$  suns and 1 sun). Due to minority-carrier trapping, under low-injection conditions the apparent lifetime  $\tau_a$  in Fig. 7.8(a) is with an area-averaged lifetime of  $\langle \tau_a \rangle = 350 \mu\text{s}$  much higher than the area-averaged lifetime of  $\langle \tau_a \rangle = 110 \mu\text{s}$  at an illumination intensity of 1 sun (Fig. 7.8(b)), where trapping effects are negligible and thus the actual recombination lifetime is measured. As can be seen from Fig. 7.8, the two lifetime images are very different. Apparently, other information than lifetime is provided by the image measured at an illumination intensity of  $3 \times 10^{-3}$  suns.

Fitting Eqs. (4.11) and (4.12) to the experimental data results in the  $N_t$  image shown in Fig. 7.9(a). The  $N_t$  image of Fig. 7.9(a) agrees qualitatively with Fig. 7.8(a), which is expected since areas of increased  $N_t$  show an earlier inset of increasing  $\tau_a$  with decreasing injection density  $\Delta n_a$  and the  $\tau_a$  image in Fig. 7.8(a) is taken at the same illumination intensity at every point of the image. Furthermore, the obtained  $N_t$  image does not correlate with the grain structure of the wafer (not shown). Thus, we applied a Dash etch [165] for 3 h to reveal a possible correlation with structural defects, especially dislocations. Indeed, the spatial distribution of dislocations shown in Fig. 7.9(b) is in agreement with the  $N_t$  distribution shown in Fig. 7.9(a). Brighter regions in Fig. 7.9(b) correspond to areas of increased dislocation density. These regions correlate well with the areas of increased trap

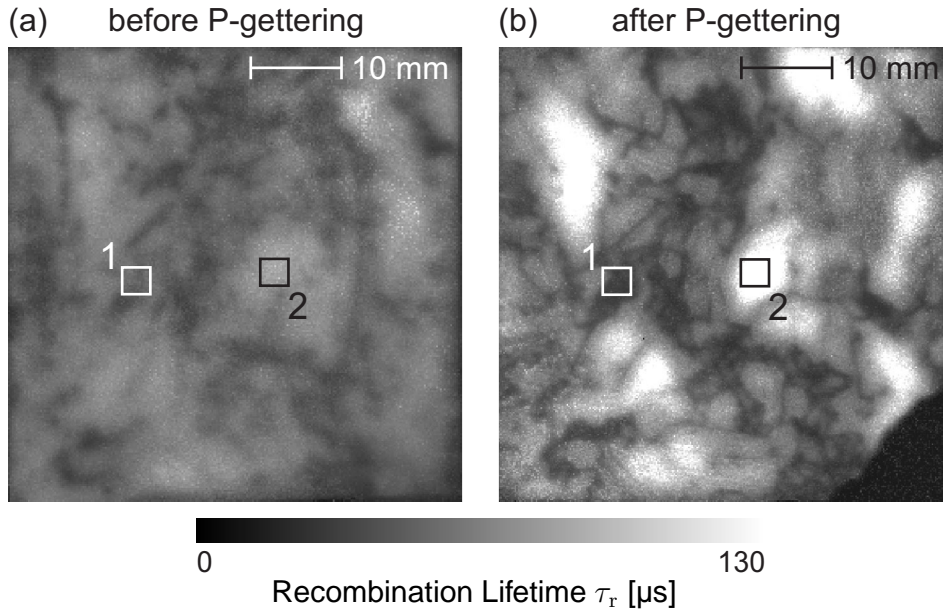


Figure 7.10: Recombination lifetime images  $\tau_r(x, y)$  determined at an injection density of  $\Delta n = 1 \times 10^{14} \text{ cm}^{-3}$ , as calculated by an automated fitting routine based on a single-level trap model for the mc-Si wafer shown in Fig. 7.8(a) before and (b) after applying a phosphorus gettering step.

density  $N_t$ , as shown in Fig. 7.9(a).

### 7.3.3.2 Impact of phosphorus gettering

Subsequent to the application of a phosphorus-gettering treatment at  $850^\circ\text{C}$  using  $\text{POCl}_3$  we measure the mc-Si wafers again (after removing the diffused  $n^+$ -regions and passivating both surfaces with  $\text{SiN}_x$ ). A comparison of the recombination lifetime determined at an injection density of  $\Delta n = 1 \times 10^{14} \text{ cm}^{-3}$  before and after gettering is shown in Fig. 7.10. The area-averaged lifetime increases from  $\langle \tau_r \rangle = (51.9 \pm 14.9) \mu\text{s}$  before gettering to  $\langle \tau_r \rangle = (65.3 \pm 33.2) \mu\text{s}$  after gettering. Moreover, one can clearly see that  $\tau_r$  increases in particular in those regions, which already showed the highest lifetimes before gettering. In regions of relatively low lifetimes before gettering, the recombination lifetime shows a reduced improvement or even decreases.

The observation of a reduced improvement of dislocated areas after a gettering treatment has already been reported by other authors. Sopori *et al.* [166] have demonstrated by photoresponse measurements of gettered and non-gettered mc-Si solar cells that the diffusion length remained unchanged in areas with higher dislocation density or even degraded after gettering. Macdonald and Cuevas [162] showed by QSSPC measurements that the dislocation-related trap density in mc-Si wafers remains unchanged even after a repeated phosphorus gettering.

Figure 7.11 shows injection-dependent lifetime curves measured in the two different

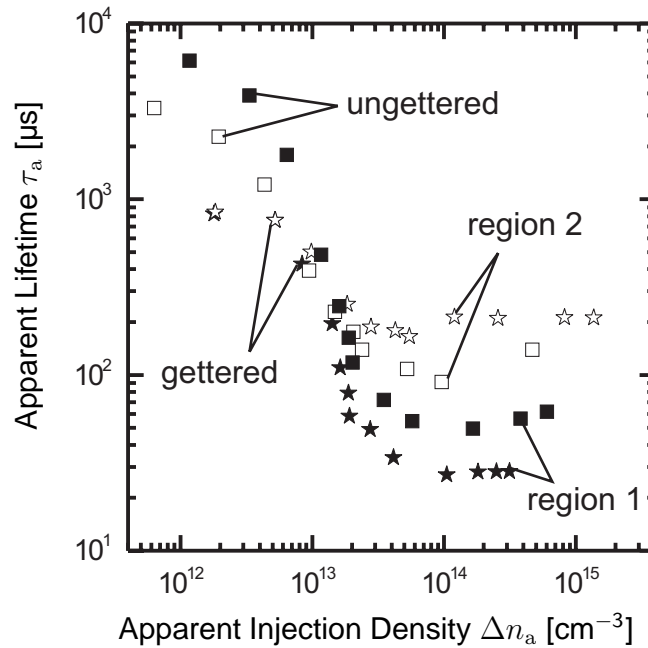


Figure 7.11: Injection-dependent lifetime curves  $\tau_a(\Delta n_a)$  measured in the two different areas (marked in Figs. 7.8-7.10) of an mc-Si wafer obtained from lock-in infrared emission measurements. The wafer is measured before (squares) and after (stars) a phosphorus gettering treatment at 850°C.

regions on the mc-Si wafer, as indicated in Figs. 7.8-7.10. The two regions are regions of highest and lowest trap densities. In region 1, we measure  $\langle N_t \rangle_1 = 2.06 \times 10^{13} \text{ cm}^{-3}$  and in region 2,  $\langle N_t \rangle_2 = 0.90 \times 10^{13} \text{ cm}^{-3}$ . The injection-dependent lifetime curves in Fig. 7.11 show that for the highest measured injection densities above  $1 \times 10^{14} \text{ cm}^{-3}$ , trapping effects are negligible and, thus, the actual recombination lifetime is measured. The curve measured in region 2 clearly reveals an increase of the recombination lifetime after gettering, whereas in region 1,  $\tau_r$  decreases after the phosphorus gettering treatment.

It is known that carrier recombination at dislocations themselves is relatively weak but strongly increases after decoration of the dislocations by transition metal impurities [167–169]. Regions with high concentrations of dislocations might exhibit higher carrier recombination, which is one important limitation of the efficiency of mc-Si solar cells [65, 166, 170, 171]. Our interpretation of the observed behaviour is that regions exhibiting higher dislocation densities contain significant concentrations of metallic impurities, which are restrained in the stress field of the dislocations [172] and partly attached to them. These metals are set free during the high-temperature gettering treatment and contaminate the surrounding region. This effect may lead to a severe degradation in the solar cell performance in regions of increased dislocation density in contrast to regions with lower dislocation densities, where the phosphorus gettering treatment mainly removes recombination-active metallic impurities from

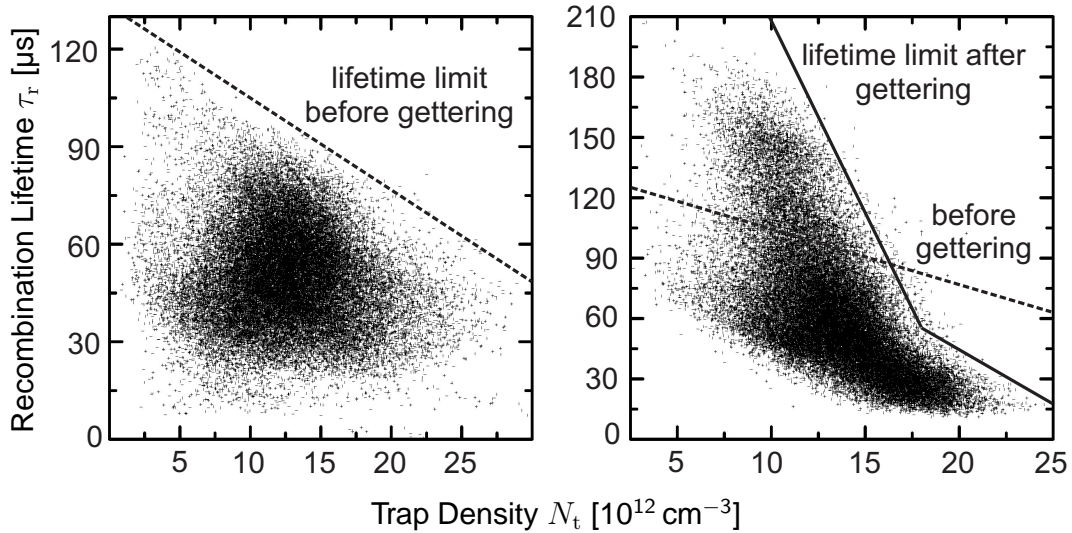


Figure 7.12: Recombination lifetime  $\tau_r$  as a function of the trap density  $N_t$  at each point of the mappings shown in Figs. 7.9 and 7.10(a) before and (b) after a phosphorus gettingting treatment. The straight lines are guides to the eyes.

the silicon bulk.

In order to quantify the correlation between recombination lifetime and dislocation density, we plot the recombination lifetime  $\tau_r$  versus the trap density  $N_t$  at each point of the mappings shown in Figs. 7.9 and 7.10. This is done before and after the phosphorus gettingting as shown in Figs. 7.12(a) and 7.12(b), respectively. Before gettingting (Fig. 7.12(a)) one cannot see a distinct correlation between  $\tau_r$  and  $N_t$ , although we observe a clear limitation of the recombination lifetime by the trap density. To demonstrate this limitation we plot a straight line as a guide to the eyes in Fig. 7.12(a), which corresponds to the maximum values for  $\tau_r(N_t)$ . After the phosphorus gettingting treatment we find that with increasing trap density  $N_t$  the limit of the recombination lifetime  $\tau_r$  decreases, as can be seen from Fig. 7.12(b). The comparison between the lifetime limits before and after gettingting reveals that for  $N_t < 1.6 \times 10^{13} \text{ cm}^{-3}$ ,  $\tau_r$  has increased after the gettingting and for  $N_t > 1.6 \times 10^{13} \text{ cm}^{-3}$ ,  $\tau_r$  has decreased as a consequence of the gettingting process. In conclusion, areas of high trap density are poorly getterable, which indicates that the recombination lifetime and, thus, the performance of mc-Si solar cells is strongly affected by the distribution of structural defects.

### 7.3.4 Trap mapping without surface passivation

As already mentioned in Sec. 7.3.3.1, the apparent lifetime image shown in Fig. 7.8(a) and the corresponding  $N_t$  image shown in Fig. 7.9(a) agree qualitatively quite well, demonstrating that a single ILM measurement already reveals if trapping at dislocations is present and which regions of the wafer are affected. In order to prove a possible industrial applicability of the trap mapping technique using an infrared

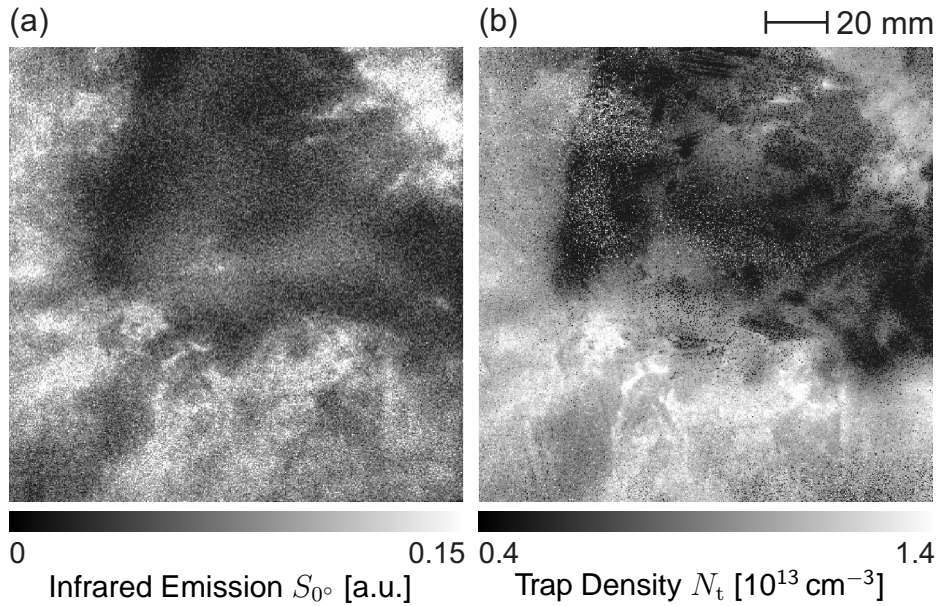


Figure 7.13: (a) Infrared emission signal  $S_{0^\circ}(x, y)$  of a block-cast mc-Si wafer without any surface treatment measured at an illumination intensity of 0.01 suns. Brighter regions correspond to areas of increased trap densities. The measurement period was 20 min. (b) Trap density image  $N_t(x, y)$  of the same wafer after etching off the saw damage and passivating both surfaces with  $\text{SiN}_x$ .

camera, we perform only one single IR emission measurement on an as-delivered mc-Si wafer without applying any surface treatment, i.e., the saw damage is still present on both wafer surfaces. Figure 7.13(a) shows the measured infrared emission picture  $S_{0^\circ}(x, y)$  of an as-cut block-cast mc-Si wafer from Photowatt ( $125 \times 125 \text{ mm}^2$ ), recorded at 1/100 suns. The measurement period was 20 min. A comparison with the  $N_t$  image shown in Fig. 7.13(b) recorded on the same wafer after etching off the saw damage and passivating both surfaces with  $\text{SiN}_x$  reveals an excellent qualitative agreement of the image contrast between the two images. As the  $N_t$  image correlates with the distribution of dislocations, a single IR measurement already provides the qualitative distribution of dislocations in an mc-Si wafer.

As mentioned in the previous Section, we expect that regions of increased dislocation density correlate with an increased density of metallic impurities, partly in the form of precipitates. A high-temperature step, such as the phosphorus gettering process, may lead to a severe lifetime degradation within highly dislocated areas. The detection of those regions might be used to estimate the contribution of poorly getterable areas of the wafer, which decrease the solar cell efficiency. Hence, we conclude that the application of a spatially resolved measurement using an IR-camera helps to identify poorly getterable areas in as-delivered mc-Si wafers without the need of any surface treatment.

### Possible industrial applicability

As the ITM technique helps to detect poorly getterable regions in multicrystalline silicon wafers, an implementation of this imaging technique to an industrial production line could prove to be very helpful. Wafers showing very strong trapping could be sorted out from the solar cell production line, which could lead to a reduction of the production cost per cell. Unfortunately, the application of the ITM technique to a multicrystalline silicon wafer at a spatial resolution of  $Z = 200 \mu\text{m}$  requires measurement periods in the range of hours. However, as demonstrated above, a single measurement of the infrared emission alone reveals already if trapping effects are present. The measurement period for the qualitative infrared emission mapping of an as-delivered multicrystalline silicon wafer as shown in Fig. 7.13(a) takes measurement periods in the range of  $\sim 20$  min.

Fortunately, there are still possibilities to further shorten the measurement period  $t$ . In general, the signal  $S$  of a photon counter such as an infrared detector is proportional to the number of photons  $N$  counted during the measurement period. Moreover, the noise signal  $S_{\text{noise}}$  is proportional to the square root of  $N$ . Hence, the signal-to-noise ratio  $SNR$  is proportional to the square root of  $N$ , i.e.,  $SNR \propto \sqrt{N}$ . The number of photons  $N$  is proportional to the measurement period  $t$  and the sample area per pixel  $A = Z^2$ , as discussed in Sec. 6.3.2, where  $Z$  is the spatial resolution. If the spatial resolution is changed from  $Z_0$  to  $Z$  or/and the measurement period from  $t_0$  to  $t$ , the change of the number of photons from  $N_0$  to  $N$  is given by the expression

$$N = N_0 \frac{t}{t_0} \frac{Z^2}{Z_0^2}. \quad (7.1)$$

In consequence, the signal-to-noise ratio changes from  $SNR_0$  to  $SNR$  given by the equation

$$\frac{SNR}{SNR_0} = \sqrt{\frac{tZ^2}{t_0Z_0^2}}. \quad (7.2)$$

Reducing the spatial resolution  $Z$  by averaging neighbouring pixels (pixel binning) as discussed in Sec. 6.3.2 would result in an increase of the signal-to-noise ratio. Provided that  $SNR/SNR_0$  shall remain constant and  $Z$  is increased, the measurement period can be decreased according to Eq. (7.1). For example, the infrared emission measurement shown in Fig. 7.13(a) has been recorded at a spatial resolution of  $Z_0 = 200 \mu\text{m}$  and a measurement period of  $t_0 = 20$  min. Increasing  $Z_0$  by a factor of 25 to  $Z = 5 \text{ mm}$  would allow for a drastically shortened measurement period of  $t_0 = 2$  s. In combination with infrared cameras having 4-times higher frame rate at constant  $NETD$  which are already commercially available, measurement periods of 1 s are achievable demonstrating the in-line applicability of our qualitative trap imaging technique.



## 7.4 Summary and conclusion

We introduced a lock-in infrared camera trap mapping technique for the investigation of spatially distributed minority-carrier trapping centres in silicon wafers. The method is termed infrared trap mapping (ITM), as it is directly derived from the infrared lifetime mapping (ILM) technique discussed in the previous Chapter. Using an automated fitting routine based on a single-level trap model, we were able to generate mappings of the trap density  $N_t$  and the energy level  $E_t$  at a spatial resolution of 200  $\mu\text{m}$ .

We applied two different theoretical models which both are capable of explaining the abnormally high effective carrier lifetimes measured in multicrystalline silicon wafers at low injection levels to our experimental data. One model assumes the presence of minority-carrier trapping centres, which is applied by the ITM technique. The other one is based on the space-charge region modulation around charged bulk defects. Both theoretical models give a reasonable qualitative agreement with measured injection-dependent lifetime curves. However, a satisfying quantitative agreement between experiment and theory is only obtained with the trapping model.

The application of the technique to an *n*-type Czochralski silicon wafer showed strong inhomogeneities in the trap densities, whereas the energy levels of the trapping centres were found to be almost independent of position. The homogeneity in  $\langle E_t \rangle = E_V + (0.587 \pm 0.005) \text{ eV}$  over the measured area was better than 1%, whereas the homogeneity in  $\langle N_t \rangle = (1.53 \pm 0.11) \times 10^{15} \text{ cm}^{-3}$  was only  $\sim 7\%$ , suggesting that only one sort of trap was measured. We observed that regions of increased trap densities correspond to regions of decreased recombination lifetimes in Czochralski silicon showing typical striation patterns. Our measurements indicated that the ITM technique detects either oxygen-related precipitates or secondary defects generated in the stress field of the oxygen-related precipitates, whereas the recombination lifetime mappings reveal areas of increased recombination due to the oxygen-related precipitates themselves.

On typical block-cast multicrystalline silicon wafers we found a strong correlation between regions of increased trap density and areas of increased dislocation density. Furthermore, areas of increased dislocation density showed a strong deterioration in the recombination lifetime after phosphorus gettering. These regions have a pronounced impact on the recombination lifetime of the multicrystalline silicon wafer and, thus, have a significant influence on device performance.

Finally, we demonstrated that one single spatially resolved measurement of the infrared emission signal of as-delivered multicrystalline silicon without any surface treatment already reveals poorly getterable regions, which decrease the efficiency in multicrystalline silicon solar cells. Hence, we conclude that a detailed information of the trap density in the as-grown silicon material is - besides the recombination lifetime - a crucial material parameter for the comprehensive assessment of the efficiency potential of multicrystalline silicon solar cells. Theoretically, it is expected that reducing the spatial resolution to 5 mm by using larger and fewer detectors in

the focal plane array facilitates an in-line applicability of a qualitative measurement in just 1 s.

# Chapter 8

## Infrared Capacitance Mapping (ICM)

The doping concentration of silicon solar cells is an important parameter that, among others, determines the electrical characteristics of the devices. The doping concentration is commonly deduced from resistivity measurements with the four-point probe technique [97] (see Sec. 3.2). A high-resolution mapping with the four-point probe technique requires measurement periods in the range of hours. Thickness variations of edge-defined film-fed grown (EFG [142]) silicon wafers, as used in the industrial solar cell production, make it difficult to obtain reliable results with the four-point probe method. Capacitance-Voltage ( $C$ - $V$ )-profiling [173] allows the determination of the doping concentration while being insensitive to thickness variations. However, with the latter technique it is very tedious to obtain high spatial resolution.

In this Chapter, we introduce a method based on the ability of free carriers to emit and absorb infrared radiation, which allows a spatially resolved determination of the capacitance of  $pn$ -junctions by means of an infrared camera. We apply the technique to measure the base doping concentration of phosphorus-diffused  $p$ -type silicon wafers [174, 175].

### 8.1 Capacitance of an abrupt $pn$ -junction

For a theoretical description of the experimental data we assume a one-sided abrupt  $pn$ -junction. The depletion-layer capacitance per unit area is defined as  $C \equiv dQ/dU$ , where  $dQ$  is the incremental increase in charge per unit area upon an incremental change of the applied voltage  $dU$ . For a  $p$ -type silicon substrate ( $N_A$ : acceptor concentration in the  $p$ -type substrate,  $N_D$ : donor concentration in the  $n$ -type emitter;  $N_D \gg N_A$ ) the capacitance per unit area is given by [74]

$$C \equiv \frac{dQ}{dU} = \frac{\varepsilon_0 \varepsilon_s}{W} = \sqrt{\frac{q \varepsilon_0 \varepsilon_s N_A}{2}} \left( U_{\text{bi}} + U - \frac{2kT}{q} \right)^{-1/2}, \quad (8.1)$$

where  $\varepsilon_s$  is the permittivity of silicon and  $W$  is the width of the depletion region.  $U$  is the applied reverse-bias voltage (positive voltage on  $n$  region with respect to  $p$  region). The built-in potential

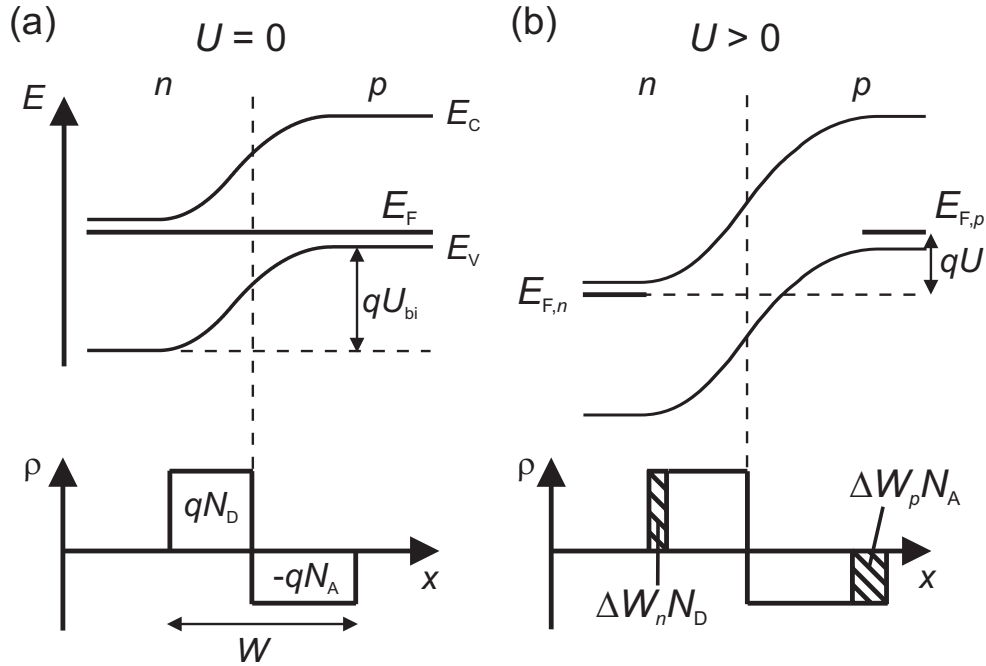


Figure 8.1: Band diagram of a  $pn$ -junction (a) without applied bias voltage and (b) with applied reverse-bias voltage  $U > 0$ . In addition, the charge density  $\rho$  is plotted for both cases (a) and (b), assuming depletion region approximation. Applying a reverse-bias voltage  $U > 0$  to the  $pn$ -junction results in an increased depletion layer width of  $\Delta W_p$  on the  $p$ -side as well as  $\Delta W_n$  on the  $n$ -side. The corresponding change of the amount of free holes within the depletion layer on the  $p$ -side is the acceptor doping concentration  $N_A$  multiplied by the change of the depletion layer width  $\Delta W_p$ , i.e.  $N_A \Delta W_p$ . Analogously, we find for the  $n$ -side  $N_D \Delta W_n$ . The sum of the change of free electrons and holes is detected by the infrared camera.

$$U_{\text{bi}} = \frac{kT}{q} \ln \left( \frac{N_A N_D}{n_i^2} \right) \quad (8.2)$$

of the  $pn$ -junction depends on the donor impurity concentration  $N_D$  and the intrinsic carrier density  $n_i$ . We assume  $N_D = 1 \times 10^{19} \text{ cm}^{-3}$ . The exact value has little impact on our results.

Figures 8.1(a) and (b) show two band diagrams of the same  $pn$ -junction in combination with the charge density  $\rho$  along the growth direction of the junction. Without applied bias voltage (Fig. 8.1(a)) the width of the depletion region is  $W$ . Applying a reverse-bias voltage  $U > 0$  to the  $pn$ -junction (Fig. 8.1(b)) results in an increase of the depletion layer width of  $\Delta W_p$  on the  $p$ -side as well as  $\Delta W_n$  on the  $n$ -side. The corresponding decrease of the amount of free carriers per area is  $N_D \Delta W_n + N_A \Delta W_p$ , which can be detected by the infrared camera.

Charge neutrality requires that the sum of all charges, the change of the amount of free carriers per area times the elementary charge  $\Delta N q$  and the change of the charge

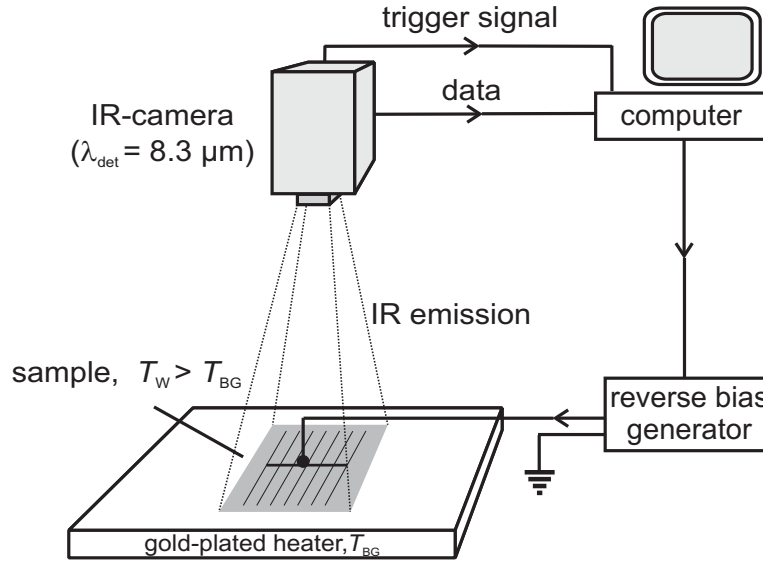


Figure 8.2: Experimental setup: The contacted silicon sample is heated to a temperature  $T_W$  by a gold-plated heater. A square-wave-shaped reverse voltage  $U > 0$  is applied to modulate the width of the space charge region  $W$ . The implied change of the charge carrier density, and thus infrared light emission per area, is detected by the infrared camera.

density due to the ionized impurity atoms  $\Delta Q$ , equals zero, i.e.  $\Delta N q + \Delta Q = 0$ . Hence, the change of the amount of free carriers per area  $\Delta N = -\Delta Q/q$  on each side of the junction introduced by application of the reverse-bias voltage  $U > 0$  is calculated using Eq. (8.1). Integrating Eq. (8.1) from 0 to  $U$  results in

$$\Delta N = \sqrt{\frac{2\varepsilon_0\varepsilon_s N_A}{q}} \left( \sqrt{\left(U_{\text{bi}} - \frac{2kT}{q}\right)} - \sqrt{\left(U_{\text{bi}} + U - \frac{2kT}{q}\right)} \right). \quad (8.3)$$

## 8.2 Measurement principle

Figure 8.2 shows a schematic of our in-house-built infrared capacitance mapping (ICM) setup. The setup is essentially the same as introduced in Fig. 5.6, with the only difference that instead of modulating the illumination intensity, we modulate the reverse-bias voltage  $U$  applied to the  $pn$ -junction. The sample temperature  $T_W$  is measured by a thermocouple and is 333 K for all measurements presented in this Chapter. The optical setup has a spatial pixel resolution of  $170\ \mu\text{m}$ . The lock-in frequency is  $f_{\text{li}} = 2.43\ \text{Hz}$ .

We use the in-phase signal  $S_{0^\circ}$  for the evaluation of the ICM measurement, since the infrared emission of the charges in the junction is in phase with the bias voltage. The

small current flowing in the reverse direction leads to a heating of the  $pn$ -junction. This thermal signal of the homogeneously heated sample, which is also small compared to the in-phase signal, is  $90^\circ$  phase-shifted to the bias voltage [176] and thus not included in  $S_{0^\circ}$ . Shunts in a  $pn$ -junction would lead to an inhomogeneous heating of the sample, which would contribute to both signals  $S_{0^\circ}$  and  $S_{90^\circ}$ . All experiments shown in this thesis are performed on  $pn$ -junctions without measurable shunts.

The infrared in-phase signal  $S_{0^\circ}$  is proportional to the excess carrier density per area  $\Delta N$  with the constant of proportionality  $M$ . Using Eq. (8.3) yields

$$S_{0^\circ} = M \cdot \Delta N = M \cdot \sqrt{\frac{2\varepsilon_0\varepsilon_s N_A}{q}} \left( \sqrt{(U_{\text{bi}} - \frac{2kT}{q})} - \sqrt{(U_{\text{bi}} + U - \frac{2kT}{q})} \right), \quad (8.4)$$

which is the infrared in-phase signal caused by a modulation of the reverse-bias voltage from 0 to  $U$ . Please note that the in-phase signal  $S_{0^\circ}$  is negative, as  $\Delta N$  represents the decrease of free carriers with applied reverse-bias voltage. For the sake of convenience we automatically multiply  $S_{0^\circ}$  by -1 to illustrate positive values.

## 8.3 Application of ICM

### 8.3.1 Calibration with FZ silicon solar cells

In order to calibrate the ICM setup, we apply a similar approach as we used for the ILM technique presented in Sec. 5.2.1. Due to the highly-doped  $n$ -type emitter of the measured silicon solar cells the optical properties of the surface change. Hence, we cannot calibrate the ICM technique according to the procedure discussed in Sec. 5.2.2 using a set of  $p$ -type silicon wafers. In case of the ICM technique, we measure the infrared in-phase signal  $S_{0^\circ}$  of various phosphorus-diffused float-zone (FZ) silicon  $pn$ -junctions with known base doping concentration  $N_A$ .

#### 8.3.1.1 Sample preparation

The FZ silicon wafers are polished on both sides, (100)-oriented, B-doped and have a thickness of 300  $\mu\text{m}$ . We measure the substrate acceptor concentration via a four-point-probe measurement. The acceptor doping concentrations  $N_A$  are  $1 \times 10^{17} \text{ cm}^{-3}$  (2 samples),  $3.2 \times 10^{16} \text{ cm}^{-3}$  and  $4 \times 10^{15} \text{ cm}^{-3}$  (each 3 samples), each with an error of  $\pm 5\%$ . Using a phosphorus diffusion process, we obtain an emitter with an  $n^+$  sheet resistance of 120  $\Omega/\square$ . After the diffusion process,  $2 \times 2 \text{ cm}^2$  mesas are etched using CP4 solution. We choose TiPdAg for front side metallisation and Al for rear metallisation, each evaporated through a shadow mask forming the front and rear side contact grid of the sample.

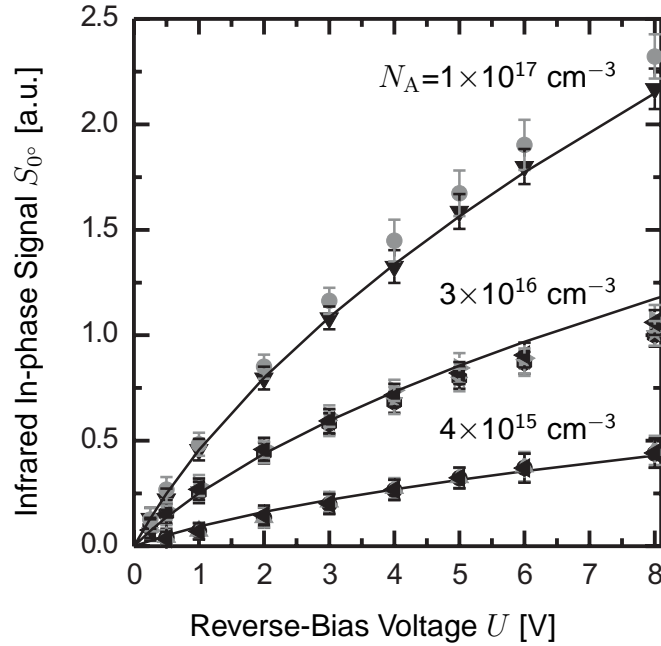


Figure 8.3: Infrared emission signal  $S_{0^\circ}$  as a function of the reverse bias voltage  $U$  of laterally homogeneous  $pn$ -junctions with three different acceptor concentrations  $N_A$ . An abrupt junction is assumed to fit the experimental data by Eq. (8.4) (solid lines), which yields a proportionality constant of  $M = 0.91 \times 10^{-12} \text{ cm}^{-2} \pm 5\%$ .

### 8.3.1.2 Determination of the calibration constant

Figure 8.3 shows the in-phase signal  $S_{0^\circ}$  as a function of the reverse-bias voltage  $U$ . We average the in-phase signal  $S_{0^\circ}$  over an area of  $1 \times 1.5 \text{ cm}^2$  and plot the standard deviation of all detector pixels in this area as error bars. The lock-in signal increases with increasing applied reverse bias. Moreover,  $S_{0^\circ}$  increases with increasing base doping concentration  $N_A$ , as expected from Eq. (8.4).

We determine a proportionality constant of  $M = 0.91 \times 10^{-12} \text{ cm}^{-2} \pm 5\%$  by fitting all experimental data with Eq. (8.4). The agreement between experiment and theory (solid lines in Fig. 8.3) is satisfactory.

According to Eq. (8.4), theory predicts an increase of the signal  $S_{0^\circ}$  for fixed applied reverse voltage modulation proportional to  $N_A^{1/2}$ . Figure 8.4 demonstrates this proportionality as a plot of the measured lock-signal  $S_{0^\circ}$  as a function of the square root of the substrate doping concentration  $N_A^{1/2}$ . A linear fit in a double-logarithmic plot of the lock-in signal versus the doping concentration (not shown) reveals an average slope of  $0.50 \pm 0.01$ , which underlines the applicability of the presented theoretical model.

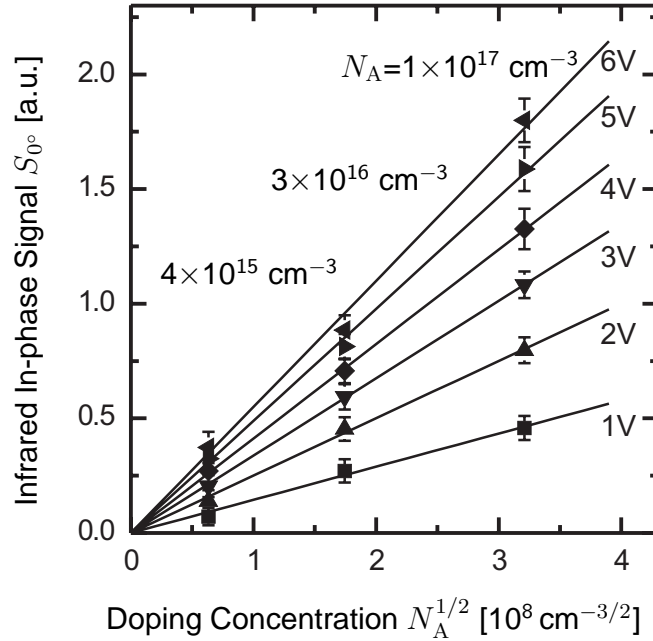


Figure 8.4: Experimental data shown in Fig. 8.3 plotted as a function of the square root of the substrate doping concentration. The linear fits demonstrate the proportionality of the lock-in signal  $S_{0^\circ}$  to  $N_A^{1/2}$ .

### 8.3.2 Doping concentration distribution in EFG silicon

In order to demonstrate an application of the ICM technique, we investigate a multicrystalline *p*-type EFG silicon wafer. The *pn*-junction is processed in the same way as the FZ silicon wafers we used for the calibration of the ICM technique. Subsequent to the emitter diffusion we etch a  $5 \times 5 \text{ cm}^2$  large mesa.

Figure 8.5 shows a measurement of the in-phase signal  $S_{0^\circ}$  as a function of the reverse-bias voltage  $U$ . Qualitatively, we find a similar result as obtained for the calibration wafers shown in Fig. 8.3. The in-phase signal  $S_{0^\circ}$  increases with increasing applied reverse-bias voltage. However, in case of the EFG silicon sample,  $S_{0^\circ}$  is lower at each applied reverse-bias voltage  $U$  compared to the in-phase signal  $S_{0^\circ}$  of all calibration wafers at the same voltage. For example, at  $U = 5 \text{ V}$  we measure for the EFG sample  $S_{0^\circ} = 0.24 \pm 0.04$  and for the three FZ calibration wafers with the lowest base doping concentration  $N_A = 4 \times 10^{15} \text{ cm}^{-3}$  an averaged infrared in-phase signal  $S_{0^\circ} = 0.32 \pm 0.05$ .

Figure 8.6(a) shows a recombination lifetime mapping of the EFG silicon wafer shown in Fig. 8.5, generated with the microwave-detected photoconductance decay technique [84]. The image clearly reveals grains with different recombination activity. Figure 8.6(b) shows an image of the acceptor concentration  $N_A(x, y)$  of the same wafer as measured by the ICM technique. The measurement period is 1 h. The reverse bias is modulated between 0 and 5 V. Averaging the in-phase signal  $S_{0^\circ}$  in between the metal grid lines and solving Eq. (8.4) for  $N_A$  leads to an acceptor con-



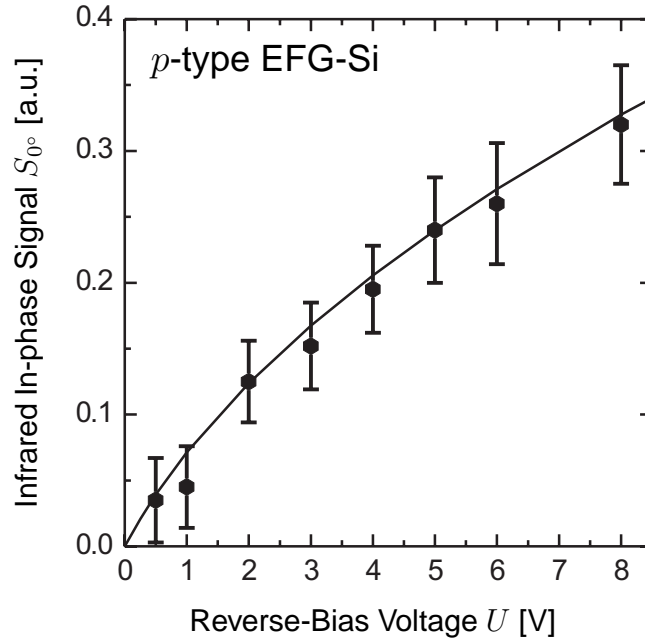


Figure 8.5: Measurement of the in-phase signal  $S_{0^0}$  as a function of the reverse-bias voltage  $U$  of a  $pn$ -junction on an EFG  $p$ -type silicon wafer. An abrupt junction is assumed to fit the experimental data using the same proportionality constant  $M$  as determined from the experimental data shown in Fig. 8.3.

centration of  $(2.3 \pm 0.2) \times 10^{15} \text{ cm}^{-3}$ , which is in excellent agreement with four-point probe measurements of the same wafer yielding  $(2.5 \pm 0.3) \times 10^{15} \text{ cm}^{-3}$ .

The error in  $M$  is 5% and results in an error of 10% for the determination of  $N_A$ . This shows that ICM permits the determination of acceptor concentrations of about  $2 \times 10^{15} \text{ cm}^{-3}$  with an accuracy of 10%. The lateral resolution of the capacitance mapping is 170  $\mu\text{m}$ . The standard deviation of the acceptor concentration signal of all evaluated detector pixels is smaller than 1%. We thus conclude that the inhomogeneity of the acceptor concentration of the  $p$ -type EFG silicon is smaller than 1%.

In addition, we plot in Fig. 8.5 a theoretical curve of the in-phase signal  $S_{0^0}$  versus the applied reverse bias  $U$  applying Eq. (8.4). For this, we use the determined values of the acceptor concentration of the EFG silicon sample and the constant of proportionality  $M$  given by our calibration. A good agreement between the experimental data and the theoretical fit is obtained.

## 8.4 Sensitivity analysis

We use the FZ silicon samples with the acceptor doping concentration of  $4 \times 10^{15} \text{ cm}^{-3}$  to investigate the sensitivity of the ICM technique. Applying a reverse bias of 5 V, the capacitance is simply derived from Eq. (8.4) as:

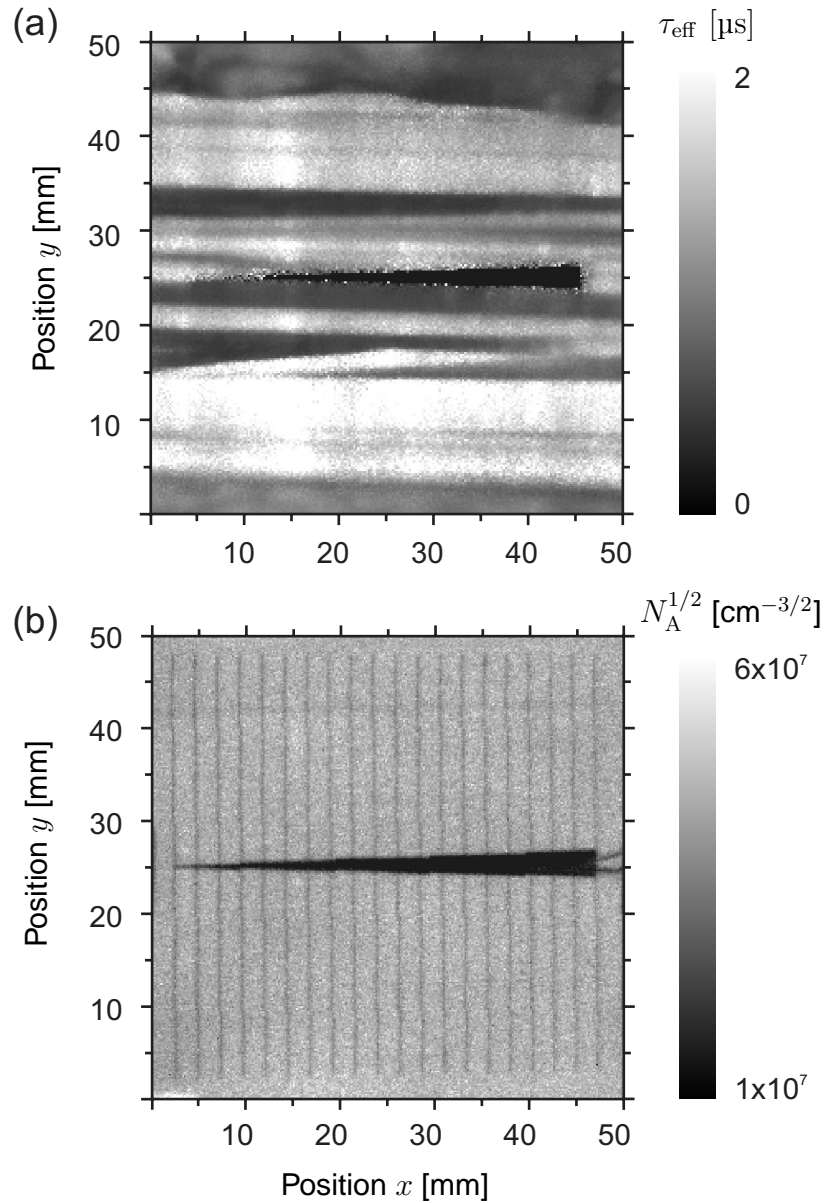


Figure 8.6: (a) Lifetime mapping by microwave-detected photoconductance decay of a *p*-type EFG silicon wafer measured at room temperature. The sample has no surface passivation. (b) Image of the square root of the doping concentration  $N_A^{1/2}$  of the same sample as measured by the ICM technique at 60°C. The applied reverse-bias voltage  $U$  is switched between 0 and 5 V at a frequency of 2.43 Hz. The doping concentration is homogeneous with  $N_A = (2.3 \pm 0.2) \times 10^{15} \text{ cm}^{-3}$ .

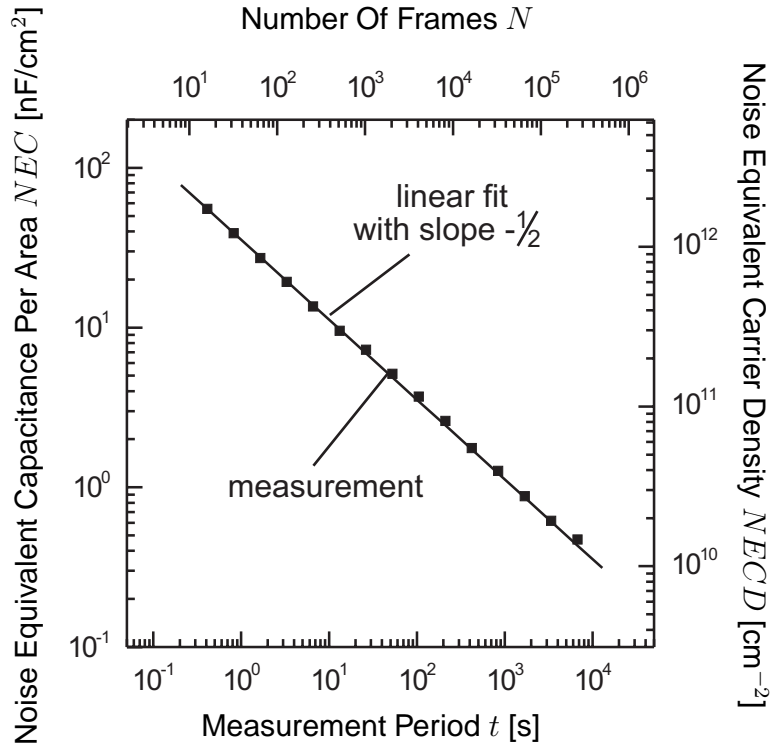


Figure 8.7: Measurement of the experimental noise equivalent carrier density  $NEC$  at  $60^\circ\text{C}$ . Image averaging leads to a sensitivity of  $1\text{ nF cm}^{-2}$  in a measurement period of 28 min. This sensitivity corresponds to a charge density of  $3 \times 10^{10}\text{ cm}^{-2}$  at a lateral resolution of  $170\text{ }\mu\text{m}$ . The applied reverse bias is periodically switched between  $0\text{ V}$  and  $5\text{ V}$ .

$$C = -\frac{\Delta N \cdot q}{U} = -\frac{S_{0^\circ} \cdot q}{M \cdot U}. \quad (8.5)$$

The signal noise is measured as the standard deviation of the in-phase signal  $S_{0^\circ}$  in an area with homogeneous capacitance [12], as discussed in Sec. 5.2.4. Applying Eq. (8.5) to the standard deviation  $\Delta S_{0^\circ}$  leads to the noise equivalent capacitance  $NEC$ .

Fig. 8.7 shows a measurement of the  $NEC$  as a function of the number of evaluated frames  $N$ . The slope of the linear fit in the double logarithmic plot shows that the  $NEC$  decreases with the square root of the inverse of the number of evaluated frames  $\sqrt{\frac{1}{N}}$ , as theoretically expected. After a measurement period of 28 min a  $NEC$  of  $1\text{ nF cm}^{-2}$  is measured. This shows that the ICM technique enables us to measure a capacitance of  $10\text{ nF cm}^{-2}$  with an accuracy of 10% after a measurement period of 28 min at a spatial resolution of  $170\text{ }\mu\text{m}$ . For comparison, Fig. 8.7 shows also the noise equivalent carrier density  $NECD$  corresponding to the  $NEC$ . After a measurement period of 56 min a  $NECD$  of  $2 \times 10^{10}\text{ cm}^{-2}$  is measured. Further noise reduction is achievable at higher temperatures  $T_W$  due to a stronger infrared

emission of the free carriers.

## 8.5 Summary and conclusion

In conclusion, we demonstrated that lock-in thermography enables a fast imaging of the capacitance of semiconductor  $pn$ -junctions.

We applied the ICM technique to determine the laterally resolved acceptor concentration  $N_A(x, y)$  of  $p$ -type multicrystalline EFG silicon wafers. The acceptor concentration determined by ICM agrees with data derived from four-point probe measurements within 10 % deviation. Our experimental findings revealed that ICM permits the determination of acceptor concentrations of about  $2 \times 10^{15} \text{ cm}^{-3}$  with an accuracy of 10 %.

The sensitivity expressed by the noise equivalent capacitance  $NEC$  depends on the measurement period. After a measurement period of 28 min we find a  $NEC$  of  $1 \text{ nF cm}^{-2}$  corresponding to a noise equivalent carrier density  $NECD$  of  $3 \times 10^{10} \text{ cm}^{-2}$  at a lateral resolution of  $170 \mu\text{m}$ . Thus, very small capacitances and carrier densities are measurable.

Deep-level transient spectroscopy (DLTS [177]) is a standard technique to analyse defects in semiconductors. This method is based on transient capacitance measurements at variable temperatures. Since ICM can be easily performed at variable temperatures [156], a new path towards spatially resolved DLTS could be opened, if the sensitivity of the ICM technique is further improved.

# Bibliography

- [1] J. Luther, Photovoltaik - Energielieferant der Zukunft, *Fach.Journal* **2005/2006**, 14–20 (2006).
- [2] W.P. Hirshman and M. Schmela, Silicon shortage - so what!, *Photon International* 100–125 (March 2006).
- [3] P.K. Kuo, T. Ahmed, L.D. Favro, H.-J. Jin and R.L. Thomas, Synchronous thermal wave ir video imaging for nondestructive evaluation, *J. of Nondestructive Evaluation* **8**, 97–106 (1989).
- [4] D.L. Balageas, P. Levesque and A.A. Deom, Characterization of electromagnetic fields using a lock-in thermographic system, *Proc. SPIE*, 274–285 (1993).
- [5] G. Busse, D. Wu and W. Karpen, Thermal wave imaging with phase sensitive modulated thermography, *J. Appl. Phys.* **71**, 3962–3965 (1992).
- [6] M. Danner and K. Bücher, Reverse characteristics of commercial silicon solar cells - impact of hot spot temperatures and module integrity, *Proc. of the 26th IEEE Photovoltaic Specialists Conference*, 1137–1140 (1997).
- [7] W. Gross, H. Scheuerpflug, T. Hierl, M. Schulz and F. Karg, Defect localization in CuInSe<sub>2</sub> thin filmsolar modules by thermal infrared microscopy, *Proc. of 2nd World Conference on Photovoltaic Energy Conversion*, 522–524 (1998).
- [8] O. Breitenstein, J. Isenberg, C. Ballif, S.W. Glunz and W. Warta, Quantitative local analysis of IV-characteristics of solar cells by thermal methods, *Proc. of 2nd World Conference on Photovoltaic Energy Conversion*, 1382–1385 (1998).
- [9] O. Breitenstein, M. Langenkamp, F. Altmann, D. Katzer, A. Lindner and H. Eggers, Microscopic lock-in thermography investigation of leakage sites in integrated circuits, *Rev. Sci. Instrum.* **71**, 4155–4160 (2000).
- [10] O. Breitenstein, M. Langenkamp, O. Lang and A. Schirmacher, Shunts due to laser scribing of solar cells evaluated by highly sensitive lock-in thermography, *Solar Energy Materials & Solar Cells* **65**, 55–62 (2001).
- [11] M. Langenkamp and O. Breitenstein, Classification of shunting mechanisms in crystalline silicon solar cells, *Solar Energy Materials & Solar Cells* **72**, 433–440 (2002).
- [12] O. Breitenstein and M. Langenkamp, *Lock-in Thermography, Basics and Use for Functional Diagnostics of Electronic Components*, Springer-Verlag, New York (2003).

- 
- [13] J. Isenberg and W. Warta, Spatially resolved evaluation of power losses in industrial solar cells by using new thermographic methods, *Prog. Photovolt: Res. Appl.* **12**, 339–353 (2004).
- [14] M. Kaes, s. Seren, T. Pernau and G. Hahn, Light-modulated lock-in thermography for photosensitive pn-structures and solar cells, *Prog. Photovolt: Res. Appl.* **12**, 355–363 (2004).
- [15] M. Bail, J. Kentsch, R. Brendel and M. Schulz, Lifetime mapping of si wafers by an infrared camera, *Proc. of 28th IEEE Photovoltaic Specialists Conference*, 99–101 (2000).
- [16] R.H. Bube, *Photoelectronic Properties of Semiconductors*, Cambridge, UK (1992).
- [17] D. Macdonald and A. Cuevas, Trapping of minority carriers in multicrystalline silicon, *Appl. Phys. Lett.* **74**, 1710–1712 (1999).
- [18] J. Schmidt, K. Bothe and R. Hezel, Oxygen-related minority-carrier trapping centers in *p*-type Czochralski silicon, *Appl. Phys. Lett.* **80**, 4395–4397 (2002).
- [19] Normenausschuss Materialprüfung (NMP) im DIN (Deutsches Institut für Normung e.V.), Bestimmung des Verunreinigungsgehaltes in Silicium mittels Infrarot-Absorption. Teil 1: Sauerstoff, Technical report, (1995), in German.
- [20] Normenausschuss Materialprüfung (NMP) im DIN (Deutsches Institut für Normung e.V.), Bestimmung des Verunreinigungsgehaltes in Silicium mittels Infrarot-Absorption. Kohlenstoff, Technical report, (1982), in German.
- [21] M.A. Green, *Silicon solar cells, advanced principles and practice*, University of New South Wales, Sydney (1995).
- [22] H.Y. Fan and M. Becker, Infrared optical properties of silicon and germanium, London Butterworth Scientific Publications, editor, *Semiconducting Materials*, 132–145, London (1951).
- [23] D.K. Schroder, R.N. Thomas and J.C. Schwartz, Free carrier absorption in silicon, *IEEE Trans. Elec. Dev.* **25**, 254 (1978).
- [24] J. Isenberg and W. Warta, Free carrier absorption in heavily doped silicon layers, *Appl. Phys. Lett.* **84**, 2265–2267 (2004).
- [25] H.Y. Fan, Infrared absorption in semiconductors, *Rep. Prog. Phys.* **19**, 107–155 (1956).
- [26] P.K. Basu, *Theory of optical processes in semiconductors*, Clarendon Press, Oxford (1997).

- 
- [27] R.A. Smith, *Semiconductors, 2nd Ed.*, Cambridge University Press, New York (1978).
- [28] H. Hara and Y. Nishi, Free carrier absorption in *p*-type silicon, *J. Phys. Soc. Japan* **21**, 1222 (1966).
- [29] P.A. Schumann, W.A. Keenan, A.H. Tong, H.H. Gegenwarth and C.P. Schneider, Silicon optical constants in the infrared, *J. Electrochem. Soc.* **118**, 145–148 (1971).
- [30] W. Spitzer and H.Y. Fan, Infrared absorption in *n*-type silicon, *Phys. Rev.* **108**, 268–271 (1957).
- [31] J. Isenberg, *Neue Infrarotmesstechniken für die Photovoltaik*, PhD thesis, Universität Konstanz (2003), in German.
- [32] J.S. Blakemore, *Semiconductor statistics*, Dover Publications, Inc., Mineola, New York (1987).
- [33] J. Schmidt, *Untersuchungen zur Ladungsträgerrekombination an den Oberflächen und im Volumen von kristallinen Silicium-Solarzellen*, PhD thesis, Universität Hannover (1998), in German.
- [34] A.G. Aberle, *Crystalline silicon solar cells - advanced surface passivation and analysis*, Habilitation, University of New South Wales, Sydney (1999).
- [35] R.J. Nelson and R.G. Sobers, Minority-carrier lifetime and internal quantum efficiency of surface-free gaas, *J. Appl. Phys.* **49**, 6103 (1978).
- [36] H. Schlangenotto, H. Maeder and W. Gerlach, Temperature dependence of the radiative recombination coefficient in silicon, *Phys. Stat. Sol. A* **21**, 357–367 (1974).
- [37] J. Dziewior and W. Schmid, Auger coefficients for highly doped and highly excited silicon, *Appl. Phys. Lett.* **31**, 346 (1977).
- [38] M.J. Kerr, P. Campbell and A. Cuevas, Lifetime and efficiency limits of crystalline silicon solar cells, *Proc. of 29th IEEE Photovoltaic Specialists Conference, New Orleans*, p. 438 (2002).
- [39] E. Yablonovitch and T. Gmitter, Auger recombination in silicon at low carrier densities, *Appl. Phys. Lett.* **49**, 587 (1986).
- [40] A. Hangleiter and R. Häcker, Enhancement of band-to-band Auger recombination in crystalline silicon, *Phys. Rev. Lett.* **65**, 215–218 (1990).
- [41] P.P. Altermatt, J. Schmidt, G.Heister and A.G. Aberle, Assessment and parametrisation of Coulomb-enhanced Auger recombination coefficients in lowly injected crystalline silicon, *J. Appl. Phys.* **82**, 4938 (1997).

- 
- [42] J. Schmidt, M. Kerr and P.P. Altermatt, Coulomb-enhanced Auger recombination in crystalline silicon at intermediate and high-injection densities, *J. Appl. Phys.* **88**, 1494 (2000).
- [43] P.P. Altermatt, J. Schmidt, M. Kerr, G. Heiser and A.G. Aberle, Exciton-enhanced Auger recombination in crystalline silicon under intermediate and high injection conditions, *Proc. of 16th European Photovoltaic Solar Energy Conference*, p. 243 (2000).
- [44] M.J. Kerr and A. Cuevas, General parametrization of Auger recombination in crystalline silicon, *J. Appl. Phys.* **91**, 2473–2480 (2002).
- [45] K. Bothe, *Oxygen-related trapping and recombination centres in boron-doped crystalline silicon*, PhD thesis, Universität Hannover (2006).
- [46] W. Shockley and W.T.J. Read, Statistics of the recombinations of holes and electrons, *Phys. Rev.* **87**, 835–842 (1952).
- [47] R.N. Hall, Electron-hole recombination in germanium, *Phys. Rev.* **87**, 387 (1952).
- [48] H. Flietner, Passivity and electronic properties of the silicon/silicon dioxide interface, *Mat. Sci. Forum* **185-188**, 73–82 (1995).
- [49] W. Füssel, M. Schmidt, H. Angermann, G. Mende and H. Flietner, Defects at the Si/SiO<sub>2</sub> interface: their nature and behaviour in technological processes and stress, *Nucl. Instrm. and Meth. in Phys. Res.* **377**, 177–183 (1996).
- [50] M.Y. Ghannam, A new  $n^+pn^+$  structure with back side floating junction for high efficiency silicon solar cells, *Proc. of the 22nd IEEE Photovoltaic Specialists Conference*, p. 284 (1991).
- [51] J.G. Fossum, R.D. Nasby and S.C. Pao, Physics underlying the performance of back-surface-field solar cells, *IEEE Trans. Elec. Dev.* **27**, 785 (1980).
- [52] T. Lauinger, J. Schmidt, A.G. Aberle and R. Hezel, Record low surface recombination velocities on 1 ohm cm  $p$ -silicon using remote plasma silicon nitride passivation, *Appl. Phys. Lett.* **69**, 1232 (1996).
- [53] J.E. Mahan, T.W. Ekstedt, R.I. Frank and R. Kaplow, Measurement of the minority-carrier lifetime in solar cells from photo-induced open circuit voltage decay, *IEEE Trans. Elec. Dev.* **ED-26**, 733–739 (1979).
- [54] B.H. Rose and H.T. Weaver, Determination of the effective surface recombination velocity and minority-carrier lifetime in high-efficiency silicon solar cells, *J. Appl. Phys.* **54**, 238–247 (1983).



- 
- [55] R.A. Sinton and A. Cuevas, A steady-state open-circuit voltage method for solar cell characterization, *Proc. of 16th European Photovoltaic Solar Energy Conference*, p. 1152 (2000).
- [56] G.L. Miller, D.A.H. Robinson and J.D. Wiley, Contactless measurement of semiconductor conductivity by rf free carrier power absorption, *Rev. Sci. Instrum.* **47**, 799 (1976).
- [57] T. Trupke, R.A. Bardos, F. Hudert, P. Würfel, J. Zhao, A. Wang and M.A. Green, Effective excess carrier lifetimes exceeding 100 milliseconds in float zone silicon determined from photoluminescence, *Proc. of 19th European Photovoltaic Solar Energy Conference*, 758–761 (2004).
- [58] T. Trupke, R. A. Bardos and M. D. Abbott, Self-consistent calibration of PL and PC lifetime measurements, *Appl. Phys. Lett.* **87**, 184102 (2005).
- [59] T. Trupke, R. A. Bardos, M. D. Abbott and J. E. Cotter, Sun-photoluminescence: Contactless determination of current-voltage characteristics of silicon wafers, *Appl. Phys. Lett.* **87**, 093503 (2005).
- [60] T. Fuyuki, H. Kondo, Y. Kaji, T. Yamazaki, Y. Takahashi and Y. Uraoka, One shot mapping of minority carrier diffusion length in polycrystalline silicon solar cells using electroluminescence, *Proc. of 31th IEEE Photovoltaic Specialists Conference*, 1343–1345 (2005).
- [61] S.W. Glunz and W. Warta, High-resolution lifetime mapping using modulated free-carrier absorption, *J. Appl. Phys.* **77**, 3243–3247 (1995).
- [62] S. Riepe, J. Isenberg, C. Ballif, S.W. Glunz and W. Warta, Carrier density and lifetime imaging of silicon wafers by infrared lock-in thermography, *Proc. of 17th European Photovoltaic Solar Energy Conference*, 1597–1600 (2001).
- [63] R. Brendel, M. Bail and B. Bodmann, Analysis of photoexcited charge carrier density profiles in Si wafers by using an infrared camera, *Appl. Phys. Lett.* **80**, 437–439 (2002).
- [64] N. Enjalbert, F. Coustier, N. Le Quang and R. Sinton, Automated in-line control of electrical parameters on large dimension mc-Si wafers on industrial scale, *Proc. of 20th European Photovoltaic Solar Energy Conference*, 1124–1127 (2005).
- [65] A. Bentzen, H. Tathgar, J. Barthez and A. Holt, High trap densities in wafers from regions of reduced lifetime in mc silicon blocks, *Proc. of 15th International Science and Engineering Conference*, 879–882 (2005).
- [66] M. Schöfthaler and R. Brendel, Sensitivity and transient response of microwave reflection measurements, *J. Appl. Phys.* **77**, 3162 (1995).

- [67] J.W. Orton and P. Blood, *The electrical characterization of semiconductors*, Academic Press, Inc., London (1990).
- [68] R.A. Sinton and A. Cuevas, Contactless determination of current-voltage characteristics and minority-carrier lifetimes in semiconductors from quasi steady-state photoconductance data, *Appl. Phys. Lett.* **69**, 2510 (1996).
- [69] T. Trupke, R.A. Bardos, M.D. Abbott, F.W. Chen, J.E. Cotter and A. Lorenz, Fast photoluminescence imaging of silicon wafers, *Proc. of 4th World Conference on Photovoltaic Energy Conversion* (2006).
- [70] R.A. Bardos, J. Cotter, T. Trupke and A. Lorenz, Comparison of  $n$  and  $p$  type ribbon grown multicrystalline silicon wafers using photoluminescence imaging, *Proc. of 4th World Conference on Photovoltaic Energy Conversion* (2006).
- [71] M.D. Abbott, J.E. Cotter, T. Trupke, K. Fisher and R.A. Bardos, Application of photoluminescence to high-efficiency silicon solar cell fabrication, *Proc. of 4th World Conference on Photovoltaic Energy Conversion* (2006).
- [72] M.D. Abbott, J.E. Cotter, T. Trupke and R.A. Bardos, Investigation of edge recombination effects in silicon solar cell structures using photoluminescence, *Appl. Phys. Lett.* **88**, 114105 (2006).
- [73] F.W. Chen, J.E. Cotter, T. Trupke and R.A. Bardos, Characterization of PECVD silicon nitride passivation with photoluminescence imaging, *Proc. of 4th World Conference on Photovoltaic Energy Conversion*, 1372–1375 (2006).
- [74] S. M. Sze, *Physics of Semiconductor Devices, 2nd Ed.*, John Wiley & Sons (1981).
- [75] M.A. Green, *Solar Cells: Operating Principles, Technology and System Applications*, University of New South Wales, Kensington (1986).
- [76] G.S. Kousik, Z.G. Ling and P.K. Ajmera, Nondestructive technique to measure bulk lifetime and surface recombination velocities at the two surfaces by infrared absorption due to pulsed optical excitation, *J. Appl. Phys.* **72**, 141–146 (1992).
- [77] M. Boulou and D. Bois, Cathodoluminescence measurements of the minority-carrier lifetime in semiconductors, *J. Appl. Phys.* **48**, 4713–4721 (1977).
- [78] K.L. Luke and L.J. Cheng, Analysis of the interaction of a laser pulse with a silicon wafer: determination of bulk lifetime and surface recombination velocity, *J. Appl. Phys.* **61**, 2282–2293 (1987).
- [79] J. Schmidt and A.G. Aberle, Accurate method for the determination of bulk minority-carrier lifetimes of mono- and multicrystalline silicon wafers, *J. Appl. Phys.* **81**, 6186–6198 (1997).

- 
- [80] A.B. Sproul, Dimensionless solution of the equation describing the effect of surface recombination on carrier decay in semiconductors, *J. Appl. Phys.* **76**, 2851–2854 (1994).
- [81] H. Nagel, C. Berge and A.G. Aberle, Generalized analysis of quasi-steady-state and quasi-transient measurements of carrier lifetimes in semiconductors, *J. Appl. Phys.* **86**, 6218–6221 (1999).
- [82] A. Cuevas and R. Sinton, Prediction of the open-circuit voltage of solar cells from the steady-state photoconductance, *Prog. Photovoltaics* **5**, 79–90 (1997).
- [83] D.T. Stevenson and R.J. Keyes, Measurement of carrier lifetimes in germanium and silicon, *J. Appl. Phys.* **26**, 190–195 (1955).
- [84] M. Kunst and G. Beck, The study of charge carrier kinetics in semiconductors by microwave conductivity measurements. I, *J. Appl. Phys.* **60**, 3558 (1986).
- [85] M. Kunst and G. Beck, The study of charge carrier kinetics in semiconductors by microwave conductivity measurements. II, *J. Appl. Phys.* **63**, 1093 (1988).
- [86] M. Schöffthaler, *Transiente Mikrowellenreflexion zur kontaktlosen Trägerlebensdauerermessung an Silizium für Solarzellen*, PhD thesis, Max-Planck-Institut für Festkörperforschung Stuttgart (1995), in German.
- [87] R. Brendel, Note on the interpretation of injection-level-dependent surface recombination velocities, *Appl. Phys. A* **60**, 523–524 (1995).
- [88] F.M. Schuurmans, A. Schönecker, A. R. Burgers and W.C. Sinke, Simplified evaluation method for light-biased effective lifetime measurements, *Appl. Phys. Lett.* **71**, 1795 (1997).
- [89] R. Brendel and M. Wolf, Differential and actual surface recombination velocities, *Proc. of 13th European Photovoltaic Solar Energy Conference*, 428–431 (1995).
- [90] A.G. Aberle, J. Schmidt and R. Brendel, On the data analysis of light-biased photoconductance decay measurements, *J. Appl. Phys.* **79**, 1491–1496 (1996).
- [91] J. Schmidt, Measurement of differential and actual recombination parameters on crystalline silicon wafers, *IEEE Trans. Elec. Dev.* **46**, 2018–2025 (1999).
- [92] F. Dannhäuser, Die Abhängigkeit der Trägerbeweglichkeit in Silizium von der Konzentration der freien Ladungsträger - I, *Solid State Elect.* **15**, 1371–1375 (1972).
- [93] J. Krausse, Die Abhängigkeit der Trägerbeweglichkeit in Silizium von der Konzentration der freien Ladungsträger - II, *Solid State Elect.* **15**, 1377–1381 (1972).

- 
- [94] J.M. Dorkel and Ph. Leturcq, Carrier mobilities in silicon semi-empirically related to temperature, doping and injection level, *Solid State Elect.* **84**, 821–825 (1981).
- [95] V. Grivitskas, M. Willander and J. Vaitkus, The role of intercarrier scattering in excited silicon, *Solid State Elect.* **27**, 565–572 (1984).
- [96] D.-H. Neuhaus, *Electrical characterisation of crystalline silicon for thin-film solar cells*, PhD thesis, University of New South Wales, Australia (2004).
- [97] L.B. Valdes, Resistivity measurements on germanium for transistors, *Proc. IRE*, volume 42, 420–427 (1954).
- [98] D.K. Schroder, *Semiconductor material and device characterisation*, John Wiley & Sons, New York (1990).
- [99] J.C. Irvin, Resistivity of bulk silicon and of diffused layers in silicon, *Bell Sys. Tec. J.* **41**, 387–410 (1962).
- [100] ASTM International, *Annual book of ASTM standards*, volume 10.05 Electronics (II) F723-99 (1999).
- [101] J.A. Hornbeck and J.R. Haynes, Trapping of minority carriers in silicon. I. *p*-type silicon, *Phys. Rev.* **97**, 311–321 (1955).
- [102] J.R. Haynes and J.A. Hornbeck, Trapping of minority carriers in silicon. II. *n*-type silicon, *Phys. Rev.* **100**, 606–615 (1955).
- [103] M. Bail, M. Schulz and R. Brendel, Space-charge region-dominated steady-state photoconductance in low-lifetime Si wafers, *Appl. Phys. Lett.* **82**, 757 (2003).
- [104] M. Bail, *Ladungsträger-Lebensdauer in kristallinem Silicium für die Photovoltaik*, PhD thesis, Friedrich-Alexander-Universität Erlangen-Nürnberg (2002), in German.
- [105] D.H. Neuhaus, Trapping and junction-related perturbations of the effective excess carrier lifetime, *Proc. of 3rd World Conference on Photovoltaic Energy Conversion*, 91–94 (2003).
- [106] P.J. Cousins, D.H. Neuhaus and J.E. Cotter, Experimental verification of the effect of depletion-region modulation of photoconductance lifetime measurements, *J. Appl. Phys.* **95**, 1854 (2004).
- [107] P.Pohl, J. Schmidt, K. Bothe and R. Brendel, Mapping of trap densities and energy levels in semiconductors using a lock-in infrared camera technique, *Appl. Phys. Lett.* **87**, 142104 (2005).

- 
- [108] M. C. Schubert, J. Isenberg, S. Rein, S. Bermejo, S.W. Glunz and W. Warta, Injection dependent carrier density imaging measurements including correction for trapping effects, *Proc. of 20th European Photovoltaic Solar Energy Conference*, 1202–1205 (2005).
- [109] S. Dauwe, J. Schmidt, A. Metz and R. Hezel, Fixed charge density in silicon nitride films on crystalline silicon surfaces under illumination, *Proc. of 29th IEEE Photovoltaic Specialists Conference*, 162–164 (2002).
- [110] S. Dauwe, *Low-temperature rear surface passivation of crystalline silicon solar cells*, PhD thesis, Universität Hannover (2003).
- [111] R. Plieninger, H. Morikawa and S. Arimoto, A new two-dimensional analytical model and experimental results on the influence of dislocations on minority carrier transport in solar cells, *Proc. of 13th European Photovoltaic Solar Energy Conference*, 395–398 (1995).
- [112] J.C. Zolper and A.M. Barnett, The effect of dislocations on the open-circuit voltage of GaAs solar cells, *IEEE Trans. Elec. Dev.* **37**, 478 (1990).
- [113] K. Misiakos and D. Tsamakis, Accurate measurements of the silicon intrinsic carrier density from 78 to 340 K, *J. Appl. Phys.* **74**, 3293 (1993).
- [114] B. Fischer, *Loss analysis of crystalline silicon solar cells using photoconductance and quantum efficiency measurements*, PhD thesis, Universität Konstanz, Konstanz (2003).
- [115] J.M. Hwang and D.K. Schroder, Recombination properties of oxygen-precipitated silicon, *J. Appl. Phys.* **59**, 2476–2487 (1985).
- [116] AIM. *AIM 640Q thermography system documentation*. Heilbronn, (2000).
- [117] Edevis GmbH. *Betriebsanleitung NDT-Thermographiesystem*. Stuttgart, (2003).
- [118] [www.iaf.frauenhofer.de](http://www.iaf.frauenhofer.de), (2005).
- [119] [www.sofradir.com](http://www.sofradir.com). Sofradir, (2005).
- [120] [www.edevis.de](http://www.edevis.de). Edevis GmbH, (2005).
- [121] B.F. Levine, Quantum-well infrared photodetectors, *J. Appl. Phys.* **74**, R1–R81 (1993).
- [122] H. Schneider, C. Schönbein, M. Walther, K. Schwarz, J. Fleissner and P. Koidl, Photovoltaic quantum well infrared photodetectors: the four-zone scheme, *Appl. Phys. Lett.* **71**, 246 (1997).

- 
- [123] J. Isenberg, S. Riepe, S.W. Glunz and W. Warta, Carrier density imaging (CDI): a spatially resolved lifetime measurement suitable for in-line process control, *Proc. of 29th IEEE Photovoltaic Specialists Conference* (2002).
- [124] M. C. Schubert, J. Isenberg and W. Warta, Spatially resolved lifetime imaging of silicon wafers by measurement of infrared emission, *J. Appl. Phys.* **94**, 4139–4143 (2003).
- [125] N.G. Nillson, Determination of carrier lifetime, diffusion length, and surface recombination velocity in semiconductors from photo-excited infrared absorption, *Solid State Elect.* **7**, 455–463 (1964).
- [126] M.A. Afromowitz, Measurement of free-carrier lifetimes in GaP by photoinduced modulation of infrared absorption, *J. Appl. Phys.* **42**, 3205 (1971).
- [127] J.A. Mroczkowski, J.F. Shanley, M.B. Reine, P. LoVecchio and D.L. Polla, Lifetime measurement in  $\text{Hg}_{0.7}\text{Cd}_{0.3}\text{Te}$  by population modulation, *Appl. Phys. Lett.* **38**, 261 (1981).
- [128] J.C. White and J.G. Smith, Observation of carrier densities in silicon devices by infrared emission, *Journal of Phys. E* **10**, 817–825 (1977).
- [129] J. Isenberg, D. Biro and W. Warta, Fast, contactless and spatially resolved measurement of sheet resistance by an infrared method, *Prog. Photovolt: Res. Appl.* **12**, 539–552 (2004).
- [130] J. Isenberg, M.C. Schubert, D. Biro, A. Froitzheim and W. Warta, Sheet resistance imaging (SRI) - a contactless and spatially resolved method for the determination of doping inhomogeneities, *Proc. of 20th European Photovoltaic Solar Energy Conference*, 674–677 (2005).
- [131] S.M. Johnson and L.G. Johnson, Contactless measurement of bulk free-carrier lifetime in cast polycrystalline silicon ingots, *J. Appl. Phys.* **60**, 2008–2015 (1986).
- [132] T. Warabisako, T. Saitoh, T. Motooka and T. Tokuyama, Contactless measurement of wafer lifetime by free carrier infrared absorption, *Proc. of the 14th Conference on Solid State Devices*, 557–560 (1982).
- [133] G.A. Landis and H. Stoddart, Measurement of minority carrier lifetime by pulsed photoabsorption decay, *Proc. of the 19th IEEE Photovoltaic Specialists Conference*, 761–763 (1987).
- [134] J. Linnros, Carrier lifetime measurements using free carrier absorption transients. I. principle and injection dependence, *J. Appl. Phys.* **84**, 275–283 (1998).

- [135] J. Linnros, Carrier lifetime measurements using free carrier absorption transients. II. lifetime mapping and effects of surface recombination, *J. Appl. Phys.* **84**, 284–291 (1998).
- [136] F. Sanii, R.J. Schwartz, R.F. Pierret and W.M. Au, The measurement of bulk and surface recombination by means of modulated free carrier absorption, *Proc. of 20th IEEE Photovoltaic Specialists Conference*, p. 575 (1988).
- [137] J. Isenberg, S. Riepe, S.W. Glunz and W. Warta, Imaging method for laterally resolved imaging method for laterally resolved measurement of minority carrier densities and lifetimes: Measurement principle and first applications, *J. Appl. Phys.* **93**, 4268–4275 (2003).
- [138] R. Brendel, M. Bail and B. Bodmann, Analysis of photoexcited charge carrier density profiles in silicon wafers by using an infrared camera, *Appl. Phys. Lett.* **80**, 437 (2002).
- [139] H. Plagwitz, M. Schaper, A. Wolf, R. Meyer, J. Schmidt, B. Terheiden and R. Brendel, 20%-efficient silicon solar cells with local contacts to the a-Si-passivated surfaces by means of annealing (COSIMA), *Proc. of 20th European Photovoltaic Solar Energy Conference*, 725–728 (2005).
- [140] S. Dauwe, J. Schmidt and R. Hezel, Very low surface recombination velocities on *p* and *n*-type silicon wafers passivated with hydrogenated amorphous silicon films, *Proc. of 29th IEEE Photovoltaic Specialists Conference*, 1246–49 (2002).
- [141] A. Cuevas and D. Macdonald, Multicrystalline silicon: a review of its electronic properties, *Proc. of the 15th International Photovoltaic Science and Engineering Conference*, 521–524 (2005).
- [142] W. Schmidt, B. Woesten and J.P. Kalejs, Manufacturing technology for ribbon silicon (EFG) wafers and solar cells, *Prog. Photovolt: Res. Appl.* **10**, 129–140 (2002).
- [143] J. Schmidt, Temperature- and injection-dependent lifetime spectroscopy for the characterization of defect centers in semiconductors, *Appl. Phys. Lett.* **82**, 2178 (2003).
- [144] F. Shimura, T. Okui and T. Kusama, Noncontact minority-carrier lifetime measurement at elevated temperatures for metal-doped Czochralski silicon crystals, *J. Appl. Phys.* **67**, 7168–7171 (1990).
- [145] S. Rein, T. Rehrl, W. Warta and S.W. Glunz, Lifetime spectroscopy for defect characterization: Systematic analysis of the possibilities and restrictions, *J. Appl. Phys.* **91**, 2059–2070 (2002).
- [146] M.C. Schubert, J. Isenberg, S. Rein and W. Warta, Temperature dependent carrier lifetime images, *Proc. of 19th European Photovoltaic Solar Energy Conference* (2004).

- 
- [147] E.R. Weber, Transition metals in silicon, *Appl. Phys. A* **30**, 1–22 (1983).
- [148] A.A. Istratov, Iron and its complexes in Si, *Appl. Phys. A* **69**, 13–44 (1999).
- [149] G.W. Ludwig and H.H. Woodbury, Electron spin resonance in semiconductors, *Solid State Phys.* **13**, 223–304 (1962).
- [150] J. Schmidt and D. Macdonald, Recombination activity of iron-gallium and iron-indium pairs in silicon, *J. Appl. Phys.* **97**, 113712 (2005).
- [151] K. Graff and H. Pieper, The properties of iron in silicon, *J. Electrochem. Soc.* **128**, 669–674 (1981).
- [152] G. Zoth and W. Bergholz, A fast, preparation-free method to detect iron in silicon, *J. Appl. Phys.* **67**, 6764–6771 (1990).
- [153] D. Macdonald, L.J. Geerligs and A. Azzizi, Iron detection in crystalline silicon by carrier lifetime measurements for arbitrary injection and doping, *J. Appl. Phys.* **95**, 1021–1028 (2004).
- [154] A.A. Istratov, H. Hieslmair and E.R. Weber, Iron contamination in silicon technology, *Appl. Phys. A* **70**, 489–534 (2000).
- [155] J.E. Birkholz, K. Bothe, D. Macdonald and J. Schmidt, Electronic properties of iron-boron pairs in crystalline silicon by temperature- and injection-level-dependent lifetime measurements, *J. Appl. Phys.* **97**, 103708 (2005).
- [156] P. Pohl and R. Brendel, Temperature dependent infrared camera lifetime mapping (ILM), *Proc. of 19th European Photovoltaic Solar Energy Conference*, 46–49 (2004).
- [157] P. Pohl, J. Schmidt, K. Bothe and R. Brendel, Trap density imaging of silicon wafers using a lock-in infrared camera technique, *Proc. of 4th World Conference on Photovoltaic Energy Conversion* (2006).
- [158] J. Schmidt, P. Pohl, K. Bothe, C. Schmiga, R. Krain and R. Brendel, Advanced defect characterization techniques in crystalline silicon-based photovoltaics, *Proc. of 21th European Photovoltaic Solar Energy Conference* (2006).
- [159] P. Pohl, J. Schmidt, C. Schmiga and R. Brendel, Defect imaging in multicrystalline silicon using a lock-in infrared camera technique, *J. Appl. Phys.* **101**, 073701 (2007).
- [160] J.R. Haynes and J.A. Hornbeck, Temporary traps in silicon and germanium, *Phys. Rev.* **90**, 152–153 (1952).
- [161] H.Y. Fan, Effects of traps on carrier injection in semiconductors, *Phys. Rev.* **92**, 1424–1428 (1953).



- 
- [162] D. MacDonald and A. Cuevas, Understanding carrier trapping in multicrystalline silicon, *Solar Energy Materials & Solar Cells* **65**, 509–516 (2001).
- [163] W.H. Press, S. A. Teukolsky, W. T. Vetterling and B. P. Flannery, *Numerical Recipes in C*, Cambridge University Press, 2nd Edition (1999).
- [164] I. Fusegawa and H. Yamagishi, Evaluation of interstitial oxygen along striations in Cz silicon single crystals with a micro-FTIR mapping system, *Semicon. Sci. Techn.* **7**, 304 (1992).
- [165] W.C. Dash, Copper precipitation on dislocations in silicon, *J. Appl. Phys.* **27**, 1193 (1957).
- [166] B.L. Sopori, L. Jastrzebski, T. Tan and S. Narayanan, Gettering effects in polycrystalline silicon, *Proc. of 12th European Photovoltaic Solar Energy Conference*, p. 1003 (1994).
- [167] T.S. Fell, P.R. Wilshaw and M.D.D Coteau, EBIC investigations of dislocations and their interactions with impurities in silicon, *Phys. Status Solidi A* **138**, 695 (1993).
- [168] V. Higgs and M. Kittler, Investigation of the recombination activity of misfit dislocations in Si/SiGe epilayers by cathodoluminescence imaging and the EBIC technique, *Appl. Phys. Lett.* **63**, 2085 (1993).
- [169] M. Kittler, W. Seifert and V. Higgs, Recombination activity of misfit dislocations in silicon, *Phys. Status Solidi A* **137**, 327 (1993).
- [170] S. Pizzini, A. Sandrinelli, M. Beghi, D. Narducci, F. Allegretti, S. Torchio, G. Fabbri, G.P. Ottaviani, F. Demartin and A. Fusi, Influence of extended defects and native impurities on the electrical properties of directionally solidified polycrystalline silicon, *J. Electrochem. Soc.* **135**, 155 (1988).
- [171] S.A. McHugo, H. Hieslmair and E.R. Weber, Gettering of metallic impurities in photovoltaic silicon, *Appl. Phys. A* **64**, 127–137 (1997).
- [172] M. Kittler and W. Seifert, Estimation of the upper limit of the minority-carrier diffusion length in multicrystalline silicon: limitation of the action of gettering and passivation on dislocations, *Solid State Phenomena* **95-96**, 197–204 (2004).
- [173] W. van Gelder and E.H. Nicollian, Silicon impurity distribution as revealed by pulsed MOS C-V measurements, *J. Electrochem. Soc.* **118**, 138–141 (1971).
- [174] P. Pohl and R. Brendel, Infrared capacity mapping of semiconductor junctions by lock-in thermography, *Appl. Phys. Lett.* **87**, 032104 (2005).

- [175] P. Pohl and R. Brendel, Mapping of solar cell base doping concentration using lock-in thermography, *Proc. of 20th European Photovoltaic Solar Energy Conference*, 140–143 (2005).
- [176] H.S. Carslaw and J.C. Jaeger, *Conduction of Heat in Solids, 2nd Ed.*, Oxford University Press, Oxford (1986).
- [177] D. V. Lang, Deep-level transient spectroscopy: A new method to characterize traps in semiconductors, *J. Appl. Phys.* **45**, 3023–3032 (1974).

# List of publications

## Publications arising from the work in this thesis

### *Refereed journal papers*

1. A. Wolf, P. Pohl and R. Brendel, Thermophysical analysis of thin films by lock-in thermography, *J. Appl. Phys.* **96**, 6306–6312 (2004).
2. P. Pohl and R. Brendel, Infrared capacity mapping of semiconductor junctions by lock-in thermography, *Appl. Phys. Lett.* **87**, 032104 (2005).
3. P. Pohl, J. Schmidt, K. Bothe and R. Brendel, Mapping of trap densities and energy levels in semiconductors using a lock-in infrared camera technique, *Appl. Phys. Lett.* **87**, 142104 (2005).
4. D. Macdonald, T. Roth, P.N.K. Deenapanray, K. Bothe, P. Pohl and J. Schmidt, Formation rates of iron-acceptor pairs in crystalline silicon, *J. Appl. Phys.* **98**, 083509 (2005).
5. P. Pohl, J. Schmidt, C. Schmiga and R. Brendel, Defect imaging in multicrystalline silicon using a lock-in infrared camera technique, *J. Appl. Phys.* **101**, 073701 (2007).
6. J. Schmidt, P. Pohl, K. Bothe and R. Brendel, Advances in contactless silicon defect and impurity diagnostics based on lifetime spectroscopy and infrared imaging, *Adv. Optoelec.*, online published (2007).

## *Papers presented at international conferences*

1. P. Pohl and R. Brendel, Temperature-dependent infrared camera lifetime mapping (ILM), *Proceedings of the 19th European Photovoltaic Solar Energy Conference*, 46–49 (2004).
2. A. Wolf, P. Pohl and R. Brendel, Determination of thermophysical properties of thin films for photovoltaic applications, *Proceedings of the 31st IEEE Photovoltaic Specialists Conference*, 1749–1752 (2005).
3. P. Pohl and R. Brendel, Mapping of solar cell base doping concentration using lock-in thermography, *Proceedings of the 20th European Photovoltaic Solar Energy Conference*, 140–143 (2005).
4. J. Henze, P. Pohl, C. Schmiga, M. Dhamrin, T. Saitho, I. Yamaga and J. Schmidt, Millisecond area averaged lifetimes in gallium-doped multicrystalline silicon, *Proceedings of the 20th European Photovoltaic Solar Energy Conference*, 769–772 (2005).
5. S. Winderbaum, A. Cuevas, J. Tan, R. Dunn, P. Pohl, J. Schmidt, J. Han and K. Roth, Unveiling the differences between dynamic and static deposition of PECVD silicon nitride for solar cells, *Proceedings of the 20th European Photovoltaic Solar Energy Conference*, 1301–1304 (2005).
6. P. Pohl, J. Schmidt and R. Brendel, Trap density imaging of silicon wafers using a lock-in infrared camera technique, *Proceedings of the 4th World Conference on Photovoltaic Energy Conversion*, 932–934 (2006).
7. J. Schmidt, P. Pohl, K. Bothe, C. Schmiga, R. Krain and R. Brendel, Advanced defect characterization techniques in crystalline silicon-based photovoltaics, *Proceedings of the 21st European Photovoltaic Solar Energy Conference*, 524–529 (2006).
8. K. Bothe, P. Pohl, J. Schmidt, T. Weber, P. Altermatt, B. Fischer and R. Brendel, Electroluminescence imaging as an in-line characterization tool for solar cell production, *Proceedings of the 21st European Photovoltaic Solar Energy Conference*, 597–600 (2006).
9. P. Pohl, J. Schmidt and R. Brendel, Infrared camera-based defect imaging: trapping versus depletion region modulation around charged bulk defects, *Proceedings of the 22nd European Photovoltaic Solar Energy Conference*, submitted (2007).
10. B. Hoex, J.L. van Hemmen, J. Schmidt, P. Pohl, M.C.M. van de Sanden and W.M.M. Kessels, Excellent surface passivation of c-Si by atomic layer deposited Al<sub>2</sub>O<sub>3</sub>, *Proceedings of the 22nd European Photovoltaic Solar Energy Conference*, submitted (2007).

# Lebenslauf

## Persönliche Daten

---

<b>Name</b>	Peter Pohl
<b>Anschrift</b>	Bergstraße 36, 91301 Forchheim
<b>Geburtsdatum</b>	7. Oktober 1976
<b>Nationalität</b>	deutsch
<b>Familienstand</b>	verheiratet

## Schulbildung

---

<b>1983 - 1987</b>	Annagrundschule in Forchheim
<b>1987 - 1996</b>	Ehrenbürggymnasium in Forchheim Abschluss der allgemeinen Hochschulreife im Juni 1996

## Universitätsausbildung

---

<b>Oktober 1996 bis April 1997</b>	<b>Universität Erlangen-Nürnberg</b> Studium der Physik
<b>Mai 1997 - Juni 1998</b>	<b>Bundeswehr und Zivildienst</b>
<b>Juli 1998 bis April 2003</b>	<b>Universität Erlangen-Nürnberg</b> Diplom-Vorprüfung im Juli 1999 Diplom-Prüfung im Februar 2003

## Anstellung

---

<b>Mai 2003 bis September 2004</b>	<b>Bayerisches Zentrum für angewandte Energieforschung (ZAE)</b> Abteilung Thermosensorik und Photovoltaik Wissenschaftlicher Mitarbeiter im Bereich Thermosensorik
<b>seit Oktober 2004</b>	<b>Institut für Solarenergieforschung (ISFH)</b> Wissenschaftlicher Mitarbeiter im Bereich Photovoltaik – Materialforschung



## Danksagung

Abschließend möchte ich mich bei allen bedanken, die zum Gelingen dieser Arbeit beigetragen haben, insbesondere bei:

Herrn Prof. Dr. Rolf Brendel für die Möglichkeit, diese Arbeit am ZAE Bayern beginnen und am ISFH erfolgreich abschließen zu können, vor allem aber für die hilfreichen Diskussionen und die offene Art, sich auch spontan Zeit zu nehmen.

Herrn Prof. Dr. Herbert Pfnür für die freundliche Übernahme des Korreferats.

Herrn Dr. habil. Jan Schmidt für die exzellente wissenschaftliche Betreuung, die zum Erfolg dieser Arbeit wesentlich beigetragen hat. Unser Gedankenaustausch in weniger wissenschaftlichen Gebieten wird mir fehlen.

Meinen Mitstreitern Klaus Ramspeck, Karsten Bothe, Christian Schmiga, Jürgen Henze und Peter Engelhart für die vielen fruchtbaren Diskussionen und Anregungen und das zur Verfügung stellen unzähliger Proben. Ebenso danke ich Dr. Bernhard Fischer, Dr. Pietro Altermatt und Dr. Nils-Peter Harder für viele kluge Antworten auf einige dumme Fragen.

Für die große Unterstützung beim Probenherstellen möchte ich mich bei Sabine Kirstein, Marita Steinhof, Ulrike Sonntag, Anja Lohse und Agnes Merkle bedanken. Ohne euch wäre ich vermutlich im Reinraum verunglückt.

Meinen Mitstreitern aus ZAE-Zeiten Dr. Barbara Terheiden, Renate Horbelt, Andreas Wolf, Heiko Plagwitz und Adnan Hammud für die angenehme Zusammenarbeit und wohlwollende Unterstützung in allen Lebenslagen. Meinem Bürokollegen Andreas möchte ich vor allem auch für die lustigen Stunden in unserem Büro danken.

Der gesamten Photovoltaik-Gruppe am ISFH für die hervorragende Arbeitsatmosphäre und viele gelungene Feiern.

Allen Mitarbeitern – auch den Ehemaligen – des ZAE Bayern in Tennenlohe für die wundervolle Zeit am ZAE, für die Unterstützung beim Aufbau des Infrarot-Lock-In-Kamerasystems und für die Leihe des Messsystems ans ISFH, wodurch ich meine Doktorarbeit am ISFH vollenden konnte.

Außerdem möchte ich mich ganz herzlich bei externen Kollegen für Ihre Unterstützung und Zusammenarbeit bedanken, insbesondere bei Dr. habil. Otto Breitenstein, Dr. Daniel Macdonald und Brahms Hoex.

Ganz besonderer Dank geht an meine Eltern und meine Familie, die mir durch ihren nie endenden Beistand viel mehr als nur das Schreiben dieser Doktorarbeit ermöglichten.

Großer Dank gilt meiner Frau Steffi für Ihre Liebe, die unsere große räumliche Distanz überbrückt hat, und die wundervolle Zeit miteinander, die ich nicht mehr missen will.